

**RELATIONSHIPS BETWEEN OBSERVED PORE AND PORE-THROAT  
GEOMETRIES, MEASURED POROSITY AND PERMEABILITY, AND  
INDIRECT MEASURES OF PORE VOLUME BY NUCLEAR MAGNETIC  
RESONANCE**

A Dissertation

by

AARON J. ADAMS

Submitted to the Office of Graduate Studies of  
Texas A&M University  
in partial fulfillment of the requirements for the degree of

DOCTOR OF PHILOSOPHY

December 2005

Major Subject: Geology

© 2005

AARON J. ADAMS

ALL RIGHTS RESERVED

**RELATIONSHIPS BETWEEN OBSERVED PORE AND PORE-THROAT  
GEOMETRIES, MEASURED POROSITY AND PERMEABILITY, AND  
INDIRECT MEASURES OF PORE VOLUME BY NUCLEAR MAGNETIC  
RESONANCE**

A Dissertation

by

AARON J. ADAMS

Submitted to the Office of Graduate Studies of  
Texas A&M University  
in partial fulfillment of the requirements for the degree of

DOCTOR OF PHILOSOPHY

Approved by:

Chair of Committee,  
Committee Members,

Head of Department,

Wayne M. Ahr  
Brian J. Willis  
Niall C. Slowey  
Robert R. Berg  
Jerry L. Jensen  
Richard L. Carlson

December 2005

Major Subject: Geology

## ABSTRACT

Relationships Between Observed Pore and Pore-Throat Geometries,  
Measured Porosity and Permeability, and Indirect Measures  
of Pore Volume by Nuclear Magnetic Resonance. (December 2005)

Aaron J. Adams, B.A., Utah State University;

M.S., Brigham Young University

Chair of Advisory Committee: Dr. Wayne M. Ahr

Carbonate reservoirs are a network of pores and connecting pore-throats that contain at least half of the world's oil. Genetic classification of carbonate pores enables one to map the pore types that have greatest influence on reservoir performance. Though NMR logging has been used to estimate pore sizes, it has not been used to identify genetic pore types or to aid in determinations of reservoir quality for different pore assemblages.

Five genetic pore types identified in 40 carbonate and 7 sandstone samples were subjected to NMR measurements. Results reveal close correspondence between NMR-derived pore volumes and 2-D pore size and shape gleaned from petrographic image analysis. Comparisons of real and synthetic pore shapes showed that shapes of all pore types in the medium size range of 0.02-0.5mm can be reliably compared with synthetic varieties, but such comparisons were unreliable for vuggy pores smaller than 0.5mm. T<sub>2</sub> relaxation times for depositional pores exhibit low amplitude, narrow wavelength responses. Moldic pores produced medium amplitude, asymmetrical wavelength



responses, and intercrystalline pores show high amplitude, narrow wavelength responses. NMR-derived pore volumes on pores with ferroan dolomite interiors underestimated pore diameter by up to 3 orders of magnitude. Calculated pore-throat sizes from MICP data correlate strongly with measured permeability.

Samples with high, intermediate, or low poroperm values displayed characteristic T2 curves confirming that reservoir quality can be estimated from NMR measurements. Future work is expected to show that NMR logging can estimate reservoir quality at field scale and aid in mapping flow units in compartmentalized reservoirs.

**DEDICATION**

*To Rachael, Ryan, Haven, and Gabriel –  
Thank you for enduring graduate studies with me.*

## ACKNOWLEDGEMENTS

This research project has required a great deal of financial and technical support. I thank my advisor Dr. Wayne Ahr for his encouragement, expertise, and friendship. I thank my committee members for their insights, both in the classroom, and specifically with this project. I am thankful for additional technical support provided by: Jim Howard at the ConocoPhillips Technology Center, Ray Guillemette with microprobe analyses, Andrew Silver and Katie Poole with core photos, Clayton Powell and Frank Platt for help in material preparations, and Freddi Curby and George Bolger for NMR and MICP measurements.

This project was financially supported by several entities including: Texas Water Resources Institute (TWRI), Gulf Coast Association of Geological Societies (GCAGS), South Texas Geological Society, and the Office of Graduate Studies at Texas A&M University. DOE also provided research assistantship funds toward this project.

I thank the Department of Geology and Geophysics at Texas A&M University for providing me the opportunity to be a teaching assistant during my graduate studies. I thank my family and friends who have provided moral strength and encouraged me to complete this study – particularly amid the challenges and changes of a growing family. And lastly, I thank God for allowing me the health and strength to endure this stage of my life.

## TABLE OF CONTENTS

		Page
ABSTRACT .....		iii
DEDICATION .....		v
ACKNOWLEDGEMENTS .....		vi
TABLE OF CONTENTS .....		vii
LIST OF FIGURES.....		xi
LIST OF TABLES .....		xx
CHAPTER		
I	INTRODUCTION.....	1
	Summary of the Problem.....	1
	Project Objectives .....	6
	Materials Available for the Study .....	8
II	GEOLOGIC SETTING OF STUDY AREAS .....	9
	Jurassic Gulf of Mexico .....	9
	Tectonic Setting.....	9
	Smackover Formation .....	11
	Stratigraphy of the Gulf Coast .....	14
	Jurassic of the Northwestern Australian Shelf .....	17
	Tectonic Setting.....	17
	Stratigraphy .....	19
	Permian Basin - West Texas .....	21
	Tectonic Setting.....	21
	Stratigraphy .....	22
III	PREVIOUS WORK .....	26
	Womack Hill Field.....	26
	Vocation and Appleton Fields.....	29
	Happy Spraberry Field .....	31
	Sandstone Samples.....	33

CHAPTER	Page
IV	METHODS..... 34
	Material Preparations ..... 36
	Core Plug Cleaning ..... 38
	Classification of Pore Space..... 39
	Depositional Porosity ..... 42
	Hybrid 1 Porosity ..... 43
	Diagenetic Porosity ..... 43
	Fracture Porosity ..... 44
	Petrographic Image Analysis (PIA) ..... 45
	PIA in This Study ..... 47
	Nuclear Magnetic Resonance (NMR) ..... 52
	How NMR Works ..... 52
	NMR in This Study..... 55
	Assumptions ..... 61
	Pore Sizes as Determined from T2 Times..... 62
	Mercury Injection Capillary Pressure (MICP) ..... 65
	How MICP Works..... 66
	MICP in This Study..... 68
	Electron Microprobe and SEM ..... 70
	Microprobe Procedures ..... 70
V	RESULTS ..... 73
	Petrographic Image Analysis (PIA) ..... 76
	Sandstones..... 76
	Carbonates..... 83
	PIA (2-D) Porosity Values and Core Analysis Porosity..... 107
	Summary of All PIA Results..... 108
	Nuclear Magnetic Resonance (NMR) ..... 111
	Sandstones..... 111
	Carbonates..... 115
	Summary of All NMR Results ..... 133
	Mercury Injection Capillary Pressure (MICP) ..... 137
	Sandstones..... 137
	Carbonates..... 139
	Summary of All MICP Results ..... 154
	Electron Microprobe ..... 159
	Sandstones..... 159
	Carbonates..... 160
	Summary of Microprobe Analyses ..... 165

CHAPTER	Page
	How Pore Sizes Compare between Methods ..... 167
VI	DISCUSSION AND INTERPRETATION..... 172
	PIA, Pore Geometry, and Their Relationship to the Genetic Classification of Porosity..... 174
	Purely Depositional and Hybrid 1-a Pores..... 174
	Hybrid 1-b (Moldic) Pores ..... 175
	Intercrystalline Pores..... 175
	Vugs: Purely Diagenetic, Enhanced Porosity .. 179
	Cement-Reduced Pores ..... 179
	Comparison of Porosity Measured by PIA and Core Analysis ..... 181
	Relationships between Pore Sizes as Determined by PIA and NMR..... 185
	Relationships between Porosity, Permeability Pore Size and Pore-Throat Size..... 187
	Porosity and Pore Types..... 187
	Permeability and Median Throat Diameter ..... 189
	Core Analysis Porosity and Permeability..... 190
	PIA Porosity and Permeability ..... 191
	PIA (2-D) Porosity and Median Throat Diameter ..... 192
	Pore Size and Pore-Throat Size Relationships. 193
	Pore Geometry Measured by NMR as a Proxy for Reservoir Quality in Carbonates..... 195
	What Does It All Mean?..... 198
VII	SUMMARY AND CONCLUSIONS..... 200
	Summary ..... 200
	Conclusions ..... 201
	REFERENCES CITED..... 202
	APPENDIX A THIN SECTION DESCRIPTIONS..... 212
	APPENDIX B PIA WORKFLOW USING IMAGEPRO PLUS©..... 218
	APPENDIX C PIA SUMMARY OF MEASUREMENTS ON THIN SECTIONS..... 234

	Page
APPENDIX D NMR DATA FOR SANDSTONES .....	242
APPENDIX E OLS AND WLS REGRESSION DATA .....	250
APPENDIX F SEM PHOTOS AND MICROPROBE DATA .....	252
APPENDIX G VARIATIONS OF RHO (SURFACE RELAXIVITY) AND SHAPE (S/V) TO DETERMINE DESIRED T2 BOUNDARY VALUE.....	273
VITA.....	277

## LIST OF FIGURES

FIGURE	Page	
2.1	Pre-rift arrangement of North America, South America, and Africa showing the proposed “fit” of the continents and incipient Gulf of Mexico .....	10
2.2	Diagrammatic representation of salt structures in final stage of development.....	12
2.3	Distribution of the Jurassic Smackover Formation and equivalents in the United States Gulf Coast.....	13
2.4	Composite diagram showing Smackover isopach thickness and the updip limit of deposition .....	16
2.5	Major basins and producing fields of the northwestern Australian shelf.....	18
2.6	Generalized stratigraphic column for four basins in the northwest Australian shelf.....	20
2.7	Composite map showing regional paleogeography of the Permian Basin including modern physiographic features .....	21
2.8	Regional chronostratigraphic and lithostratigraphic summary for the Permian Basin.....	24
2.9	Block diagram of depositional environments, geometry of deposits, and channel patterns in the Midland Basin .....	25
3.1	Type log for the Womack Hill field .....	28
4.1	Soxhlet distillation unit used to extract hydrocarbons from core plugs.....	38
4.2	Classification of fifteen carbonate pore types .....	41
4.3	Genetic classification of porosity after Ahr .....	42
4.4	Cartoon sketches of 2-D intersections of a hypothetical volume of 3-D pores, pore-throats, and rock.....	46



FIGURE	Page
4.5 A simplified sketch of the NMR bench top measurement device.....	56
4.6 Cumulative NMR porosity graphs derived from T2 relaxation times.....	60
4.7 Lab equipment used to measure capillary pressure.....	67
4.8 Synthetic capillary pressure data derived from NMR runs on sandstones.....	69
4.9 Optical photos of rock chips prior to microprobe analysis .....	72
5.1 Sandstone core photo .....	77
5.2 Depositional intergranular porosity in sandstone.....	77
5.3 Sorted pores from a thin section image prior to PIA.....	78
5.4 Sandstone with enlarged pores caused by dissolution of unstable volcanic grains.....	77
5.5 Plot of pore geometry for all sandstones.....	79
5.6 Plot of pore geometry for sandstones without clay or ‘vugs’ .....	79
5.7 Frequency distribution of sandstone interparticle pores by pore size .....	81
5.8 Fraction of 2-D measured porosity in sandstones by pore size.....	81
5.9 Comparison of 2-D and 3-D measurements of porosity in sandstone core plugs.....	82
5.10 Hand specimen of ooid grainstone dominated by depositional (intergranular) porosity .....	84
5.11 Thin section photograph of oolite grainstone dominated by Hybrid 1-a porosity.. .....	84
5.12 Pores selected from thin section image of oolite grainstone.....	85

FIGURE	Page
5.13 Distribution of pore geometry for all pore sizes from three carbonate samples exhibiting strong depositional attributes.....	85
5.14 Distribution of pore sizes in carbonate rocks with depositional attributes .....	87
5.15 Distribution of 2-D measured porosity by pore size in carbonates ...	87
5.16 Core photo of skeletal grainstone containing moldic pores .....	90
5.17 Oopel moldic pores.. .....	90
5.18 Photomicrograph of oopel moldic pores .....	91
5.19 Oomoldic pores sorted by size using PIA .....	91
5.20 Pore geometry of Hybrid 1-b (moldic) pores in carbonates.....	92
5.21 Histogram of small, medium, and large pore sizes in samples with moldic pores.....	92
5.22 Distribution of 2-D porosity in carbonates with moldic pores.....	93
5.23 Dolomite hand sample.....	95
5.24 Thin section photograph of intercrystalline pores in a fine-grained matrix.....	95
5.25 Intercrystalline pores in a fine-grained dolomite .....	96
5.26 Thin section photo of intercrystalline porosity in dolomite .....	96
5.27 Pore geometry of intercrystalline pores in carbonate rocks .....	97
5.28 Pore size distribution for carbonate rocks exhibiting intercrystalline pores .....	97
5.29 Distribution of 2-D porosity by pore size in samples with intercrystalline pores .....	98
5.30 Thin section image of abundant separate vugs and intercrystalline pores .....	100

FIGURE	Page
5.31 Hand specimen of vuggy carbonate .....	100
5.32 Touching vugs and intercrystalline pores in dolostone.....	101
5.33 PIA touching vugs sorted by size.....	101
5.34 Thin section photograph showing possible fractures in carbonate rock.....	102
5.35 Hand sample of broken core.....	102
5.36 PIA pore size distributions for carbonates exhibiting vugs.....	103
5.37 PIA porosity distribution for carbonate samples with abundant vuggy porosity.....	103
5.38 Pore geometry in five carbonates with high aspect ratios.....	104
5.39 Pore geometry in carbonate samples with separate and touching vugs.....	104
5.40 Core sample of carbonate containing cement-reduced pores.....	106
5.41 Thin section photo of pore space reduced by cementation .....	106
5.42 2-D porosity as compared with core analysis porosity for sandstones and carbonates.....	107
5.43 PIA pore geometry by pore type and pore size for all samples.....	110
5.44 T2 relaxation curves for sandstones with depositional pores.....	113
5.45 T2 porosity curves for sandstones with depositional pores.....	113
5.46 Possible T2 pore size distributions for sandstones.....	114
5.47 Pore size boundaries superimposed on T2 curves in sandstones .....	114
5.48 T2 relaxation curves for carbonates with depositional pores.....	117
5.49 T2 porosity curves for carbonates with depositional pores.....	117

FIGURE	Page
5.50 Possible T2 pore size distributions for carbonates with depositional pores.....	118
5.51 Pore size boundaries superimposed on T2 curves in carbonates with depositional pores.....	118
5.52 T2 relaxation curves for carbonates with Hybrid I-b (moldic) pores .....	121
5.53 T2 porosity curves for carbonates with Hybrid I-b (moldic) pores...	121
5.54 Possible T2 pore size distributions for carbonates with moldic pores.....	122
5.55 Pore size boundaries superimposed on NMR T2 curves in carbonates with moldic pores.....	122
5.56 T2 relaxation curves for carbonates with intercrystalline pores.....	124
5.57 T2 porosity curves for carbonates with intercrystalline pores .....	124
5.58 Possible T2 pore size distributions for carbonates with intercrystalline pores .....	125
5.59 Pore size boundaries superimposed on NMR T2 curves in carbonates with intercrystalline pores .....	125
5.60 T2 relaxation curves for carbonates with non-touching vugs .....	127
5.61 T2 porosity curves for carbonates with non-touching vugs .....	127
5.62 T2 relaxation curves for carbonates with touching vugs.....	128
5.63 T2 porosity curves for carbonates with touching vugs .....	128
5.64 Possible T2 pore size distributions for carbonates with touching vugs.....	129
5.65 Pore size boundaries superimposed on carbonates with touching vugs.....	129
5.66 T2 relaxation curves for carbonates with cement-reduced pores .....	131

FIGURE	Page
5.67 T2 porosity curves for carbonates with cement-reduced pores.....	131
5.68 Possible T2 pore size distributions for carbonates with cement-reduced pores.....	132
5.69 T2 relaxation curves for all samples .....	135
5.70 T2-derived porosity curves for all samples .....	136
5.71 Thin section photomicrograph of depositional intergranular pores in sandstone.....	138
5.72 Synthetic capillary pressure curves estimated from NMR runs on sandstones.....	138
5.73 Thin section photomicrograph of depositional pores in carbonate ...	139
5.74 Capillary pressure curves for carbonates with pores exhibiting depositional attributes .....	140
5.75 Distribution of pore-throat sizes in carbonates with pores exhibiting depositional attributes .....	140
5.76 Wetting phase saturation curve for carbonates exhibiting pores with strong depositional attributes .....	141
5.77 Thin section photomicrograph of moldic pores .....	142
5.78 Capillary pressure curves for carbonates with moldic pores.....	143
5.79 Distribution of pore-throat sizes in carbonates with moldic pores....	143
5.80 Wetting phase saturation curves for carbonates with moldic pores ..	144
5.81 Thin section photomicrograph of intercrystalline pores .....	145
5.82 Capillary pressure curve for carbonates with intercrystalline pores .	146
5.83 Distribution of pore-throat sizes in carbonates with intercrystalline pores .....	146

FIGURE	Page
5.84 Wetting phase saturation curves for carbonates with intercrystalline pores .....	147
5.85 Thin section photomicrograph of dolomite with vugs .....	148
5.86 Capillary pressure curves for carbonates with vugs.....	149
5.87 Distribution of pore-throat sizes in carbonates with vugs.....	149
5.88 Wetting phase saturation curves for carbonates with vugs .....	150
5.89 Thin section photomicrograph of cement-reduced pores in carbonate.....	151
5.90 Capillary pressure curves for carbonates with cement-reduced pores.....	152
5.91 Distribution of pore-throat sizes in carbonates with cement-reduced pores.....	152
5.92 Wetting phase saturation curves for carbonates with cement-reduced pores.....	153
5.93 Summary diagram of capillary pressure behavior for 40 carbonate samples sorted by pore type.....	156
5.94 Summary diagram of pore-throat distributions for 40 carbonate samples sorted by pore type.....	157
5.95 Summary diagram of wetting-phase saturation for 40 carbonate samples by pore type... ..	158
5.96 BSE image of framboidal pyrite on the interparticle pore walls of sandstone... ..	159
5.97 BSE image of framboidal pyrite in carbonate pores exhibiting depositional attributes .....	160
5.98 BSE image of Hybrid 1-b (moldic) pores in carbonate.....	161
5.99 BSE image of vugs in dolomite.....	162

FIGURE	Page
5.100 BSE image of fine-grained dolostone with intercrystalline pores.....	163
5.101 BSE image of cement-reduced pores in dolomite .....	164
5.102 Pore size comparison for carbonate samples exhibiting pores with depositional attributes .....	169
5.103 Pore size comparison for carbonate samples with moldic pores.....	169
5.104 Pore size comparison for intercrystalline pores in carbonates .....	170
5.105 Pore size comparison for carbonates with touching vugs .....	170
5.106 Pore size comparison for carbonates with non-touching vugs.....	171
5.107 Pore size comparison for carbonates with cement-reduced pores.....	171
6.1 PIA measured pore geometry for pores of different origin.....	177
6.2 Similarity in pore geometry for pores of different origin.....	178
6.3 Relationship of pore geometry to genetic pore types within specific size classes.....	181
6.4 2-D vs. 3-D porosity by pore origin .....	183
6.5 Comparisons of core and PIA measurements of porosity in dolomite reservoirs.....	184
6.6 Comparison of medium and large pore diameter as determined from PIA and T2 relaxation times.....	186
6.7 Comparison of NMR and core analysis porosity values by by pore type.....	188
6.8 Comparison of median pore-throat size and permeability by by pore type.....	189
6.9 Comparison of core porosity and permeability in 40 carbonates.....	190
6.10 Relationship of PIA porosity and core permeability by pore type....	191

FIGURE	Page
6.11 Comparison of PIA-measured porosity and median throat aperture.....	192
6.12 Pore size determined from T2 times as compared with median throat aperture.....	193
6.13 Relationship of median throat diameter and median PIA pore diameter... ..	194
6.14 Paired values of porosity and permeability grouped by pore origin.....	196
6.15 Hypothetical NMR logging response in carbonate reservoir flow units of best, intermediate, and poorest quality .....	197



## LIST OF TABLES

TABLE	Page
1.1 Summary of materials available for this project .....	8
2.1 Stratigraphic column, ages, dominant lithology, and depositional environments of sediments deposited in the Mississippi interior salt basin, Gulf of Mexico.....	15
4.1 Table of available core plug data including location, depth, and date of preparation.....	37
4.2 Test objects for PIA measurement of pore geometry used in this study.....	51
4.3 2-D PIA pore shape factor values used in petrophysical measurements.....	51
4.4 Sandstone measurements of diameter, radius, length, mass, fluid density, bulk volume, pore volume, and core plug porosity.....	57
4.5 Calibration data preparatory to T1 and T2 measurements of sandstone core plugs.....	58
4.6 Summary of NMR total porosity and prerequisite measurement data for 7 sandstones .....	60
4.7 Bin sizes used in PIA measurement of pore diameter.....	64
5.1 Summary of 2-D porosity values for seven sandstones .....	80
5.2 Summary of PIA pore measurements by pore origin.....	109
5.3 Summary of T2 curve characteristics for all rocks and pore types.....	134
5.4 Summary of MICP measurements for all rock types and pore types.....	155
5.5 Summary of microprobe measurements and distribution of paramagnetic minerals by pore type .....	166

TABLE	Page
6.1 Comparison of 2-D and 3-D porosity as measured in dolomite reservoirs from Kansas and Wyoming .....	184
6.2 Summary table of pore sizes as determined by PIA and NMR techniques.....	186

## CHAPTER I

### INTRODUCTION

Carbonate rocks contain at least 50% of the world's oil and natural gas. These resources are contained in a complex network of pores and pore-throats that may be depositional, diagenetic, fractured, or hybrids of those end-members. It can be unproductive and expensive to obtain borehole cores, core analyses, and wireline log data for research that may lead to predicting reservoir flow characteristics. The primary objective of this study is to investigate a new method for characterizing the distribution of connected pores in carbonate reservoirs. The study should provide means for more effective field development and production at lower risk. The focus of the project is at the scale governing fluid flow in the rock – the pore scale.

### SUMMARY OF THE PROBLEM

Unaltered porosity in terrigenous clastic rocks is generally intergranular (between grains). Although diagenesis affects siliciclastics, it generally reduces intergranular porosity by cementation or authigenic mineral growth and it rarely enhances porosity. Compaction also reduces porosity in sandstones that have ductile grains or clayey matrix. Fracture porosity is arguably less common in siliciclastics than

---

This dissertation follows the style of the American Association of Petroleum Geologists Bulletin.

in carbonates, but it does exist. In short, pore characteristics (total porosity, pore geometry, and pore and pore-throat connections) in sandstones are determined mainly by depositional processes and may be modified by cementation and compaction. Because sandstone porosity is intergranular and dependent on depositional texture, depositional facies maps can be used as proxies for porosity maps. As long as porosity is depositional (intergranular), a linear relationship of the form  $\phi = a + b \log k$  is reliable. For example, Bryant et al. (1993) have shown that permeability is best estimated in Fontainebleau Sandstone using a geologic model that considers processes such as grain packing, compaction, and cementation. These factors are directly related to detrital depositional rock textures and the associated pore space between grains. The relationship between depositional textures and the resultant pore system enables geologists and engineers to estimate permeability from "porosity logs" such as the neutron, density, and acoustic logs once there is an established porosity-permeability relationship from measurements taken on one or more cores.

Field-scale poroperm predictions and maps for sandstone reservoirs are commonly based on facies characteristics established from core descriptions, nearby outcrops, cuttings, or even from interpreting the shape of gamma ray and resistivity curves. The log responses are often used to estimate "fining-upward" and "coarsening-upward" trends that suggest certain types of deposits. Some of the more modern devices (such as the NMR tool) are used for borehole measurements to determine total NMR porosity, in situ permeability, fluid saturations, oil viscosity, and bulk volumes of irreducible water. To this end, the NMR tool is particularly useful in discriminating pore

sizes and pore characteristics in the subsurface. As long as those pore characteristics are related to depositional, intergranular pores, powerful interpretations can be made in reservoir characterization studies.

In strong contrast to porosity created only by deposition of siliciclastic sands, carbonate porosity exists in three end-member genetic categories: depositional, diagenetic, and fracture. Carbonate pore types may be unrelated to depositional texture; instead they may represent diagenetic processes that occurred at rock-water interfaces long after sedimentation. Pore size, shape, and total pore volume are rarely determined by depositional processes alone. Pore and pore-throat connections are rarely simple connections of intergranular pore spaces. Permeability may not follow a simple linear relationship with porosity. Log shapes do not identify coarsening and fining upward trends or facies character in carbonates. And even though the NMR tool may distinguish large and small pores in carbonate rocks, it can not discriminate between pore types of different origin (i.e. depositional and diagenetic forms). Furthermore, carbonate reservoir porosity and permeability are rarely distributed uniformly at field scale. To some extent this may be a function of original depositional anatomy, but it is typically influenced also by diagenetic or fracture processes.

Petrophysical measures of porosity and permeability on core plugs is commonly the basis for scaling-up from borehole to field dimensions. Although this practice is applied to all types of pore systems, it can result in misidentification of common reservoir characteristics where non-depositional pore systems dominate. For

example, in diagenetic pore systems Lucia (1983) showed that larger dolomite crystal sizes were the key to estimating permeability from interparticle porosity.

It is most desirable to locate reservoir zones with isotropic rock properties. Permeability, the parameter that describes flow, is closely related to pore-throat geometry; therefore, information from mercury injection capillary pressure measurements can be used as a proxy for permeability. With information about pore sizes, shapes, total percent porosity, and porosity-permeability relationships, one can establish poroperm "facies" within carbonate reservoirs. Moreover, the best, intermediate, and poorest "quality" pore systems within the interval of interest can be distinguished. Such poroperm zones are also known as "flow units" (Ebanks et al., 1992) and a relative quality assessment of each unit is its "flow unit rank".

Examination of reservoir rock samples enables one to classify porosity using a genetic classification and ultimately to develop a geological model to predict the 3-D distribution of each genetic pore system at field scale. The goal is to upscale from pore

to core to borehole to field scale to predict the spatial distribution of good, intermediate, and poor flow, baffle and barrier units. Thereafter, field development plans can be recommended for improved economic returns on enhanced recovery programs, and compartmentalized reservoirs can be managed more effectively. Accomplishing this goal has been a major challenge, as revealed by recent reservoir characterization studies (Parra et al., 2001, Feazel et al., 2004, Mancini et al., 2004).

The present state of knowledge about NMR logging in carbonate reservoirs is inadequate to identify fundamental relationships between pore characteristics and permeability so that borehole measurements made with the NMR tool can provide reliable and reproducible information about reservoir anatomy and pore system distribution, evolution and quality. The results of this research should close that gap in our basic knowledge.

## PROJECT OBJECTIVES

1. Identify and evaluate different pore “facies” from four different locations and formations on the basis of pore origin:
  - Happy Spraberry Field, Permian Clearfork Formation, Garza County, Texas
  - Vocation/Appleton Fields, Upper Jurassic (Oxfordian) Smackover Formation, Escambia and Monroe Counties, Alabama
  - Womack Hill Field, Upper Jurassic Smackover Formation, Clarke and Choctaw Counties, Alabama
  - Northwest Australian Shelf, Jurassic Elang/Plover Formations
2. Compare the T2 spectra for each rock/pore pair and assess their relationships to one another and to genetic classifications of porosity. It is hypothesized that the most abundant sizes and shapes of each pore type that uniquely identify specific types of carbonate pores will be distinct from one another as indicated by differences in T2 curve shape.
3. Determine which pore sizes (small, medium, and large) as determined by PIA are best estimated from T2 relaxation times in depositional, diagenetic, and hybrid pore types.
4. Define the relationships between pore sizes measured by NMR and PIA as they relate to pore-throat sizes that characterize specific rock/pore pairs.
5. Identify and describe the relationships between MICP and permeability and compare those relationships with NMR pore volume data as they relate to permeability.



6. Compare porosity measurements from NMR (3-D pore volume data) with analysis by PIA (2-D area data) and finally with core analysis (measured values) to determine the degree to which the different measurements correspond and at what level of relative precision they correspond. A basic hypothesis is that high degrees of correspondence between these measurements will indicate which fundamental rock properties serve as proxies for connectivity.
7. Establish a new quality ranking scheme for fluid flow in carbonate reservoirs which has widespread applications in subsurface petroleum reservoirs, and other subsurface storage facilities. This will involve determining the extent to which the latest generation of NMR tools provides data to enable operators to predict pore type and pore origin from NMR log responses alone.
8. Determine the ideal magnification for the study of porosity networks in thin sections and establish digital measurement categories of pore sizes and shapes.
9. Develop and document a procedure to obtain quantitative measures of porosity in thin section using Image-Pro® Plus.

## MATERIALS AVAILABLE FOR THE STUDY

Forty-seven borehole cores were available for this study from four different geographic and geological settings; they include: 1) Appleton/Vocation Fields, Alabama (Jurassic, Smackover Formation), 2) Womack Hill Field, Alabama (Jurassic, Smackover Formation), 3) Happy Spraberry Field, West Texas (Permian, Clearfork Formation), and 4) the Northwest Australian shelf (Jurassic, Elang/Plover Formations). Table 1.1 presents a summary of materials used in this project.

**Table 1.1. Summary of materials available for this project.**

<u>Data Type</u>	<u>Vocation/Appleton Fields</u>	<u>Womack Hill Field</u>	<u>Happy Field</u>	<u>Australian Shelf</u>
Geographic Location	Alabama Gulf Coast	Alabama Gulf Coast	West Texas	NW Australia
Formation Name(s)	Smackover	Smackover	Clearfork	Elang/Plover
Formation Age(s)	Upper Jurassic	Upper Jurassic	Permian	Jurassic
Original rock core	slabbed core	broken whole core	4" whole core	1.5" whole core
Core Photo Library created	yes	yes	yes	yes
General lithology	carbonate	carbonate	carbonate	sandstone
Number of core plugs cut	23	11	6	7
Number of thin sections prepared	23	11	6	7
Thin section photo library created	yes	yes	yes	yes
Number SEM mounts prepared/used	4	1	1	3
Number of NMR reports	23	11	6	7
Number of MICP reports	23	11	6	7 (synthetic)
Number of wells represented	6	2	2	Not available

## CHAPTER II

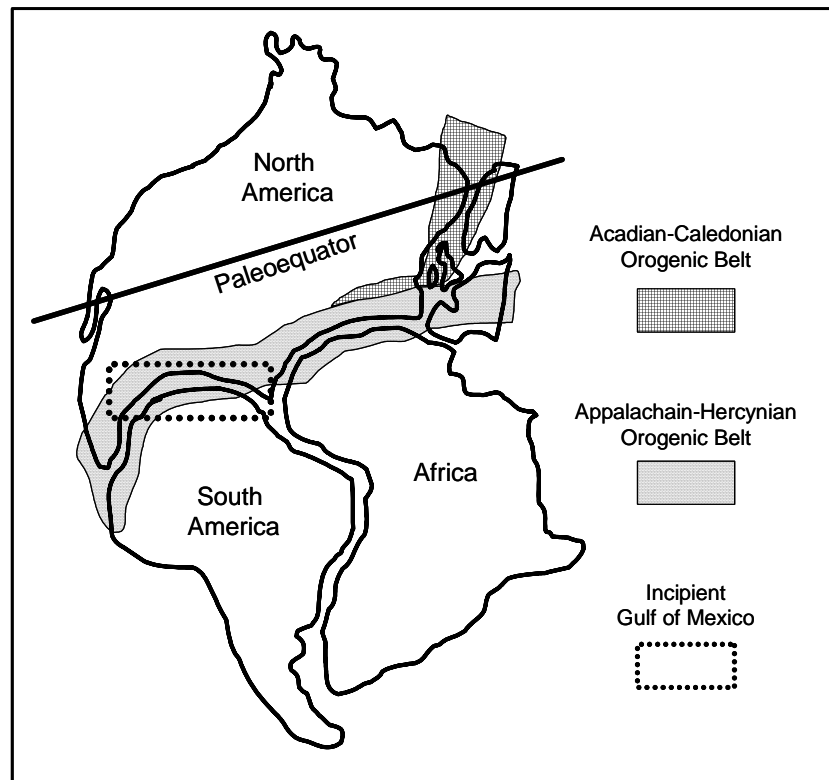
### GEOLOGICAL SETTING OF STUDY AREAS

This chapter reviews the tectonic and stratigraphic settings of three general geographic and geological localities. The areas reviewed include: Jurassic carbonates from the Ancestral Gulf of Mexico, Jurassic sandstones from the Northwest Australian Shelf, and Permian carbonates from West Texas.

#### JURASSIC GULF OF MEXICO

##### Tectonic Setting

The Early Mesozoic (Triassic) marked the onset of breakup of the Supercontinent Pangea. The present day Gulf of Mexico (GOM) began to form as the South American/African landmasses drifted away from North America. Concomitant with the rifting event was the initiation of Caribbean regional tectonics (Walper and Rowett, 1972; Salvador, 1987). The separation of the landmasses (Fig. 2.1) created a sphenochasm (basement pull-apart region) often referred to as the Mississippi embayment (Walper and Rowett, 1972). This triangular shaped structural depression (sphenochasm) formed between several megashear fault zones, and was a major depocenter throughout the Late Mesozoic and Cenozoic (Walper and Rowett, 1972). Rifting of the major continental blocks continued into the Late Jurassic, at which time the Yucatan peninsula reached its present-day configuration. Thereafter, the GOM basin became tectonically stable (Salvador, 1987).



**Figure 2.1.** Pre-rift arrangement of North America, South America, and Africa showing the proposed “fit” of the continents and incipient Gulf of Mexico. Mountain belts formed 260 MY ago, showing collision zone areas of crustal plates prior to opening of the Atlantic Ocean. Modified after Walper and Rowett (1972).

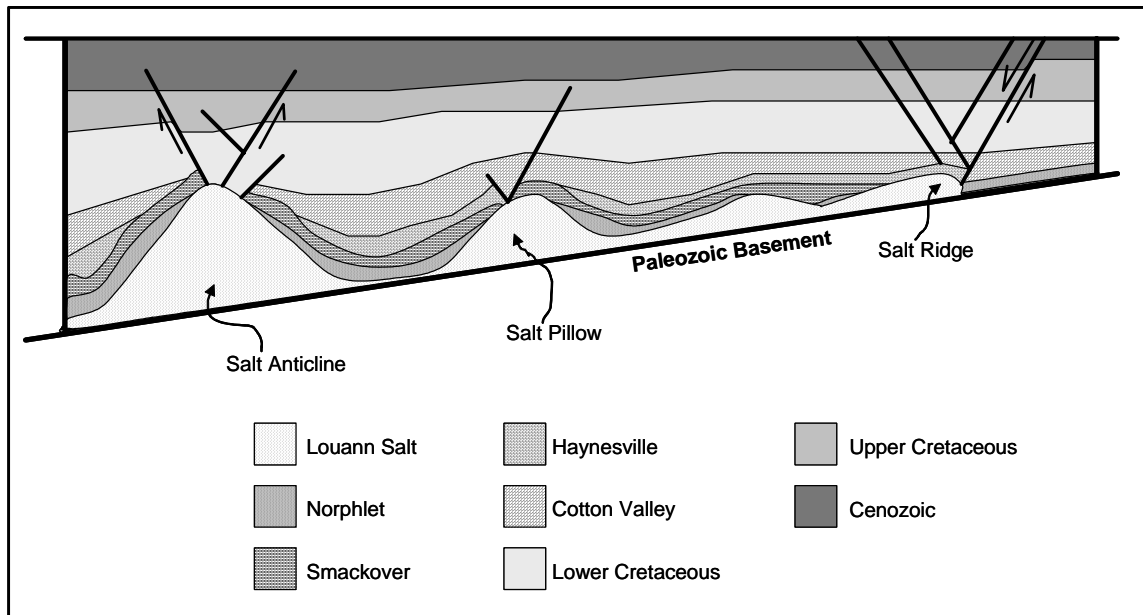
Sedimentation in the GOM was controlled by mega fault zones and tensional grabens which filled with redbeds and volcanics (Salvador, 1987). Marine deposition was restricted to embayments of the Pacific Ocean in northwest and central Mexico. Not until the Callovian (Middle Jurassic) did sea waters reach the developing GOM. After the Callovian marine transgression occurred, there was widespread evaporite (i.e., Louann Salt) deposition which blanketed much of the paleotopography of the time (Salvador, 1987). After extensive evaporate deposition, the Norphlet sands and silts

were deposited. Sedimentation continued through the Oxfordian, where Smackover grainstones and mudstones from shoal facies were deposited (Townsend, 1986).

Basement paleohighs such as the Baldwin High, Wiggins Arch, and Choctaw and Conecuh ridge complexes were areas of thin or no Smackover deposition, serving rather as source areas for siliciclastic input (Mancini et al., 1990). Overburden on the Louann Salt coupled with a southward dipping depositional profile caused the salt to move southward (Hughes, 1968). Salt ridges, pillows, and anticlinal structures formed in the downdip section (Fig. 2.2). Peripheral salt ridge complexes are the probable cause of the Gilbertown fault zone, within which Womack Hill Field is located (Meyers, 1975; Hopkins, 2002).

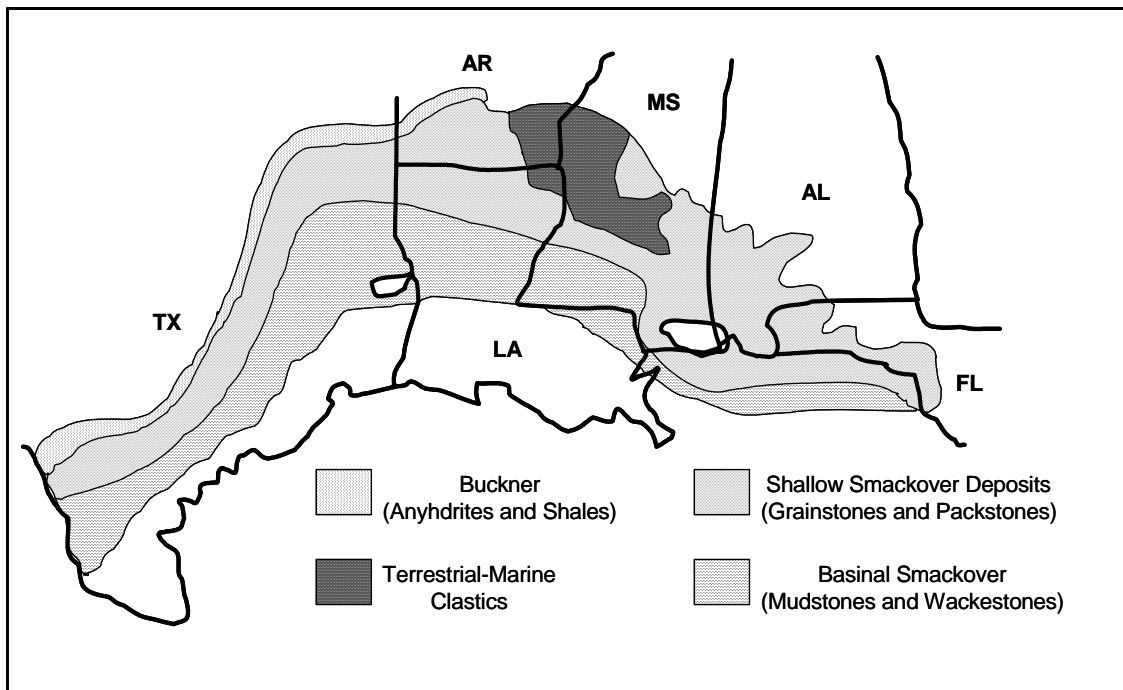
### Smackover Formation

The Smackover formation was deposited on a carbonate ramp (Ahr, 1973; Mancini and Benson, 1980). It is Oxfordian (Late Jurassic) in age based upon the occurrence of fossil ammonites (Imlay, 1945). Throughout much of southwestern Alabama, the Smackover consists of a lower mudstone-dominated lithofacies (overlying the Norphlet Sandstone) and an upper grain-supported lithofacies overlain by the Buckner anhydrite (Mancini and Benson, 1980). Both combination and salt-related traps are common, and reservoir rocks include grainstone, dolomitized grainstone, wackestone, packstone (Mancini and Benson, 1980). The Smackover Formation was deposited in an arcuate belt around the ancestral GOM from Mexico to Florida (Fig. 2.3). In Mexico the Smackover is known as the Zuloaga and Novillo Formations



**Figure 2.2. Diagrammatic representation of salt structures in final stage of development. Modified after Hughes, 1968. No scale.**

(Salvador, 1987). The downdip limit of Smackover deposition is unknown in the GOM, but it has been postulated to exist in the basin center as interpreted from seismic reflection data (Mancini and Benson, 1980).



**Figure 2.3. Distribution of the Jurassic Smackover Formation and equivalents in the United States Gulf Coast. Modified after Crevello and Harris, 1984.**

### Stratigraphy of the Gulf Coast

The Eagle Mills Formation was deposited during the Upper Triassic and consists of terrestrial red beds, shales, mudstones and siltstones, and unconformably overlies Paleozoic basement rocks (Table 2.1) (Salvador, 1987; Johnston et al., 2000). During Callovian times, the Werner Formation was deposited on the Eagle Mills. The Werner Formation is an evaporate succession up to 500 ft thick composed primarily of anhydrite and minor shallow water and terrigenous siliciclastics (Salvador, 1987). The Callovian-aged Louann salt overlies the Werner Formation, where it may reach thicknesses of up to 6000 ft (Salvador, 1987).

Oxfordian deposits of southeast Mississippi, southern Alabama, and the Florida panhandle consist of two major units; the Norphlet Sandstone, and the Smackover Formation, respectively (Table 2.1). The Norphlet Formation is a continental siliciclastic deposit which formed in an arid climate (Wilkerson, 1981). The contact of the Norphlet with the overlying Smackover is commonly abrupt, but gradational over an interval of only a few feet or less on paleohighs such as the Wiggins Arch and Conecuh ridge complex (Kopaska-Merkel and Mann, 1993).

The Smackover Formation was deposited on a carbonate ramp in the Gulf Coast (Ahr, 1973; Mancini and Benson, 1980), but in southwest Alabama there were pre-existing ridges and basins which strongly influenced its depositional style (Kopaska-Merkel and Mann, 1993). High-energy facies were deposited in areas rimming exposed paleohighs, and near the updip limit of Smackover deposition.



Microbial reefs commonly occur on paleohighs near the Conecuh ridge structure (Fig. 2.4), where they form significant petroleum reservoirs including Vocation/Appleton Fields (Parcell, 1999; Morgan, 2003). The Upper Jurassic Smackover Formation is the major hydrocarbon producer in the state of Alabama having produced 69.5 million bbls of oil, 63 million bbls of condensate, and 237 Mcf of gas since the first Smackover discovery in 1967 (Benson, 1985).

**Table 2.1. Stratigraphic column, ages, dominant lithology, and depositional environments of sediments deposited in the Mississippi interior salt basin, Gulf of Mexico. Modified after Townsend, 1986.**

SERIES	STAGE	ROCK UNIT	DOMINANT LITHOLOGY	DEPOSITIONAL ENVIRONMENT
Lower Cretaceous	Berriasian	Cotton Valley Group	silty shales sandstone	terrestrial littoral
	Tithonian			
Upper Jurassic	Kimmeridgian	Haynesville Formation	oolitic limestone evaporates and shales	restricted marine
		Buckner Anhydrite member	massive anhydrite	sabkah
	Oxfordian	Smackover Formation	oolitic grainstones carbonate mudstones	shallow marine shoals open marine
		Norphlet Formation	sandstone black shale – siltstone	shoreface/alluvial lagoon
		Pine Hill anhydrite member	anhydrite	restricted marine
Middle Jurassic	Callovian	Louann Salt	massive halite	restricted marine
		Werner Formation	massive anhydrite with black shale interbeds	restricted marine
Lower Jurassic? - Upper Triassic		Eagle Mills Formation	terrestrial shales, mudstones, sandstones	alluvial
Paleozoic		Paleozoic basement rock		

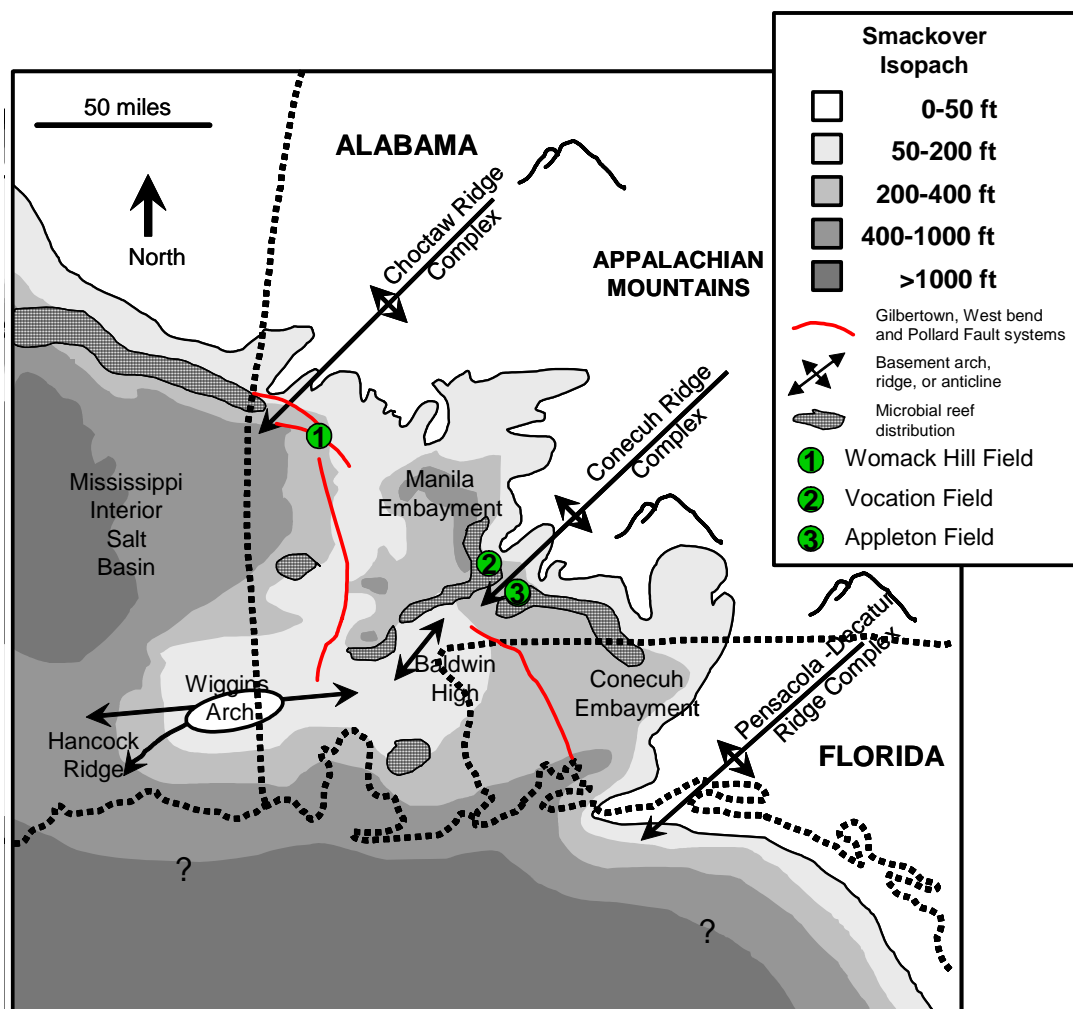


Figure 2.4. Composite diagram showing Smackover isopach thickness and the updip limit of deposition (Tew et al., 1993). Structural features of the region (Mancini et al., 1990; Kopaska-Merkel and Mann, 1993), location of microbial reefs (Parcell, 1999), and location of Womack Hill, Vocation, and Appleton Fields also shown.

The Smackover underlies the Buckner Anhydrite Member of the Haynesville Formation. The basal Buckner is dominated by evaporites confined to restricted basins that are interpreted to represent lagoons ponded behind Smackover barrier islands (Ahr, pers comm.) and by peritidal strata on the flanks and crests of paleohighs (Kopaska-Merkel and Mann, 1993). The base of the Buckner is considered to be time-parallel by

Mann (1990) but it is difficult to identify along the basin margins of the Ancestral Gulf where it was deposited in a sabkha environment (Kopaska-Merkel and Mann, 1993).

## JURASSIC OF THE NORTHWEST AUSTRALIAN SHELF

### Tectonic Setting

The Northwest Shelf of Australia is part of the continental margin of Western Australia that extends southwestward to about 22° S and northeastward to about 130° E (Fig. 2.5). It was formed by a series of major tectonic episodes that began in Late Paleozoic time and continued into Cretaceous times, and that resulted in the complete breakup of eastern Gondwana and the formation of the Indian Ocean (Butcher, 1989).

The basins and sub-basins shown in Figure 2.5 were created by extensional tectonism and superimposed over a regionally extensive, intracratonic basin of older Paleozoic rocks (Butcher, 1989). The northwest shelf is sometimes referred to as the Westralian Superbasin, divided into the (Northern) Carnarvon, offshore Canning, Browse, and Bonaparte Basins, respectively. The Superbasin contains an estimated total of 2.1 billion bbls of discovered oil reserves, 1.7 billion bbl of condensate, and 113 tcf of gas (Longley et al., 2002).

With the exception of salt diapirs (or domes) and their accompanying structures in the Permian section of the Bonaparte basin, the principal drilling targets of the Northwest Shelf have been drape structures, where post-rift marine shales were draped over horst blocks containing prerift (Triassic to Mid-Jurassic) continental sands (Forrest and Horstman, 1986). As well control has increased and more seismic data were

acquired, greater attention has been given to postrift (Late Jurassic) stratigraphy. As a result, a number of small fields have been discovered associated with more recent structural activity (Forrest and Horstman, 1986).

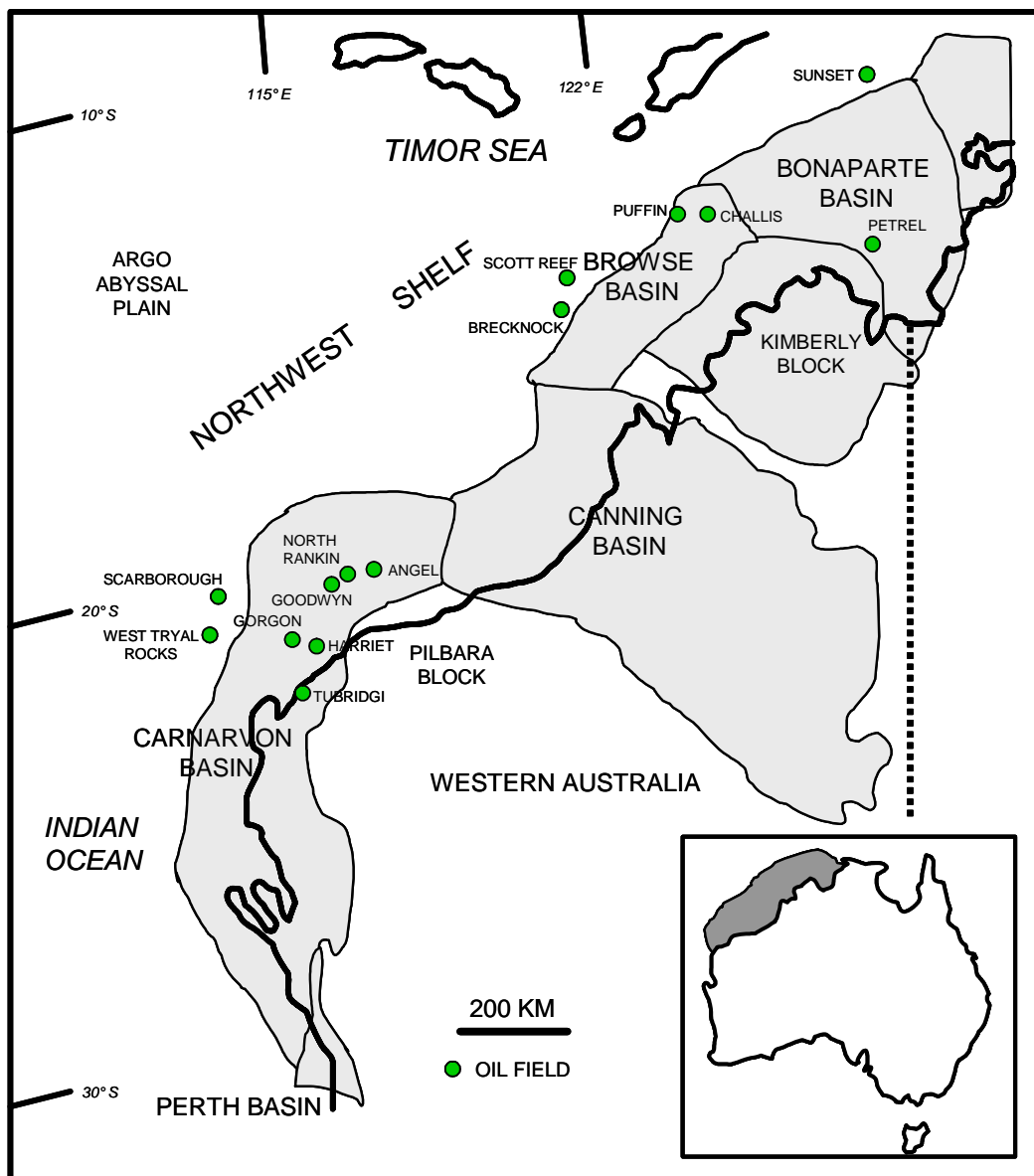
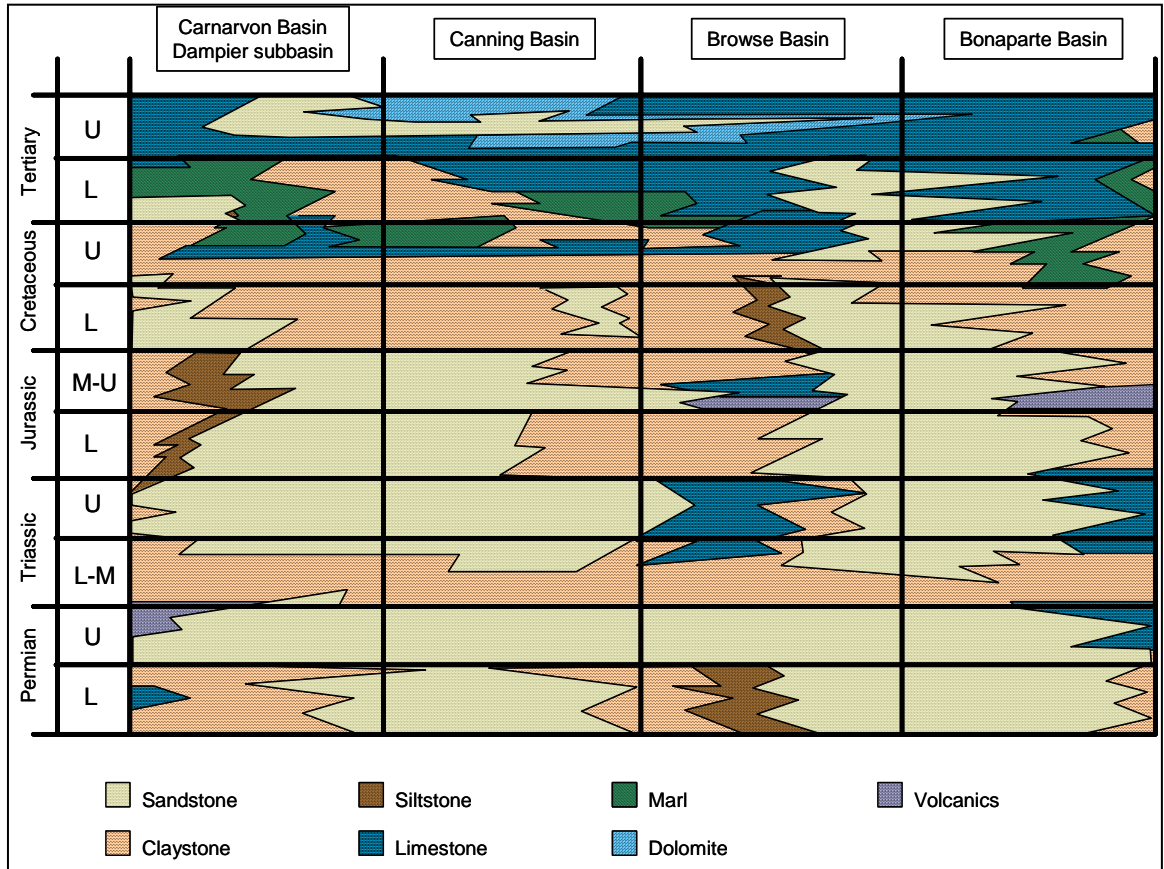


Figure 2.5. Major basins and producing fields of the northwestern Australian shelf. Modified after Butcher, 1989. The Borrow, Dampier, and Beagle subbasins are part of the larger Carnarvon Basin (Robertson et al., 1976).

## Stratigraphy

Well control is generally sparse in the region making the interpretation of stratigraphic units difficult. Except for specific field areas with multiple wells, the regional stratigraphy is worked out on a broad basis using paleontology as the major means of describing stratigraphic relationships. Even in the most heavily drilled areas, well control is too sparse to be of use in interpreting seismic stratigraphic relationships (Forrest and Horstmann, 1986). Furthermore, stratigraphic relationships are complicated because formation names vary from sub-basin to sub-basin (Howard, personal comm.), particularly within the Jurassic succession (Mollan et al., 1970) from which samples in this study were obtained.

A general stratigraphy of the four adjacent shelf basins of the Northwest Australian Superbasin is shown in Figure 2.6. The sandstone samples in this study come from the Elang and Plover Formations on the northwest Australian shelf (Howard, personal comm.). The Elang and Plover Formations are Jurassic in age (Edwards et al., 2001) and are dominated by sandstones that contain moderate amounts of clay and silt, particularly around basin margins. There are also Middle to Upper Jurassic volcanic rock outcrops on the northeast portions of the shelf (Robertson et al., 1976).

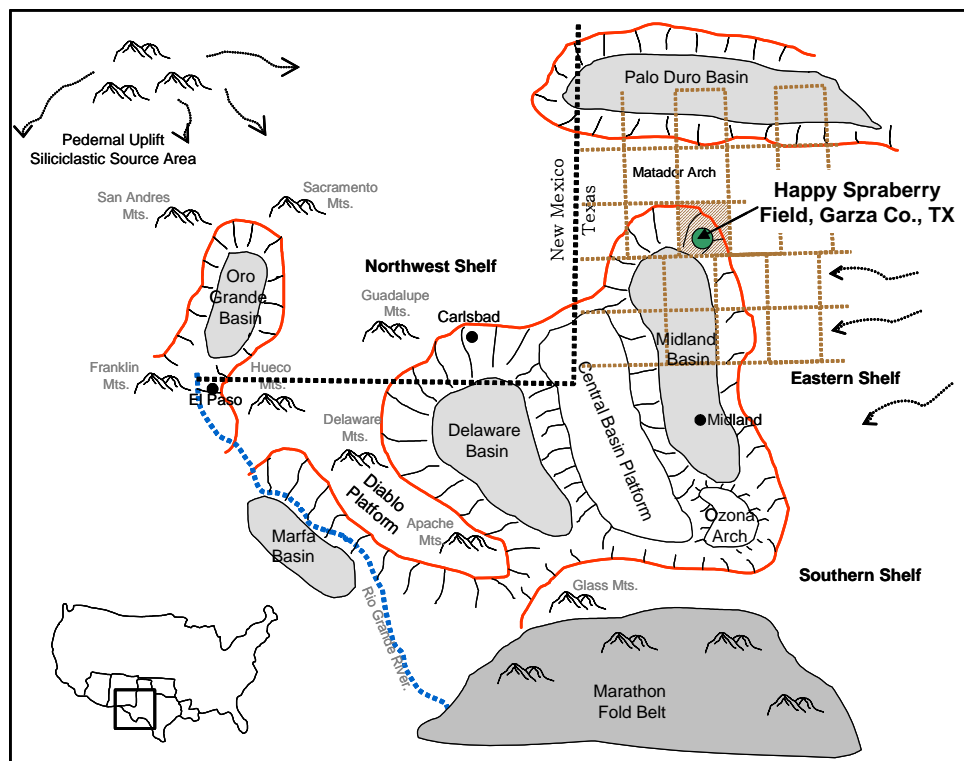


**Figure 2.6. Generalized stratigraphic column for four basins in the northwest Australian shelf. Modified after Robertson et al., 1976.**

## PERMIAN BASIN - WEST TEXAS

### Tectonic Setting

The Permian Basin of west Texas and southeastern New Mexico is an intra-cratonic foreland basin. The basin formed in response to the formation of the Ouachita-Marathon Fold and Thrust event during the Gondwana-Laurasia collision, and was segmented into several sub-basins and topographic highs (Ross, 1986). Of particular relevance to this study is the formation of the Midland basin, located between the central basin platform and the eastern shelf margin of the Permian Basin proper (Fig. 2.7). The eastern margin of the Midland basin is bounded by the Chadbourne Fault Zone, the



**Figure 2.7. Composite map showing regional paleogeography of the Permian Basin including modern physiographic features (modified after Atchley et al., 1999; Handford, 1981). Map shows location of Happy Spraberry Field in Garza County, Texas.**

inflection point where sediments transition from shelf to basin depositional styles (Yang and Dorobek, 1994).

During Early Permian time, the Midland basin was a marine embayment in which mixed siliciclastic and carbonate deposition occurred, including abundant siliciclastic turbidites in the deeper parts of the basin (Ward et al., 1986). Deposition of the carbonate interval in Happy Spraberry field took place landward of the steepening on the platform (Layman, 2002). Happy field is part of the Lower Clearfork Formation.

### Stratigraphy

Happy Spraberry Field is located in Garza County, Texas. It is situated near the margin of the (Permian) Midland Basin on the Eastern Shelf (Fig. 2.7). The field name should not be confused with the deep water turbidites of the Spraberry Formation, which occurs in the central deep of the Midland Basin (Handford, 1981).

The Midland basin stratigraphic section consists largely of shallow-marine shelf to shelf-margin carbonates and deep-basin deposits of Pennsylvanian and Permian age (Adams, 1951). The high-relief depositional paleotopography between the shelf margin and the deep basin make for abrupt facies changes and difficulty in shelf-to-basin correlations (Handford, 1981). Despite these difficulties, work by Jeary (1978), Handford (1981), and Atchley et al. (1999) suggests that the Dean Formation in the Midland Basin is the equivalent of both the lower Clearfork and Tubb Formations of the eastern shelf. Furthermore, the Spraberry Formation (Midland basin proper) is coeval with the upper Clear Fork and Glorieta Formations of the central basin platform as well



as the Yeso and Abo Formations of the Midland basin and its corresponding northern shelf (Fig. 2.8). The Lower Leonardian deposits at Happy Field are shelf margin carbonates (Fig. 2.8), and are probably time equivalent with the Dean Sandstone in the Midland basin, and Abo (Lower Clearfork) fluvial deposits on the northern shelf (Atchley et al., 1999; Crabaugh, 1988). Discontinuity across the slope break, coupled with poor well control make similar correlations at other nearby locations particularly difficult.

A sketch of the different depositional environments of the Midland basin during Clearfork time is shown in Figure 2.9. Happy Spraberry field is located on the northern margin of the Midland basin, at the carbonate shelf margin. This carbonate margin on the northern shelf stood about 1800 ft (~ 600m) above the adjacent Midland basin during deposition of the Clearfork formation, and prograded basinward over resedimented carbonate debris forming the slope (Handford, 1981). Slumps, debris flows, and turbidity currents were the principal mechanisms by which carbonate sediment was moved downslope into the basin. Turbidity currents carried the finest sediment into the most distal or remote parts of the basin. Carbonate productivity was prolific enough to result in net progradation of the shelf margin and continuously heal erosional features caused by waves, currents, and massive landslope failures (Handford, 1981).

Hydrocarbons in the Permian Basin occur in Cambrian to Cretaceous age carbonate and siliciclastic rocks, but most of the oil (71% OOIP) and gas (53% OGIP) is produced from Paleozoic strata (Ward et al., 1986), such as those deposits in Happy Spraberry field.

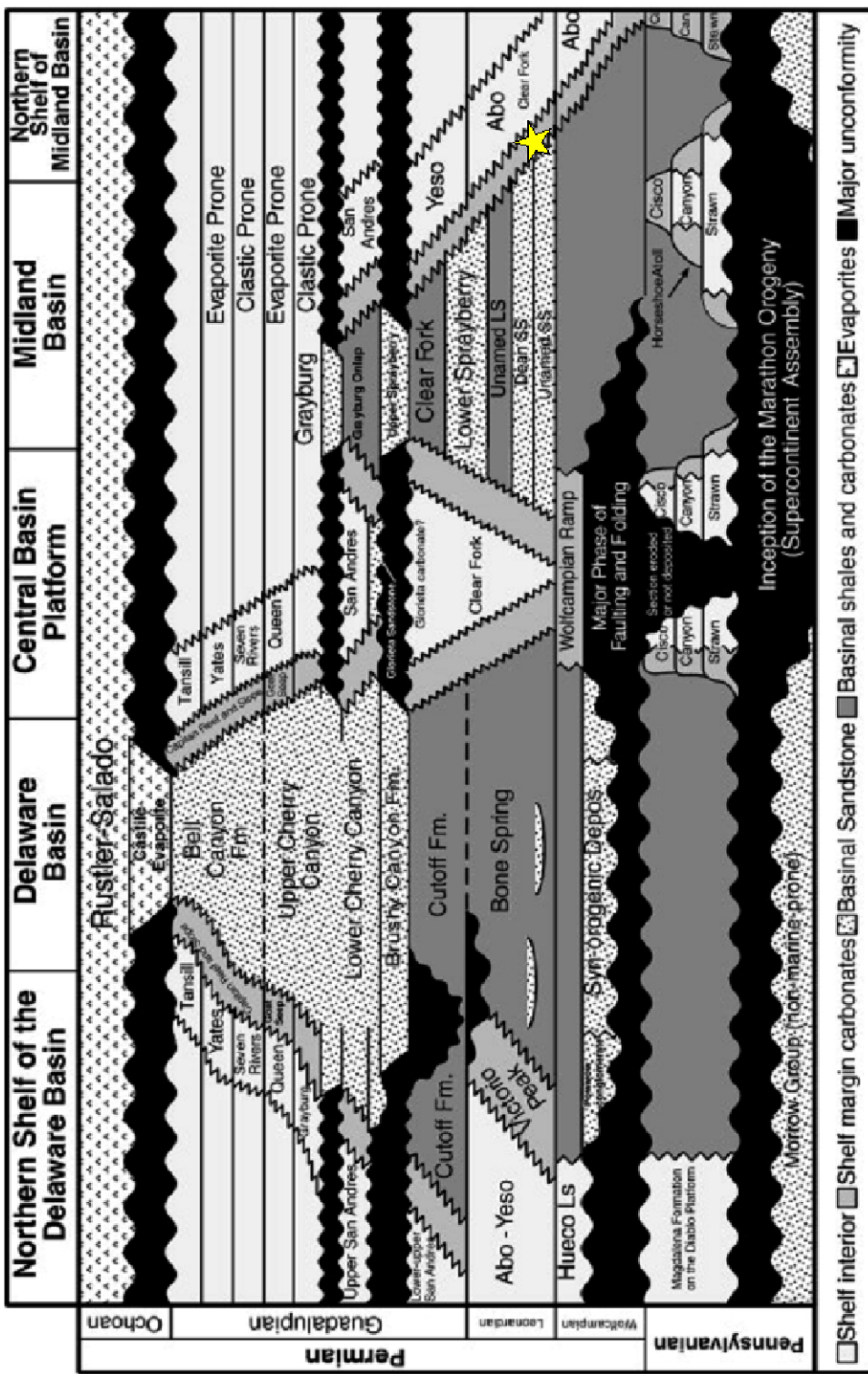
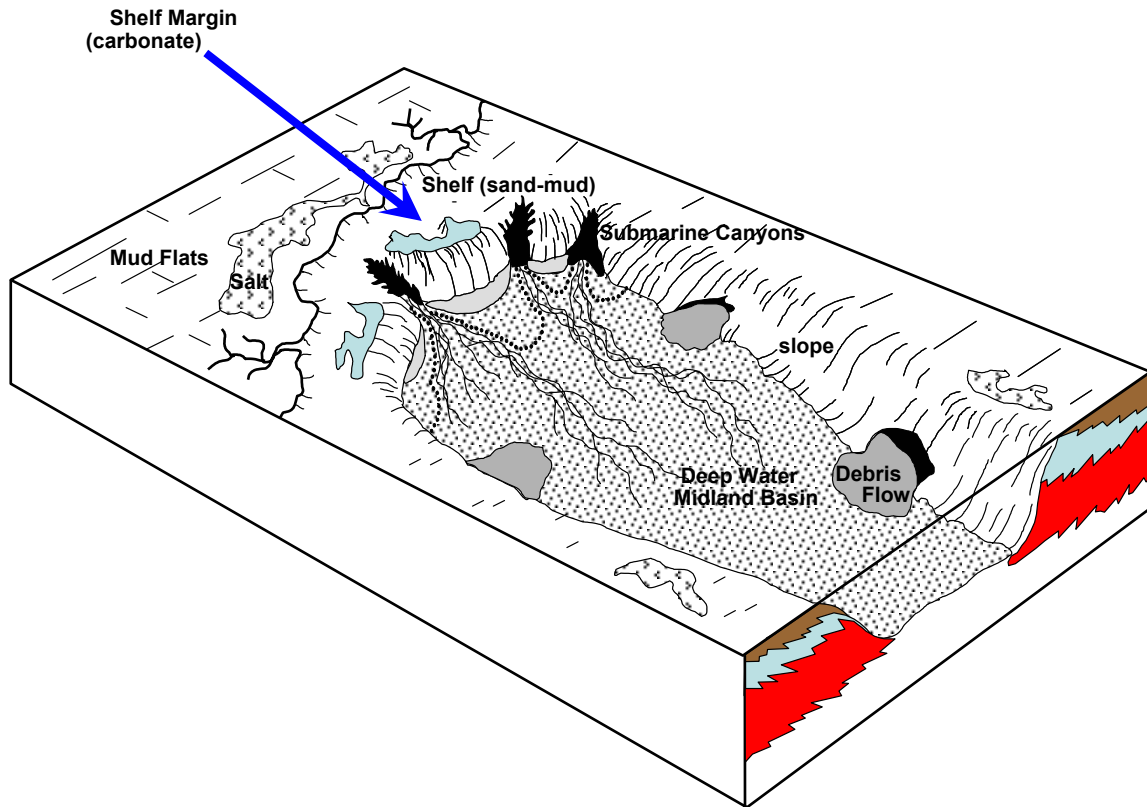


Figure 2.8. Regional chronostratigraphic and lithostratigraphic summary for the Permian Basin. Happy Field is a shelf-margin carbonate deposit of Lower Leonardian age, shown by the location of the star. Chart modified from Atchley et al., 1999.



**Figure 2.9.** Block diagram of general distribution of depositional environments, geometry of deposits, and channel patterns in the Midland Basin. Happy Spraberry field would be located on the northern margin of the cartoon, at the carbonate shelf margin (arrow). Modified from Handford, 1981.

## CHAPTER III

### PREVIOUS WORK

This chapter summarizes the previous work on Jurassic and Permian reservoir rocks that form the basis of the rock material used in this study. In about 1990, Ahr and his students from Texas A&M University became interested in identifying which of many pore-scale rock characteristics were most influential in determining fluid flow in carbonate reservoirs. This thesis differs from earlier work by Ahr and his students in that it incorporates new information on the previously-studied reservoirs, uses a wider base of geological examples (including sandstones), and incorporates nuclear magnetic resonance measurements that had not been used in the earlier work.

#### WOMACK HILL FIELD

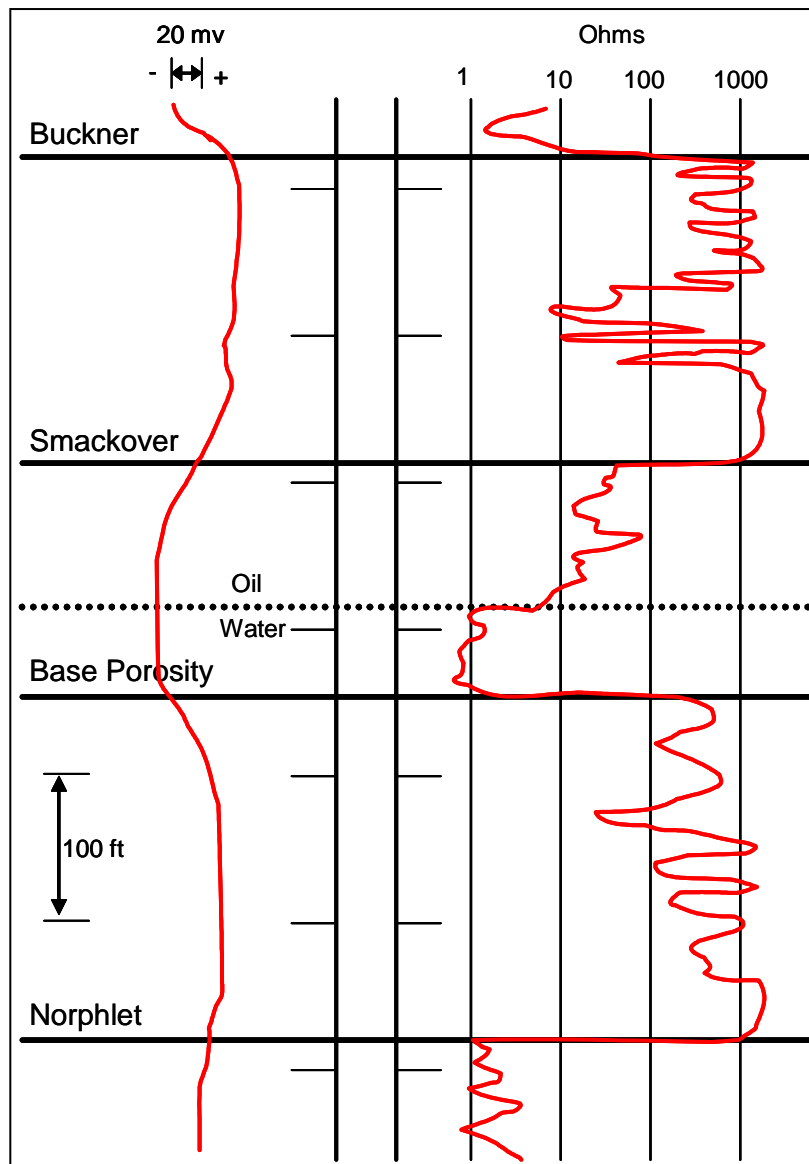
Womack Hill field, Clarke and Choctaw Counties, Alabama, has been producing oil from the Smackover since 1970, and has been on a production decline since 1977 (Avila, 2002). Smackover stratigraphic relationships in the field were identified by Meyers (1975) from electrical log response characteristics. A type log with formation boundaries for Womack Hill field stratigraphy is shown in Figure 3.1.

Townsend (1986) studied the depositional and diagenetic characteristics of Smackover reservoir rocks at Womack Hill field. His focus was to identify the stages and distribution of diagenetic changes utilizing thin section petrography. He found only weak trends relating diagenetic patterns to depositional facies along the Smackover ramp profile.

Tedesco (2002) studied dolomitization in Womack Hill field reservoir rocks in order to define relationships between depositional and diagenetic attributes in the Upper Jurassic Smackover Formation of the Eastern Gulf coastal plain. He concluded that grainstones from Womack Hill field occur at the top of parasequences, and that they exhibit high poroperm values relative to lower parts of parasequences. This pattern was confirmed by infill drilling during subsequent field development.

Hopkins (2002) studied reservoir characteristics at Womack Hill field using integrated petrologic and petrophysical data. She concluded that reservoir porosity is a hybrid phenomenon consisting of diagenetic overprints on depositional pore types, and that extensive diagenesis can either enhance or destroy reservoir quality depending on original conditions, magnitude, and direction of diagenetic change. Hopkins' (2002) work incorporated measurements from a probe permeameter and other petrophysical analyses to bridge lab results with wireline logging runs. The final integrated model and workflow were useful to identify "petrofacies" that exhibited high recovery potential and that should increase ultimate recovery.

Avila (2002) characterized Upper Smackover reservoirs at Womack Hill field using petrophysics in combination with production history plots and decline curve analyses on production and injection wells. He noted the difficulty in correlating porosity from electric logs with porosity from core analysis. Nevertheless, the results of his study were helpful in increasing the recovery of 1.9 MMSTB (under current operating conditions). His work has become essential for reservoir simulation models of the Womack Hill reservoir which must consider both petrophysics and geological



**Figure 3.1. Type log for the Womack Hill field. SP and Resistivity responses are shown as well as the base of porosity. Formation boundaries are illustrated. Modified after Meyers, 1975.**

aspects. Both Avila's (2002) and Hopkins' (2002) studies were undertaken to help explain and manage the production decline in the field since 1977.

Mancini et al. (2004) incorporated much of the petrographic, borehole log, petrophysical, and well performance data of the field in reservoir models. To date, NMR measurements have not been made on rocks from this reservoir, particularly in conjunction with image analysis, standard petrography, and mercury injection capillary pressure measurements to determine the genetic identity of pore types, evolution of the pore systems, and the cause-effect relationships that determine wireline log responses. This study incorporates those measurements to develop new insights into the origin of the pore system, its measurable properties and the manner in which pore types influence petrophysical behavior.

#### VOCATION AND APPLETON FIELDS

The Vocation and Appleton fields are located in Escambia and Monroe Counties, Alabama where they have been producing from grainstone buildups and microbial reefs in the Smackover Formation since its initial discovery in 1983 (Mancini et al., 2002). The field is approaching abandonment owing to steep production declines and consequent low profitability. Several integrated reservoir studies have been made to identify ways to enhance remaining recovery potential (Mancini et al., 2002; Parcell, 2002; Morgan, 2003).

Morgan (2003) mapped best quality flow units for these fields and found that well-connected intercrystalline/vuggy porosity of dendroidal thrombolites was the highest quality flow unit. Morgan's work built upon the study by Ahr and Hammel

(1999) which developed a method to rank and map the relative quality of flow units based on genetic pore types and their associated poroperm values.

Other approaches to reservoir characterization at Appleton field include the recent seismic modeling work by Mancini et al. (2002). The study resulted in establishment of a method to discriminate between the productive upper Smackover facies, the underlying Buckner anhydrite, and the Paleozoic basement rock based on variations in seismic reflection characteristics at field scale.

Parcell (2002) focused his reservoir characterization efforts on thrombolite reef buildups in the Smackover Formation at Vocation-Appleton. He divided the reef buildups into five “types” based on patterns of microbial fabric, which in turn were interpreted to have developed in response to different hydrologic regimes, sedimentation rates, and substrate types. The key to the classification of these altered reef fabrics was found in the application of sequence stratigraphy, notably by pinpointing relative sea level changes.

Type I reef fabrics consisted of layered thrombolites that often contained constructed voids from reef growth. Type II reefs were composed of reticulate and “chaotic” fabric and Type III were classified as dendroidal thrombolites. Types IV and V microbialites consisted of stromatolitic crusts and oncoidal pack/grainstones, respectively. Types I, II, and (especially) III were the best “quality” reef fabrics for hydrocarbon recovery in the fields. Type III fabrics were the best quality reservoir type because they were extensively dolomitized, reticulate fabrics and consequently exhibited diagenetically-enhanced, vuggy/intercrystalline porosity.



This study will incorporate NMR responses from core plugs from reef fabrics (Types I, II, and III) identified by Parcell (2002) and Morgan (2003). It is possible that this work will provide insight into how NMR responses change within the different reef fabrics, and it will provide ways to link NMR T2 responses with the best quality flow units (pore networks) identified by other means. The results can then be compared to previous attempts to determine best and poorest flow unit rank. To date, the NMR tool has not been tested as a means to discriminate between reef fabrics and their attendant flow unit properties. In addition, absolute pore dimensions and pore-size distributions that will be helpful in linking petrophysical response to reef fabric will be made using image analysis. The results may be further compared to Parcell's reef types to determine if certain reef fabrics have distinct 2-D pore geometry.

#### HAPPY SPRABERRY FIELD

Happy Spraberry Field, Garza County, Texas, produces from the Permian Clearfork Formation. Rocks in the field include oolitic/skeletal packstones and grainstones, floatstones, *Tubiphytes* bindstones, and silt and fine-grained sandstones, all of which were deposited on the eastern Shelf of the Midland Basin (Ward et al., 1986).

Ahr and Hammel (1999) ranked and mapped flow unit quality in the different reservoir zones of the field by comparing porosity/permeability values from thin sections and from core analyses. The identification of best, intermediate and worst "quality" flow units were mapped as a series of ten-foot thick stratigraphic slices. Best "quality" zones (ie. highest paired values of porosity and permeability) generally followed

depositional facies, except in rare instances where diagenesis had modified porosity to such an extent that it no longer conformed to depositional unit boundaries.

Roy (1998) conducted a companion study on half of the cores in the field, and confirmed the interpreted stratigraphic architecture of the field established by Hammel (1996). Together they concluded that four flow units existed in the field; 1) the grainstone; 2) the boundstone; 3) the skeletal packstone, and 4) the wackestone/silt-shale facies.

Layman (2002), studied thin sections from Happy field and measured pore geometry with digital image analysis techniques. He compared pore geometry to petrophysical characteristics to test the hypothesis that Hammel and Roy had correctly identified and mapped the best reservoir quality zones. Layman did not conduct comparison studies between siliciclastic and carbonate pore types, nor did he conduct any studies with NMR measurements.

In summary, carbonate rocks from three different geographical localities have been obtained for this project because they exhibit a variety of carbonate pore types, were derived from several carbonate rock types, and spanned Paleozoic through Mesozoic times. Previous workers have examined cores, thin sections, and some petrophysical aspects of some of these rocks using various techniques. Each has added to the knowledge of pore-scale characteristics that affect reservoir quality. The results of their work have been used to map flow, barrier, and baffle zones in their respective fields. None of the previous work in these fields has incorporated NMR measurements.

## SANDSTONE SAMPLES

Sandstones have not been incorporated into any of the previous work by Ahr and his graduate students. The sandstones add a new dimension to pore scale studies of this kind because they represent only one kind of genetic end-member porosity (depositional). Furthermore, NMR measurements on sandstones are well understood in the logging industry, and depositional (interparticle) pores in sandstones serve as a standard with which pore types in carbonates may be evaluated. Using interparticle sandstone pores as the starting point, carbonate rocks with a variety of depositional, diagenetic, and hybrid forms of pores can be compared to the ‘standard’, as well as to one another.

The current project builds on the previous work at each of the carbonate field localities by providing new types of measurements that can be used to further characterize pore-scale controls on subsurface flow quality. Additional rock material (both sandstone and carbonate), direct measurements on that rock material, the NMR response, and the capillary pressure measurements all contribute to a better understanding of reservoir quality – and how that quality can be identified in other subsurface deposits where expensive core analyses may not be possible.

## **CHAPTER IV**

### **METHODS**

This chapter outlines material preparations and procedures used to obtain pore-scale measurements on 40 carbonate and 7 sandstone core plugs. Original one-inch diameter cylinders were drilled in whole cores and then cleaned. The carbonate core plugs were first sent to NUMAR labs to obtain NMR measurements, and thereafter shipped to PetroTech Associates for MICP testing. The sandstone core plugs were personally taken to ConocoPhillips Research Labs in Bartlesville, Oklahoma, where NMR measurements were there collected under the direct supervision of Dr. Jim Howard. Trimmed end segments from the core plugs were professionally prepared into thin sections at National Petrographic Labs, including epoxy impregnation (to identify pore space) and Alizarin Red S stain to discriminate carbonate minerals.

Routine petrography was used to classify porosity by origin using the system developed by Ahr (2005). The preferred choice of classification of pore space and its

end-member processes are summarized. Digital photos of thin section fields of view were then obtained. Image analysis software was used to measure sizes and shapes of pores as well as total visible porosity. Pore width boundary dimensions used by the PIA software were chosen at 0.02, 0.5, and 1.0mm diameter, respectively. The lower bin size value was a lower size limit recommended by Anselmetti et al. (1998) in their image analysis studies. Fewer than 10 of the thousands of measured pores were greater than 1 mm, thus 1mm was chosen as the upper bin size limit. Basic background on the NMR and MICP test procedures, limitations, and specific applications used this study are explained later.

Nine rock samples were examined with SEM to identify paramagnetic minerals that may affect the NMR response. The SEM techniques used to map the location of paramagnetic minerals across 1cm<sup>2</sup> rock surfaces are also discussed later in this chapter.

## MATERIAL PREPARATIONS

Forty-seven rock cores of various lengths, locations, and depths were available for this study (Table 4.1). Rocks that contained end-member genetic pore types (and associated hybrids) were examined to accomplish the project objectives (Chapter I). Nine rock samples from Vocation and Appleton fields were ‘inherited’ from a previous study by Morgan (2003) and 14 additional hand samples from these two fields were chosen to supplement the existing suite of diagenetic pore types. Rock cores from other locations (i.e. Womack Hill and Happy fields) were used because they contained examples of end-member and hybrid pore types (Hopkins, 2002; Layman, 2003) not available in Jurassic equivalents from Appleton and Vocation fields. Core material from Womack Hill field and Australia were a unique and key part of the data set because they exhibited exclusive detrital depositional porosity.

After the necessary rock material was obtained, one-inch diameter plugs were drilled into cylinders, parallel to bedding. Rocks were drilled in the Department of Geology and Geophysics Rock Mechanics Lab located at Texas A&M University. Core plugs were drilled at 800 rpm with continuous water flow on the drill bit.

**Table 4.1. Table of available core plug data including location, depth, and date of preparation. Samples were prepared by Aaron Adams in 2003-2004. Nine core plugs were prepared by Dylan Morgan in 2001 (bold).**

#### Appleton Field, Alabama

Field	Well ID	Depth (ft)
Appleton	3986	12,944
Appleton	3986	12,964
<b>Appleton</b>	<b>3986</b>	<b>12,970</b>
<b>Appleton</b>	<b>3986</b>	<b>12,999</b>
<b>Appleton</b>	<b>3986</b>	<b>13,024</b>
Appleton	4633-B	12,868
<b>Appleton</b>	<b>4633-B</b>	<b>12,948</b>
<b>Appleton</b>	<b>4633-B</b>	<b>12,969</b>
<b>Appleton</b>	<b>4633-B</b>	<b>12,984</b>
Appleton	4633-B	13,014
Appleton	4633-B	13,016
Appleton	3854	12,885
Appleton	3854	12,890
Appleton	3854	12,891.5

#### Vocation Field, Alabama

Field	Well ID	Depth (ft)
Vocation	2935	14,144
Vocation	2935	14,150
<b>Vocation</b>	<b>2935</b>	<b>14,078</b>
<b>Vocation</b>	<b>1599</b>	<b>13,987</b>
Vocation	1599	14,017
Vocation	1599	14,059
Vocation	1599	14,087
Vocation	1599	14,131
<b>Vocation</b>	<b>5779</b>	<b>13,946</b>

Bold samples prepared by  
Dylan Morgan in 2001

#### Womack Hill Field, Alabama

Field	Well ID	Depth (ft)
Womack	P4575	11,120
Womack	P4575	11,129
Womack	P4575	11,146
Womack	P4575	11,156
Womack	P4575	11,174
Womack	P4575	11,192
Womack	P1591	11,405
Womack	P1591	11,411
Womack	P1591	11,413
Womack	P1591	11,515
Womack	P1591	11,528

#### Happy Field, Texas

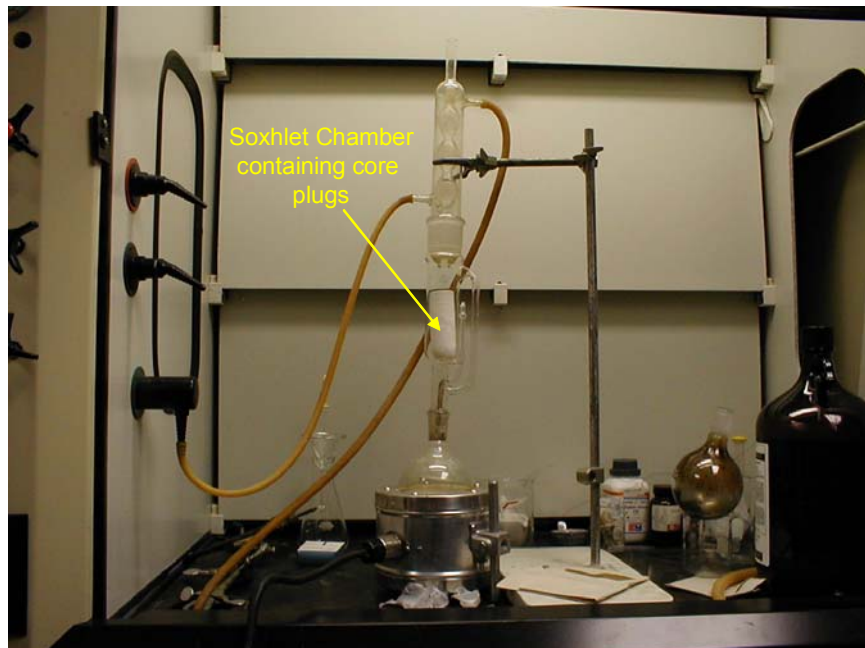
Field	Well ID	Depth (ft)
Happy	19-7	5,009.0
Happy	19-7	4,956.0
Happy	19-3	4,956.5
Happy	19-3	4,925.0
Happy	19-3	4,972.5
Happy	19-3	4,923.2

#### Northwest Australian Shelf

Sample #	Depth (ft)
16	unavailable
19	unavailable
20	unavailable
21	unavailable
23	unavailable
24	unavailable
27	unavailable

### Core Plug Cleaning

Forty carbonate samples - 9 from a study by Morgan (2003) and 31 specifically collected for this research - were cleaned at Texas A&M University at the Rock Properties Lab in the Department of Petroleum Engineering. A Soxhlet apparatus was used to extract hydrocarbons using simple distillation (Fig. 4.1). Prior to cleaning, core plug length and width dimensions were measured using a caliper tool. This step was necessary to ensure that each individual sample could be identified after the cleaning process. Toluene and methanol were boiled in the bottom flask. The gases then condensed, saturated the core plugs, and extracted pore-plugging compounds. The solvent was repeatedly flushed with a siphon and the process was repeated until the core



**Figure 4.1.** Soxhlet distillation unit used to extract hydrocarbons from core plugs. Photo taken from <http://webpages.marshall.edu/~vanhooose3/SoxhletExtractionApparatus.html>.



plugs were “clean” (up to 72 hours). Clean was defined as the point when the solvent remained clear after flushing. Core plugs were checked under fluorescent light to test for the presence of extractable hydrocarbons.

After hydrocarbon extraction was finished, the samples were dried overnight at 100°C to remove residual moisture. Care was taken to avoid decrepitation of samples during drying. Sandstone core plugs were shipped to the ConocoPhillips Technology Center in Bartlesville, Oklahoma, and cleaned in similar fashion preparatory to NMR measurement (Howard, personal comm.).

#### CLASSIFICATION OF PORE SPACE

Carbonate petrology was the fundamental means used to determine pore genesis. Ahr’s genetic classification of porosity was the easiest way to relate the final geologic products (observed pores) to their pore-forming processes (geologic causes). More importantly, it provided a way to relate pore origin to subsurface processes which can be mapped between wells. The classification does include some elements of classification schemes from earlier workers. However, it has the advantage over other schemes because it is easily applied to flow unit mapping in the subsurface.

A classification of carbonate reservoir porosity was published by Archie (1952), where he related visible pores to various “crystal” arrangements at 10x magnification. Later work by Choquette and Pray (1970) classified carbonate porosity on the basis of whether it was observed as fabric selective, non-fabric selective, or both. Modifiers such as epi, meso, and telogenetic denoted zones of creation and modification of porosity in

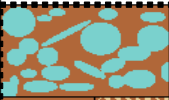
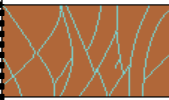
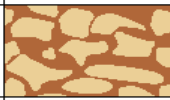
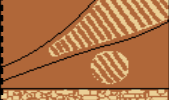






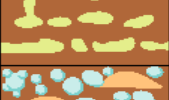
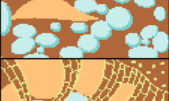



sedimentary carbonates. Other modifiers such as micro, meso, and megapore denoted basic pore size scales which roughly correspond to common silt, sand, and gravel sized particles.

Choquette and Pray (1970) identified fifteen basic pore types (Fig. 4.2).

A further development in the classification of carbonate porosity includes the effect of vugs, whether the vugs are connected (touching) or not, and the extent to which vuggy porosity contributes to total porosity (Lucia, 1983). Vuggy porosity is diagenetic in origin and Lucia's (1983) classification does not include mode of origin for different types of pores. His scheme does not provide help in predicting the spatial distribution of genetic pore types or in mapping flow units (Ahr, 2005). Lucia's classification is objective rather than genetic and doesn't identify the origin of pore types.

An "objective" porosity classification was proposed by Ehrlich et al. (1991a). In their scheme pore origin was ignored and the classification was based entirely on pore geometry. Their classification system considered 300 measurement variables to yield 7 pore types in sandstones alone, and at least 15 additional pore types in carbonates. Ehrlich's classification is difficult for practicing geologists to apply to subsurface stratigraphic scenarios.

It was desirable in this research to use a classification system which could be applied to subsurface stratigraphy such that flow units could be mapped between wells. Ahr's genetic classification of porosity was the best choice for this purpose because it classified pores by their geological origin and related pore geometry, vug type, and their

Fabric-selective		Not fabric-selective		Fabric-selective or not	
	Interparticle		Fracture		Breccia
	Intraparticle				
	Intercrystal		Channel		Boring
	Moldic		Vugs		Burrows
	Fenestral				
	Shelter		Cavern+		Shrinkage
	Growth-Framework	+ Man-sized or larger pores With channel or vug shapes			

**Figure 4.2. Classification of fifteen carbonate pore types. The five most common types of pores in this study are outlined in black. Modified after Choquette and Pray (1970). [http://www.slb.com/Hub/Docs/connect/reference/Middle\\_East\\_Well\\_Evaluation/wer20/carbon.pdf](http://www.slb.com/Hub/Docs/connect/reference/Middle_East_Well_Evaluation/wer20/carbon.pdf)**

formative geologic processes and end products into a user-friendly conceptual model (Fig. 4.3). Genetic pore types are useful criteria that have been used to identify flow units in stratigraphic context and correlated from point to point at field scale (Ahr and Hammel, 1999). Neglecting pore origin in mapping subsurface flow units can lead to erroneous correlations because diagenetic influences can persist across facies boundaries. A basic explanation of the genetic classification of porosity by Ahr follows below.

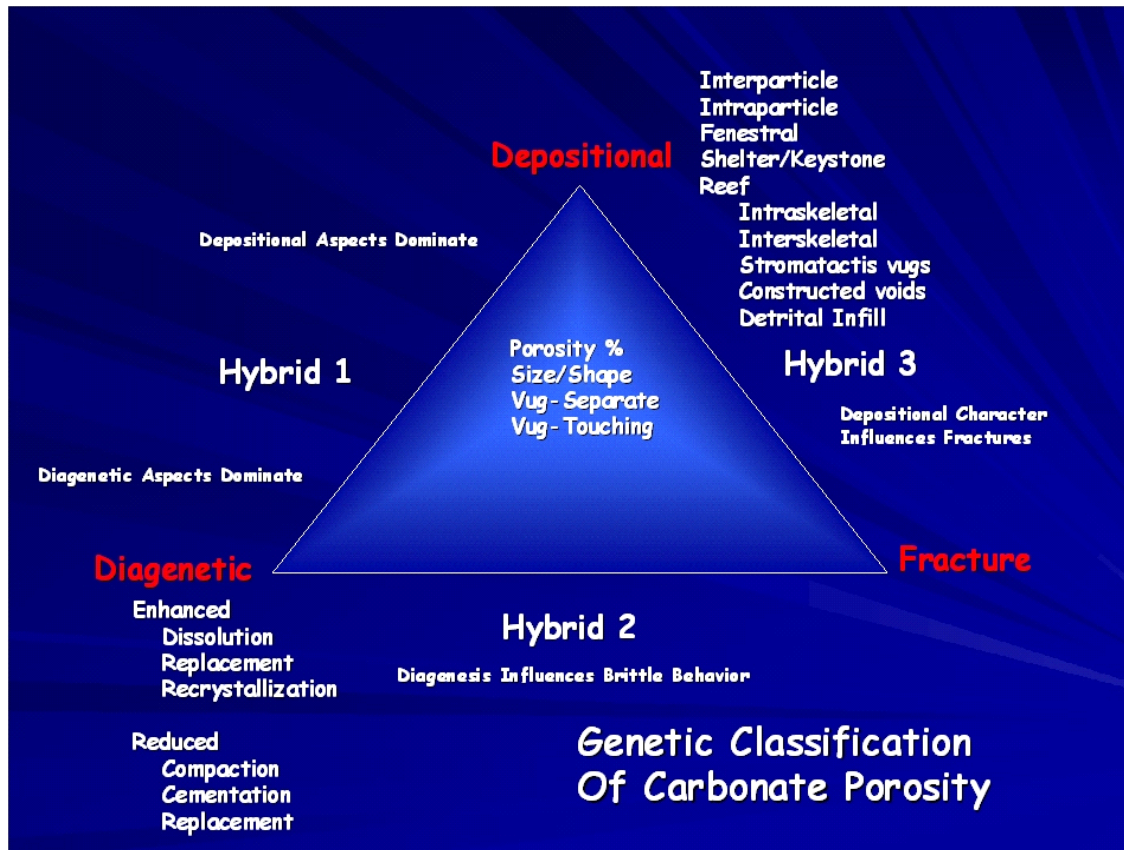


Figure 4.3. Genetic classification of porosity after Ahr (2005).

### Depositional Porosity

Depositional pores are those which reflect depositional textures formed during detrital sedimentation. Depositional pores include: intergranular, intragranular, fenestral, shelter, and keystone pore types (Ahr, 2005). Sandstones and carbonate grainstones used in this study exhibit mainly intergranular depositional pores.

### Hybrid 1 Porosity

Hybrid 1 pores contain elements of both depositional and diagenetic processes. In this study, they occur as: a) altered inter/intragranular pores with strong depositional attributes, and b) moldic pores that were created when detrital grains accumulated during detrital deposition then were chemically unstable and removed from the rock by post-depositional dissolution. Moldic pores may preserve the original exterior grain shape of the deposited grains – provided that subsequent dissolution processes did not distort grain shape beyond recognition. Oomoldic and skelmoldic grainstones and packstones in this study exhibited moldic pore types.

### Diagenetic Porosity

Post-depositional processes may either enhance or reduce porosity. Diagenetic processes which enhance the porosity of the rock may include dissolution, replacement, or recrystallization. Dissolution creates porosity by removal of some or all of the rock

volume. Karst terrains are examples of major porosity generation by dissolution of the host rock. The same process occurs on field, core, and pore scales.

Diagenetic processes may reduce porosity by compaction, cementation, or replacement. Loose sediment aggregates shift from cubic to more rhombic packing during burial, thereby reducing pore space. Ductile grains may deform to fill pre-existing pore space. Cementation around or between grains reduces porosity by filling pore space with mineral precipitates. Dolomitization is a common form of replacement in which calcite is replaced by dolomite.

#### Fracture Porosity

Fracture porosity forms as a result of brittle failure under differential stress. Fractures can be quite common in carbonate reservoirs, but were not found in the rocks used in this study.

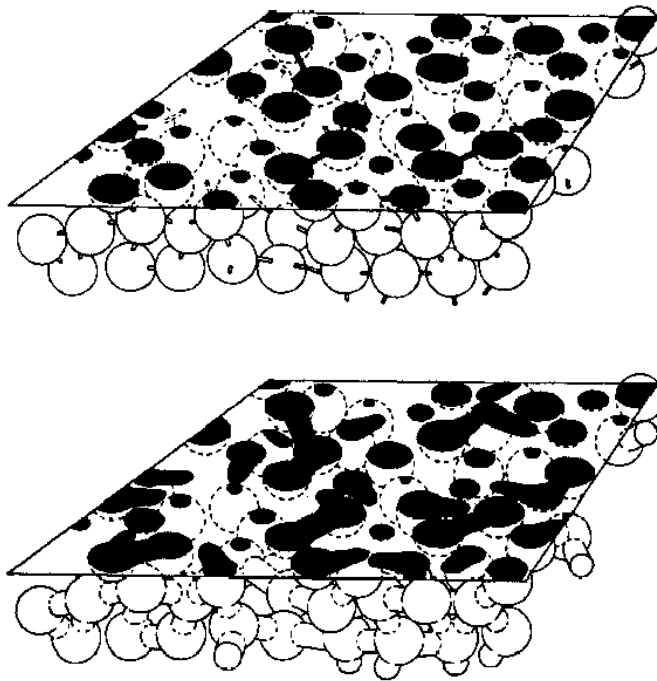
## PETROGRAPHIC IMAGE ANALYSIS (PIA)

Petrographic Image Analysis (PIA) is a method used to measure objects in thin section or SEM. For example, Davies (1990) used PIA to rapidly scan percussion side wall cores to identify damaged zones. PIA provides a means of: 1) rapidly measuring total rock porosity in 2-D for which pore area in thin section is a proxy, 2) sorting pore images into selected size categories, and 3) measuring pore geometry (i.e. roundness and aspect) on objects (pores) identified in the digital images.

Application of PIA in reservoir geology has developed in part as a way to relate pore geometry in reservoir rocks to spatial and petrophysical data (Ehrlich, 1984). The three-dimensional character of carbonate pore networks can be observed directly by dissolving the rock matrix from an epoxy-impregnated sample, leaving only a pore cast behind (Wardlaw, 1976). However, most observations of pore networks are 2-D views from thin sections or SEM images. Thin sections provide less information than 3-D pore casts but are more cost efficient than pore casts and do not destroy the rock. In spite of a change in the dimension of observation, thin section and SEM 2-D views have provided substantial information about the 3-D volume from which they were derived – including the pore space. In some literature a “porel” (Ehrlich et al., 1991a), short for porosity element, is used to describe the 2-D equivalent of a pore taken from a 3-D volume. Ehrlich et al., (1984) specifically noted that 2-D “slices” were related geometrically or statistically to the “true” 3-D pore volume, particularly in simple intergranular porosity where cubic or rhombohedrally-packed spheres were modeled. Diagenetic or other changes in the original 3-D pore network were reflected in the 2-D slice (aka transfer

function), which can be tedious to interpret in cases where a great variety of grain and pore types are present. Simply stated, the complexity of the 2-D to 3-D transform function increases with the increase in the abundance of non-spherical grains or pores.

Ehrlich and Davies (1989) showed how changes in pore and pore-throat geometry of sandstones in 3-D corresponded to changes in pore and pore-throat geometry imaged in 2-D. They used examples of spherical pores connected by cylindrical pore-throats in basic models, and demonstrated that similar trends exist in carbonate rocks with multiple pore types (Fig. 4.4).



**Figure 4.4.** Cartoon sketches of 2-D intersections of a hypothetical volume of 3-D pores, pore-throats, and rock. Pores and pore-throats (black) show a corresponding transform in pore geometry from 2-D to 3D space. These are similar cartoons, the difference being that the lower has larger pore-throats relative to the upper cartoon. Modified from Ehrlich and Davies (1989).



Ehrlich et al., (1984) used sandstone thin sections from the Tuscaloosa formation to illustrate an image erosion-dilation procedure which processes image data in the computer after the images were obtained. The method employs iterations to remove small pores and then processes remaining size and shape information with proprietary computer algorithms. Ehrlich and Davies (1989) commented on the technique such that “the pore geometry of a single microscopic field of view was described in terms of approximately 300 variables”. As many as 7 pore “types” were generated by the Ehrlich and Davies (1989) method in sandstones alone. Ehrlich et al. (1991a), McCreesh et al. (1991), and Ehrlich et al. (1991b) have each used the erosion-dilation technique to link pore geometry in sandstones (as determined by image analysis) to mercury injection capillary pressure measurements on replicate samples.

#### PIA in This Study

The imaging software Image-Pro® Plus was used in this study. Commercial digital imaging software provides a rapid and cost efficient method of measurement of both individual and collective characteristics of digitized objects in a field of view or collectively from an entire thin section. The step-by-step procedure for obtaining pore measurements with this commercial software is given in Appendix B. No proprietary data processing was needed, and pore geometry variables were simplified into four (not 300) measurement criteria; roundness, aspect, area, and width. Mean values of those variables were determined within bin size groups for each thin section (Appendix C), and spreadsheets with minimum, maximum, and average length, width, roundness, area,

and perimeter from a thin section containing > 10,000 pores were obtained in a matter of minutes.

### *Selection of Size Bins*

Given the range of possible pore sizes in a given rock, a constraint on the number of measurement bins was necessary. Four bin sizes had the most reproducible results in trial runs and were used as templates for all rocks (sandstone and carbonate) in this study. The smallest bin size contained pores <0.02mm diameter. This is the approximate thickness of a thin section and a bin size cutoff value recommended by Anselmetti et al. (1998) and Ehrlich (1984). The middle pore size bin was chosen between 0.02-0.5mm. Lucia (1995) showed that carbonate reservoirs absent of vugs most frequently contained particles smaller than 0.5mm. For this reason, it was anticipated that the bulk of the measurements would occur in pores surrounded by particles of such size. However, many of the dolomites (particularly Appleton and Vocation fields) in this study contained numerous vugs that measured between 0.5 and 1mm, but rarely did individual pores measure more than 1mm. Therefore, bin size cutoff values of 0.02, 0.5, and 1.0mm were used in this study and represent a combination of literature-recommended sizes and parsimony.

The end result of this specified routine was rapid and cost-efficient identification of total visible porosity, size, shape, and abundances of several pore types – all grouped by their genetic origin and managed within specific bin size constraints.

### *PIA Pore Geometry and Calculation of 2-D Porosity*

The basic procedure to obtain pore measurements by PIA is simplified into the following four steps. First, thin sections were placed on the mechanical stage of a petrographic microscope such that adjacent fields of view were digitally photographed across the entire thin section area. Second, the live camera images were projected onto the monitor and carefully examined to ensure maximum contrast between dyed epoxy and rock. Fields of view on the margins of the thin section were traced by hand to exclude unwanted areas or features (Appendix B). The live camera view was set to snap rectangular images that simplified collection of adjacent view fields. Third, blue epoxy was differentiated from the rest of the field of view and assigned a temporary “false” color. Fourth, selected groups of objects (i.e. pores) were sorted into their respective bin sizes and further measured by the software for porosity, roundness, aspect values, and width.













Total 2-D porosity was determined by measuring the area of the thin section occupied by dyed epoxy. The area containing epoxy was considered a reasonable estimate of effective porosity. This visible porosity value was reported as the average of 22-30 fields of view from a given thin section (Plate 1). It was hypothesized in this study that total porosity measured in routine core analyses along with porosity inferred from NMR values would consistently appear greater than porosity measured by PIA. This pattern was expected in all cases where a significant portion of the porosity was found in pore sizes below an optical microscope resolution of 25X. Additional reasons why PIA may underestimate NMR porosity was that the 2-D view may not represent a

maximum diameter slice through the pore, thus appearing to measure an object of smaller size than truly existed in 3-D. And also the fact the NMR was able to detect and include very small pores in its final calculation of porosity. These same small pores are not easily visible using standard microscopy and account for real porosity invisible to PIA.

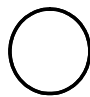


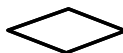

Aspect ratio is the ratio between the major and minor axes of an ellipse that is more-or-less a proxy for the object to be measured. Aspect ratios are always greater than or equal to 1. Roundness was calculated by Image-Pro® Plus in a way that circular objects had a roundness equal 1; other shapes had a roundness value greater than 1. Both aspect and roundness values are numbers without units.

Simple shapes were used to test the response of the aspect ratio and roundness (Table 4.2) routines in the software to basic circular, square, star, and corresponding elongate-shapes. Tiab and Donaldson (2004) present a table of 2-D pore shape factors (Table 4.3). These ‘factors’ include roundness measurements by PIA in which the pore shape factor is given by the expression  $f_{ps} = L^2_p / 4\pi A_p$  (Tiab and Donaldson, 2004). However, these pore shape ‘factors’ do not include elongation, a characteristic of fenestral pores, solution channels, and fractures, nor do they include star-like shapes that mimic the irregular edges of non-round vug or pore walls.

**Table 4.2. Test objects for PIA measurement of pore geometry used in this study. All objects are equal area.**

Very Non-Round >>>1	5.848  1.279	9.678  5.156	25.491  20.983
Non-Round >>1	1.769  1.158	2.948  3.465	10.059  13.828
Near-Round >1	1.223  1.020	1.950  4.083	5.499  15.584
Round =1	1.082  1.001	1.986  3.959	6.621  15.569
Roundness Aspect	Equant $L = W$	Elongate $L > W$	Very Elongate $L \gg W$

**Table 4.3. 2D PIA pore shape factor values used in petrophysical measurements. Note similar roundness values in test objects of similar shape (Table 8) and absence of aspect and extremely non-round object forms in the shape factor table. Taken from (Tiab and Donaldson, 2004).**

2D PIA Pore Shape Factors	
Pore Shape	$f_{ps}$ (2D)
	1.00
	1.27
	1.65
	3.75
	5.84

## NUCLEAR MAGNETIC RESONANCE (NMR)

The principle of nuclear magnetic resonance (NMR) has been known for several decades from its applications in the medical profession (Selley, 1998). It has been used in borehole logging since the 1950's (Brown and Gammon, 1960), but has only recently come into its own owing to the advances in technology that have made the method effective and applicable in the petroleum industry (Selley, 1998). NMR logging can measure porosity, permeability, mobile and irreducible water, and gas (Coope, 1994). Other parameters such as liquid viscosity, presence of clays, presence of vugs, grain size, and presence of fractures can be indicated by NMR logging under certain conditions (Coates, et al., 1999). In short, NMR logging can provide information about: 1) the quantities of fluids in the rock, 2) the properties of these fluids, and 3) the sizes of pores that contain these fluids (Coates, et al., 1999).

### How NMR Works

Fundamentals about the way in which NMR works are found in Cambden (1994), Allen et al., (1997), Watson and Chang, (1997), Coates et al., (1999), and Kasap et al. (1999). To summarize, both the bench top NMR tool and NMR logging tool operate on the basis of hydrogen proton spin behavior. The bench top tool subjects the brine saturated rock sample to a strong magnetic field. The H<sup>+</sup> ions in the liquid align themselves to the magnetic field. This first alignment to the tool's magnetic field is called the polarization time, or T1 time. Then a second magnetic field (perpendicular to the first field) is produced. The second field is then switched off.

The time required for the protons to return to their original polarized state in the 1<sup>st</sup> field is the relaxation or T2 time, which is measured by the tool in micro or milliseconds. Energy absorbed from the magnetic field is proportional to the density of the H<sup>+</sup> nuclei, or in other words, proportional to the porosity of the rock. The ratio of T1 to T2 is proportional to the pore volume and is reported as a distribution curve of pore volumes along a time axis. No absolute volumes for the pore size classes are given because assumptions about pore shape and diffusion effects must be made. Because T2 time is a measure of surface-to-volume ratio, rapid-relaxation in T2 time corresponds to smaller pore sizes; longer T2 relaxation times are associated with larger pores.

NMR is gaining popularity as its use becomes better understood, its application more widespread, and its resultant measurements more reliable. Many recent reservoir characterization studies have employed NMR technology in different ways with varying degrees of success. Aivano and Howard (2001) used NMR to study permeability of the Morrow Formation. In this case T2 overestimated permeability relative to conventional core analysis, and was adjusted to match values from routine core measurements. Prenski (2001) found that NMR can be included in the 'logging-while-drilling' suite of tools useful in both light and heavy hydrocarbon recovery programs. This was due to the ability of NMR to discriminate fluid types. Mallett et al. (2000) have applied NMR cryoporometry to concrete. Their technique froze liquid in the rock and then began warming it at incremental stages. Solid brine that was frozen in the small pores and pore-throats melted first, and was detected by NMR as a corresponding small pore-size distribution. They pointed out the need for detailed core analysis and the proofing of the

NMR response to 2-D images taken from the rock samples to verify that the NMR tool was ‘seeing’ the same distribution of pores identified in 2-D images. Romero et al. (2000) correlated T2 spectra with different siliciclastic facies and Hodgkins and Howard (1999) found that NMR was a competitive technique that could supplant routine core analysis on low resistivity sands from the Gulf of Mexico. They showed that T2 spectra compared well with other distributions of pore sizes – particularly those measured by laser particle size analysis.

With respect to NMR T2 cutoff times (defined as the empirically-derived value below which represents the bulk volume of irreducible water - 33 milliseconds for sandstones, and 92 milliseconds for carbonates (Coates et al., 1999), Willard et al. (1998) noted that T2 cutoffs used for intergranular porosity are not good predictors of permeability in vuggy porosity. Nurmi et al. (1998) discussed applications of NMR logging to discriminate between vugs and micro porosity in carbonates. With similar objectives in mind, Parra et al. (2001) used NMR successfully in combination with acoustic logs in carbonate aquifers of South Florida. They were able to identify vuggy pore space in the region surrounding the borehole using the two techniques in tandem (Parra et al., 2001).

Ausbrooks (1999) and Ausbrooks et al., (1999) measured the amount of vuggy porosity in Oligocene carbonates from the Bohai Basin, China. They found that core photos of gastropod packstones and grainstones have similar pixel counts of porosity with high-resolution borehole imagery in 2-D. The end result was the development of a technique to relate core-calibrated borehole images to NMR behavior in vuggy rock.



Lodola (2004) used NMR T2 relaxation data to discriminate between depositional and diagenetic pores in Cretaceous carbonates from the Shuaiba formation of the Middle East.

### NMR in This Study

#### *Carbonate Samples*

NMR T2 relaxation time distributions were determined for 40 carbonate core plugs by NUMAR Lab Services located in Houston, Texas. Prior to measurement, the samples were trimmed to right cylinders and dried in a convection oven. Helium porosity, air permeability and grain density were then measured. Samples were then saturated in 4% KCl brine. Bulk volumes were determined by the Archimedes' method. Each 100% brine-saturated sample was stored in an air-tight vial and measured for NMR characteristics using NUMAR's CoreSpec-1000<sup>TM</sup>. The measurements were performed under a homogenous magnetic field using 1 MHz frequency pulses at interecho spacing ( $T_E$ ) of 0.6 and 1.2ms (Curby, personal comm.). The T2 data were used to obtain NMR measured porosity, and to construct a distribution of pore sizes for the core plug.

#### *Sandstone Samples*

NMR T2 relaxation time distributions were determined for 7 sandstone core plugs at the ConocoPhillips Research Labs located in Bartlesville, Oklahoma. A bench top NMR instrument (Fig. 4.5) was used to measure T1 and T2 relaxation times at

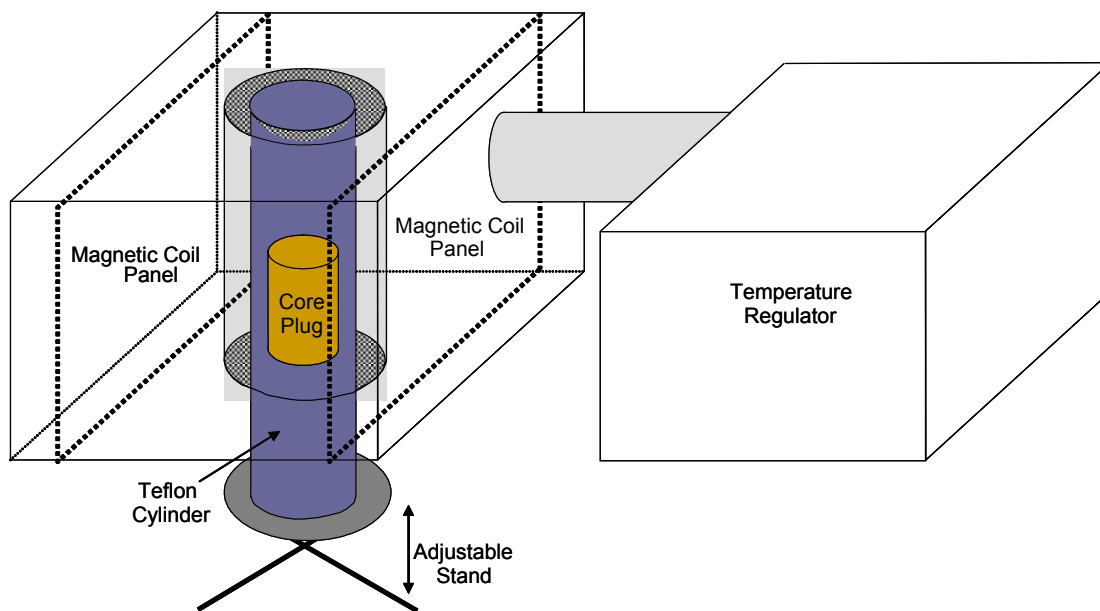


Figure 4.5. A simplified sketch of the NMR bench top measurement device.

$S_w=100\%$  and  $S_{wirr}$ . The T2 data were used to obtain NMR measured porosity, and to construct a distribution of pore sizes for the core plug.

One inch diameter core plugs were first saturated in a synthetic brine (approximate seawater) solution for several days. Each saturated core plug weight ( $S_w=1$ ) was recorded (Table 4.4). Density of the synthetic brine solution was 1.01g/cc as reported by the Bartlesville Lab. Core plug bulk volume, core plug pore volume, and core plug porosity were calculated by:

$$(Eq 1.) V_b (cm^3) = r^2 (cm) * \pi * length (cm)$$

$$(Eq 2.) V_p (cm^3) = M_{p_{S_w=1}}(g) - M_{p_{S_{wirr}}}(g) / \rho_{fl}(g/cc)$$

$$(Eq 3.) \phi (\%) = V_p/V_b * 100$$

where:  $V_b$  = bulk volume of the core plug  
 $V_p$  = pore volume of the core plug  
 $M_{p_{S_w=1}}$  = mass of core plug at  $S_w=1$   
 $M_{p_{S_{wirr}}}$  = mass of core plug at  $S_{wirr}$   
 $\rho_{fl}$  = density of fluid brine

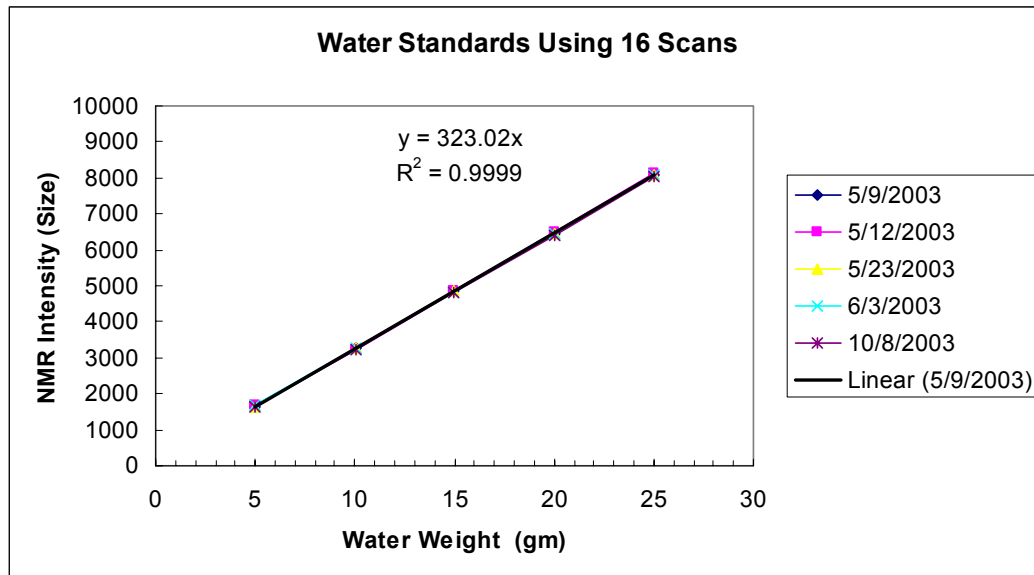
A Maran Ultra® resonance instrument was calibrated by comparing NMR response from a porosity standard (i.e. Berea Sandstone) with known porosity, and a brine sample, assuming linearity in NMR response (Table 4.5).

**Table 4.4. Sandstone measurements of diameter, radius, length, mass, fluid density, bulk volume, pore volume, and core plug porosity.**

Sample Number	Diameter cm	Radius cm	Length cm	Mass $S_w=1$ g	Mass (dry) g	$\rho$ fluid g/cc	Core Bulk Vol	Core Pore Vol	Core Porosity %
16	2.410	1.205	4.413	47.0438	44.6404	1.01	20.13	2.38	11.82
19	2.410	1.205	4.530	50.2198	49.2740	1.01	20.66	0.94	4.53
20	2.417	1.209	4.244	44.6829	42.5575	1.01	19.47	2.10	10.81
21	2.416	1.208	4.484	48.8860	47.2986	1.01	20.56	1.57	7.65
23	2.410	1.205	4.102	42.5138	39.8683	1.01	18.71	2.62	14.00
24	2.416	1.208	4.054	44.2659	43.2990	1.01	18.59	0.96	5.15
27	2.416	1.208	4.291	47.3227	45.6979	1.01	19.67	1.61	8.18

**Table 4.5. Calibration data preparatory to T1 and T2 measurements of sandstone coreplugs. A Berea sandstone with known porosity and a water standard are used to calibrate the NMR benchtop instrument.**

Standard	Core Porosity	Core Bulk Vol.	Core Pore Vol	Sum Ai = NMR Ampl	SIZE Calc NMR	No. Scans	Gain NMR RG	Ms
	18.15	58	10.527	235,774	232105.4	128	52	1813



Date	5/9/2003	5/12/2003	5/23/2003	6/3/2003	10/8/2003
Wt. (g)	Intensity	Intensity	Intensity	Intensity	Intensity
25.0274	8073	8124	8088	8094	8049
20.0258	6453	6482	6451	6471	6415
14.9927	4861	4840	4850	4835	4800
10.023	3254	3225	3266	3278	3235
4.9917	1644	1673	1633	1676	1625

After calibration was complete, the NMR measured porosity of the core plugs was determined (Table 4.6 and Fig. 4.6). The calculation works independent of lithology, and in the logging industry, is often considered the most accurate measurement of porosity provided that the following three conditions were satisfied: 1)

Sufficiently long polarization time existed such that all hydrogen nuclei were completely polarized, 2) a sufficiently short echo spacing existed to detect decay of H<sup>+</sup> in very small (clay sized) pores, and 3) the number of H<sup>+</sup> nuclei in the fluid was equal to an equivalent volume of water (Coates et al., 1999).

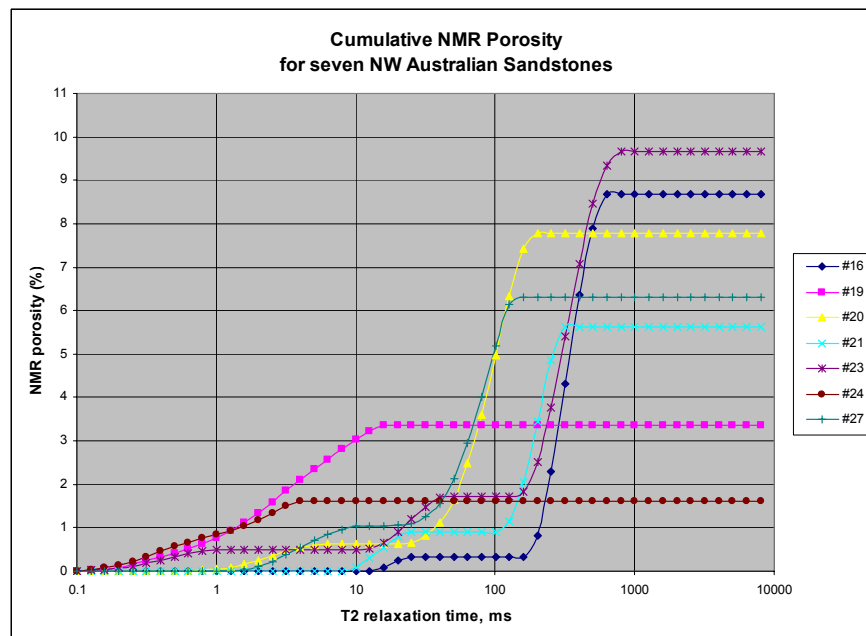
The respective calculations of core porosity, core bulk volume, and core pore volume were determined using Equations 1-3. The NMR amplitude was reported as the dimensionless sum of all amplitudes for that sample, neglecting the last value after the amplitude plateau was achieved (Appendix D). SIZE (Calc NMR) was the calculated populations for each time constant (i.e. the calculated amplitudes for each time value). The number of scans (No. Scans) was determined by the user - typically between 16 and 256. Because the instrument measures the decay of spin in hydrogen nuclei, the number of scans necessary to detect H<sup>+</sup> protons was increased as saturation values approached Swirr. In other words, fewer scans proved sufficient to measure proton density in core plugs with greater water saturation values. The number of scans was determined by trial and error so as to find the detectable limit of H<sup>+</sup> within a budgeted time frame. The Gain (NMR RG) was an instrument sensitivity measure, set at a consistent 100 for these sandstones (Howard, personal comm.). The Ms was a time measurement, essentially amplitude/scan (i.e. Size/No. Scans). Coeff was determined using the Berea sandstone standard with a known porosity to derive a coefficient for calculating the NMR volume for all of the sandstone core plugs. Specifically, Coeff was determined using the Berea sandstone and water standards data (Table 4.5), where:

(Eq. 4)  $\text{Coeff} = [(\text{Core pore volume of Standard}) * (\text{Gain (NMR RG) of Standard})] / (\text{Ms of Standard}) * (\text{Gain (NMR RG) of desired sample})]$

NMR (pore) Volume was determined by the Ms value / Coeff value. The NMR porosity (%) was calculated using the NMR pore volume / core bulk volume x 100% (Table 4.6).

**Table 4.6. Summary of NMR total porosity and prerequisite measurement data for 7 sandstones.**

Sample Number	Core Porosity %	Core Bulk Vol.	Core Pore Vol	Sum Ai = NMR Ampl	SIZE Calc NMR	No. Scans	Gain NMR RG	Ms	Coeff	NMR Vol.	NMR Porosity
16	11.82	20.13	2.38	31190.50	37092.9	64	100	579.58	0.0030	1.75	8.69
19	4.53	20.66	0.94	16607.71	14673.7	64	100	229.28	0.0030	0.69	3.35
20	10.81	19.47	2.10	28854.89	32112.2	64	100	501.75	0.0030	1.51	7.78
21	7.65	20.56	1.57	19489.16	24500.0	64	100	382.81	0.0030	1.16	5.62
23	14.00	18.71	2.62	37932.77	38315.4	64	100	598.68	0.0030	1.81	9.66
24	5.15	18.59	0.96	6183.75	6379.7	64	100	99.68	0.0030	0.30	1.62
27	8.18	19.67	1.61	22128.71	26241.8	64	100	410.03	0.0030	1.24	6.29



**Figure 4.6. Cumulative NMR porosity graphs derived from T2 relaxation times. For each given relaxation time, in incremental porosity is computed. The cumulative NMR porosity is the summation of the incremental porosities.**

### Assumptions

As shown in Equation 6, T2 conversions to pore volume make certain assumptions about the surface relaxivity constant ( $\rho$ ) and the surface-to-volume ratio (i.e. pore shape). The surface relaxivity constant ( $\rho$ ) varies with mineralogy. Timur (1972) was the first to demonstrate that the value of  $\rho$  varies with mineralogy such that carbonate rocks were about 1/7 as effective as sandstones at increasing the relaxation rate of hydrogen protons in interstitial waters. In other words, carbonate surfaces exhibited weaker surface relaxivity than quartz surfaces in lab tests (Coates et al., 1999).

A conceptual analogue to understand surface relaxivity (the  $\rho$ -constant) is a room lined with not-so-sticky fly paper. The hydrogen nuclei in water or hydrocarbons undergo diffusion, like mosquitoes flying around in the room. Because the fly paper isn't very sticky, a mosquito may bounce off the wall several times before it finally sticks to the fly-papered wall. The time evolution of the density of mosquitoes (or H<sup>+</sup> protons) flying around the room is described by Eq. 6, and the stickiness of the fly paper corresponds to the surface relaxivity (Kenyon, 1997).

Typical  $\rho$  values have been reported at ~ 5 microns/second in carbonate rocks compared to ~ 15-20 microns/second for sandstones in lab studies by Chang et al. (1997). The range of  $\rho$  values for sandstones, glass bead packs, silica gels, clean/crushed quartzes, and sandstones ranges from 0.37-46.0 microns/second. The presence of paramagnetic minerals may cause even faster rates of  $\rho$  (Dunn et al., 2002). Timur's (1972) values of surface relaxivity are based upon empirical data, and faster T2

relaxation rates can be expected where paramagnetic minerals are present at the pore wall interface (Howard, personal comm.).

$S/V$  is the geometrical factor which models pore geometry. Because  $T_2$  is proportional to  $V/S$  (i.e. pore size), spherical pores can be modeled as  $S/V=3/r$ , where  $r$  is the pore radius (Chang et al., 1997). Pore geometry is simplified into: spheres ( $6/d$ ), cylinders ( $4/d$ ), and sheets ( $2/d$ ), where  $d$  is the diameter. These end members (spheres, cylinders, sheets) represent the range of physical space for all pore shapes between 3-D and 2-D. This basic mathematical relationship for the  $T_2$  conversion oversimplifies most carbonate pore geometries – given the variety of pore types which can exist in 3-D! In other words, before a comparison of  $T_2$  times can be made with 2-D data, one must consider: 1) that pore shape was adequately described by these end-member pore geometries, and 2) that the  $\rho$  value representing surface relaxation was not adversely affected by the presence of paramagnetic minerals on the pore walls.

#### Pore Sizes as Determined From $T_2$ Times

NMR  $T_2$  distributions were the result of surface interaction of  $H^+$  protons at the rock/pore interface, and were converted into a distribution of pore volumes. The NMR benchtop tool was used to determine  $T_2$  relaxation times. The  $T_2$  times were then converted into pore volumes using the relaxivity equation:

$$(Eq. 6) \quad 1/T_2 = \rho^*(S/V)$$



where T2 (milliseconds) is transverse relaxation time, and  $\rho$  is surface relaxivity (which measured the rock surface's ability to enhance relaxation). The complete relaxation equation is:

$$(Eq. 7) \quad 1/T2_{(measured)} = 1/T2_{(surface)} + 1/T2_{(bulk)} + 1/T2_{(diffusion)}$$

1/T2 is used because rates are additive, while relaxation times (rate constants) are not. We were interested in  $1/T2_{(surface)}$  because it was the major factor influencing the T2 measurement (Howard, personal comm.).  $1/T2_{(diffusion)}$  was minimized by using short echo spacings and  $1/T2_{(bulk)}$  was reduced to negligible value by using the low-viscosity synthetic seawater (Howard personal comm.). The T2 of the water was 3.3 seconds, and  $1/T2$  was a small number and ignored when compared to  $1/T2$  for a T2 in the 100's of milliseconds range. A "complete" analysis would have removed the effect of bulk water relaxation, but is seldom done in routine NMR testing except when the measured T2's approach that of bulk water (i.e. large pores and low surface relaxivity) (Howard, personal comm.). Rearranging Equation 6 to solve for pore radius using measured T2 (in seconds) values gives:

$$(Eq. 8) \quad \text{Pore radius (microns)} = (\rho * T2 * 3 \text{ (or other shape factor)})$$

Equation 8 is the basis for converting NMR relaxation times to absolute pore diameter (i.e. = radius\*2). Equation 9 was derived from Equation 8 so as to solve for the T2

values which corresponded with the PIA bin size limits determined in the earlier phases of the project (Table 4.7). In this way the bin size boundary values could be identified on the T2 curve, and most abundant sizes could be compared between the two techniques. This was particularly useful in evaluating portions of the NMR curve which fell between 0.02-0.5mm diameter pore sizes.

(Eq. 9) Desired T2 (milliseconds) = desired pore diameter (microns) / ( $\rho$  \* 6 (or other shape factor))

**Table 4.7. Bin sizes used in PIA measurement of pore diameter. Four bins were chosen with pore diameter sizes shown in millimeters. Corresponding T2 times assume spherical pore shapes in 3D, and a rho ( $\rho$ ) value of 100 microns/second to show technique.**

Boundary values for pore bins					
Bin	1	2	3	4	5
PIA pore diameter (microns)	<20	20	500	1000	>1000
NMR T2 (milliseconds)	<33	33	833	1667	>1667

## MERCURY INJECTION CAPILLARY PRESSURE (MICP)

Except where abundant fractures or enlarged pore-throat connections exist, the majority of pore-throats in rocks are only a few microns or less in size. When the rock contains two immiscible fluids, one of the fluids tends to wet the rock surfaces preferentially and is labeled the “wetting” fluid. The relative wetting characteristics of the system are functions of the chemical properties of the fluids and the rock surfaces (Tiab and Donaldson, 2004). Mercury is commonly used in capillary measurements because of its non-wetting character.

Purcell (1949) was the first to use mercury injection measurements for the purpose of obtaining information about capillary pressure and permeability on drill cuttings in a more rapid, reliable fashion than was otherwise available at the time. Limitations on Purcell’s (1949) experiments such as low pressures (<100psi) and long wait times (often several weeks) to obtain saturation curves was a major drawback to the alternative permeable diaphragm method in determining permeability. An additional alternative method, the centrifuge, required tedious calculations and elaborate equipment. Therefore, a more efficient setup was desired. Mercury injection was proposed, and an entire capillary pressure curve could be produced in 30-60 minutes. A major advantage of this procedure was that the method would work on samples of both regular and irregular shapes and sizes, and throughout a wide range of capillary pressures.

Swanson (1981) correlated capillary pressure with permeability on over 1300 sandstone and carbonate samples. Permeability values reported in this study also

followed the Swanson method to obtain permeability values. Pore-throat radius was determined in the lab at each pressure increment (Bolger, personal comm.).

### How MICP Works

Basic MICP procedures are described by Bradley (1987) and Tiab and Donaldson (2004) and summarized as follows. A core sample is inserted in the mercury chamber and evacuated (Fig. 4.7). Mercury is forced into the core under pressure. The volume of mercury injected at each pressure determines the non-wetting phase saturation. This procedure is continued until the core sample is filled with mercury or the injection pressure reaches some predetermined value.

If the rock sample returns a high percentage of mercury as the pressure is decreased, it is considered to have a high withdrawal efficiency or recovery efficiency (Ahr, 2005). High recovery efficiency is a desirable property of reservoir rocks, as it can be a proxy for subsurface reservoir recovery efficiency. Mercury recovery efficiency is formally defined by Wardlaw and Taylor (1976) as “the ratio of the volume of mercury withdrawn from a sample at minimum pressure to the volume injected at maximum pressure before the pressure was reduced.” Assuming fluid properties are constant, there are four major factors relative to the pore and pore-throat system that contribute to mercury recovery efficiency: 1) pore and pore-throat ratio, 2) pore-to-pore accessibility, 3) coordination number of pores (heterogeneous pore distribution), and 4) pore-throat roughness (Wardlaw and Cassan, 1978).



**Figure 4.7. Lab equipment used to measure capillary pressure. Left photo shows penetrometers (sample holders). Right photo shows porosimeter used at PetroTech Associates lab in Houston, TX. Photos courtesy of George Bolger and PetroTech Associates. Used with permission.**

In a water-wet reservoir, oil that becomes disconnected with the mainstream flow to the well bore and then is left stranded behind small pore-throats is described as “snap-off”. Snap-off in MICP tests was the process whereby a continuous filament of mercury disconnected during reduction of capillary pressure (Wardlaw et al., 1988). If pores increase in size relative to pore-throat size, the continuity of the non-wetting phase was disrupted. When lost, the non-wetting phase became immobile, leaving oil in the reservoir. Therefore, measurements of pore and pore-throat sizes can help predict the tendency of the fluid to experience snap-off (McCreesh et al., 1991).

In summary, if the properties of the fluid are constant, physical characteristics of the pore-throats govern the ability of fluid to flow through the rock at the pore-throat scale (Wardlaw, 1979). Determinations of pore-throat size, as well as a distribution of pore-throat sizes under variable pressure in the rock are determined from capillary pressure measurements.

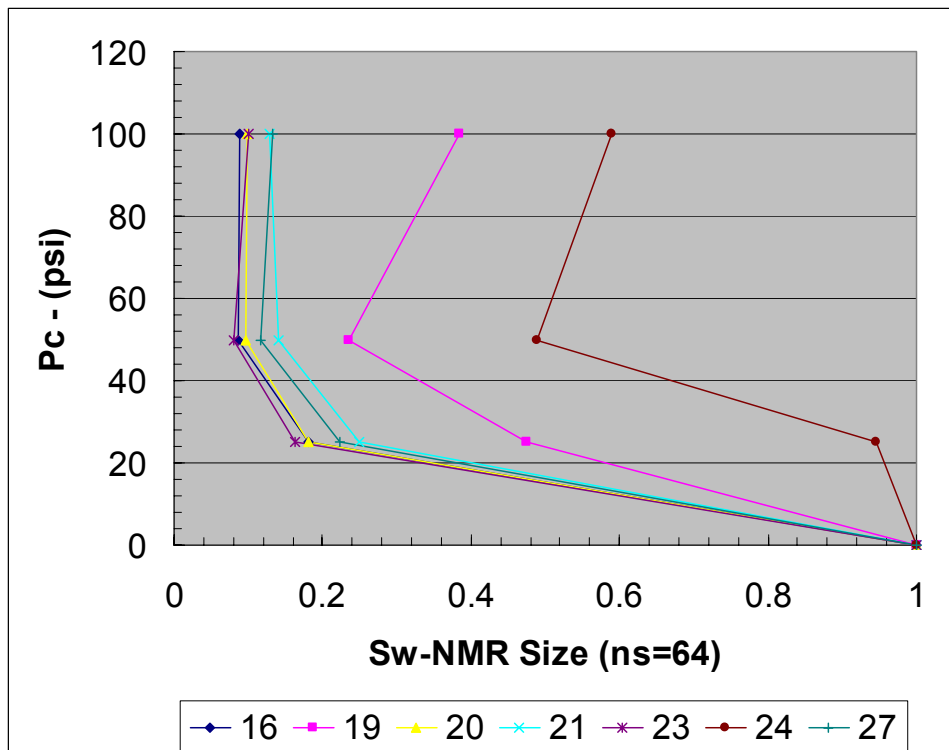
### MICP in This Study

#### *Carbonates*

MICP measurements were made on 11 samples from Womack Hill field, Alabama, on 23 samples from Appleton and Vocation fields, Alabama, and on 6 samples from Happy field, Texas. Mercury was injected at incremental pressures ranging from 1.64-1065 psia with equilibration times of 20 seconds until 45.5 psia; then at 45 seconds thereafter. This cycle was followed by an imbibition cycle from 1,050-14.2 psia. A second injection cycle was then done at pressures of 14.2-60,000 psia. Drainage – imbibition – drainage curves were created for each sample based upon wetting phase saturations at these incremental mercury injection pressures at 214 points. Incremental pore aperture size distributions were also determined for each sample by the lab. Mercury–derived porosity values were also determined, typically within two porosity units reported by routine core analysis (Bolger, personal comm.).

### Sandstones

The sandstones were not included in routine MICP testing due to a shortage of funds. Instead, NMR data were used to generate a synthetic capillary pressure curve (Fig. 4.8). To produce this curve, 4 NMR runs were made at brine saturations of 100%, 50%, 25%, and at  $Sw_{irr}$ . Water saturation was reduced to the necessary level by centrifuging. Samples were measured at each saturation level with the NMR bench top tool to obtain the corresponding NMR pore volume value. The NMR Size (number of proton counts for a given time interval) was recorded at each decreasing level of brine saturation. This technique estimated capillary pressure,  $P_c$ .



**Figure 4.8.** Synthetic capillary pressure data derived from NMR runs on sandstones. Two sandstones (#16 and #24) contained clays, were cemented, and had low NMR-measured porosity values relative to the other sandstone samples.

## ELECTRON MICROPROBE AND SEM

Microprobe analyses and SEM were used to show the presence and distribution of paramagnetic minerals which may affect the NMR response. Rocks samples ( $1\text{cm}^2$ ) for microprobe analyses were taken from the vacuum epoxy-impregnated butt segments of the core plugs that were previously used for making thin sections. The vacuum-impregnated ends simplify sample preparation and the rapid identification of pore space in backscatter electron (BSE) images (Guillemette, personal comm.).

### Microprobe Procedures

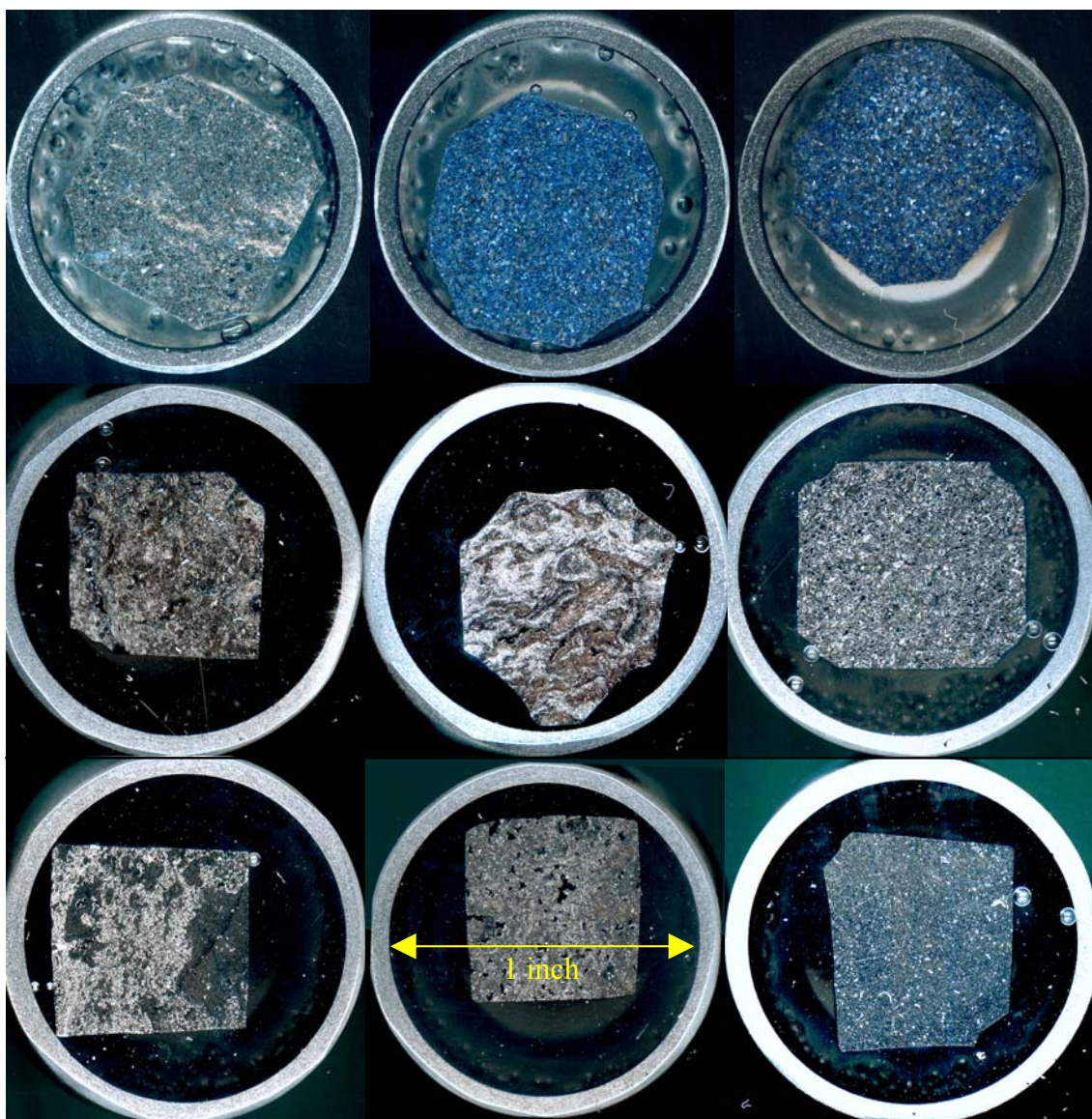
A Cameca SX-50 (Texas A&M University) microprobe was used to obtain backscatter electron images, x-ray surface maps, and quantitative chemical data to: 1) determine chemical composition on grains and cements across rock surfaces, 2) acquire high resolution images to show the distribution of paramagnetic minerals along pore walls, and 3) to obtain high resolution image mosaics used in image analysis studies. Nine samples (3 sandstones, 6 carbonates) were examined in this way to specifically show the distribution of iron across a  $1\text{cm}^2$  slice of rock (Fig. 4.9). The rock samples were mounted in epoxy cylinders and carbon coated prior to microprobe analysis.

Two procedures were used to detect the distribution of paramagnetic minerals within the rock. The instrument was set with an electron beam current of 10 nanoamps, a beam spacing of 20 microns, and a beam width of several microns. First, x-ray scan maps of Si, Fe, Ti, Al, K, Mg, S, and P were created for each sample. The x-ray scans produced maps of each of the detected elements across the corresponding  $1\text{cm}^2$  sample



surface. These element maps were compared to one another to detect simultaneously occurring elements in the same locations and the likely minerals associated with those elements. For instance, the occurrence of pyrite (Fe + S), dolomite (Mg + Ca), clays (Al + K + Si), quartz (Si), anhydrite (Ca + S), and other minerals were common.

Areas containing paramagnetic minerals (usually framboidal pyrite in sandstones and Fe-dolomite along pore walls in some carbonates), were then specifically verified using the microprobe. Electron backscatter (BSE) images with high reflectivity (higher density and correspondingly higher mean atomic numbers), showed the proximity of the paramagnetic grain to the pore walls in both sandstone and carbonate lithologies. Once a grain was identified and analyzed compositionally, grains and pore walls with similar BSE brightness were assumed to have the same elemental composition. Equating brightness with mineral composition assumed that no bias in brightness was caused by polishing effects during preparation of the rock chips (Guillemette, personal comm.). In the case of Fe-dolomite located at the pore walls, quantitative chemical data was collected. The X-ray scans, energy-dispersive spectrometry (EDS) results, quantitative analyses of Fe-dolomite, and BSE distributions of pyrite are shown in Appendix F.



**Figure 4.9. Optical photos of rock chips prior to microprobe analysis. Epoxy-filled cylinders measure 1-inch internal diameter. Top row sandstones, bottom two rows are carbonates.**

## CHAPTER V

### RESULTS

This chapter is divided into major sections based on measurement techniques. Pore types in thin section (7 sandstones and 40 carbonates) were observed and identified using a petrographic microscope and then classified using Ahr's genetic classification of porosity (Chapter IV). Next, PIA (petrographic image analysis) measurements of pore aspect and roundness and NMR T2 relaxation measurements were made. Capillary pressure measurements were made on the core plugs to determine pore-throat sizes and size distributions. Finally, the SEM microprobe was used to identify types and locations of paramagnetic minerals within pores.

PIA (petrographic image analysis) measurements were the first quantitative data obtained after completing standard petrographic study and classification of the pores in thin section. PIA measurements of aspect, roundness, area, and size (Chapter 4) were obtained on pores from each of the 47 thin sections. Statistical data for the measurements are included in Appendix H. Depositional pores in sandstones and carbonates, followed by hybrid 1, and diagenetic pore types were grouped separately in pore geometry plots. PIA 2-D porosity was calculated as the average area of dyed epoxy across the entire thin section. The fraction of the 2-D measured porosity from small (less than 0.02mm), medium (0.02-0.5mm), and large (greater than 0.5mm) pores was determined for each thin section then compared with 3-D measured porosity values. The same size breakdown of small, medium, and large pores is used in subsequent data plots of pore geometry. The purpose of the measured porosity comparison in 2-D was to

show the reliability of the PIA measurements to predict 3-D pore volume by pore type. A tabular and graphical summary of PIA pore geometry measurements by pore origin concludes this major section.

NMR (nuclear magnetic resonance) measurements of T2 relaxation time (Chapter IV) were made on all 47 rock samples. Sandstone NMR measurements were made at the ConocoPhillips Research Lab, and NMR measurements on carbonate samples were made by NUMAR Labs. T2 curves were converted to pore-size distributions by rock type and pore type. Sandstone and carbonate core plugs were organized by pore origin as were the PIA measurements: depositional, hybrid 1a (pores with strong depositional attributes) and hybrid 1b (moldic pores), diagenetic porosity-enhancing, and diagenetic porosity-reducing. A tabular and graphical summary of NMR characteristics concludes this major section.

Capillary pressure measurements completed the series. MICP measurements were not made on the sandstones due to budget constraints; therefore, synthetic capillary pressure curves were created for those samples using NMR responses at incremental decreases in the volume of brine in the core plug. Photomicrographs are included with each pore type to show visual comparisons of the rock with the corresponding capillary pressure test results. MICP data is reported by pore type as are PIA and NMR data: sandstones first, followed by carbonates with depositional, hybrid 1, diagenetic pore-enhancing, and diagenetic pore-reducing pore types. A tabular and graphical summary of the MICP measurements grouped by pore origin concludes this section.

SEM microprobe data were obtained for each pore type, particularly to detect minerals that may have magnetic properties that influence NMR measurements. X-ray scan maps and quantitative compositional data from the probe are included in Appendix F. Probe results showed that dolomitized reef fabrics – particularly those with touching vugs – exhibited the greatest abundances of paramagnetic minerals along pore walls. This causes vug sizes to be underestimated. The true sizes of the vugs were verified using thin section measurements. Fe-dolomite was identified at the pore wall interface by electron microprobe analysis and showed a progressive decrease in the amount of Fe from the pore wall toward the interior of the dolomite matrix. Finally, summary graphs of each representative pore type were created. PIA and NMR pore-size data, in combination with MICP pore-throat aperture data illustrate relationships between pore and pore-throat sizes.

## PETROGRAPHIC IMAGE ANALYSIS (PIA)

### Sandstones

#### *Depositional Pores*

Seven sandstone core plugs from the Northwestern shelf of Australia were used in this study. The samples exhibit depositional interparticle (between grain) pores, they are well-sorted, rounded, medium to coarse sand-sized quartz arenites (Figs. 5.1-5.2). Two of the seven quartz sandstones contained clay as discontinuous ribbons oriented parallel to the long axis of the core plug. In rare instances the sandstones contained large pores (Fig. 5.4), interpreted to be dissolution vugs after unstable volcanic grains (Appendix A). Therefore four of the seven sandstones exhibited the best examples of depositional, interparticle pore space. They contained mostly triangular-shaped, interparticle pores in thin section. Pore images in all of the rocks, both sandstone and carbonate, were sorted into four size categories (Chapter IV) using PIA (Fig. 5.3).

Aspect ratios of 1.9 and roundness values of 2.5 were typical values for interparticle pores in sandstones (Figs. 5.4-5.5). Triangular test objects (Chapter IV) had aspect and roundness values of about 1. Thus the triangular pores in thin section were not perfect equilateral triangles. Measurements of aspect ratio and roundness were made on the pores identified in each of 22 fields of view per thin section. Hundreds of pores were rapidly measured and grouped according to the pre-set bin sizes (Chapter IV). Figures 5.4 and 5.5 showed the reproducible nature of interparticle pore geometry in sandstones, particularly in the middle (0.02-0.5mm) size group. The most reproducible results were found in the four sandstones that lacked clay and enlarged vugs (Fig. 5.6).





Figure 5.1. Sandstone core photo.

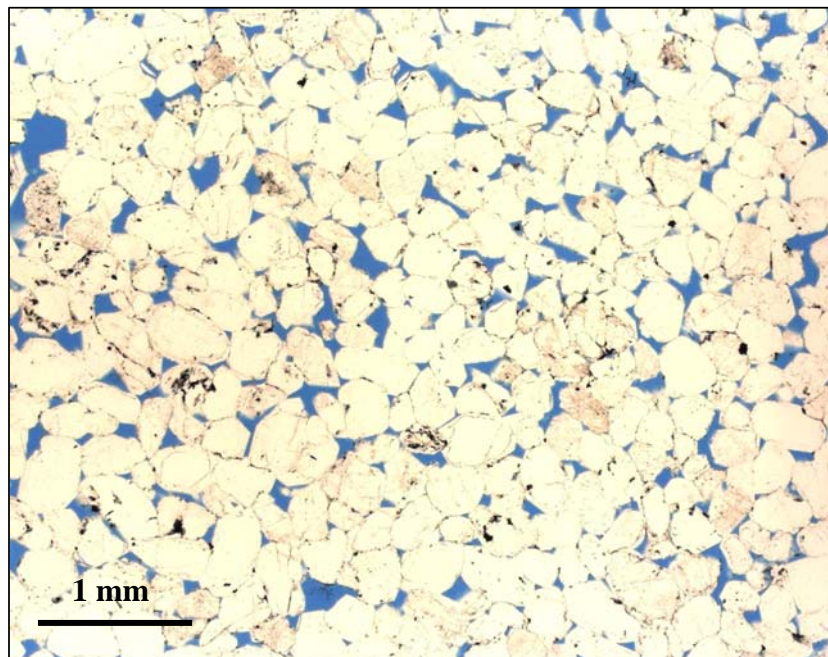


Figure 5.2. Depositional intergranular porosity in sandstone. Image taken in plain light at 25x magnification. Blue areas are pore spaces.

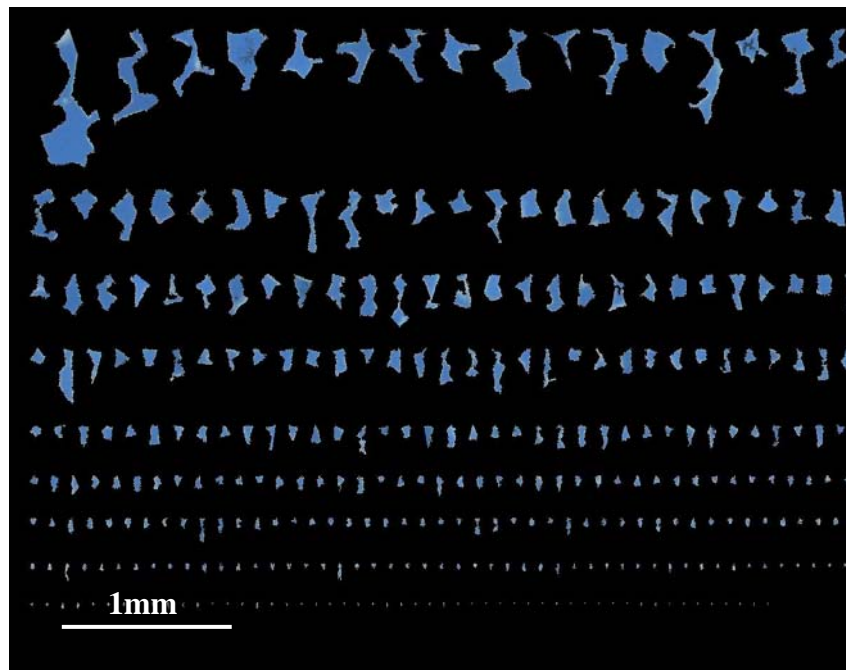


Figure 5.3. Sorted pores from a thin section image prior to PIA. Sandstone #16.

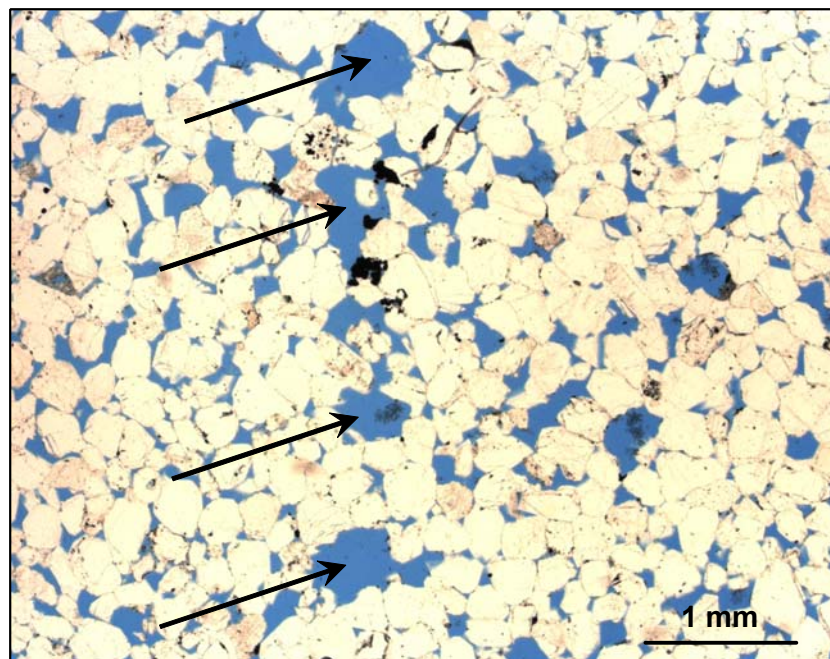


Figure 5.4. Sandstone with enlarged pores (shown by arrows) caused by dissolution of unstable volcanic grains. Blue is porosity, photo taken under plain light, 25x magnification.



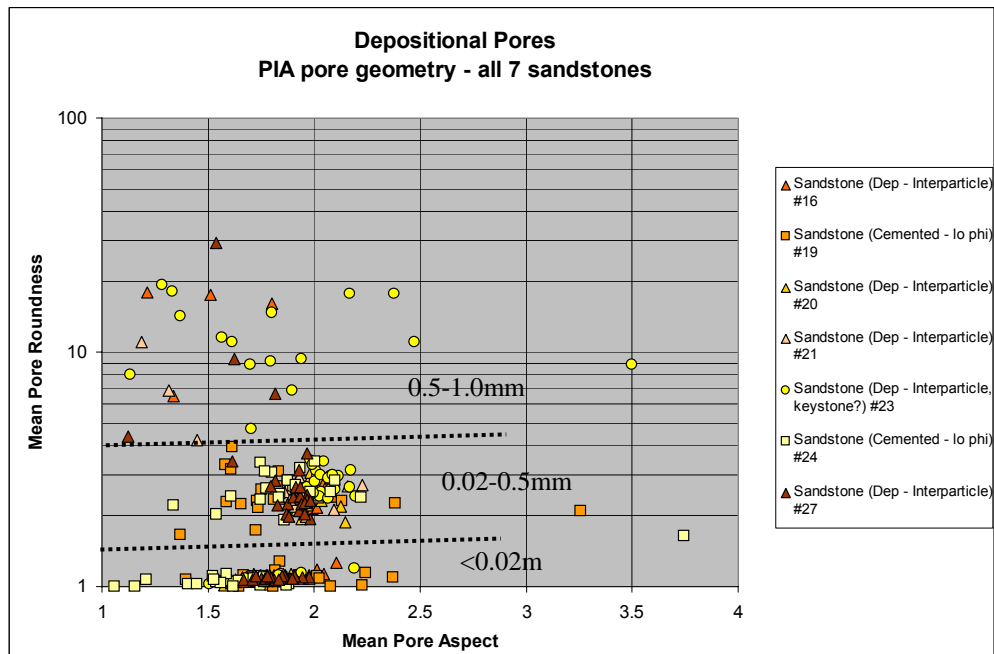


Figure 5.5. Plot of pore geometry for all sandstones. Aspect and roundness values of 1 mean equidimensional shapes (Ch 4) observed in these sandstones as being triangular. Dashed lines separate small, medium, and large pores.

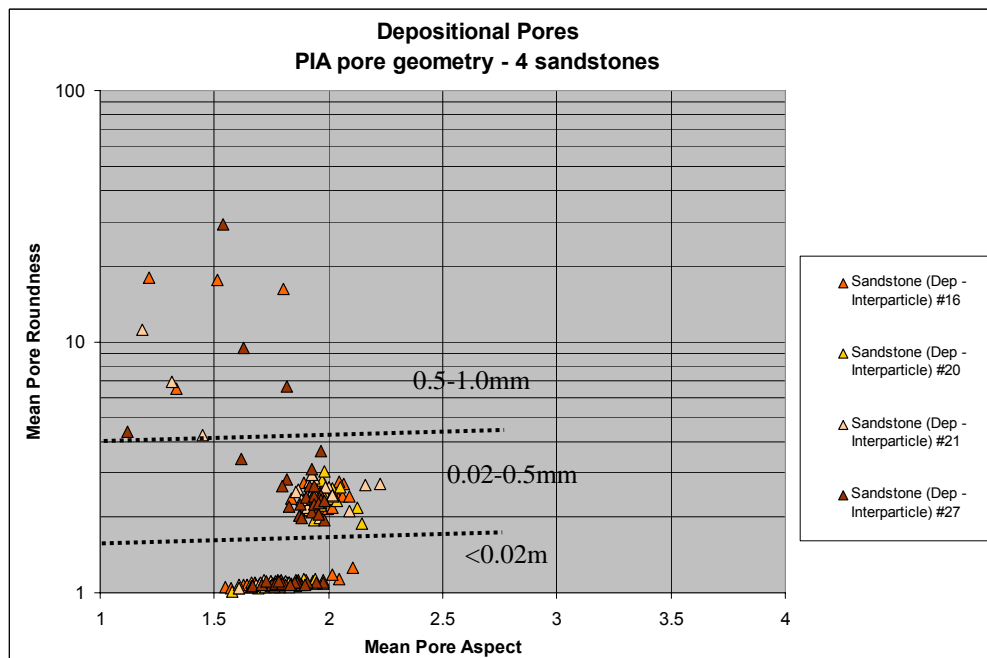


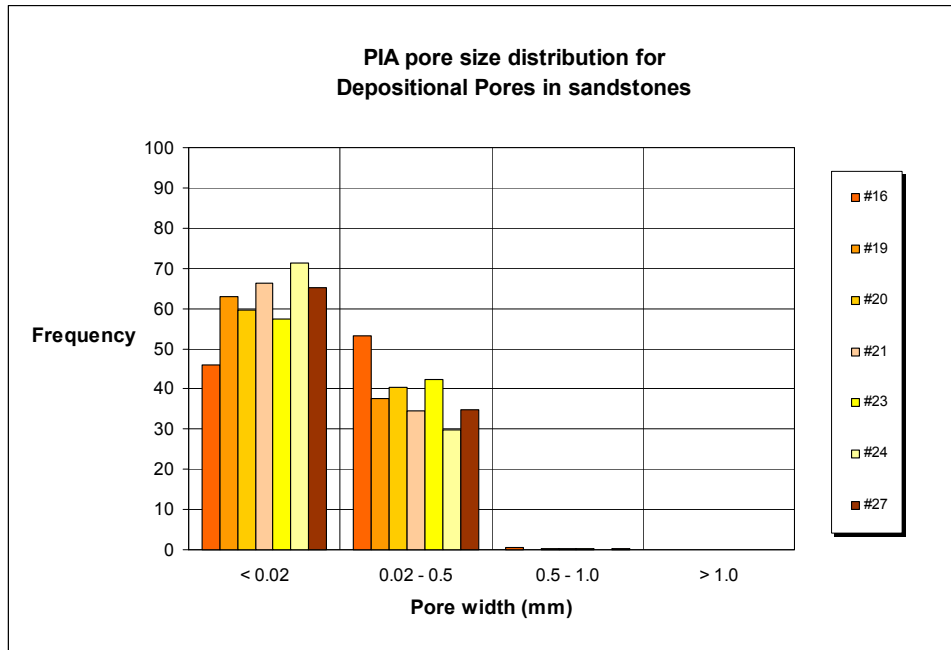
Figure 5.6. Plot of pore geometry for sandstones without clay or 'vugs'.

The percent area occupied by pores (dyed epoxy) in thin sections is given as 2-D porosity. Values were determined by averaging the area of pore space in each of 22 fields of view. The sandstones had measured 2-D porosity values between 0.6-14.4% owing to compaction or presence of clays (Table 5.1). The fraction of 2-D sample porosity from each size bin was determined by normalizing the pore area from each bin size to the total pore area of the thin section (Appendix C). 45-70% of the depositional pores in the sandstones were contained in pores <0.02mm. 30-55% of the depositional pores in sandstone measured 0.02-0.5mm. Less than 1% of the pores in any sandstone measured larger than 0.5mm diameter (Fig. 5.7). Over 90% of the total porosity in the sandstones was contained in pores 0.02-0.5mm in size (Fig. 5.8).

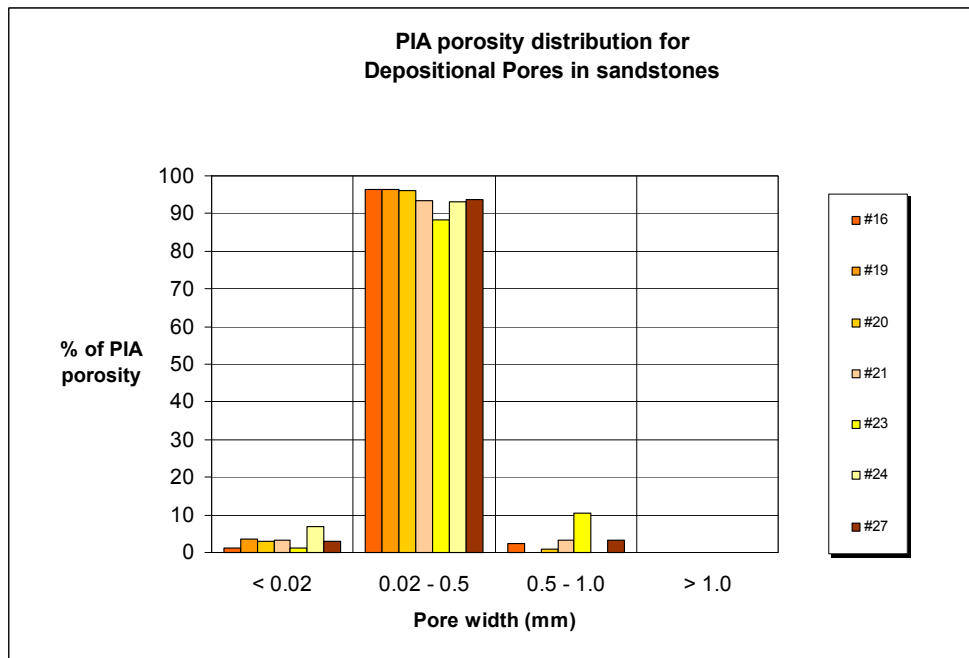
**Table 5.1. Summary of 2-D porosity values for seven sandstones.**

Sample #	Lithology	2-D Porosity (%)
16	Qtz Arenite	8.87
19	Qtz Arenite	0.61
20	Qtz Arenite	7.42
21	Qtz Arenite	6.46
23	Qtz Arenite	14.38
24	Qtz Arenite	1.21
27	Qtz Arenite	6.49

In summary, seven sandstones were examined in thin section and found to exhibit depositional interparticle pores in 2-D. Measured porosity values ranged from 0.6-14.4%. The geometry of the pores was estimated to be generally triangular. PIA measurements showed that over 90% of the total pore space in these sandstones represents individual pores measuring 0.02-0.5mm diameter. These pores had measured average aspect ratios of 1.9 and roundness values of 2.5.



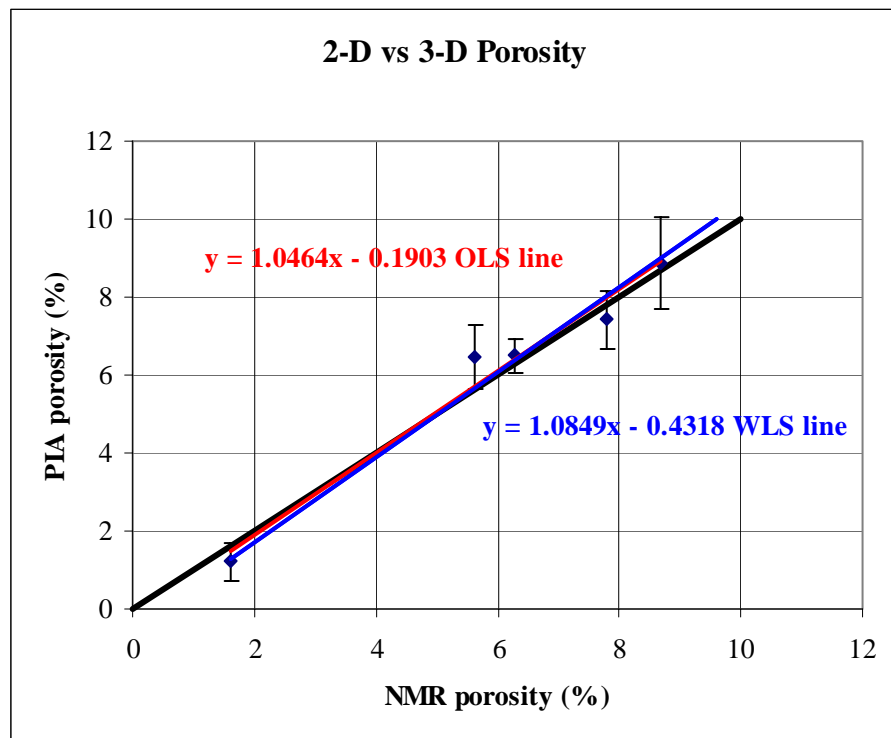
**Figure 5.7. Frequency distribution of sandstone interparticle pores by pore size.**



**Figure 5.8. Fraction of 2-D measured porosity in sandstones by pore size.**

*PIA Estimate of Core Porosity in Sandstones*

An original least squares (OLS) and weighted least squares (WLS) regression test was done to test the relationship of 2-D and 3-D measurements of porosity (Fig. 5.9). Tabular data and details of the regression are located in Appendix E. The sandstones used in the regression did not contain enlarged pores (dissolved volcanic grains). Both OLS and WLS tests showed that PIA successfully predicted 3-D measured values of core plug porosity.



**Figure 5.9.** Comparison of 2-D and 3-D measurements of porosity in sandstone core plugs. Each data point is the average 2-D value of porosity as determined from 22 thin section fields of view. 95% confidence intervals are shown around individual data points.

## Carbonates

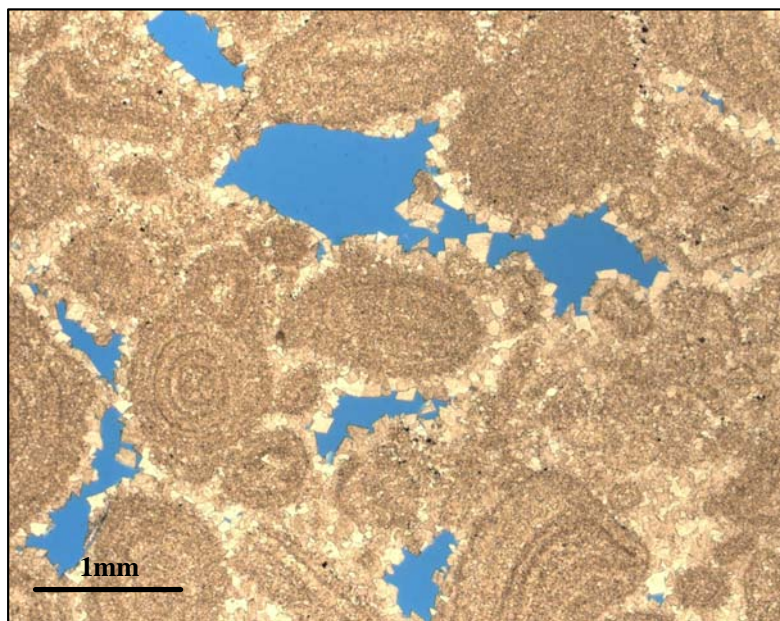
### *Hybrid I-a Pores*

Three of the forty carbonate samples were Appleton field ooid grainstones containing hybrid I-a pores, and serve as the best direct comparison with depositional pores in the sandstones. These hybrid pores show strong depositional attributes (Ch 4). Individual ooids were visually estimated to be 0.25-1.0mm diameter. The original depositional porosity of these three samples was slightly reduced by post-burial cementation and minor intraparticle dissolution. The modification, however, was not substantial enough to disguise original interparticle pore space. Original depositional texture in thin sections and hand samples is revealed by circular grain shapes and microstructure of the ooids (Figs. 5.10-5.11).

These 3 ooid grainstones and packstones exhibited interparticle porosity with a strong depositional signature. The present condition of the pores differed from a purely depositional geometry (as represented in the sandstone samples) in that the carbonate pores were moderately affected by diagenesis. This is demonstrated by the wider scatter of pore geometry values relative to the sandstones. Post-depositional cementation moderately altered the shape of the larger interparticle pores such that the pore walls were lined with blocky calcite crystals (Fig. 5.11). These patterns were identified in thin section as non-round, equant to elongate crudely triangular pore shapes. Large pores (>0.5mm) show particularly non-round pore geometry (Fig. 5.12-5.13).



**Figure 5.10.** Hand specimen of oolite grainstone dominated by depositional (intergranular) porosity. Sample from Vocation Field, Well# 1599: 14,017ft.



**Figure 5.11.** Thin section photograph of oolite grainstone dominated by Hybrid 1-a porosity. Note isopachous blocky calcite lining most of the ooid grains. Image taken at 25x magnification with plain light. Sample from Vocation Field, Well 1599: 14,017ft.



Figure 5.12. Pores selected from thin section image of oolite grainstone. Pores sorted by size show star-like shapes, with non-round and elongated forms. Sample from Vocation Field, Well 1599: 14,017ft..

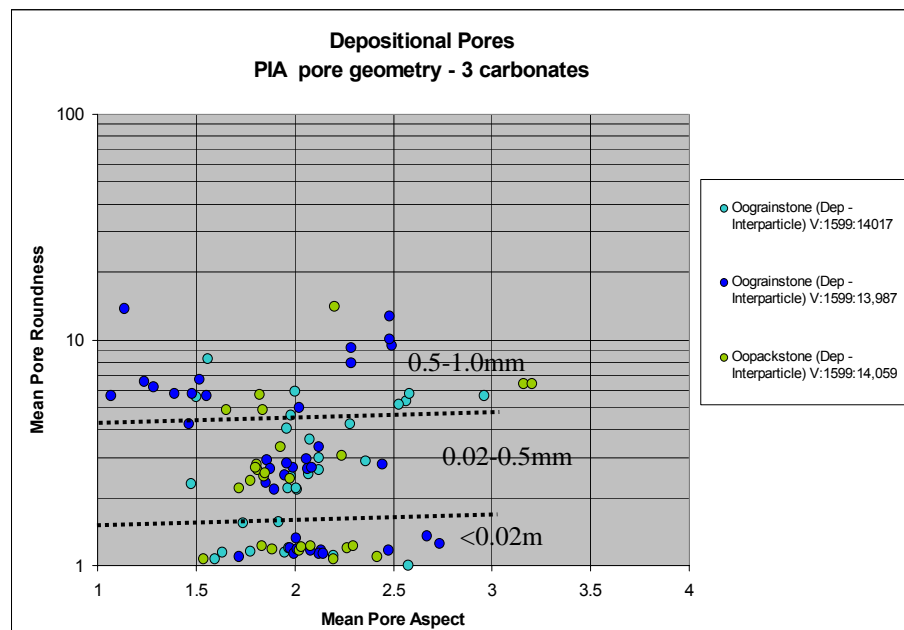


Figure 5.13. Distribution of pore geometry for all pore sizes from three carbonate samples exhibiting strong depositional attributes. Each data point represents the average measurements of pore roundness and aspect on dozens of pores from a single thin section field of view.

The 2-D porosity for these samples was determined by averaging the area dyed by blue epoxy across the entire thin section. The 2-D measured porosity in carbonate samples exhibiting strong depositional attributes ranged from 3.7-6.7%. The distribution of the total number of pores in these carbonates is as follows: 43% are small (<0.02mm) pores, 51-53% are medium sized (0.02-0.5mm) pores, and 2-5% are large (>0.5mm) pores (Fig. 5.14). Of the thin section porosity in these carbonate samples, 30-70% exists within the small pores, 15-50% of the porosity exists in middle sized pores, and 12-17% exists in the largest (>1.0mm) size as seen in cross sectional dimension (Fig. 5.15).

In summary, three carbonates were examined in thin section and exhibited hybrid I-a pores. These rocks show the strongest depositional attributes (i.e. preservation of depositional interparticle pore space) relative to all other carbonate samples and are the most comparable pore type to depositional interparticle pores as seen in the sandstones. The 2-D measured porosity in these rocks is 3.7-6.7%. The geometry of hybrid I-a pores was visually estimated to be generally a mixture of triangular, non-round, and slightly elongate forms including “stars” in the large (>0.5mm) pore size group. Aspect ratios of 1.8 and roundness values of 2.5 distinguish hybrid I-a pores in the middle (0.02-0.5) pore size group, similar to the pore geometry of depositional pores in sandstones.



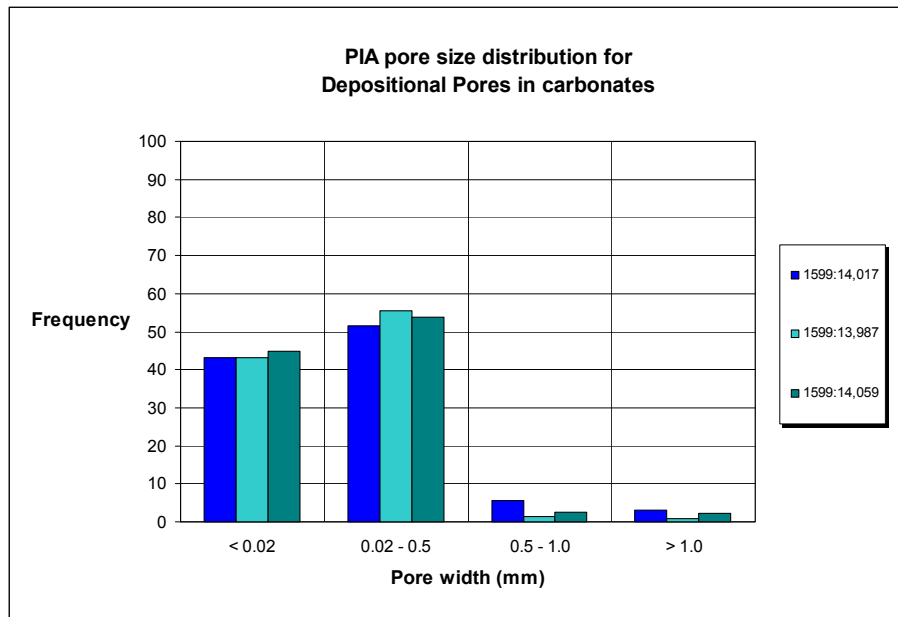


Figure 5.14. Distribution of pore sizes in carbonate rocks with depositional attributes.

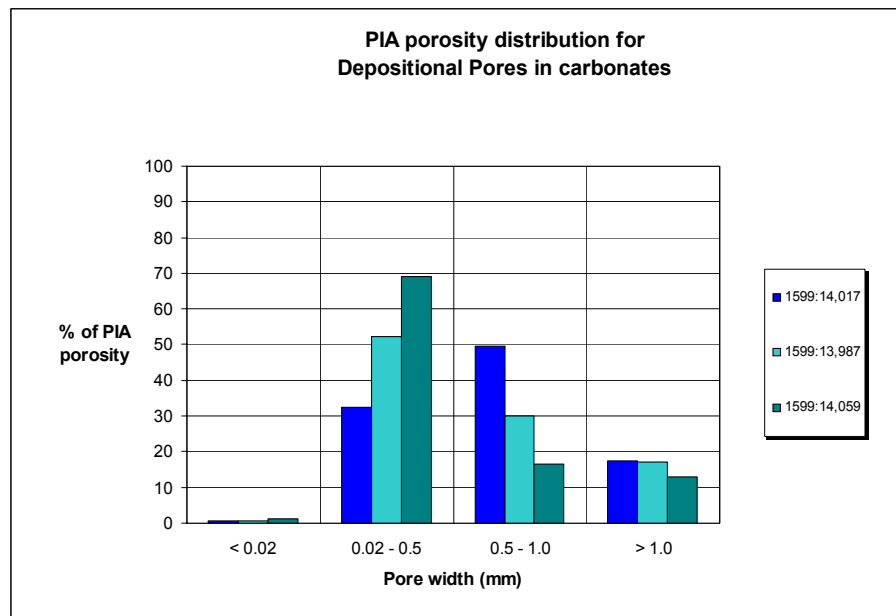


Figure 5.15. Distribution of 2-D measured porosity by pore size in carbonates.

### *Hybrid I-b (Moldic) Pores*

Hybrid I-b pores are predominantly molds; pores that were created by a combination of depositional and diagenetic geologic processes (Ch 4). Pores of this kind differ from the depositional pores in the sandstones as well as the strongly depositional (Hybrid I-a) pores in carbonates in that diagenesis was more significant in altering the pore system. Six rocks from Womack Hill field and Happy field exhibited moldic pores that result from the preferential dissolution of metastable skeletal grains and ooids (Figs. 5.16-5.19).

Pore geometry was determined for each of 4 possible pore size groups; small (<0.02mm), medium (0.02-0.5mm), large (0.05-1.0mm), and very large (>1.0mm). These are the same size categories of pores used in the sandstones, as well as in all carbonate samples. Measurements of pore geometry (Fig. 5.20) showed that small pores exhibit the greatest degree of elongation as evidenced by aspect ratios of 1.6-2.2. Medium pores also have aspect ratios of 1.6-2.2 but higher roundness values of 1.8-4 relative to small pores. One sample with a high degree of data scatter in pore geometry contains a variety of pore types, including skeletal molds, intraparticle pores, and incomplete molds. This rock exhibits a complicated pore system in terms of various

pore types, mixed constituent composition, and post-depositional cementation and associated porosity reduction (PIA porosity measured at 0.1%).

The measured 2-D porosity is 0.1-16.9% for carbonates with hybrid 1-b (moldic) pores. Of the total measured 2-D porosity less than 15% is from small pores (<0.02mm), while 80-95% is from medium pores (0.02-0.5mm) as visible in cross sectional dimension. Less than 5% of the measured 2-D porosity came from large (>0.5mm) pores (Figs. 5.21-5.22)

In summary, carbonate rocks that contained hybrid 1-b (moldic) pores are interpreted to have formed from dissolution of metastable ooid and skeletal grains. Measured porosity in 2-D for these carbonates ranged from 0.1-16.9%. Medium (0.02-0.5mm) pores contained 80-95% of the total 2-D porosity, and small (<0.02mm) pores contained <15% of the measured 2-D porosity. The medium size pores had the most reproducible pore geometry including aspect ratios of 1.6-2.2 and roundness values of 1.8-4.0.

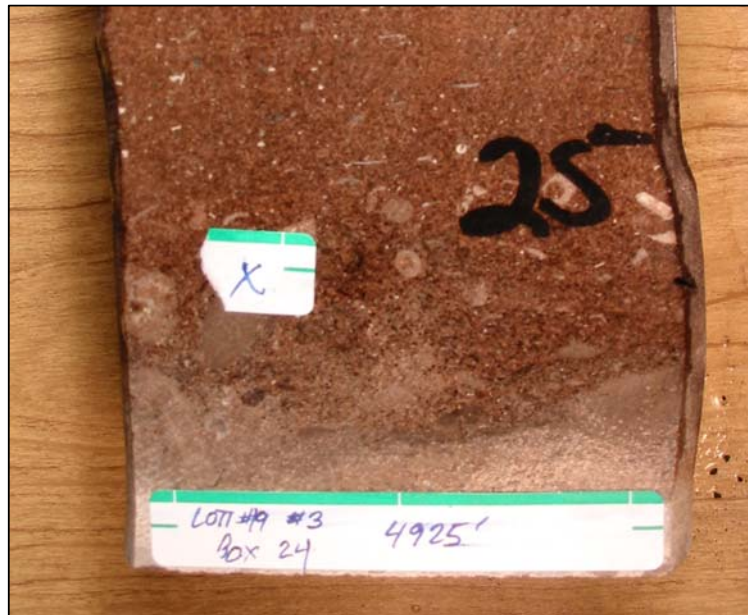


Figure 5.16. Core photo of skeletal grainstone containing moldic pores. Sample Lott#19-3; 4925ft, 4" diameter core width.

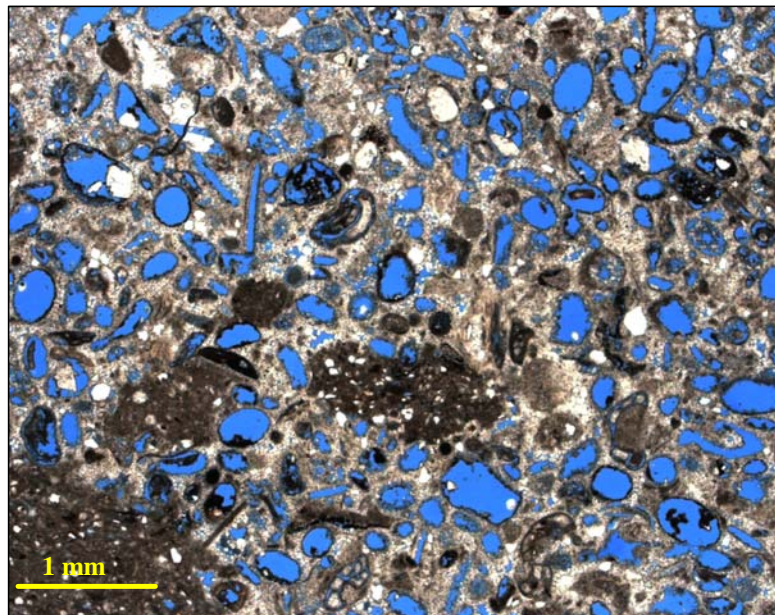


Figure 5.17. Oolitic moldic pores. Sample is taken from Well# 19-3:4925. Photo taken at 25x magnification under plain light, Blue is porosity.

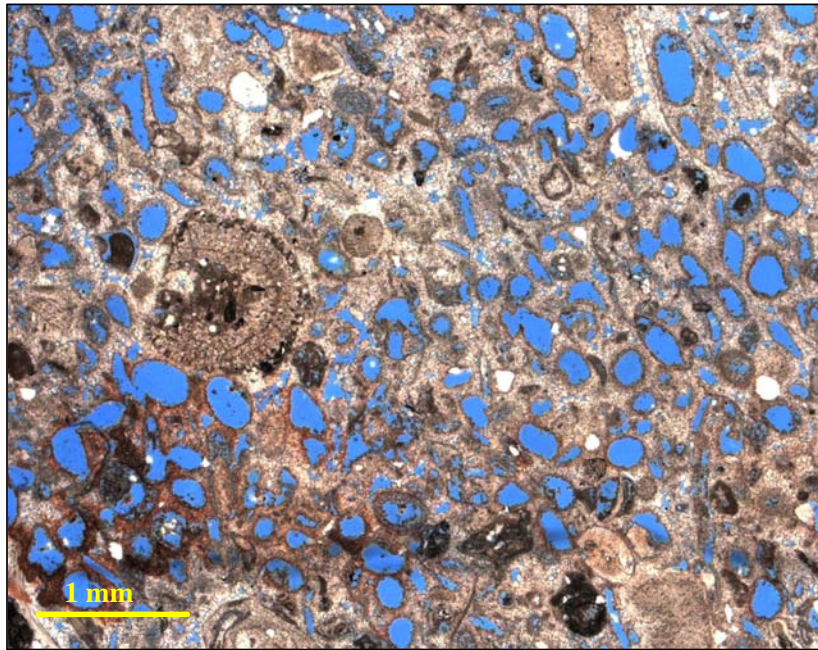


Figure 5.18. Photomicrograph of oolitic moldic pores. Sample taken from Well# 19-3:4923.2. Photo taken at 25x magnification.

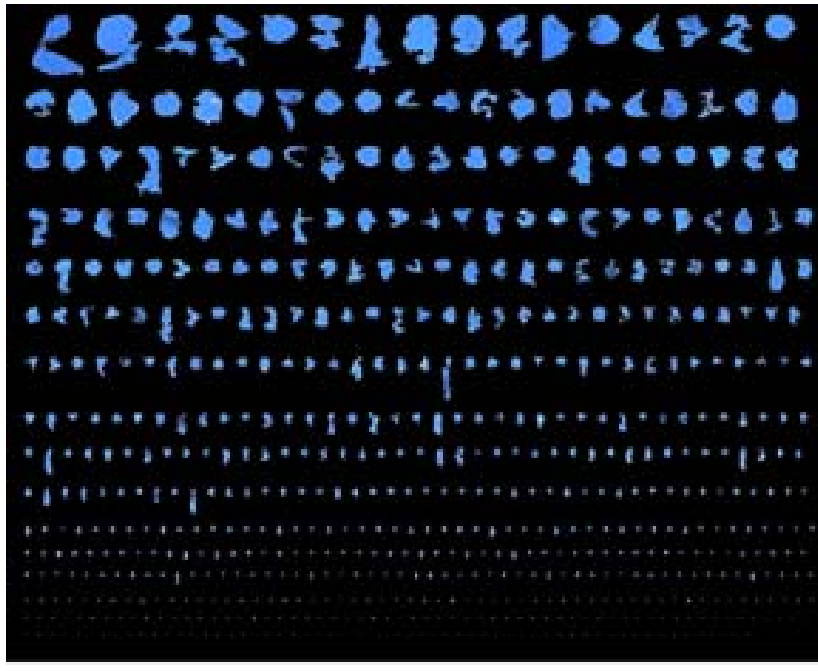


Figure 5.19. Oomoldic pores sorted by size using PIA. Well # 19-3; 4923.2ft.

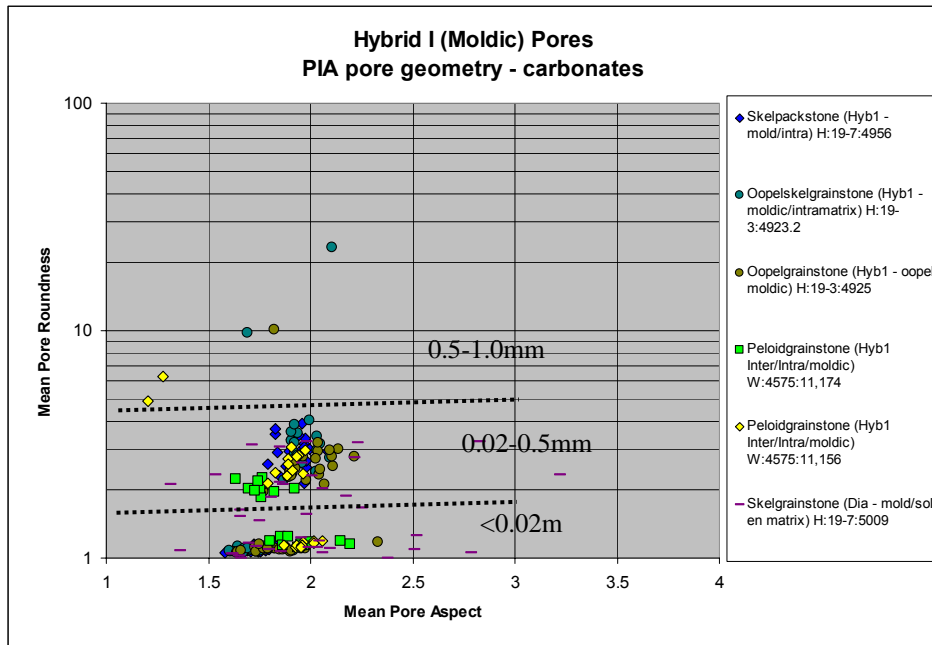


Figure 5.20. Pore geometry of Hybrid 1-b (moldic) pores in carbonates.

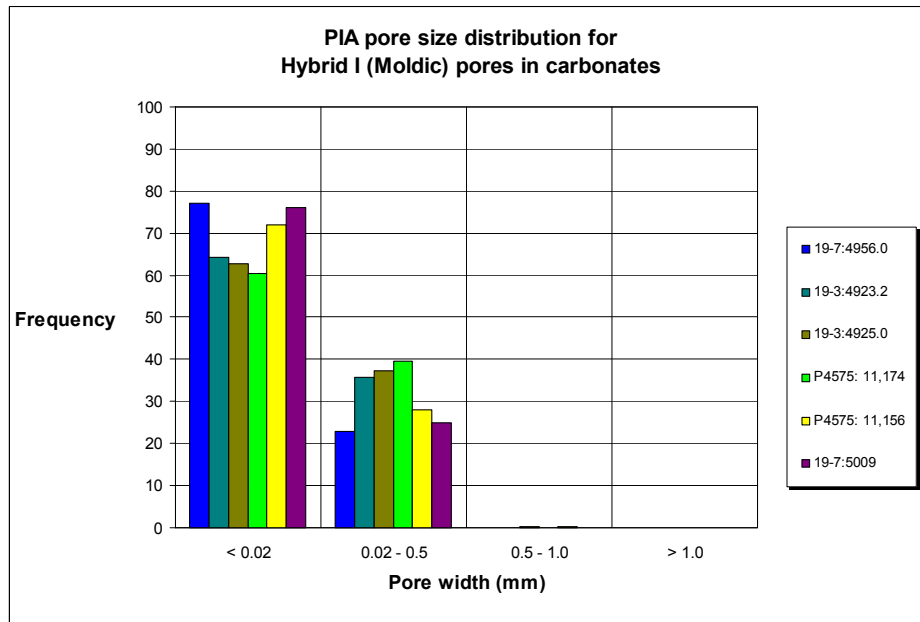
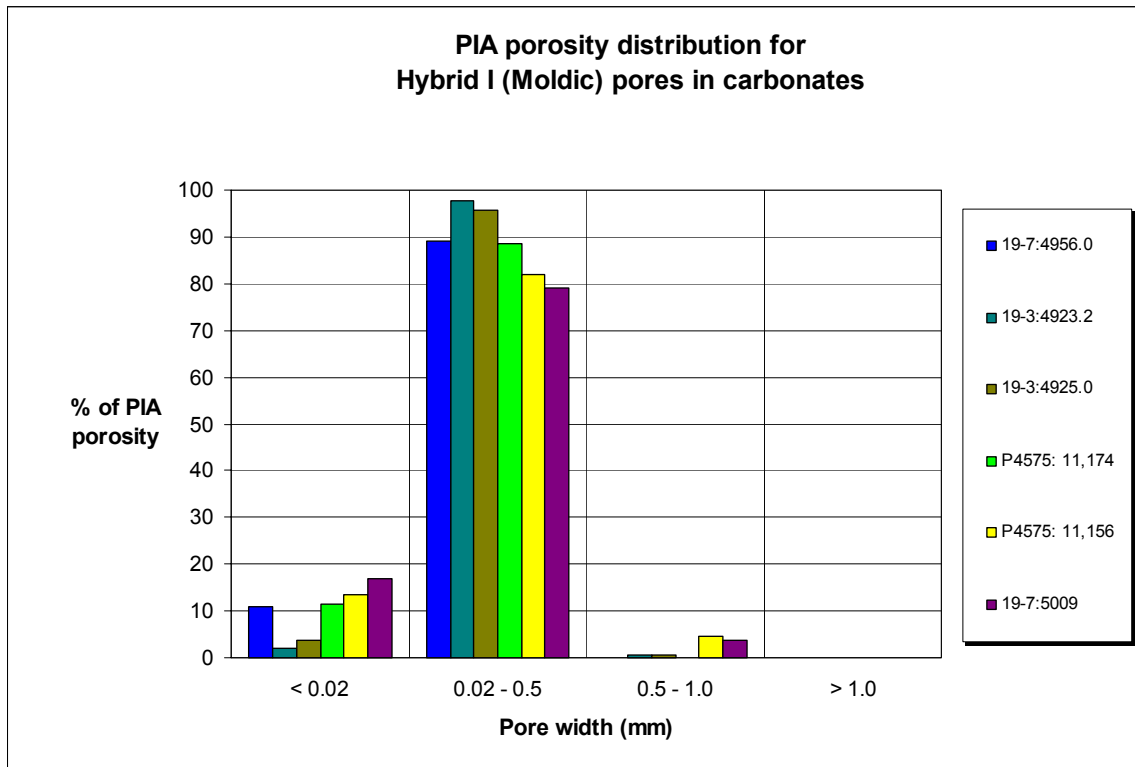


Figure 5.21. Histogram of small, medium, and large pore sizes in samples with moldic pores.



**Figure 5.22.** Distribution of 2-D porosity in carbonates with moldic pores.

*Diagenetic - Intercrystalline Pores*

Nine carbonate samples consisted only of crystalline dolomite in which no visible traces of original depositional fabric or texture were visible (Fig. 5.23). Patches of calcite or anhydrite were identified in some areas of the thin section. The intercrystalline dolomite pores are completely diagenetic in origin (Figs. 5.24-5.26). Lucia and Major (1994) have shown that the dolomitization process itself does not create porosity, but that the original rock texture is perhaps the most important factor to consider in the evolution of porosity during dolomitization. The precursor textures of the rocks in this study are not recognizable because of extensive dolomitization. The intercrystalline pores in this study represent the space between solids in a generally uniform distribution of rhombic dolomite crystals. In thin section views these pores are mostly rhombic or partially rhombic in shape exhibiting angular pore walls. The crystals and attendant pores both measured between 50-150 microns in cross sectional dimension.

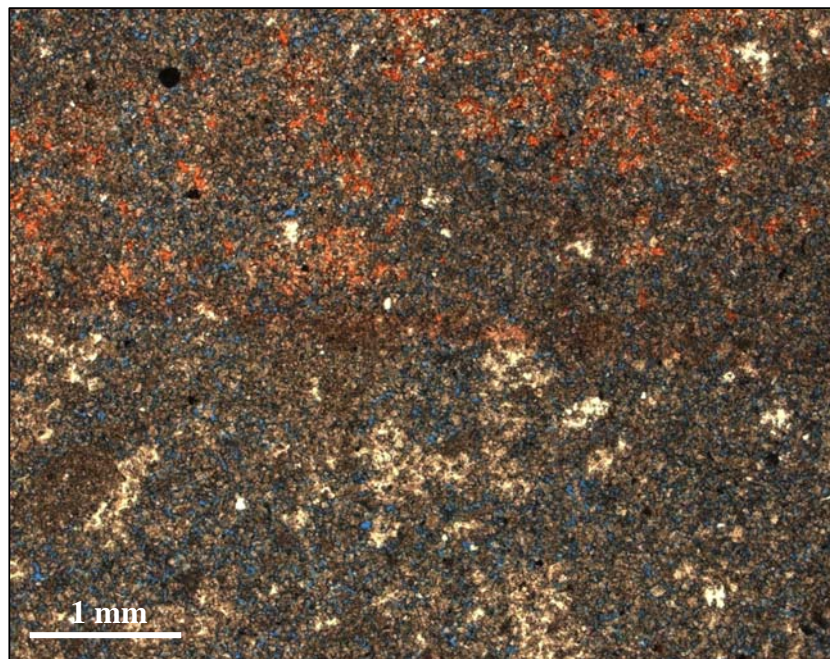
Measurements of pore geometry (Fig. 5.27) show that small pores (<0.02mm) have aspect ratios ranging from 1.6-2.4. Medium pores (0.02-0.5mm) have aspect ratios of 1.6-1.8, and roundness values of 1.1-4. No large pores were present.

The 2-D measured porosity for thin sections exhibiting this pore type ranged from 0.01-0.9% (Plate 1). These 2-D measured porosity values were low, as small pores are difficult to resolve in thin section (Figs. 5.28-5.29).

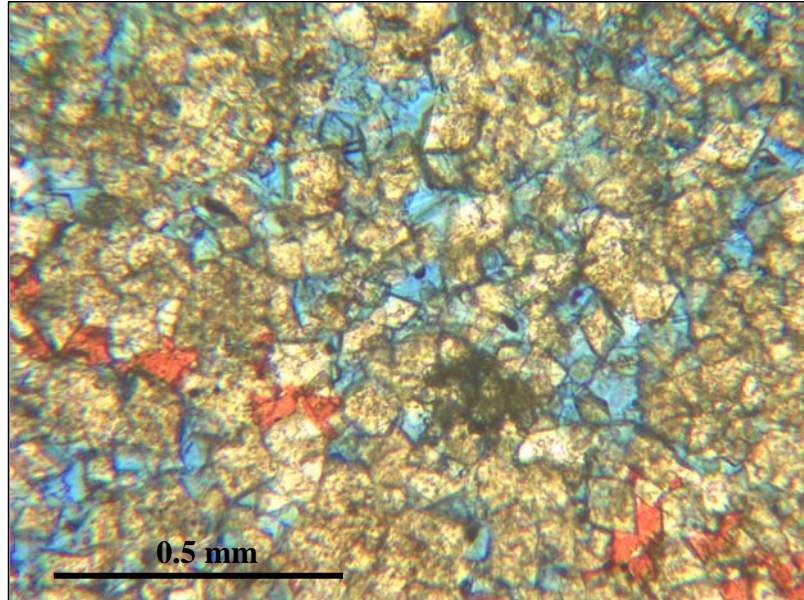




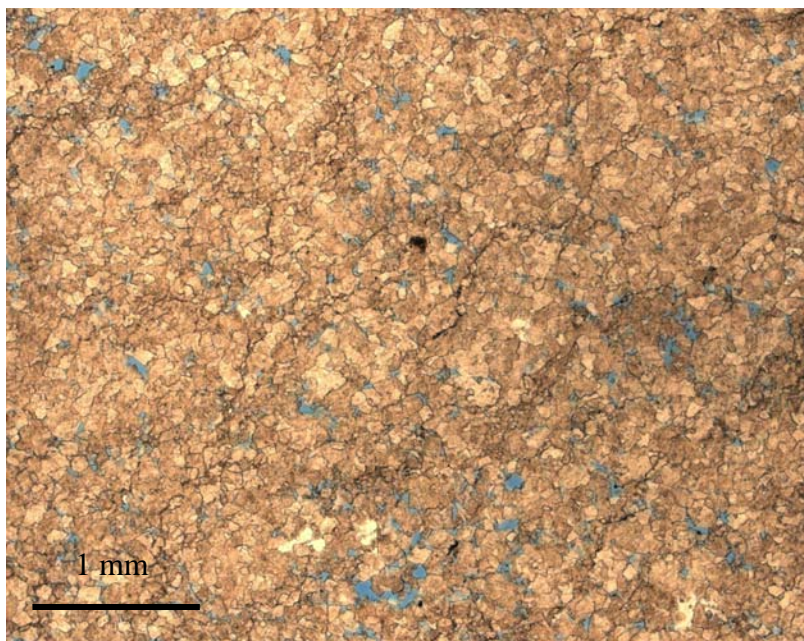
**Figure 5.23.** Dolomite hand sample. Taken from Well # 4575: 11,192. Hole at left side of sample is the hole from a 1-inch diameter core plug.



**Figure 5.24.** Thin section photograph of intercrystalline pores in a fine-grained matrix. Irregular patches of calcite cement present (stained red in top half of picture). Photo taken at 25x magnification. Sample is from Well# 4575: 11,192.



**Figure 5.25.** Intercrystalline pores in a fine-grained dolomite. Red areas are calcite crystals. Photo taken at 100x magnification. Sample Well# 4575: 11,192.



**Figure 5.26.** Thin section photo of intercrystalline porosity in dolomite. Photo taken at 25x magnification. Blue is porosity. Sample from Vocation field, Well 2935: 14,078ft.

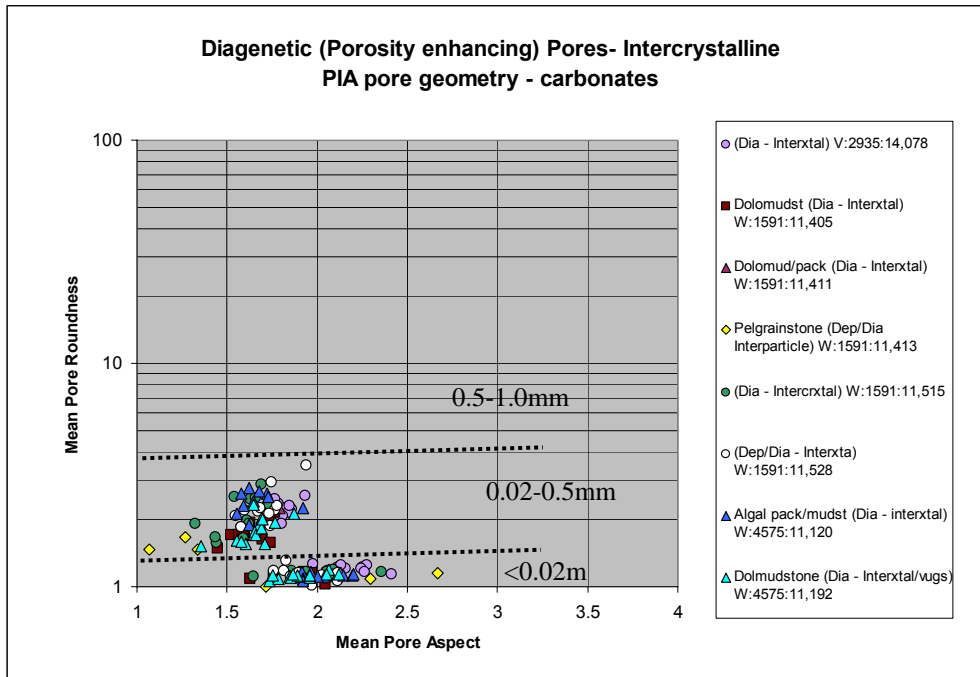


Figure 5.27. Pore geometry of intercrystalline pores in carbonate rocks.

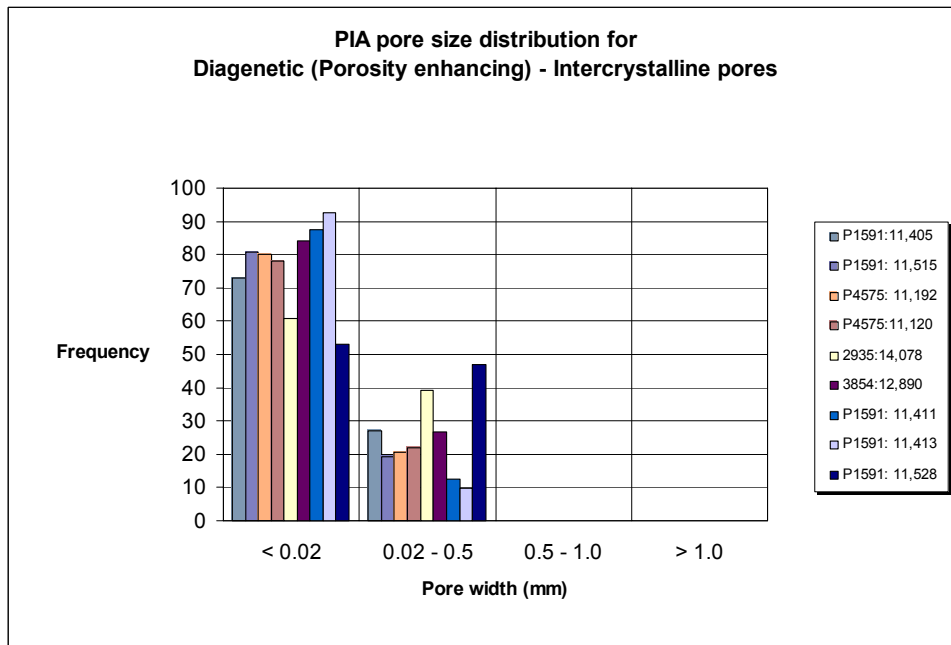
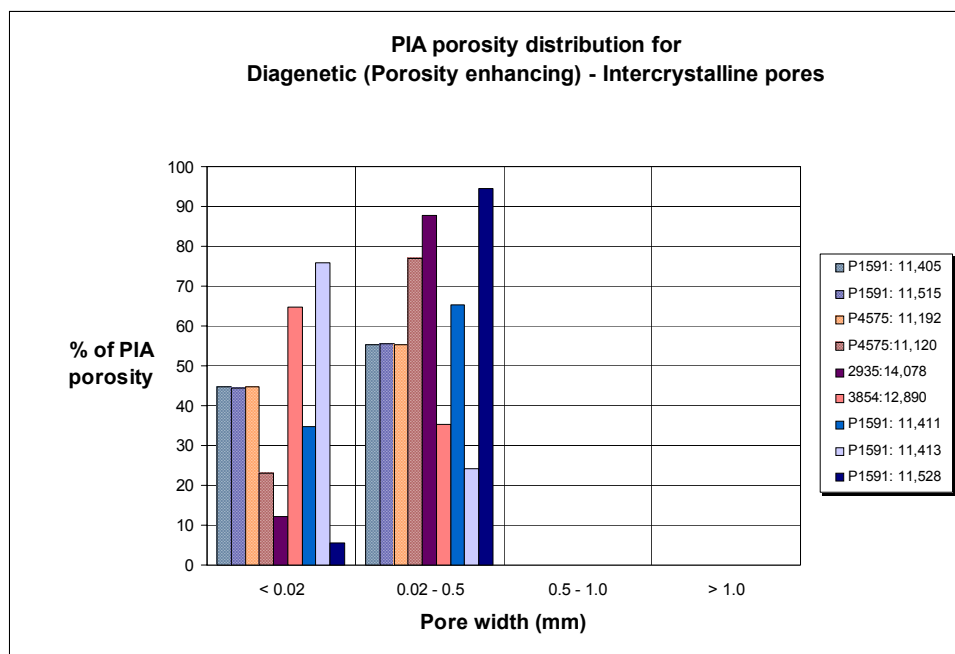


Figure 5.28. Pore size distribution for carbonate rocks exhibiting intercrystalline pores.





**Figure 5.29. Distribution of 2-D porosity by pore size in samples with intercrystalline pores.**

In summary, nine carbonate rocks exhibited intercrystalline porosity after complete replacement by dolomite. These intercrystalline pores represent the space between solids in a generally uniform distribution of rhombic dolomite crystals. In thin section these pores were mostly rhombic or partially rhombic in shape exhibiting angular pore walls. Measured porosity in 2-D for these carbonates ranged from 0.01-0.9%, due to the small pore spaces which were difficult to resolve in thin section. Of the measured 2-D porosity, 25-95% was from a combination of small (<0.02 mm) and medium (0.02-0.5mm) pores. Pore geometry for middle sized (0.02-0.5mm) pores had aspect ratios of 1.6-1.8 and corresponding roundness values of 1-1.4.

*Vugs: Purely Diagenetic, Enhanced Porosity*

Fifteen samples from Vocation and Appleton fields exhibited separate vugs (Figs. 5.30-5.31) and touching vugs (Figs. 5.32-5.35) in addition to intercrystalline pores. Large pores ( $>0.5\text{mm}$  vugs) are common in these rocks and have notably high roundness values (Fig. 5.36-5.37). In rare instances, these rocks contain possible fractures (Figs. 5.34-5.35) which are identified by PIA as objects with extremely high (10-100) aspect ratios (Fig. 5.38). Aspect ratios in small pores ( $<0.02\text{mm}$ ) ranged from 1.7-2.5 owing to the connectivity of many interparticle pores in 2-D. Medium pores (0.02-0.5mm) had aspect ratios of 1.8-2.2 and roundness values between 2 and 3. Separate vugs (pores  $>0.5\text{mm}$ ) had aspect ratios of 1-2.2, and roundness values of 4-28. Touching vugs (pores  $>0.5\text{mm}$ ) had similar roundness values as compared to the separate vugs, but had greater aspect ratios of 2.3-3.9 (Fig. 5.39).

The measured 2-D porosity in these vuggy rocks ranged from 4.2-11%. In rocks with both separate and touching vugs, 65-95% of the 2-D porosity was identified in medium pores (0.02-0.5mm). Vugs held 18-25% depending on size (Fig. 5.37).

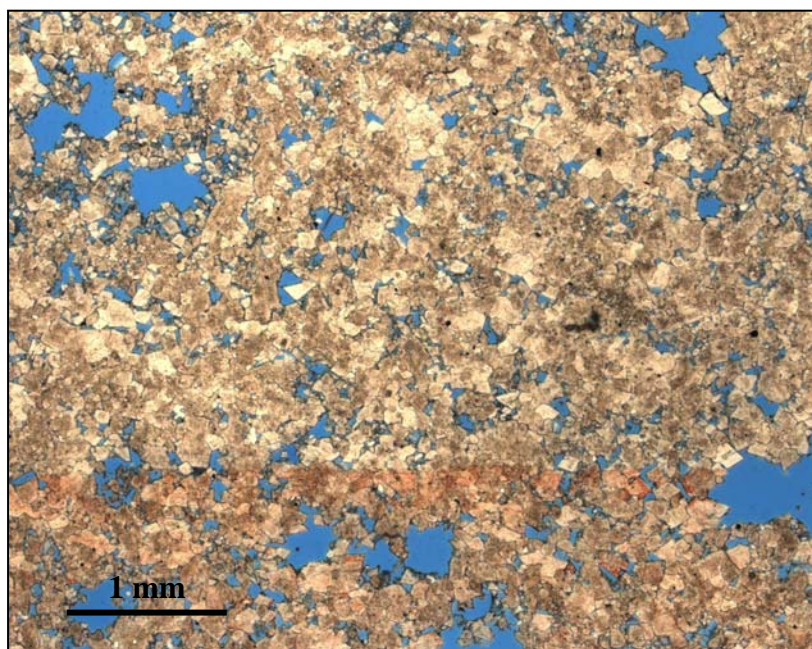


Figure 5.30. Thin section image of abundant separate vugs and intercrystalline pores. Sample Well # 3986:12,964. Photo taken at 25x magnification. Red area on bottom third of picture is Alizarin-Red- S stain for calcite.



Figure 5.31. Hand specimen of vuggy carbonate. Sample from Appleton field, Well # 3986, 12,964.

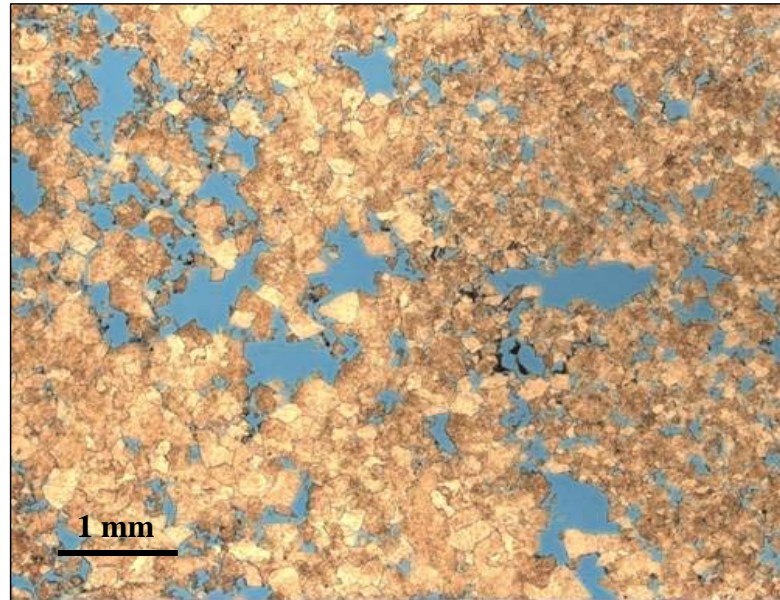


Figure 5.32. Touching vugs and intercrystalline pores in dolostone. Blue is porosity.

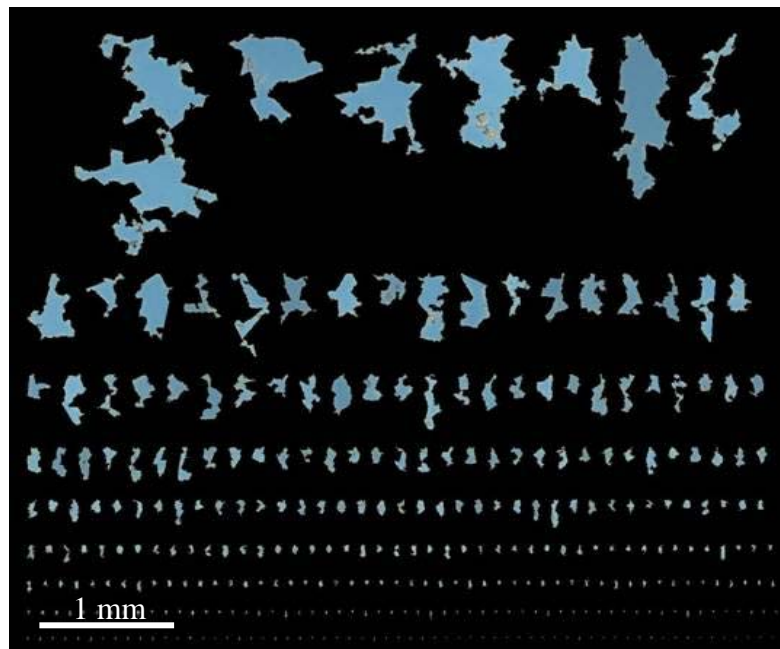


Figure 5.33. PIA touching vugs sorted by size. Abundant vugs characterized by irregular non-round shapes. Touching vugs identified as pores with greater aspect ratios.



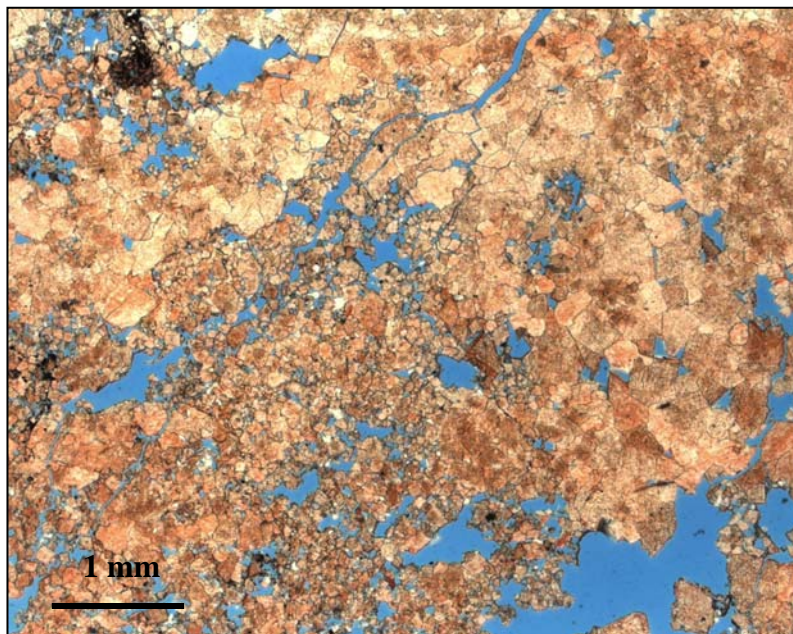


Figure 5.34. Thin section photograph showing possible fractures in carbonate rock. Sample is taken from Well# 1599:14,087. Photo taken at 25x magnification.



Figure 5.35. Hand sample of broken core. Taken from Well# 1599:14,087.



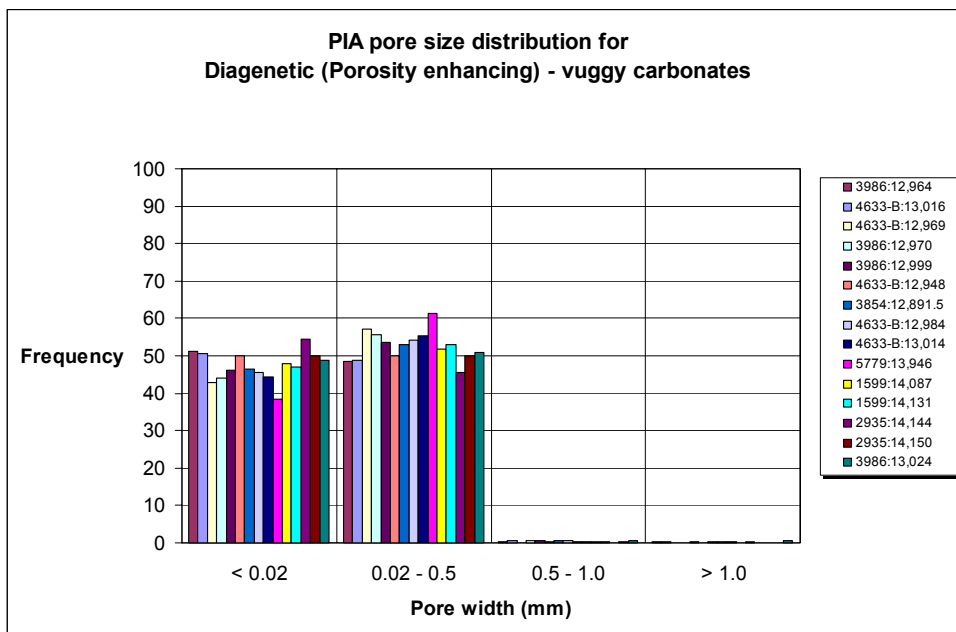


Figure 5.36. PIA pore size distributions for carbonates exhibiting vugs.

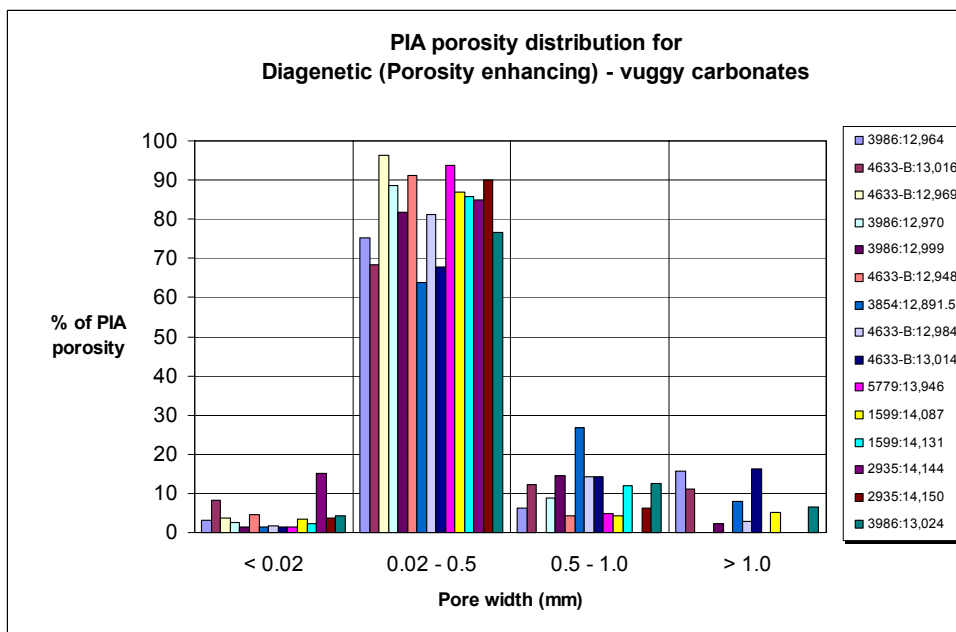
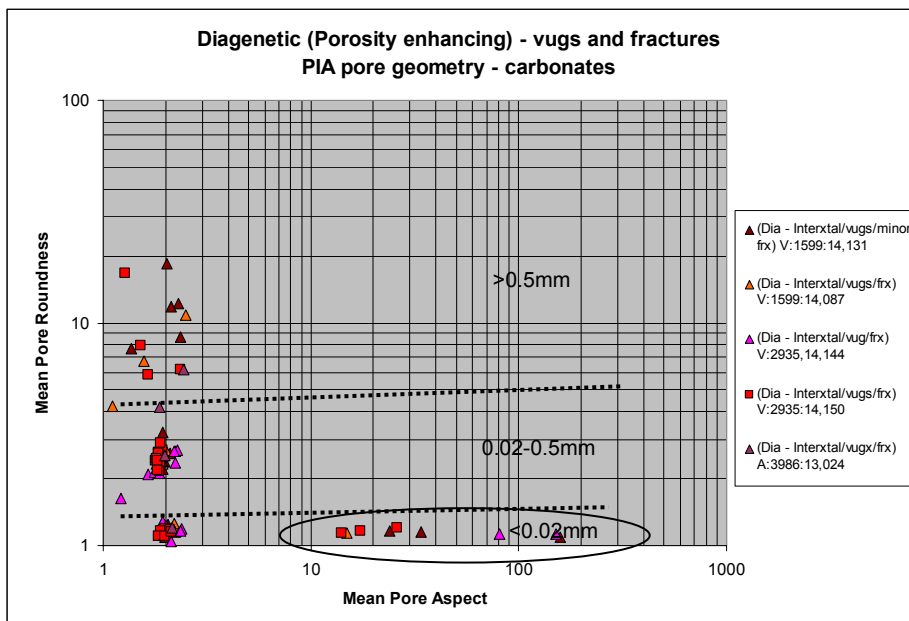
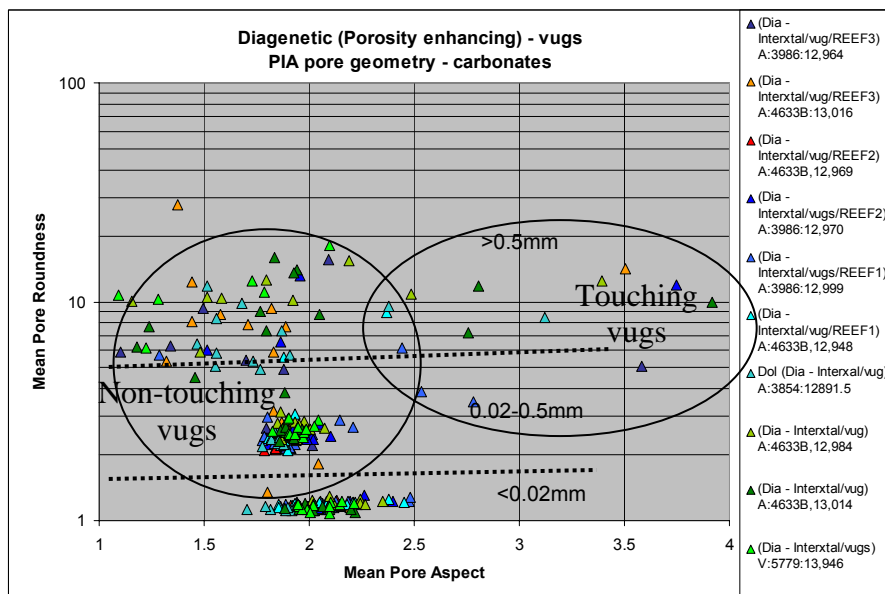


Figure 5.37. PIA porosity distribution for carbonate samples with abundant vuggy porosity. The greatest percentage of porosity comes from pores 0.02-0.5mm in size. In strong contrast to other non-vuggy samples however, there is an abundance of porosity from pores >0.5mm in size.



**Figure 5.38. Pore geometry in five carbonates with high aspect ratios. The pores are identified as possible fractures in thin section (circled). Note log scales.**



**Figure 5.39. Pore geometry in carbonate samples with separate and touching vugs. These dolomitized reef rocks contained an abundance of both separate and touching vugs. Touching vugs have greater aspect ratios. Red and bright green triangles show only separate vugs in thin section.**

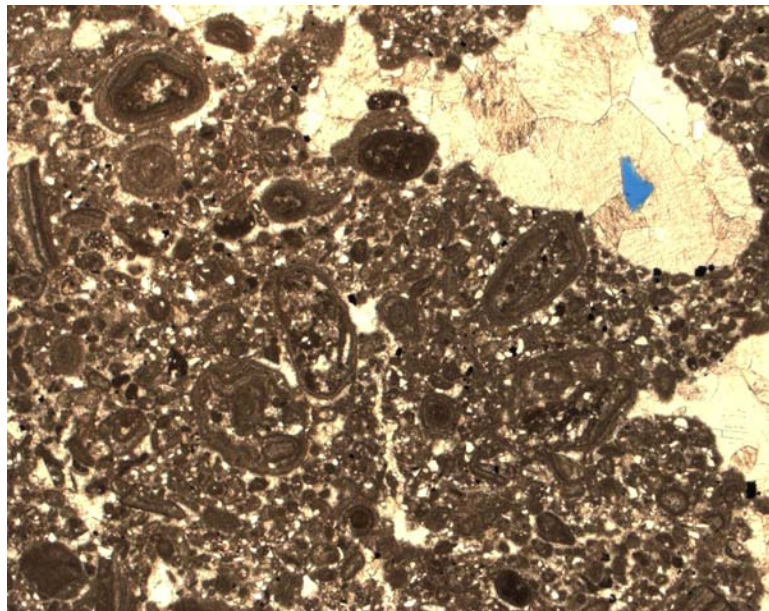
In summary, 15 carbonate samples from Appleton and Vocation fields contained dolomitized reef material which exhibited a combination of vuggy and intercrystalline pores. The large pore sizes were most diagnostic in differentiating vugs from interparticle pores. Samples that exhibited separate vugs had aspect ratios of 1.2-2.0 and roundness values of 4-28. Samples with touching vugs had aspect ratios of 2.3-3.9, and roundness values of 4-28. PIA readily discriminated high aspect ratios (10-100) in a few rocks which are interpreted as possible fractures. The 2-D porosity for these rocks is between 4.2-11%. Of the 2-D area both separate and touching vugs accounted for 10-30% of the 2-D measured total, the remaining portion from smaller vugs and intercrystalline pores of middle (0.02-0.5mm) size.

#### *Cement-Reduced Pores*

Four of the carbonate rocks exhibited diagenetic pores that were significantly reduced by cementation (Figs. 5.40-5.41). PIA was not generally useful in obtaining measurements on these thin sections.



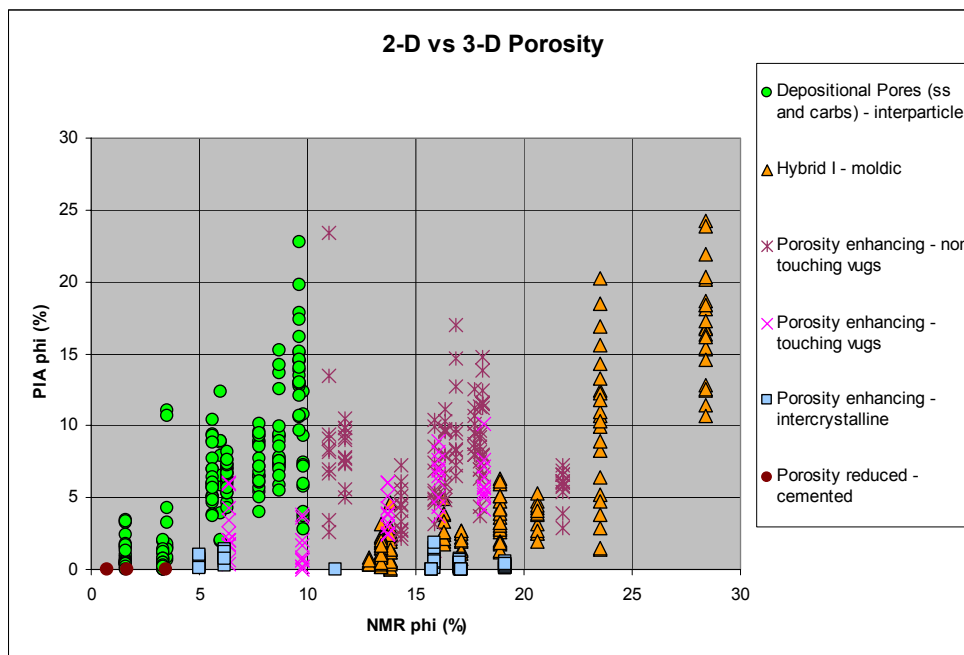
**Figure 5.40.** Core sample of carbonate containing cement-reduced pores. Sample taken from Appleton field, Well 4633-B; 12,868ft.



**Figure 5.41.** Thin section photo of pore space reduced by cementation. A single isolated pore is shown in blue.

### PIA (2-D) Porosity Values and Core Analysis Porosity

PIA porosity measurements underestimate core analysis porosity particularly in rocks that have undergone significant diagenetic alteration. Figure 5.42 illustrates the ranges of 2-D porosity as compared with core analysis porosity. The best estimates occur in rocks which exhibit strong depositional attributes. These rocks contain mostly interparticle pore space and include carbonate ooid grainstones and all of the sandstones. Dolomitized rocks exhibiting only intercrystalline pores cannot be adequately measured in 2-D. In other diagenetic rocks there is minimal likelihood of capturing maximum cross sectional areas of molds and vugs.



**Figure 5.42. 2-D porosity as compared with core analysis porosity for sandstones and carbonates. Each data point is the PIA porosity measurement for a single field of view in a given thin section. Data grouped by pore origin.**

### Summary of All PIA Results

Petrographic image analysis (PIA) was used to measure the size and shape of pores in sandstone and carbonate thin sections (Table 5.2 and Fig. 5.43). Interparticle 'triangular' pores of depositional origin in sandstones and hybrid 1-a pores with strong depositional attributes in carbonates exhibited similar aspect and roundness values in middle sized (0.02-0.5mm) pores. Over 90% of the interparticle pore space was contained in depositional pores of this size. The best 2-D estimates of core analysis porosity are from both sandstones and carbonates dominated by depositional pores.

Hybrid 1b (moldic) pores had a wider range of aspect ratio and roundness values relative to pores of depositional origin. These pores are altered beyond that of Hybrid 1a pores in that chemically unstable grains were removed from the rock producing partial or complete molds of the original grains. Dissolved skeletal grains account for the broader ranges of pore geometry in all pore sizes as compared to the depositional pores. Moldic pores did occasionally have pore geometries similar to the triangular depositional pores, but likely represent a fortuitous 2-D 'slice' of an original 3-D grain. Ooid molds often retained original circular grain shapes across all pore sizes.

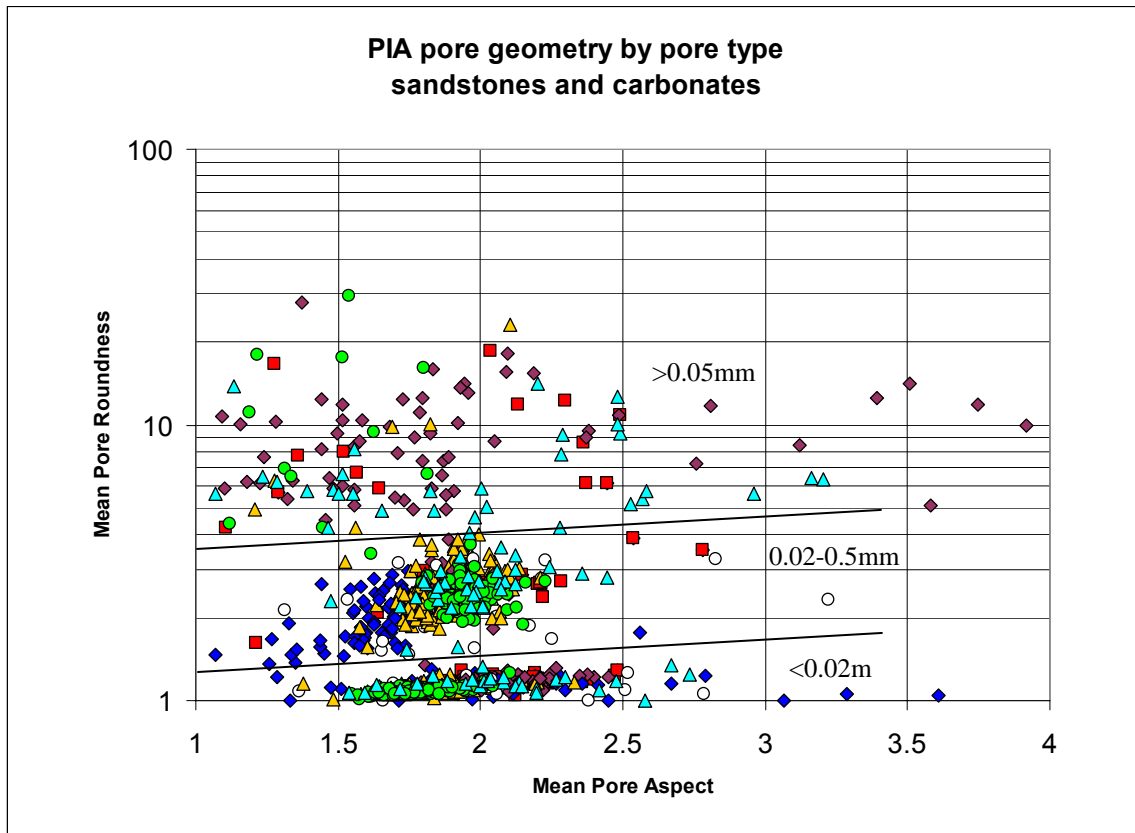
Diagenetic pores include the intercrystalline, vuggy, and cemented pores that result from dolomitization, dissolution, and cementation, respectively. Intercrystalline pores exhibited the lowest aspect and roundness values of any pore type in the medium (0.02-0.5mm) pore size group. In many instances, dolomitized reef rock exhibited large vugs that are interpreted to have formed by dissolution processes. The vugs were differentiated from smaller intercrystalline pores using PIA and they are the most

abundant data in the large (>0.05mm) pore size group. Touching vugs are differentiated from non-touching vugs by aspect ratio. Roundness values in the vugs are similar and alone do not discriminate touching and non-touching forms.

Diagenetically-reduced pores were difficult to measure using PIA because most of the porosity had been occluded by cementation. Where measurements were possible, PIA did not produce reliable or conclusive patterns owing to the small sizes of the remnant pores.

**Table 5.2. Summary of PIA pore measurements by pore origin. Pore geometry values are estimated from Figure 5.41.**

Summary of PIA Pore Measurements						
Pore Origin	Pore Type	Lithology	Pore Geometry		Size (mm) Class	Fraction of 2-D Porosity (%)
			Aspect Ratio	Roundness		
Depositional	Interparticle	Sandstone	1.9	2.5	0.02-0.5	>90
	Interparticle	Carbonate	1.8	2.5	0.02-0.5	35-75
Hybrid 1	Moldic	Carbonate	1.6-2.2	1.8-4.0	0.02-0.5	80-95
Diagenesis - enhanced	Separate vugs	Carbonate	1.1-2.0	4.5-28.0	>0.5	15-30
	Touching vugs	Carbonate	2.3-3.9	4.5-28.0	>0.5	15-30
	Intercrystalline	Carbonate	1.1-1.7	1.3-2.8	0.02-0.5	25-95



**Figure 5.43.** PIA pore geometry by pore type and pore size for all samples. Green circles = Sandstone depositional pores. Blue triangles = carbonate depositional pores. Gold triangles = Hybrid 1-b (moldic) pores. Blue diamonds = intercrystalline pores. Purple diamonds = touching vuggy pores. Red squares = separate vuggy pores. White circles = cement-reduced pores.



## NUCLEAR MAGNETIC RESONANCE (NMR)

### Sandstones

#### *Depositional Pores*

T2 relaxation times (Appendix D) were obtained for 7 sandstone core plugs that exhibited depositional intergranular pores. T2 tabular data were plotted in Excel to display T2 relaxation curves (Fig. 5.44) and NMR-derived porosity for each sandstone sample (Fig. 5.45). The sandstones showed two NMR curve shapes. Two fast relaxation curves (between 0.1-20 milliseconds) characterized sandstones with clay matrix, mechanical compaction or silica cementation. Five of the T2 curves are similar in shape and amplitude and are more representative of unaltered interparticle depositional pore space. The five similar T2 curves each had a one modal peak between 100-400ms and a wavelength of less than one decade amplitude time. Small isolated secondary bumps on the T2 curve occurred at about 10ms. NMR-derived porosity for the sandstone core plugs ranged between 1.6-9.7%.

Conversion of the T2 relaxation curve to a distribution of pore diameters required assumptions to be made about pore geometry and surface relaxation ( $\rho$ ) effects (Chapter

IV). In order to address both assumptions spheres, cylinders, and sheet-like pores were each modeled with multiple  $\rho$  values (Fig. 5.46). The resulting pore size distributions were then plotted and compared with known pore sizes measured directly on the rock. The bold black curve provides the best representation of the pore size distribution in this sandstone because: 1) the satellite peaks have very fast relaxation times ( $<33\text{m/sec}$ ) that represent bound water and can be essentially ignored as part of the effective pore system (Coates et al., 1999), 2) the NMR determined pore size at the highest amplitude was about 63 microns, similar to the PIA mean pore size of 63 microns (Appendix C), 3) circles are acceptable substitutes for triangles with respect to pore roundness (see Table 4.2), and 4) the presence of framboidal pyrite along pore walls warrants higher  $\rho$  values (Dunn et al., 2002; Howard, personal comm). More than 90% of the pore space was found within medium size (0.02-0.5mm) pores (Fig. 5.47).

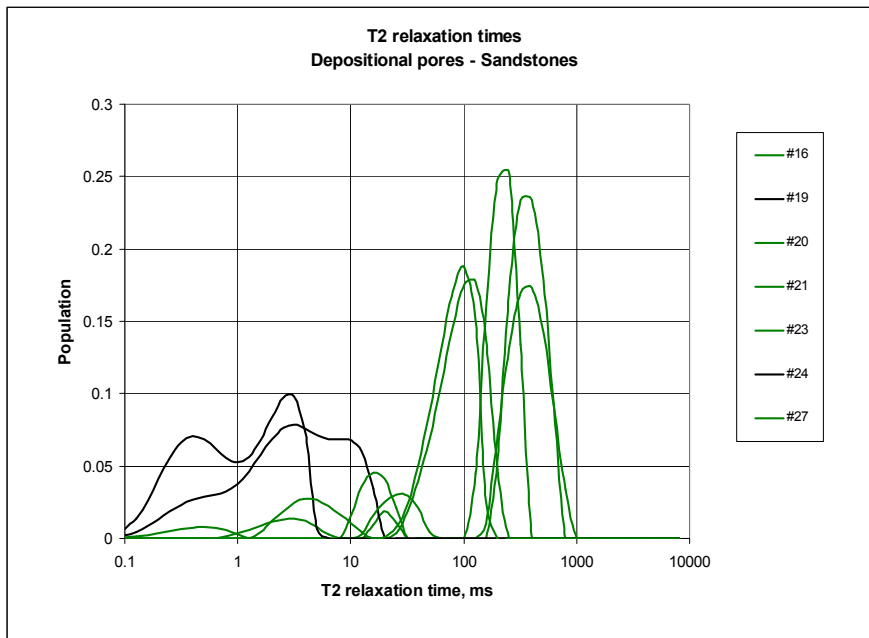


Figure 5.44. T2 relaxation curves for sandstones with depositional pores.

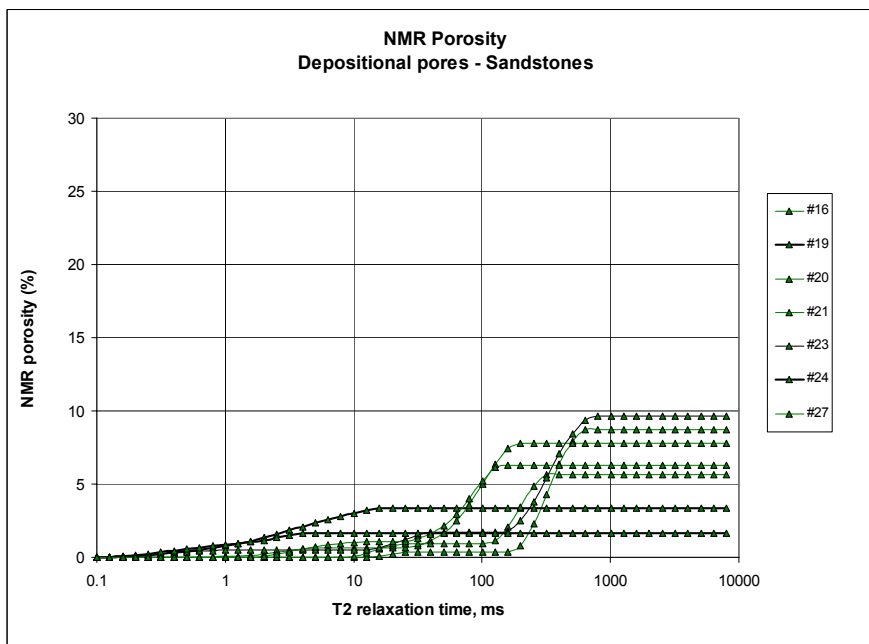


Figure 5.45. T2 porosity curves for sandstones with depositional pores.

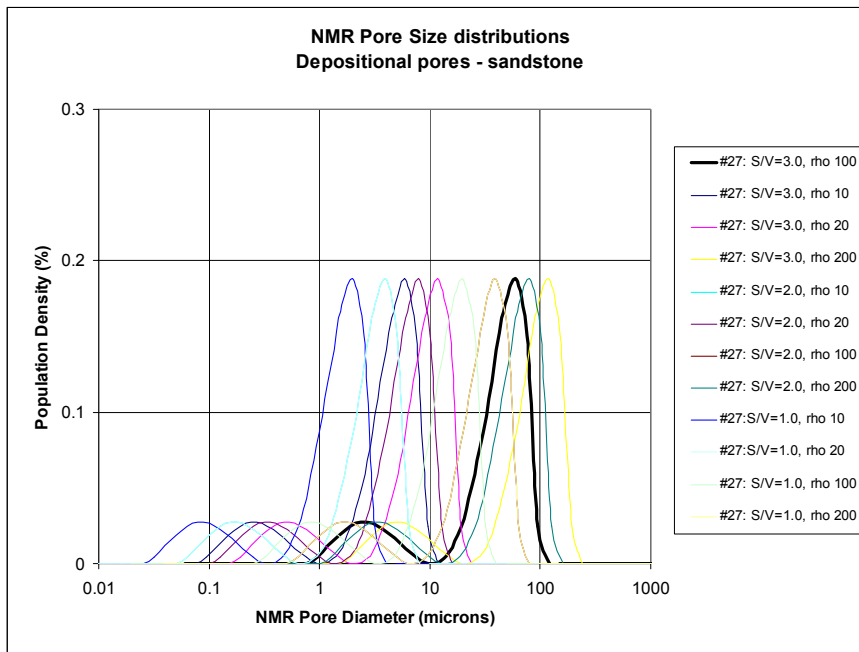


Figure 5.46. Possible T2 pore size distributions for sandstones.

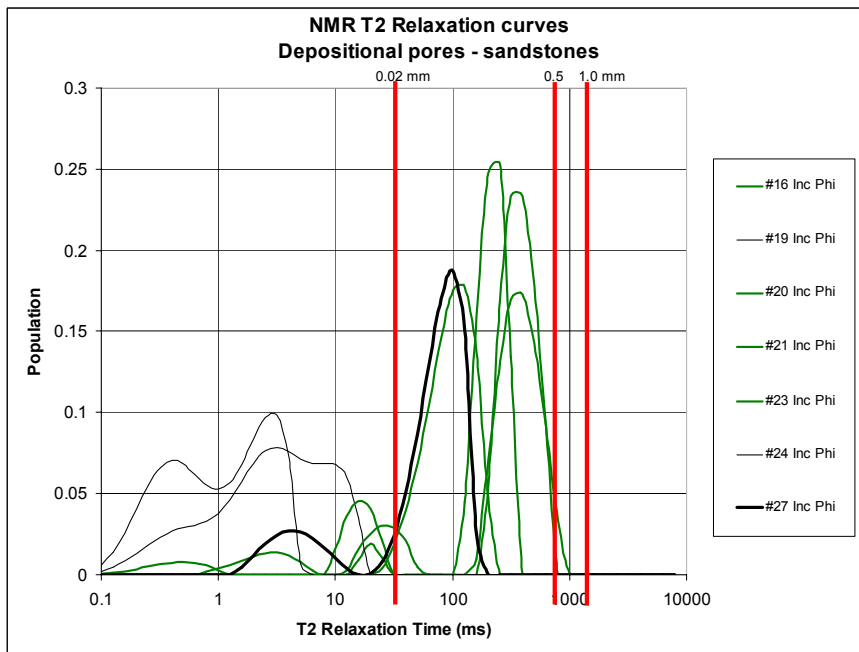


Figure 5.47. Pore size boundaries superimposed on T2 curves in sandstones.

## Carbonates

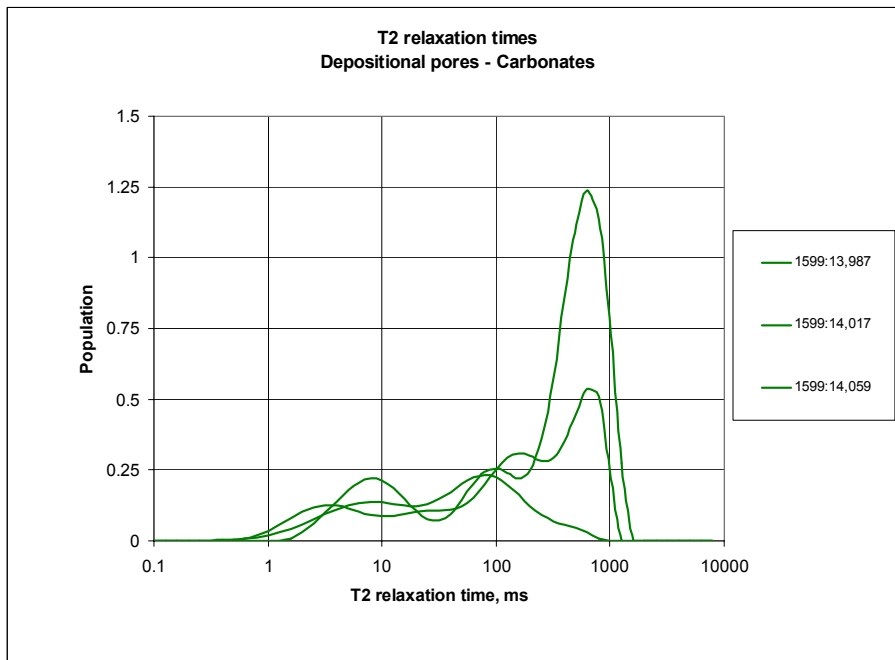
### *Depositional and Hybrid 1-a Pores*

T2 relaxation times (Appendix D) were measured in three carbonate samples (Fig. 5.48) that had NMR-derived porosity between 3.5-9.7% (Fig. 5.49). These rocks exhibited Hybrid 1-a pores, (pores with strong depositional attributes). Like the sandstones, assumptions about pore shape and  $\rho$  were necessary to make the pore size conversion. To address both assumptions, spheres, cylinders, and sheet-like pores were each modeled with multiple  $\rho$  values. Timur (1972) showed that the value of  $\rho$  depends on surface mineralogy and is weaker in carbonates than in sandstones. Timur's published  $\rho$  value (5microns/sec) for carbonates is a first order approximation and assumes spherical pores. Later work by Foley et al. (1996) showed that the presence of paramagnetic ions could affect surface relaxation rates and hence obscure NMR pore size. The effective pore system is found in T2 relaxation times greater than 92 milliseconds (Coates et al., 1999).

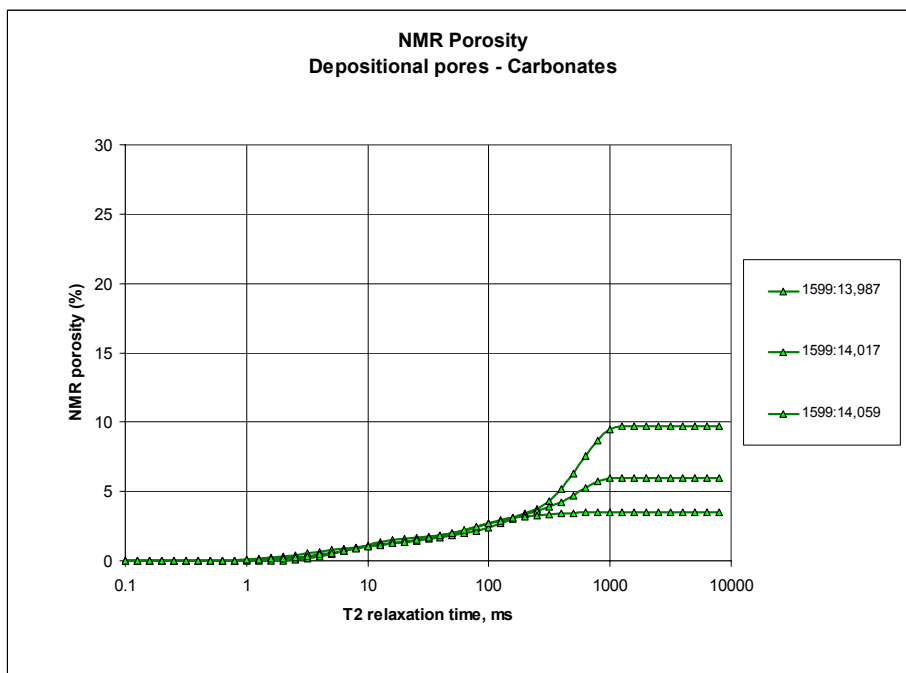
In this study, pore geometry is determined by direct measurement, and paramagnetic minerals which affect  $\rho$  values are identified with the microprobe (Appendix F). Resultant pore size distributions were plotted and compared with known pore sizes as were directly measured on the rock. In this way the assumptions are better constrained when determining NMR pore size. Although pores with depositional attributes are observed in these thin sections, differences in the T2 curves are noticeable

from sample to sample. Each T2 curve is poly-modal and two of the curves show the highest amplitude peak at 630 milliseconds. Amplitude variation at the 630 millisecond location varies between samples because of differences in cementation. NMR detects the same pore sizes in these rocks, but in differing abundances. Poorly sorted ooids and skeletal grains are a likely reason for lower amplitude peaks (smaller pores) located at 1-100ms.

The bold black curve (Fig. 5.50) was chosen as the best estimate of NMR pore size for this samples because: 1) there is no effective pore system below the 92millisecond cutoff, 2) the mean PIA pore size was 80 microns, 3) circles (and therefore spheres) are reasonable substitutes for crude triangular pore shapes, and 4) the presence of diagenetic pyrite and minor ferroan dolomite warrants a higher  $\rho$  value. Middle sized (0.02-0.5mm) pores contained 30-70% of the porosity from direct rock measurements (Fig. 5.51).



**Figure 5.48.** T2 relaxation curves for carbonates with depositional pores.



**Figure 5.49.** T2 porosity curves for carbonates with depositional pores.

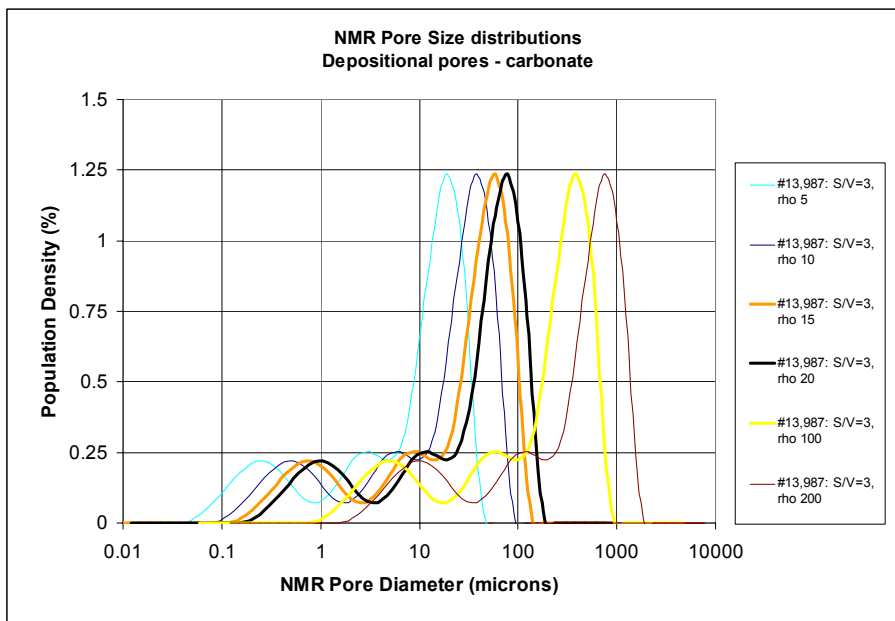


Figure 5.50. Possible T2 pore size distributions for carbonates with depositional pores.

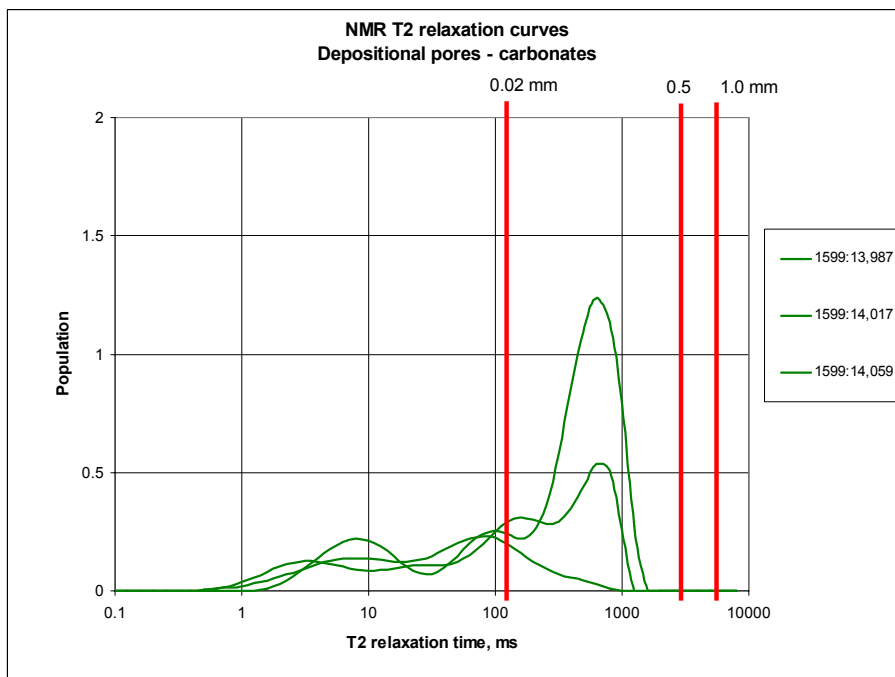


Figure 5.51. Pore size boundaries superimposed on T2 curves in carbonates with depositional pores.



*Hybrid 1-b (Moldic) Pores*

T2 relaxation times (Appendix D) were measured on nine carbonate samples with Hybrid 1-b (moldic) pores and are plotted using Excel (Fig. 5.52). Moldic pores were created by a combination of depositional and diagenetic processes. Hybrid 1-b pores are differentiated from (Hybrid 1-a pores) by the presence of ooid and skeletal grain molds. NMR-derived porosity was 12.9-28.5% in these rocks (Fig. 5.53).

Eight of the nine samples exhibit similar NMR curve shapes. These samples are ooid and skeletal grainstones from Womack and Happy fields. One sample exhibits exceptionally well-preserved ooid molds only; skeletal grains were absent. The general T2 curve shape for moldic pores shows shorter relaxation times in the rocks with small skeletal molds, and high amplitude peaks at 100-400ms. Quintero et al., (1999) have suggested that grain-supported carbonate textures with high porosity (>15%) have NMR T2 curves spanning greater than one decade in time, though diagenetic effects on the original rock fabric were not discussed. Rocks in this study have porosity greater than

13%, have T2 curves spanning more than one decade time and exhibit skeletal and ooid molds. T2 curve width is not sufficient to discriminate grainy textures of purely depositional origin from grainy textures of hybrid origin.

As with prior examples, calculating NMR pore size from T2 relaxation times required certain assumptions about pore geometry and surface relaxation effects ( $\rho$ ). Spheres were used as proxies for oomoldic pores because spheres are interpreted as circles in thin section. A  $\rho$  value of 15microns/sec was chosen; close to Timur's (1972) published value. The highest NMR amplitude was at about 80 microns, the same size directly measured on the average pore in 2-D. The bold curve (Fig. 5.54) is therefore most representative of the pore size distribution for the carbonate samples with hybrid 1-b (moldic) pores. The estimated 2-D distributions of small, medium, and large pores are shown in Figure 5.55.

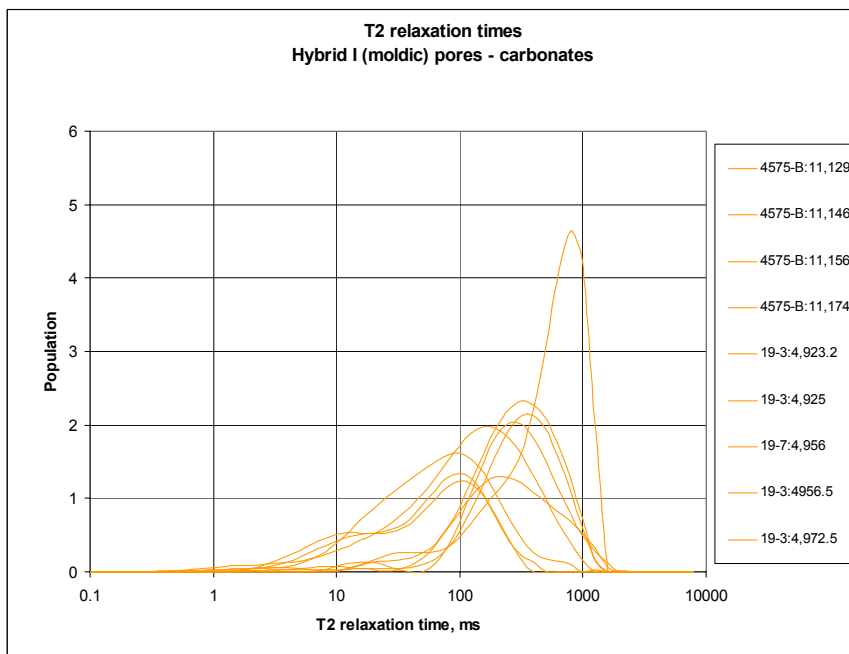


Figure 5.52. T2 relaxation curves for carbonates with Hybrid I-b (moldic) pores.

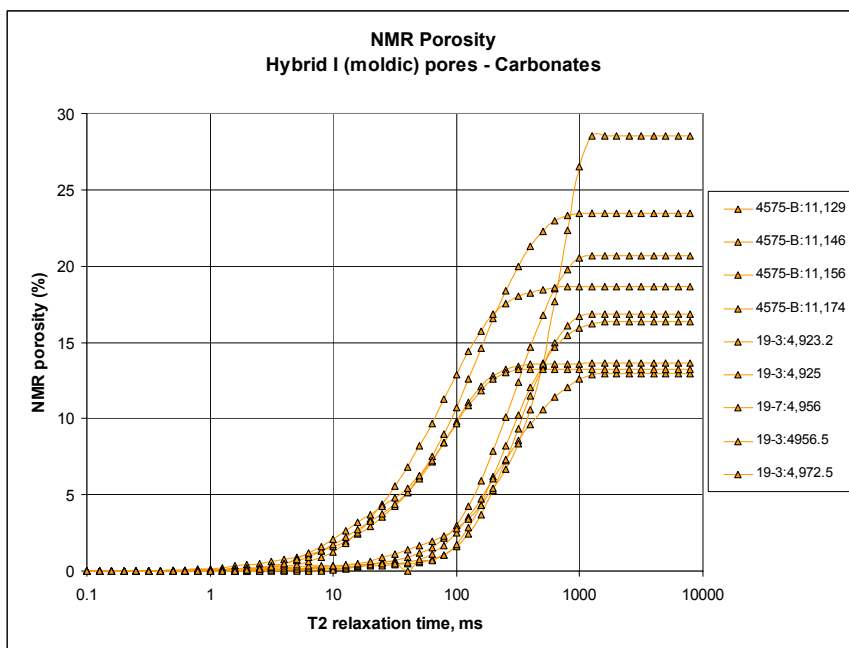


Figure 5.53. T2 porosity curves for carbonates with Hybrid I-b (moldic) pores.

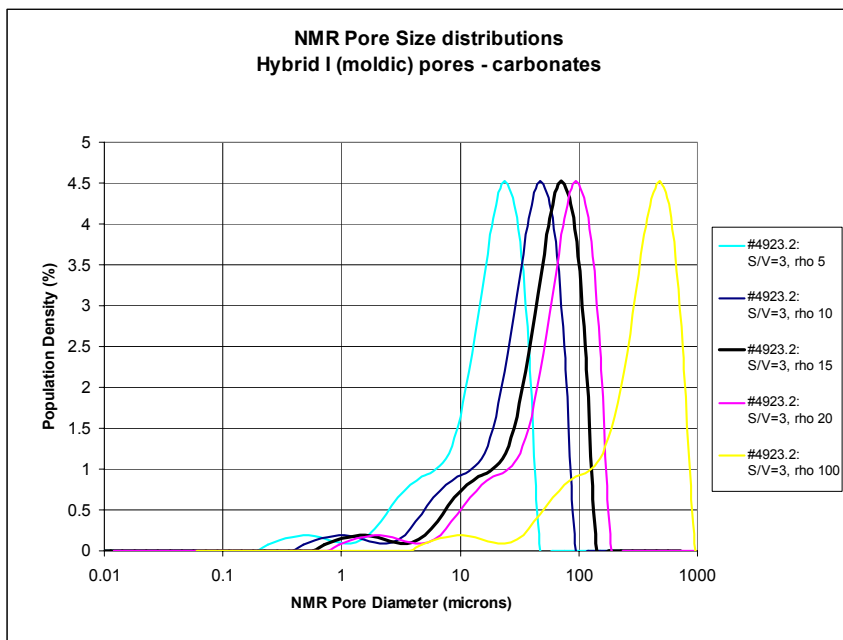


Figure 5.54. Possible T2 pore size distributions for carbonates with moldic pores.

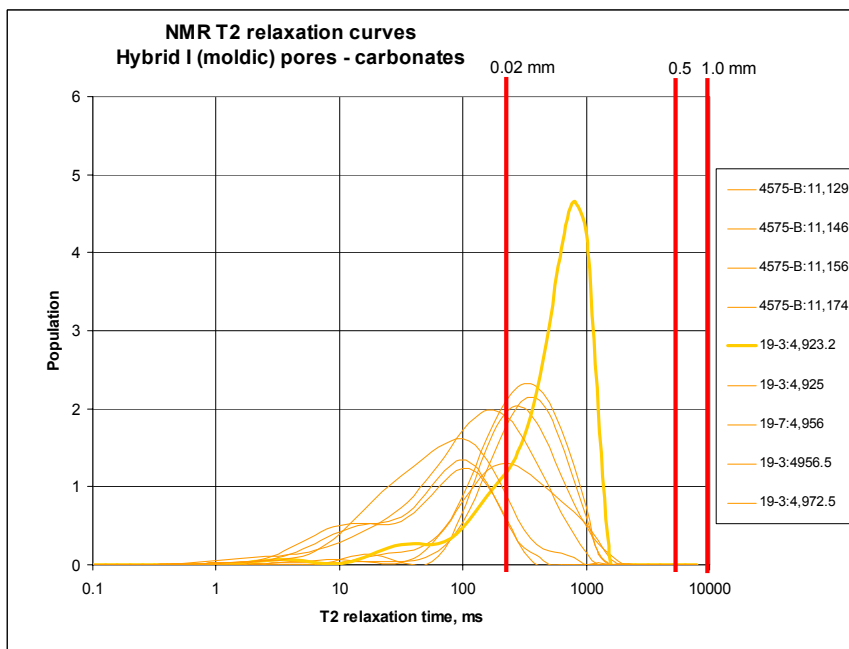


Figure 5.55. Pore size boundaries superimposed on NMR T2 curves in carbonates with moldic pores.

*Diagenetic - Intercrystalline Pores*

T2 relaxation times for nine dolomite samples with purely diagenetic, intercrystalline porosity are given in Appendix D. T2 relaxation curves are shown in Fig. 5.56 and NMR porosity was calculated at 5.0-19.1% (Fig. 5.57). T2 curves generally have one mode between 30 and 500ms. Six of the curves have modes between 100 and 200ms. These samples show a range of amplitude values between 0.8 and 4.8; suggesting that the NMR measurements are influenced by variations in the amount of intercrystalline pore space from rock to rock but that pore sizes were generally consistent. The curves show narrow wavelengths of less than one decade time on the x-axis.

As with prior examples, calculating NMR pore size from T2 relaxation times required certain assumptions about pore geometry and surface relaxation effects ( $\rho$ ). Spheres were assumed in the T2 conversion to pore size (Fig. 5.58) and  $\rho$  was estimated at 20micron/sec because diagenetic pyrite was found in the rock. Note that the black curve is probably most representative of these samples of intercrystalline pores. The 2-D estimates of small, medium, and large pore sizes show on the T2 curve are shown in Figure 5.59.

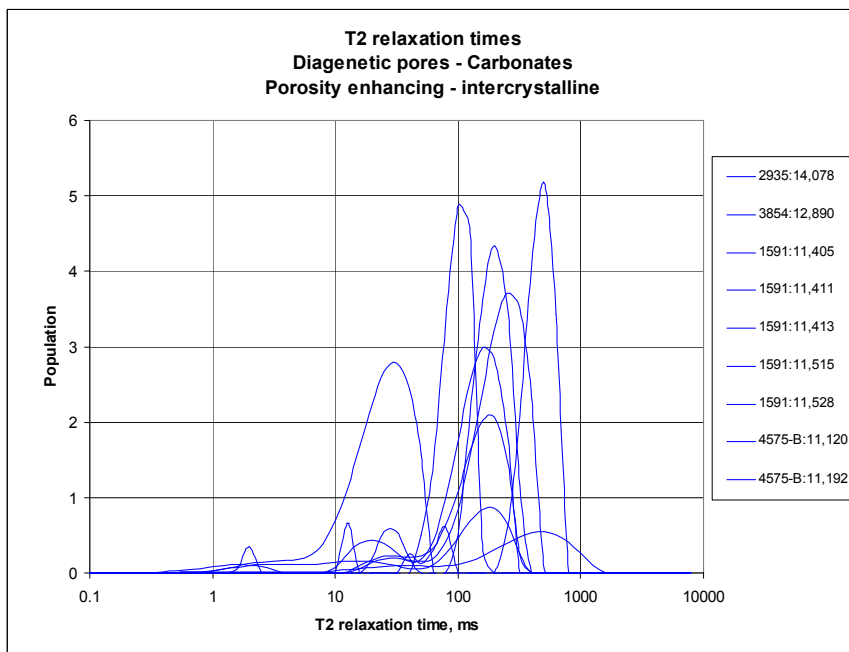


Figure 5.56. T2 relaxation curves for carbonates with intercrystalline pores.

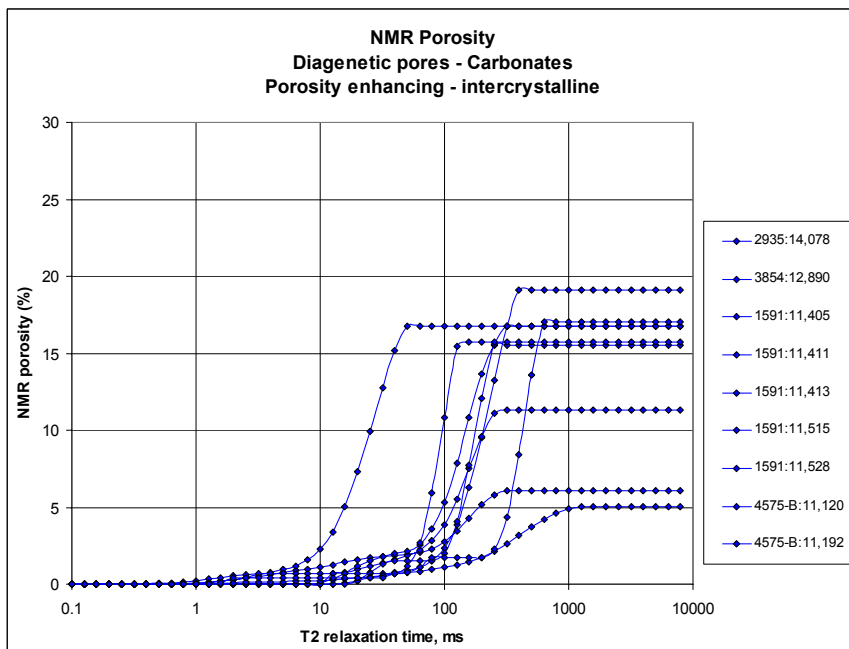
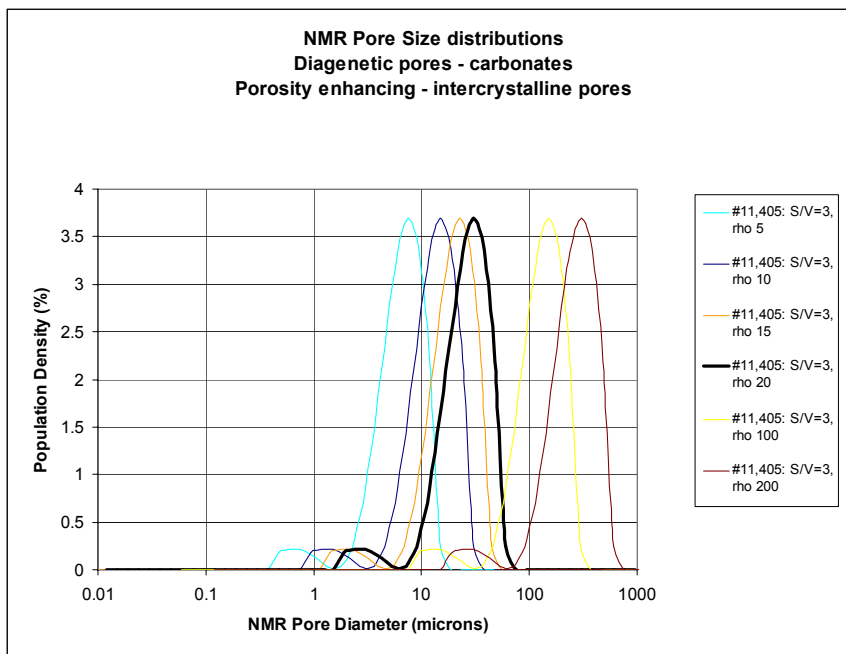
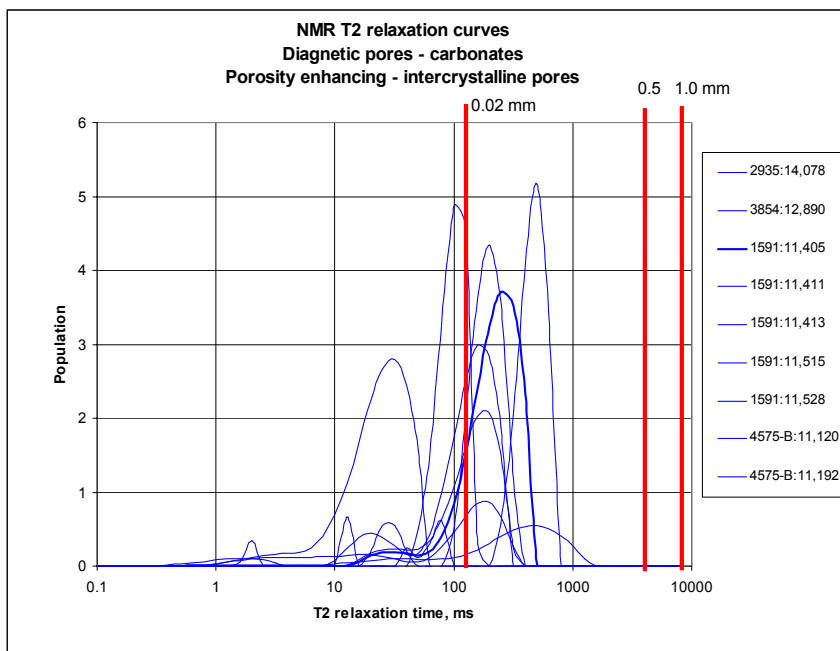


Figure 5.57. T2 porosity curves for carbonates with intercrystalline pores.



**Figure 5.58. Possible T2 pore size distributions for carbonates with intercrystalline pores.**



**Figure 5.59. Pore size boundaries superimposed on NMR T2 curves in carbonates with intercrystalline pores.**

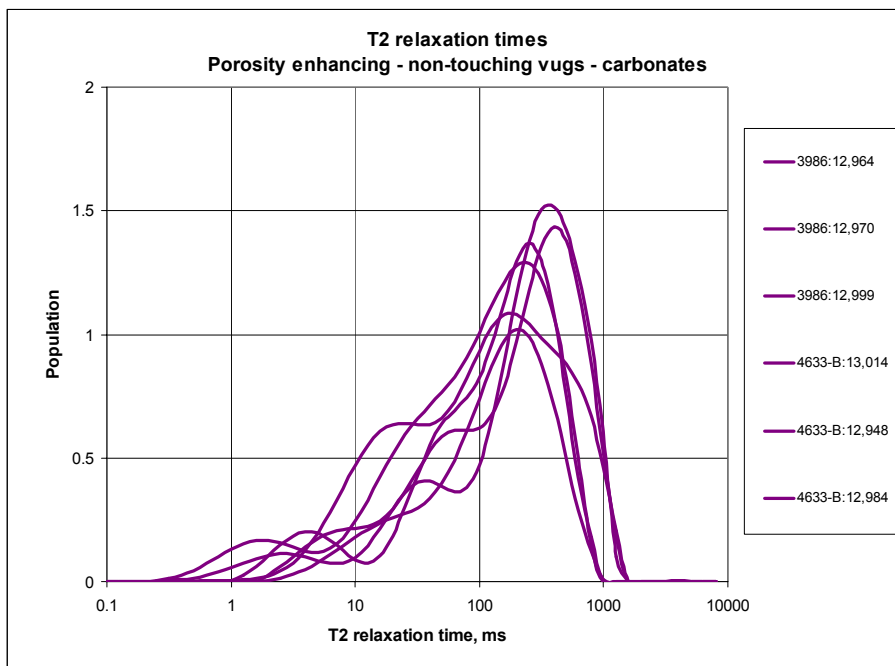
*Vugs: Purely Diagenetic, Enhanced Porosity*

T2 relaxation times for fifteen samples, which include separate and touching vugs, are given in Appendix D. All of the samples are from Appleton and Vocation fields, and were reefs prior to dolomitization and dissolution processes. Many of the samples were taken from similar wells at successive depths (Plate 1). Six samples exhibiting separate vugs show similar T2 curve shapes and curve locations (Fig. 5.60). The T2 curves are broad; spanning at least three decades across the T2 time axis and each showing tri-modal curve peaks. NMR-derived porosity for these samples with separate vugs is 10.8-17.6% (Fig. 5.61).

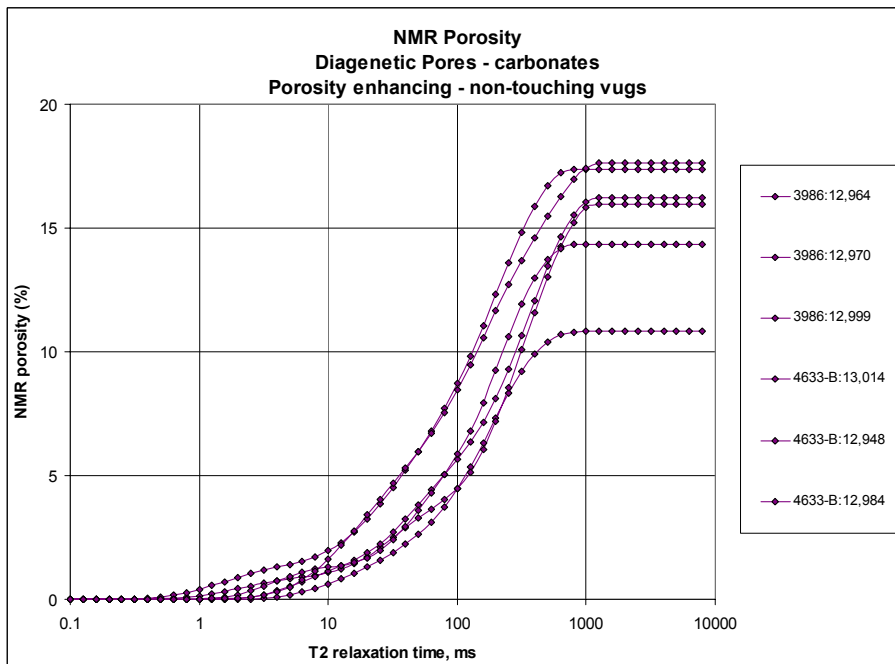
Nine samples exhibited touching vugs (Fig. 5.62). The T2 curves for these rocks also span at least three decades in T2 time and generally show poly-modal amplitude peaks. The T2 curves are not near replicates of one another; a characteristic found in samples with separate vugs. The differences in curve shape are therefore interpreted to be differences in the degree of dissolution from rock to rock. The NMR-derived porosity for samples with touching vugs is 6.4-21.2% (Fig. 5.63).

Like previous examples, assumptions of pore geometry and  $\rho$  were necessary to convert T2 relaxation times into pore sizes. Samples with vugs assumed spheres in the calculation, though vugs have non-spherical shapes in thin section (Fig 5.64). The bold curve was chosen as the best representation of the sample with vugs. The  $\rho$  value of 15





**Figure 5.60.** T2 relaxation curves for carbonates with non-touching vugs.



**Figure 5.61.** T2 porosity curves for carbonates with non-touching vugs.

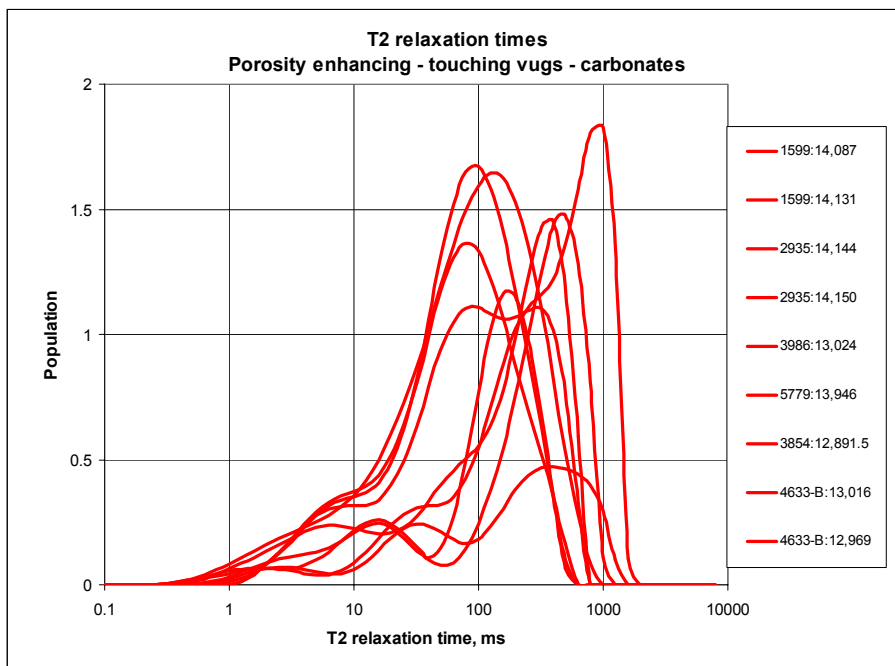


Figure 5.62. T2 relaxation curves for carbonates with touching vugs.

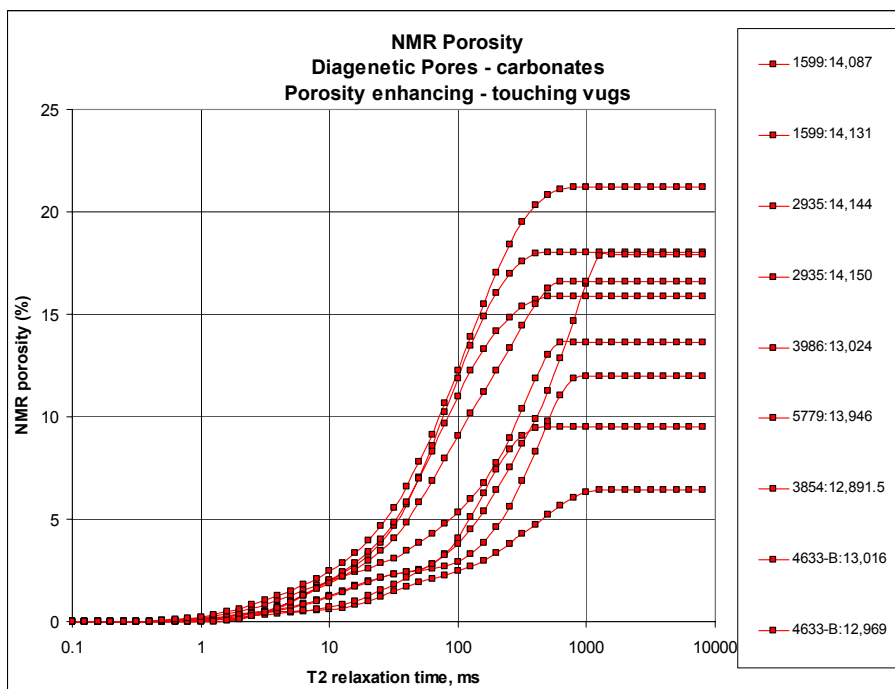


Figure 5.63. T2 porosity curves for carbonates with touching vugs.

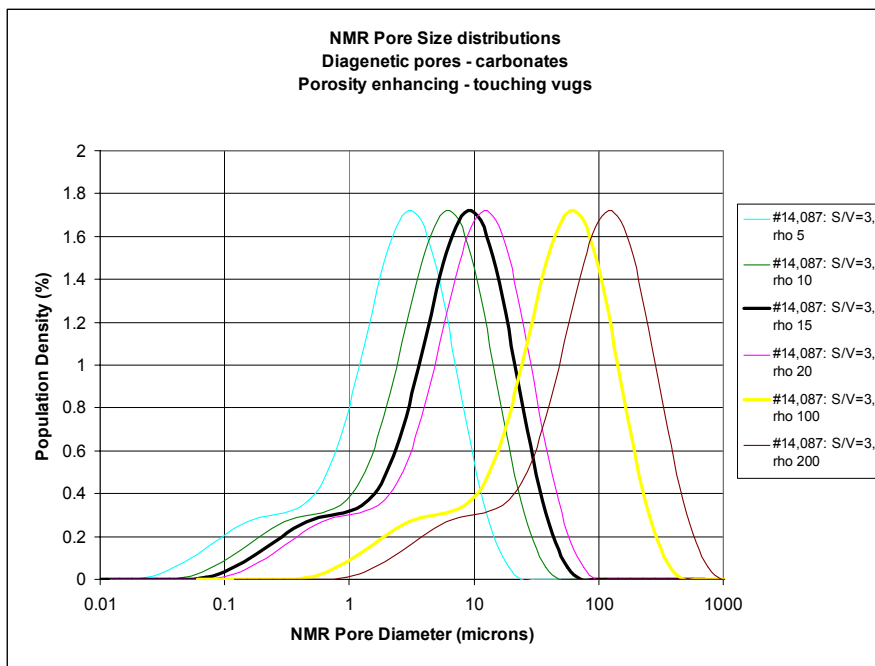


Figure 5.64. Possible T2 pore size distributions for carbonates with touching vugs.

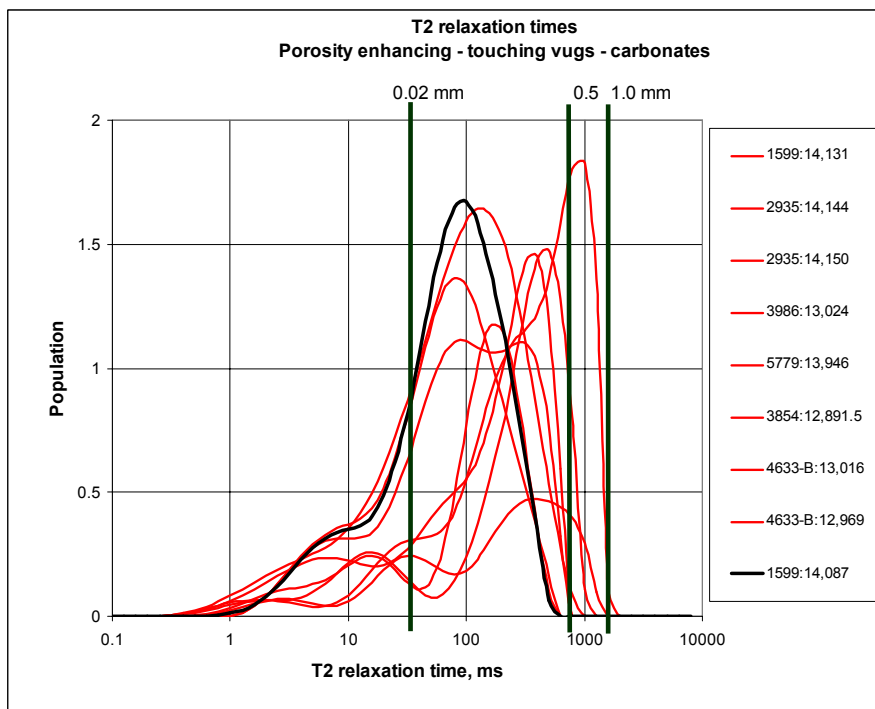


Figure 5.65. Pore size boundaries superimposed on carbonates with touching vugs.

microns/sec is greater than Timur's (1972) proposed value, but acceptable because of high iron concentrations along the vug perimeter. Estimates showing the location of small, medium, and large pores on the T2 curve are shown in Figure 5.65.

#### *Cement-Reduced Pores*

T2 relaxation times for 4 carbonate samples with diagenetically-reduced porosity after cementation are given in Appendix D. Samples with cemented pores have T2 curves quite different from any other pore type. In these samples amplitude peaks occur at very short relaxation times (Fig. 5.66). This is interpreted to be an effect of the cementation process which created small pores. NMR-derived porosity for samples with cemented pores is between 0.7 and 4.1% (Fig. 5.67). Spheres were assumed in the calculation of NMR pore sizes (Fig. 5.68), though the specific shapes of the small, cemented pores were difficult to see in cross sectional view. Timur's (1972) first-order approximation of  $\rho$  for carbonates was used in this case because only trace amounts of iron were found in the samples.

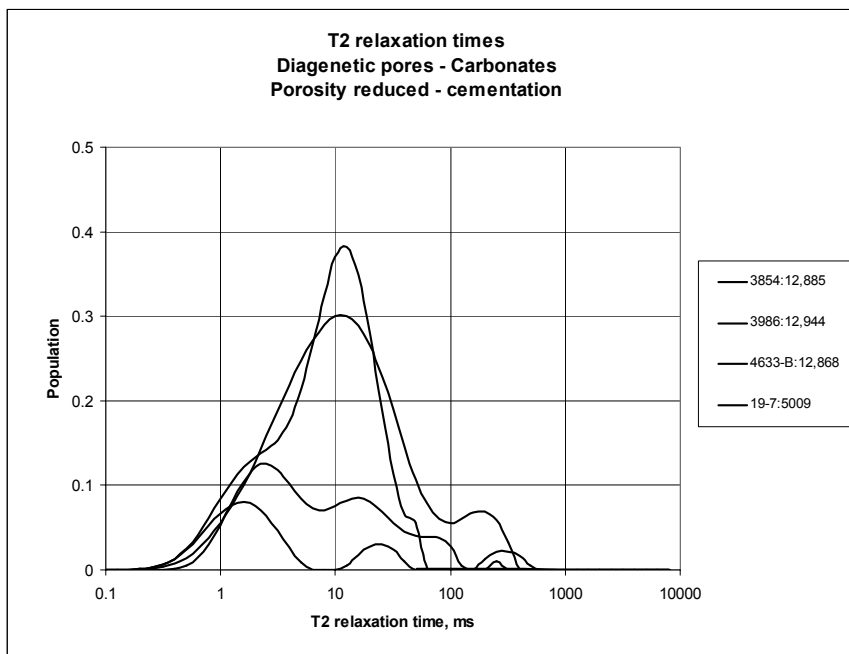


Figure 5.66. T2 relaxation curves for carbonates with cement-reduced pores.

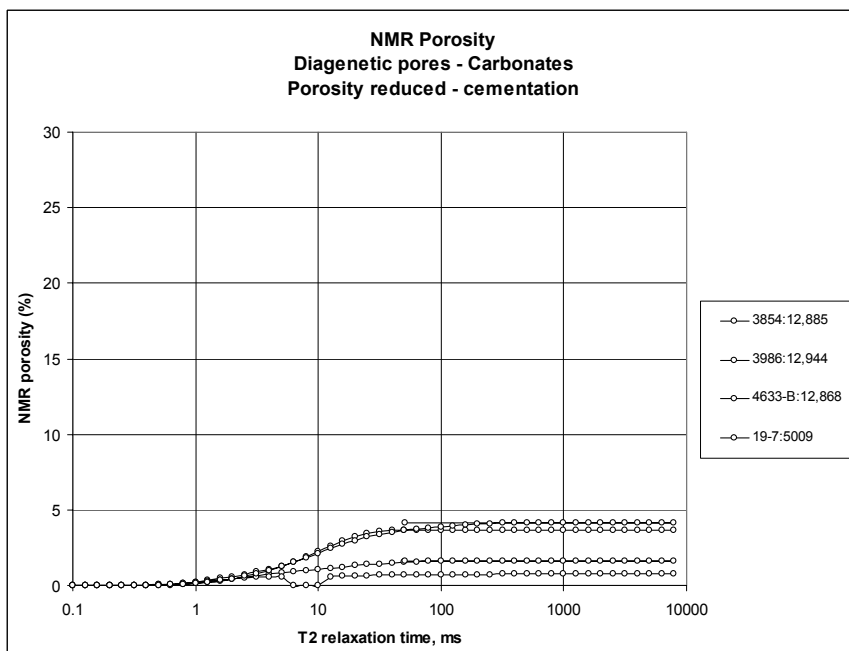
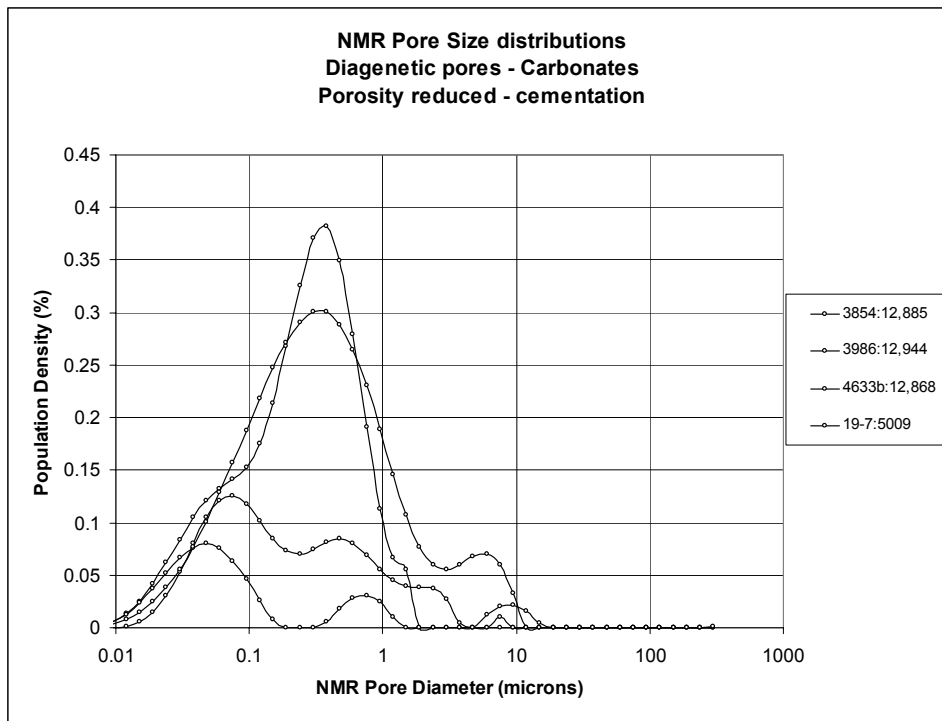


Figure 5.67. T2 porosity curves for carbonates with cement-reduced pores.



**Figure 5.68. Possible T2 pore size distributions for carbonates with cement-reduced pores. Spheres assumed and a  $\rho$  value of 5 microns/sec is used.**

### Summary of All NMR Results

Nuclear magnetic resonance (NMR) was used to measure the T2 relaxation times on 7 sandstone and 40 carbonate samples. The samples were grouped according to genetic pore types (Chapter IV) along with their corresponding T2 curves (Fig. 5.69) General characteristics of T2 curve shape are summarized in Table 5.3.

Carbonates with pores diagenetically reduced by cementation exhibited T2 curves with the lowest amplitudes; accompanied by very short T2 relaxation times. High T2 amplitudes characterize rocks with vugs, molds, intercrystalline, and interparticle pores. Higher amplitude values are associated with higher abundances of pores.

All curves exhibit from 1 to 3 modes. Depositional pores in both sandstones and carbonates, oomoldic (Hybrid 1-a) pores, and intercrystalline pores typically exhibit 1 mode. Hybrid I-b pores (both skeletal and ooid molds) and some touching vugs exhibit bimodal curves. Separate vugs, some touching vugs, and diagenetic pores reduced by cementation had tri-modal curves.

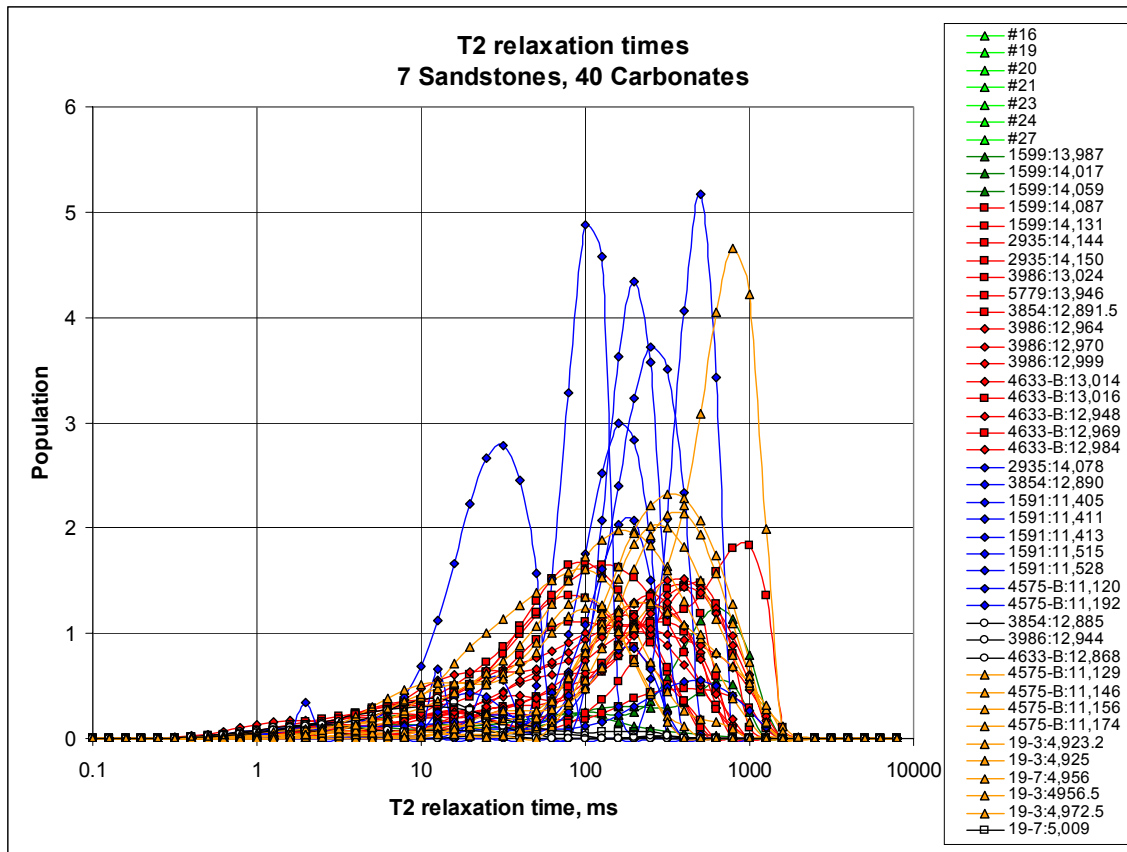
Depositional pores in sandstones and carbonates, and Hybrid 1a and Hybrid 1b pores, as well as intercrystalline pores exhibited near symmetric, narrow wavelengths less than 1 decade in T2 time. Moldic pores and rocks with both separate and touching vugs displayed fast-skewed, with curve widths spanning 3 decades in T2 time. Carbonates with pores reduced by cement exhibited slow-skewed, intermediate (1-3 decade width) T2 wavelengths.

NMR-derived porosity values are shown in Figure 5.70. Carbonate rocks with diagenetic pores reduced by cementation had the lowest NMR-derived porosity values (0.7-4.1%). Intermediate NMR-derived porosity was found in sandstones and carbonates containing depositional pores. Samples with mold and diagenetic pores enhanced by dissolution had the highest values of NMR-derived porosity, up to 28.5%.

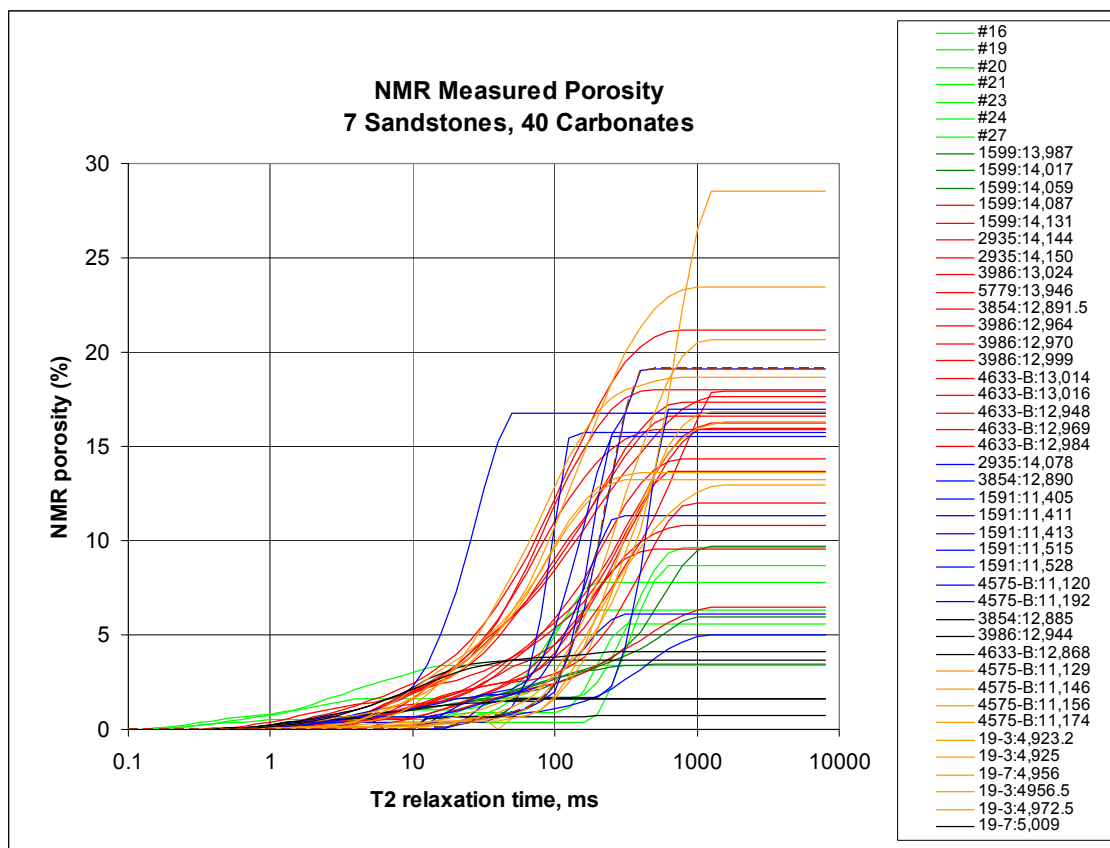
**Table 5.3. Summary of T2 curve characteristics for all rocks and pore types.**

Summary of NMR T2 Measurements							
Pore Origin	Pore Type	Lithology	T2 Curves				NMR porosity (%)
			Peak Amplitude (ms)	# of Modes	Wavelength (# decades)	Symmetry Style	
Depositional	Interparticle	Sandstone	252	1	Narrow (<1)	symmetric	1.6-9.7
	Interparticle	Carbonate	630	1	Narrow (<1)	symmetric	3.5-9.7
Hybrid 1	Moldic (oids)	Carbonate	794	1	Intermediate (1-3)	symmetric	28.5
	Moldic (oids and skeletal)	Carbonate	316	2	Wide (>3)	fast-skewed	12.9-23.5
Diagenesis - enhanced	Separate vugs	Carbonate	398	3	Wide (>3)	fast-skewed	10.8-17.6
	Touching vugs	Carbonate	100-1000	2 or 3	Wide (>3)	fast-skewed	6.4-21.2
	Intercrystalline	Carbonate	100-500	1	Narrow (<1)	symmetric	5.0-19.1
Diagenesis - reduced	Cemented	Carbonate	12	1 or 2 or 3	Intermediate (1-3)	slow skewed	0.7-4.1





**Figure 5.69.** T2 relaxation curves for all samples. Light green triangles=sandstone depositional pores. Dark green triangles=carbonate depositional pores. Red squares=touching vugs. Red diamonds=non-touching vugs. Blue=intercrystalline pores. White diamonds=cement-reduced pores. Orange=Hybrid I-b (moldic) pores.



**Figure 5.70.** T2-derived porosity curves for all samples. Light green triangles=sandstone depositional pores. Dark green triangles=carbonate depositional pores. Red squares=touching vugs. Red diamonds=non-touching vugs. Blue=intercrystalline pores. White diamonds=cement-reduced pores. Orange=moldic pores.

## MERCURY INJECTION CAPILLARY PRESSURE (MICP)

### Sandstones

#### *Depositional Pores*

MICP measurements were not made on sandstone samples (Fig. 5.71) because of a shortage of funds. NMR data were used to generate synthetic capillary pressure curves for the sandstones (Chapter IV). All but two of the sandstone samples exhibited similar capillary pressure curves (Fig. 5.72) estimated as having low entry pressures and filling of pore space at low pressure. The “folding back” of some curves is the result of combining multiple data sets in order to create a single array and is not recommended as the best procedure to estimate  $P_c$  from NMR (Howard pers comm.). For this batch of samples the  $P_c=100$ psi data were collected at one time whilst the  $P_c=25$  and  $50$  were measured several weeks later after resaturating the core plugs. The handling of the samples likely removed some loose edges and corners affecting the overall mass balance and NMR estimate of  $P_c$  (Howard, pers comm.).

Samples with the lowest porosity (3.3% and 1.6%) contained clays and were cemented. NMR is not sensitive enough to distinguish pores from pore-throats. A distribution of pore-throat sizes from NMR was not possible, though comparison of depositional pore-throats in carbonates was calculated at about 30 microns.

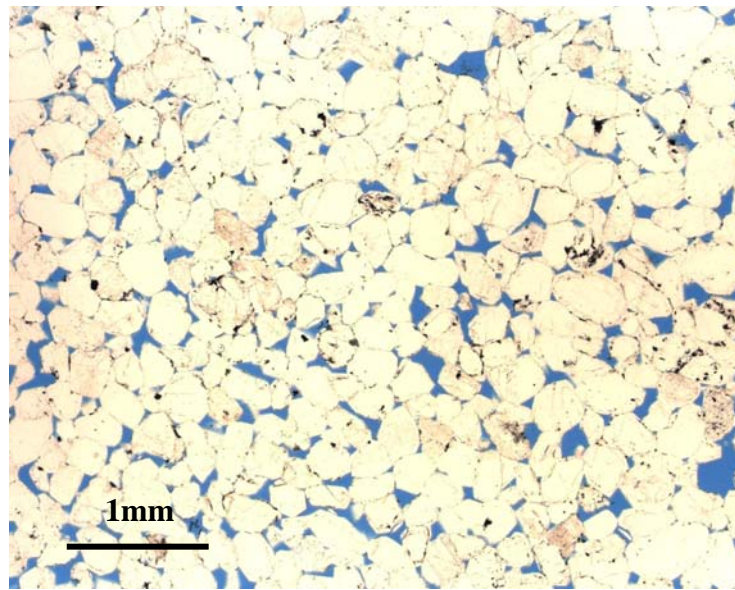


Figure 5.71. Thin section photomicrograph of depositional intergranular pores in sandstone. Blue is pore space. Plain light image.

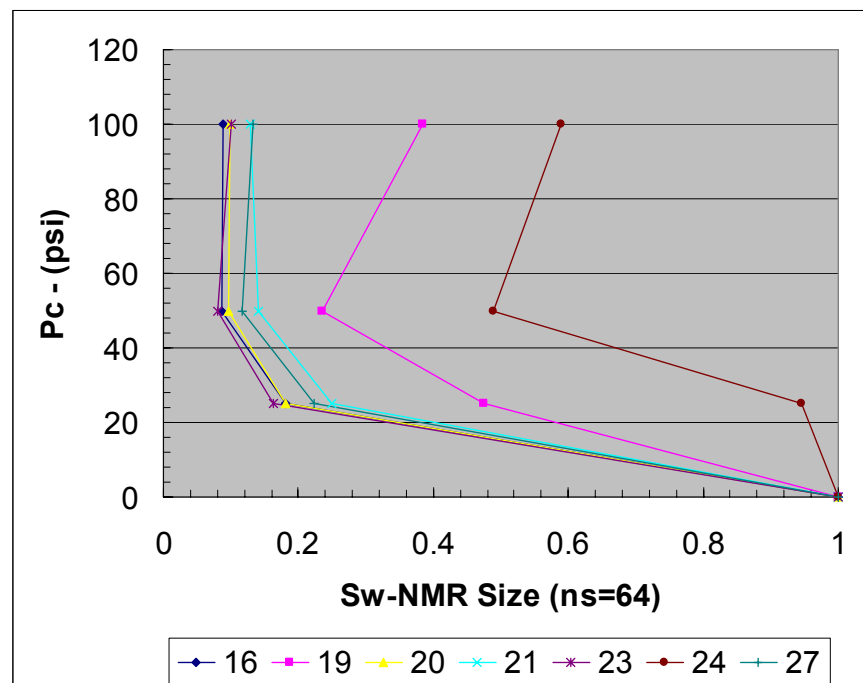
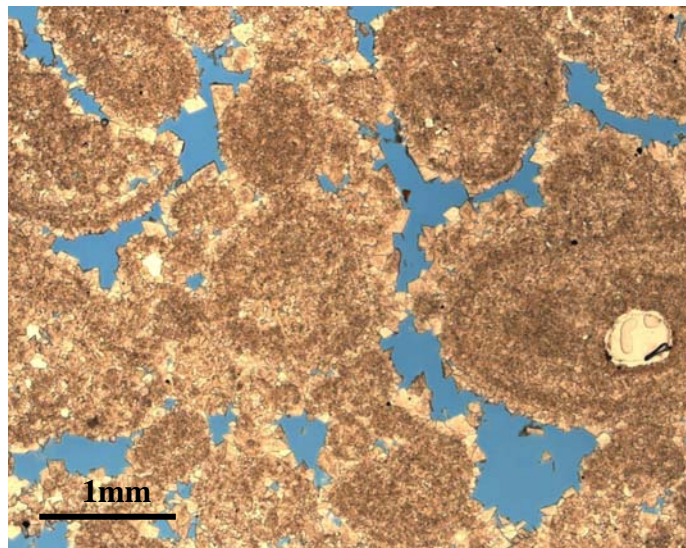


Figure 5.72. Synthetic capillary pressure curves estimated from NMR runs on sandstones. Two sandstones (#16 and #24) contained clays, were cemented, and had low NMR-measured porosity values relative to the other sandstone samples.

## Carbonates

### *Depositional and Hybrid 1-a Pores*

Two of 40 carbonate samples contained pores with strong depositional attributes. These are generally interparticle pores with minor amounts of cement around individual ooid grains (Fig. 5.73). Pore-throats comprised  $< 7\%$  of the measured pore volume (Fig. 5.74). A distribution of pore-throat sizes for samples with depositional pores (Fig. 5.75) show effective median throat sizes for the two samples to be 30 and 40 microns. The range of pore-throat sizes for these samples was 10-100 microns. Pores with strong depositional attributes in carbonates were characterized by low entry pressures (3 psi) and a large pore volume was filled by non-wetting phase at low pressure. A steep increase in capillary pressure occurred at about 30% wetting phase saturation (Fig. 5.76).



**Figure 5.73. Thin section photomicrograph of depositional pores in carbonate. Blue is pore space. Plain light image.**

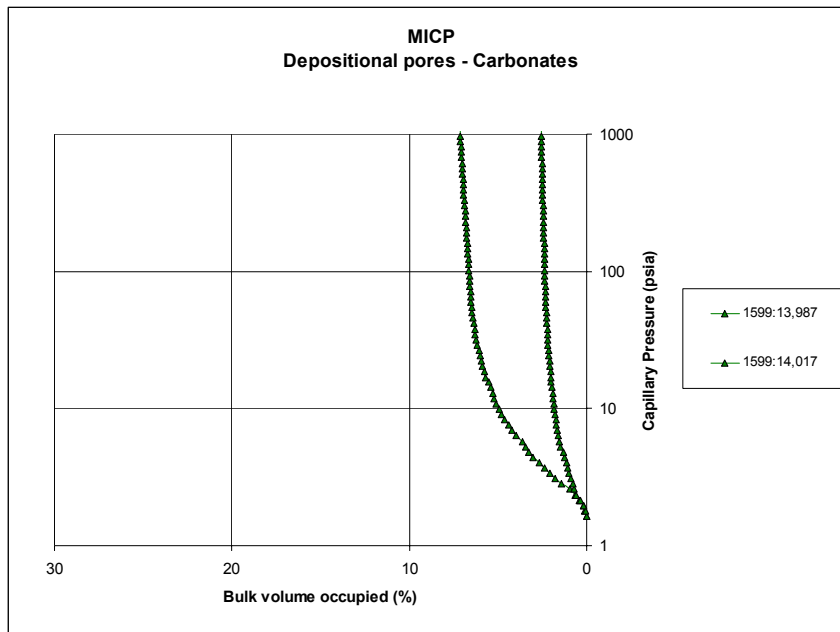


Figure 5.74. Capillary pressure curves for carbonates with pores exhibiting depositional attributes.

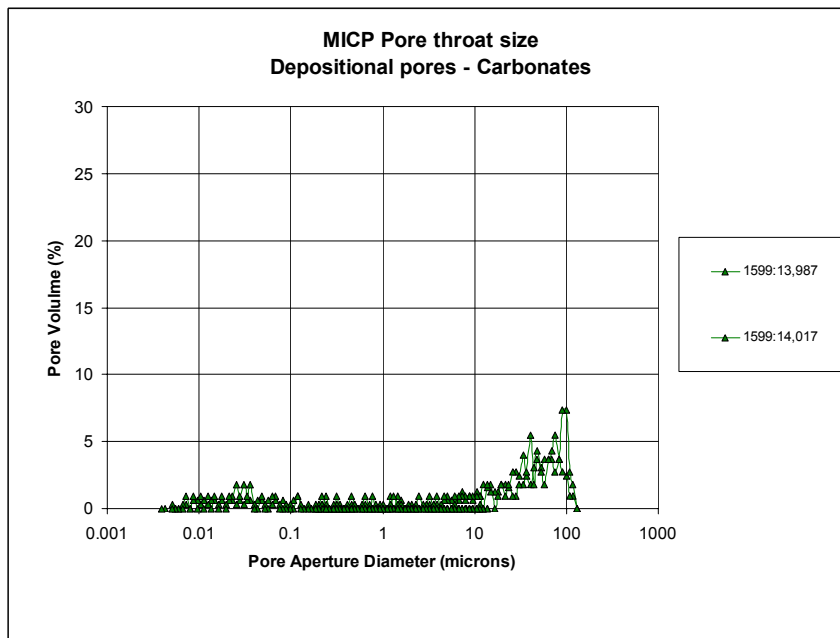
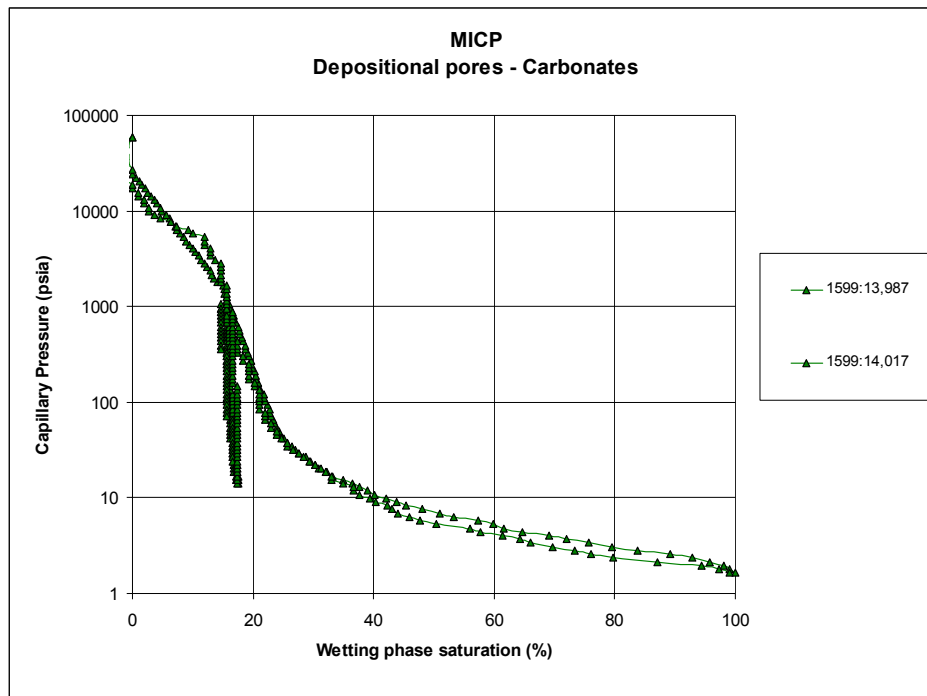


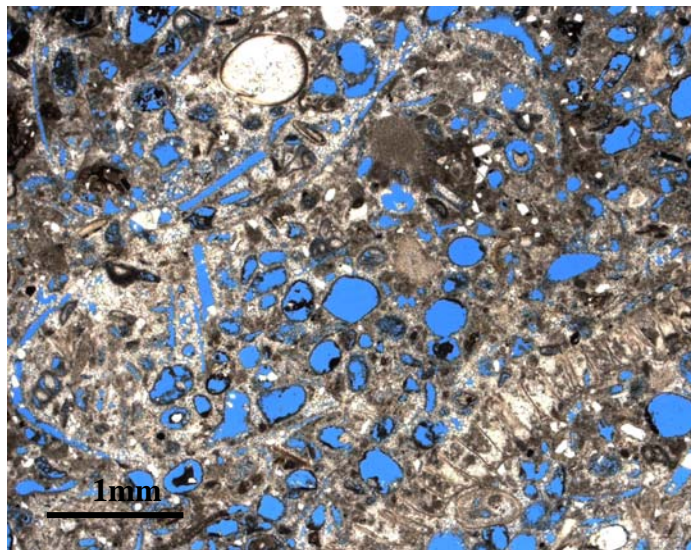
Figure 5.75. Distribution of pore-throat sizes in carbonates with pores exhibiting depositional attributes.



**Figure 5.76. Wetting phase saturation curve for carbonates exhibiting pores with strong depositional attributes.**

### *Hybrid 1-b (Moldic) Pores*

Of the 40 carbonate samples, 9 exhibit hybrid 1-b (moldic) pores (Fig. 5.77). These pores form from a combination of depositional and diagenetic processes. Capillary pressure curves for these samples are shown in Figure 5.78. Note that the two lower curves represent exclusively oomoldic pores. Moldic pores in these nine samples were signified by displacement pressures of 10-50psi. Samples exhibiting exclusively oomoldic pores show the largest volumes of pore space filled at the lowest pressures. A steep increase in capillary pressure occurred at about 20% wetting phase saturation (Fig 5.79). Figure 5.80 shows the distribution of effective pore-throats for these samples. Median throat size ranged from 1.3-6.2 microns, and the total range of aperture sizes was 0.1-10 microns. Pore-throats contained less than 10% of the pore volume in samples with moldic pores.



**Figure 5.77. Thin section photomicrograph of moldic pores. Blue is pore space. Plain light image.**



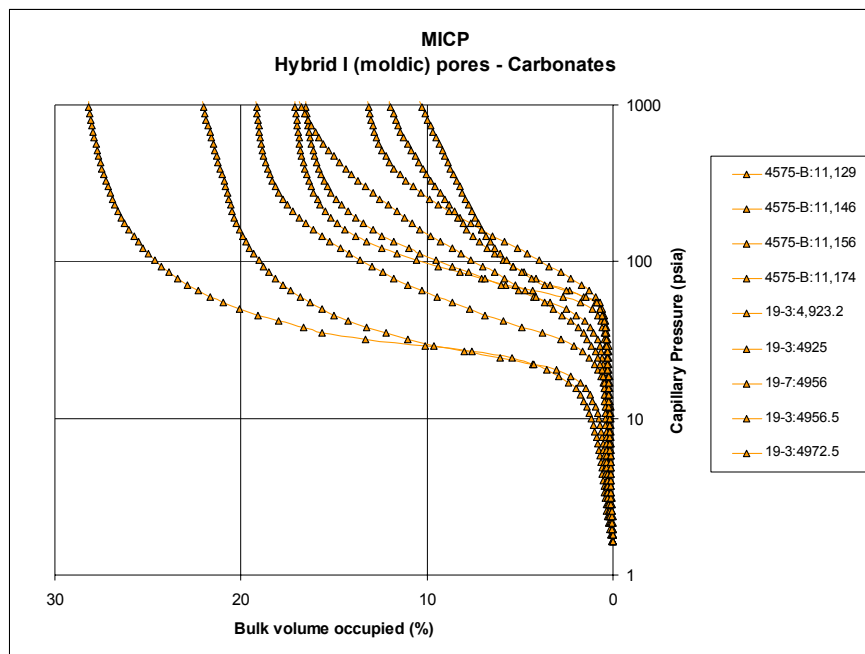


Figure 5.78. Capillary pressure curves for carbonates with moldic pores.

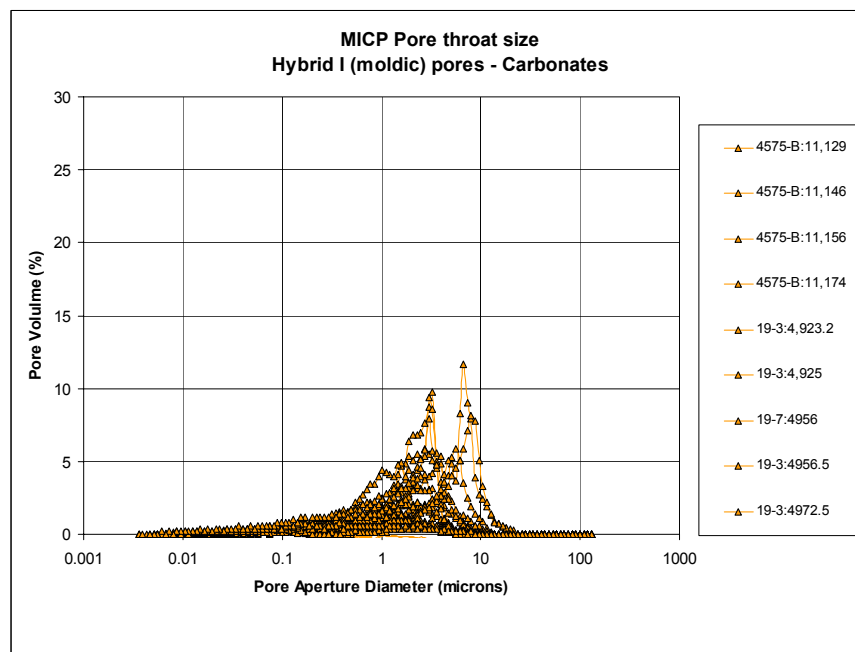


Figure 5.79. Distribution of pore-throat sizes in carbonates with moldic pores.

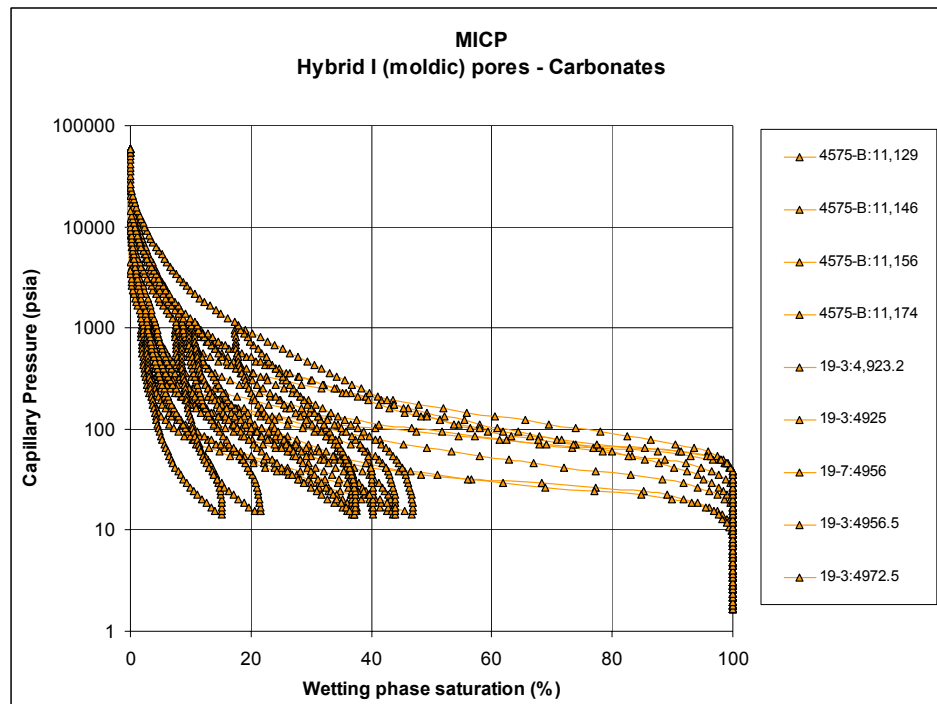
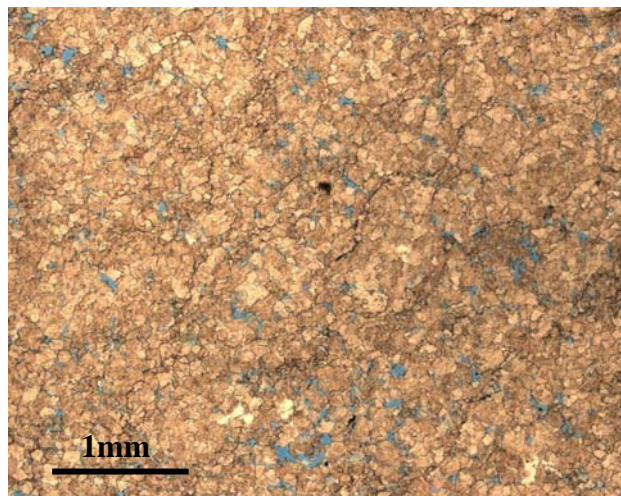


Figure 5.80. Wetting phase saturation curves for carbonates with moldic pores.

*Diagenetic - Intercrystalline Pores*

Of 40 carbonate samples, 9 are crystalline dolostones formed by replacement of limestone precursors. These samples exhibit intercrystalline pores (Fig. 5.81). Samples with higher measured porosity show similarity in capillary pressure behavior as do the samples with lower measured porosity (Fig. 5.82). Intercrystalline pores in carbonates had moderate entry pressures (25-300 psi) and the largest volumes of pore space were filled at near uniform pressures. A moderate increase in capillary pressure occurred at about 20% wetting phase saturation (Fig. 5.84). Effective pore-throat size for these rocks (Fig. 5.83) ranged from 0.3-8 microns in diameter, with median aperture values of 0.26-6.8 microns from sample to sample. The volume of mercury that occupied pore-throats comprised less than 10 % of the total pore volume in four samples and up to 28% of total pore volume in 5 samples. This variation in pore-throat volume corresponds to the variation in median throat sizes as illustrated in Figure 5.83.



**Figure 5.81.** Thin section photomicrograph of intercrystalline pores. Blue is pore space. Image taken in plain light.

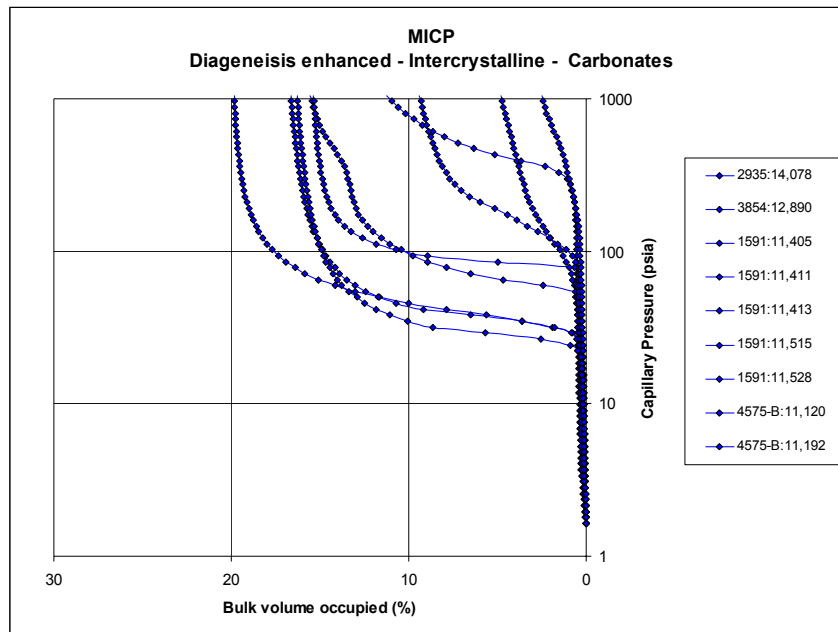


Figure 5.82. Capillary pressure curve for carbonates with intercrystalline pores.

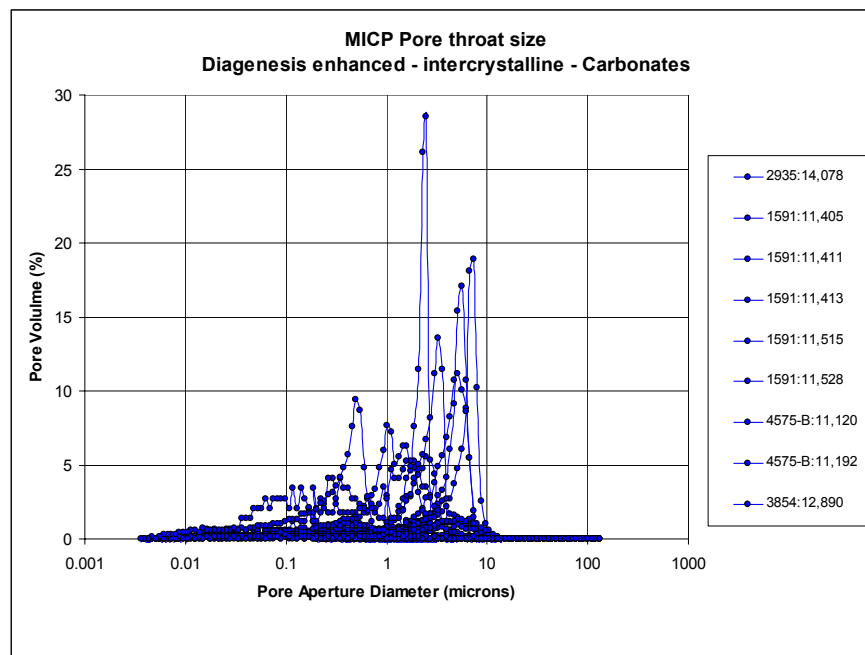
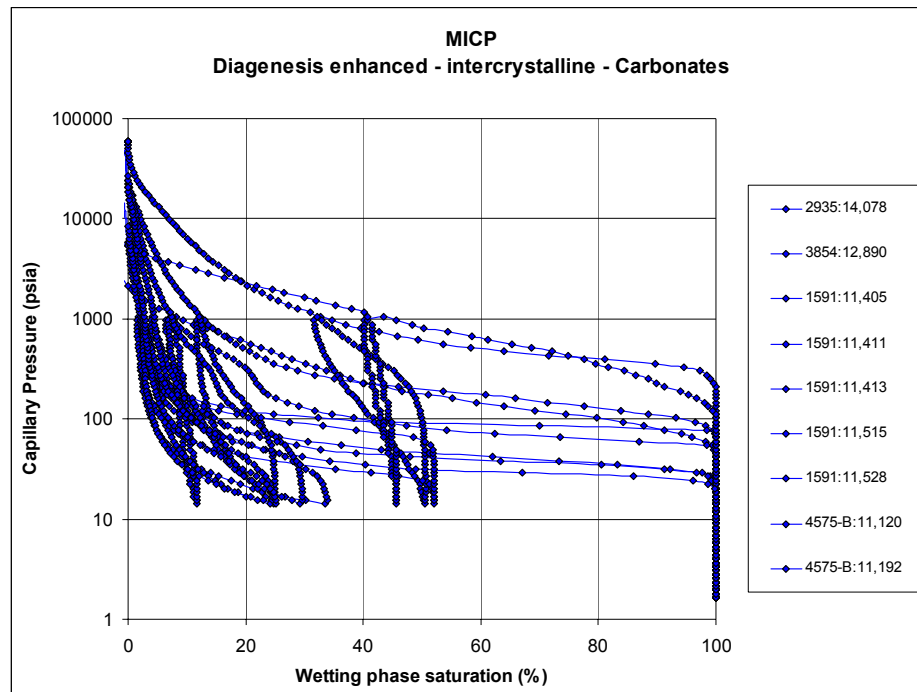


Figure 5.83. Distribution of pore-throat sizes in carbonates with intercrystalline pores.

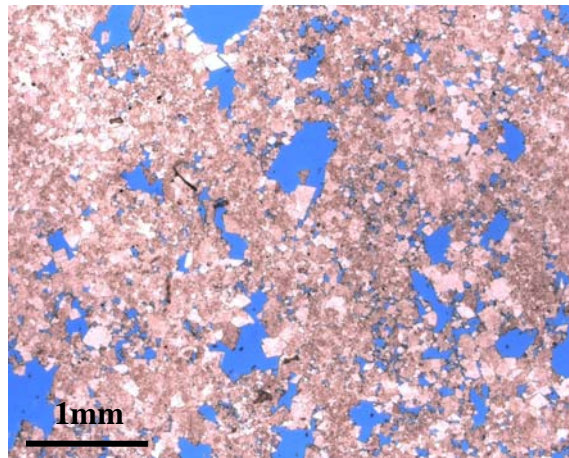


**Figure 5.84. Wetting phase saturation curves for carbonates with intercrystalline pores.**

*Vugs: Purely Diagenetic, Enhanced Porosity*

Of the 40 carbonate samples in this study, 15 are characterized by vuggy pores (Fig. 5.85). Vuggy pores are characterized by low entry pressures (2-8 psi). Note that there is a coupled increase in the volume of filled pore space with pressure (Fig. 5.86). Samples with separate and/or touching vugs do not exhibit distinct differences in capillary pressure behavior. A gradual but continual rise in capillary pressure occurred in all samples from initial entry to about 20% wetting phase saturation, where pressure is greater and the curve is steeper.

Distributions of pore-throats (Fig. 5.87) and wetting phase saturation (Fig. 5.88) for samples with vugs are provided. Pore-throats range from 1-100 microns in this sample set. Samples with touching vugs have median pore-throats of 7.6-20.3 microns. Samples with separate vugs have median pore-throats of 3.1-26.1 microns. For the samples with vugs, 3 had pore volumes between 5-16%, and 12 had pore volumes less than 5 %.



**Figure 5.85. Thin section photomicrograph of dolomite with vugs. Blue is pore space. Plain light image.**

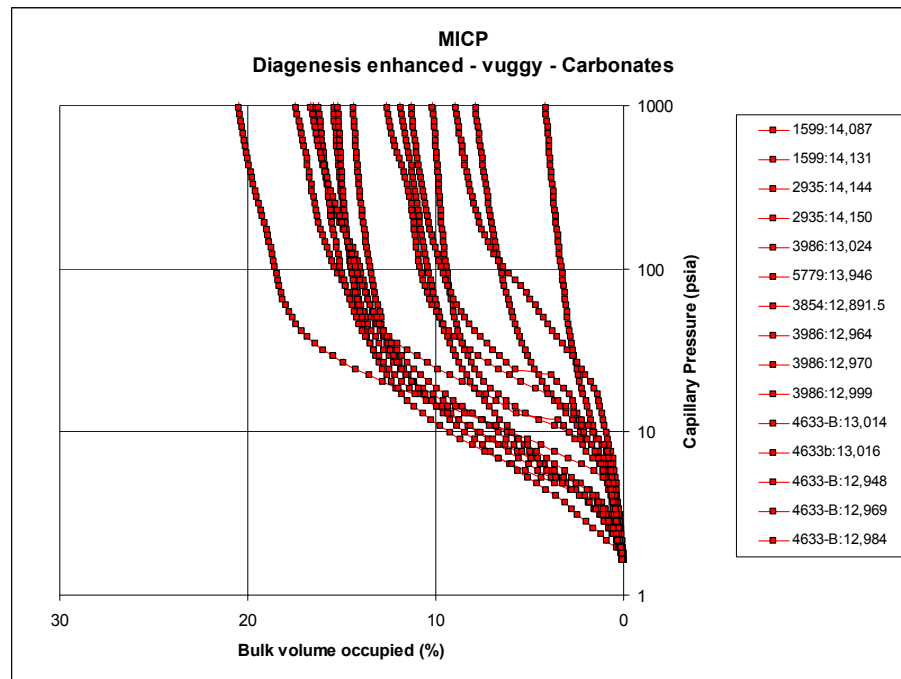


Figure 5.86. Capillary pressure curves for carbonates with vugs.

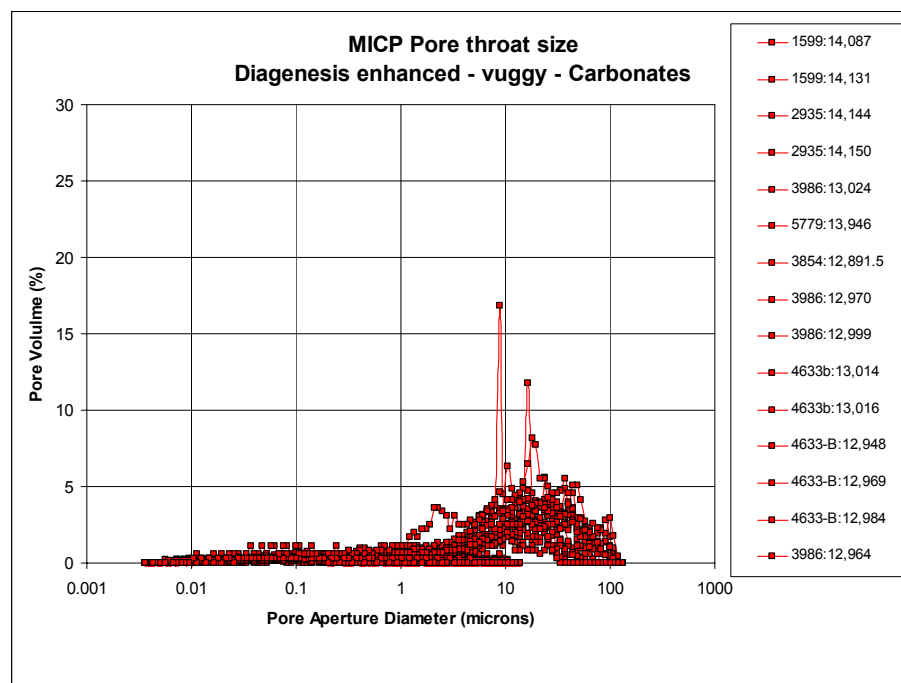
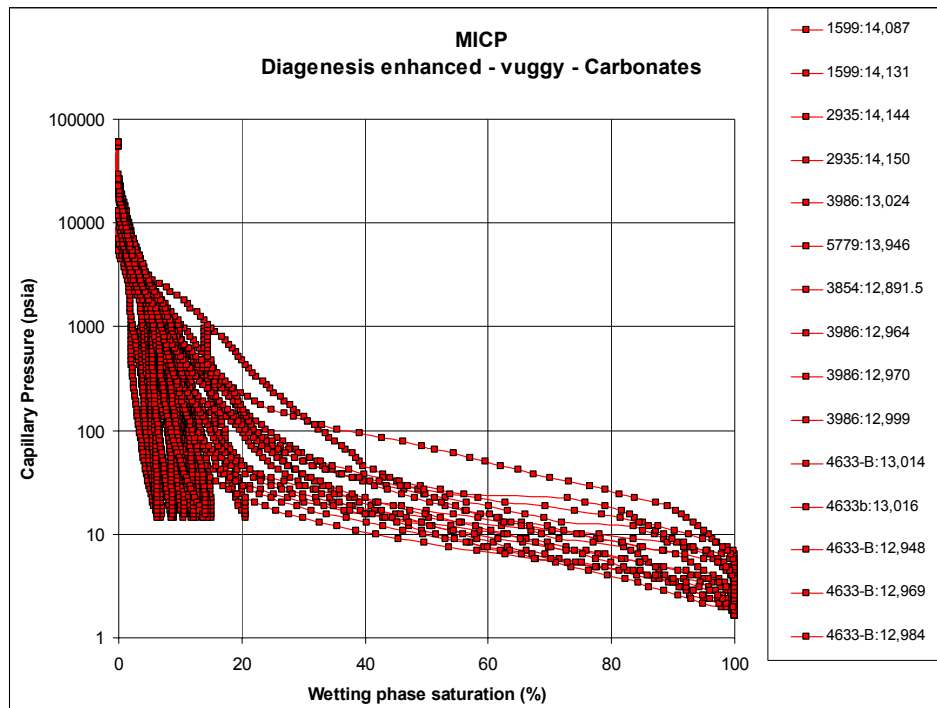


Figure 5.87. Distribution of pore-throat sizes in carbonates with vugs.

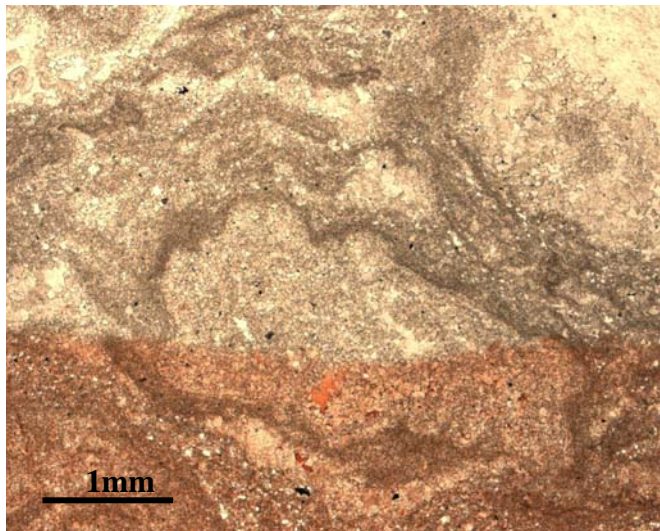


**Figure 5.88. Wetting phase saturation curves for carbonates with vugs.**



### *Cement-Reduced Pores*

Four of the 40 carbonate samples exhibit diagenetically-reduced porosity that resulted from cementation (Fig. 5.89). Capillary pressure measurements on these samples show high displacement pressures (670-4400 psi) with minimal intrusion of mercury into the pore space even at very high pressure (Fig. 5.90). Pore-throat sizes for these samples are very small (0.004-0.8 microns) and median values range from 0.01-0.5 microns from sample to sample (Fig. 5.91). Large volumes of the wetting phase fill pore space at very high pressure (Fig. 5.92). Pore-throat volume comprises 5-8% of the total pore volume in these samples.



**Figure 5.89.** Thin section photomicrograph of cement-reduced pores in carbonate. No visible porosity. Plain light image. Red area is stained calcite.

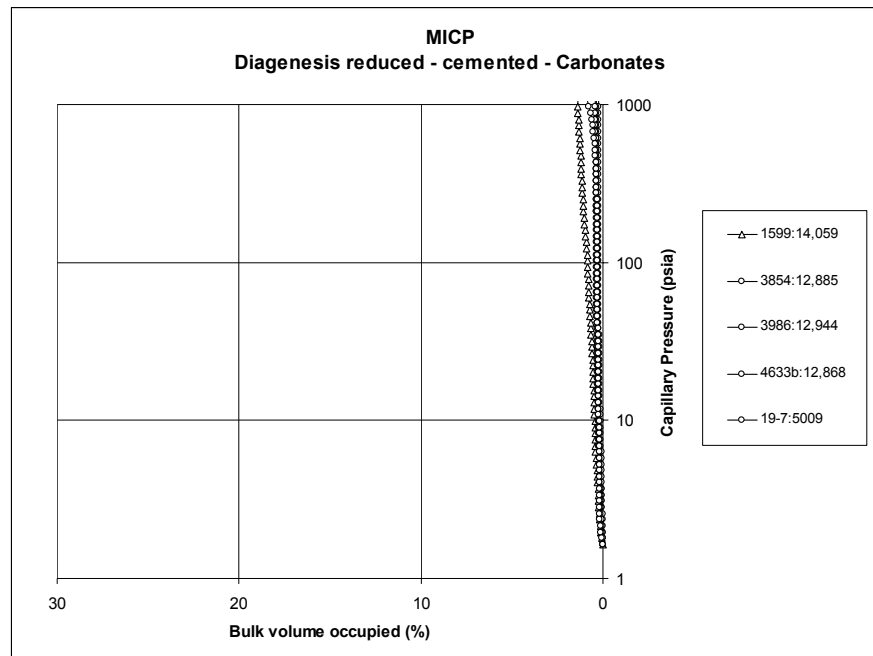


Figure 5.90. Capillary pressure curves for carbonates with cement-reduced pores.

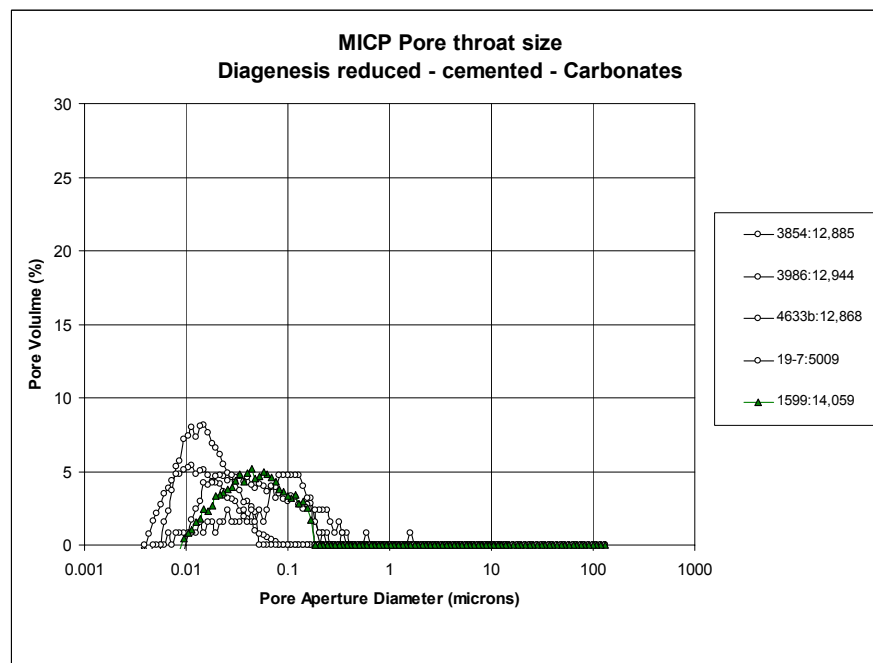


Figure 5.91. Distribution of pore-throat sizes in carbonates with cement-reduced pores.

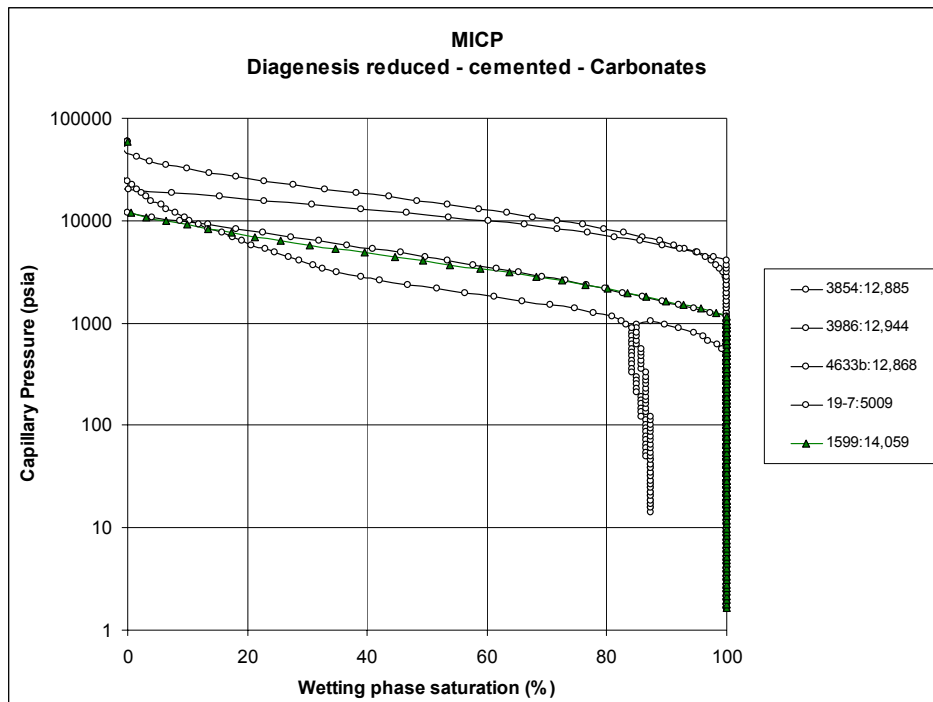


Figure 5.92. Wetting phase saturation curves for carbonates with cement-reduced pores.

### Summary of All MICP Results



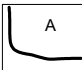
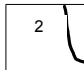
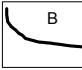


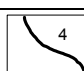
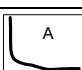

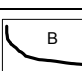
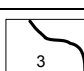
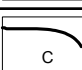

Mercury injection capillary pressure (MICP) measurements were used to determine pore-throat distributions for 40 carbonate core plugs (Figs. 5.93-5.95). Table 5.4 summarizes the capillary pressure measurements by pore type. Of the samples exhibiting depositional interparticle pores, estimates of pore-throat size from NMR synthetics (sandstones) and calculated median throat sizes (carbonates) were greater than 10 microns. The volume of pore space filled at low pressures in the sandstones was greater than in the carbonates. This difference is interpreted as an effect of cementation around individual ooids.

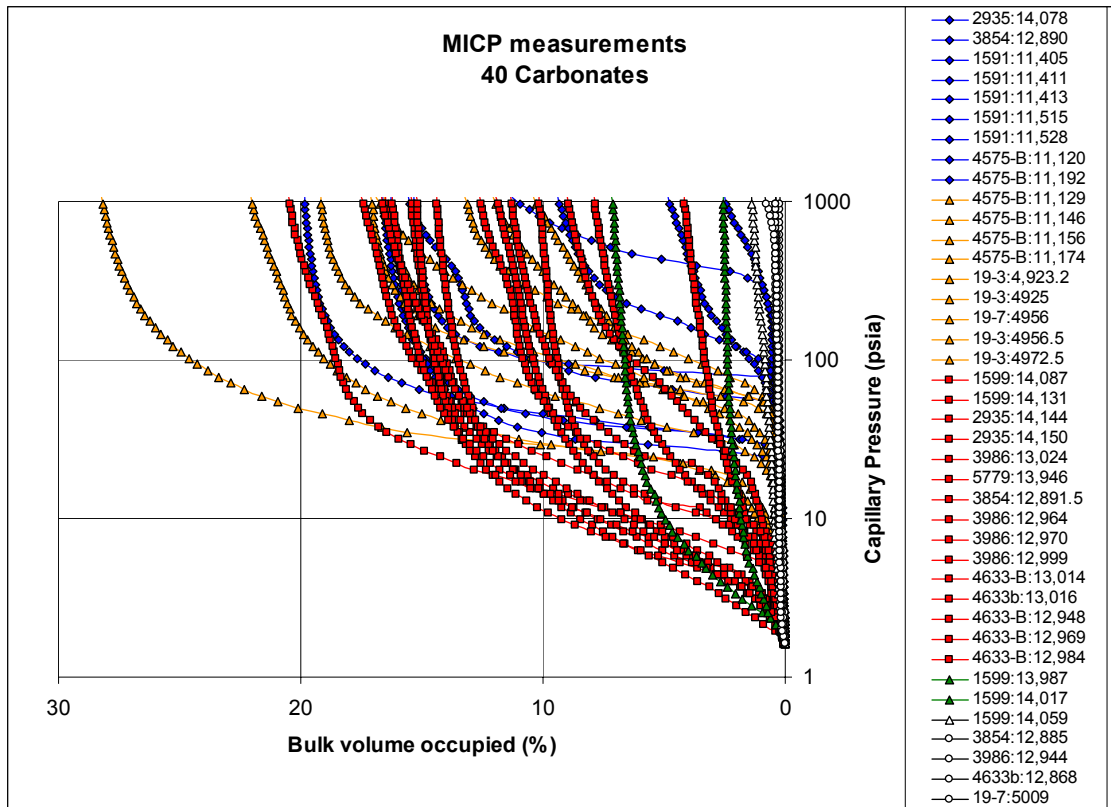
Samples with separate and touching vugs exhibited different capillary pressure behavior relative to other pore types. Lucia (1983) emphasized the importance of vugs in his field classification of porosity. He suggested that knowledge of the percent of touching and non-touching vugs could be used in combination with matrix porosity to estimate capillary pressure. Samples with touching vugs in this study had larger median throat sizes than those with separate vugs as indicated by greater volumes of pore space filled at lower pressures. Median pore-throat size and the range of pore-throat sizes within both vug types add new understanding to the size of the connections between the vugs themselves.

Samples exhibiting moldic and intercrystalline pores showed similar capillary pressure curves, with ooid molds filling considerably more pore volume at low pressure. Note that the samples with moldic pores generally had larger pore-throats than the samples with intercrystalline pores.

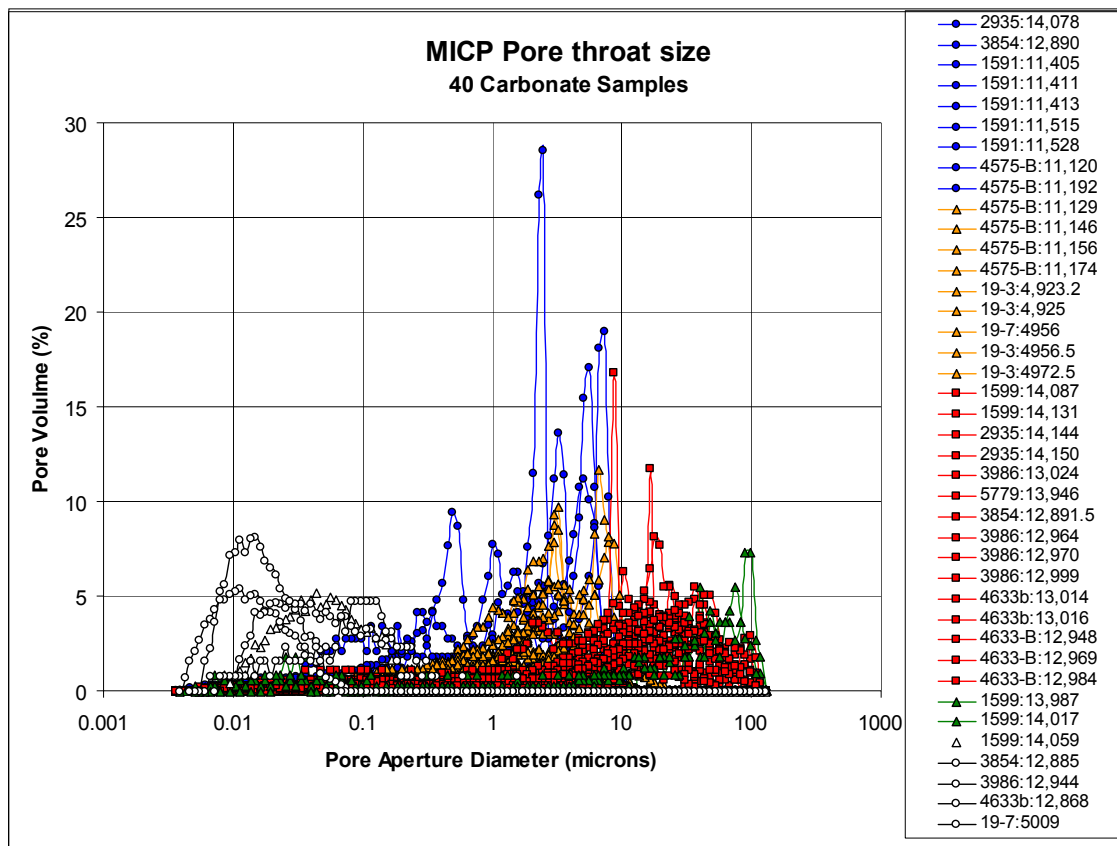
Samples with cement-reduced pores exhibited very low volumes of occupied pore space even at very high pressures.

**Table 5.4. Summary of MICP measurements for all rock types and pore types.**

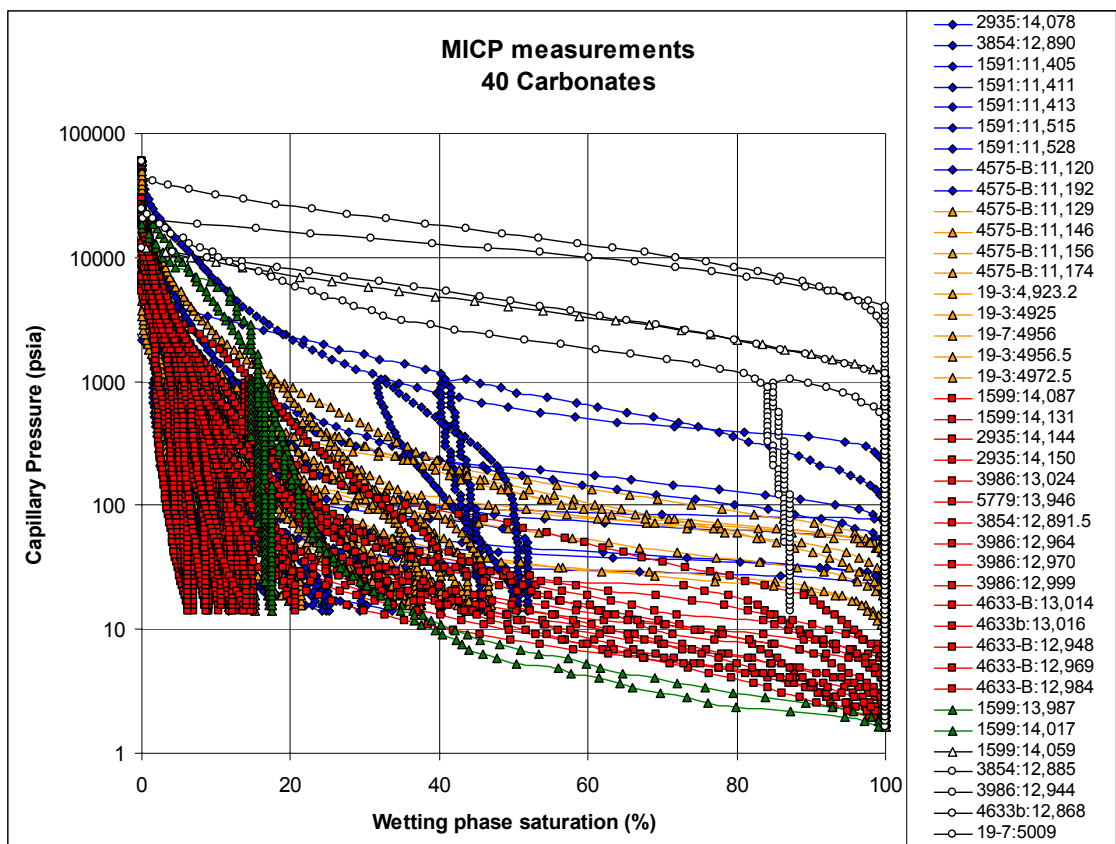
Pore Origin	Pore Type	Lithology	MICP					MICP wetting phase curve style	MICP pressure volume curve style
			Median Pore Aperture (microns)	Pore throats (microns)	Pore throat volume (%)	Entry Pressure (psi)			
Depositional	Interparticle	Sandstone	Not determined	Not Determined	Not Determined	Not Determined			
		Carbonate	30.0-40.0	10.0-100.0	< 7.0	1.6-1.8			
Hybrid 1	Moldic	Carbonate	1.3-6.2	0.1-10.0	< 10.0	10.0 - 50.0			
Diagenesis - enhanced	Touching vugs	Carbonate	7.6-20.3	1.0-100.0	< 5.0	2.0-8.0			
	Non-Touching Vugs	Carbonate	3.1-26.1	1.0-100.1	< 5.1	2.0-8.1			
	Intercrystalline	Carbonate	0.26-6.8	0.3-8.1	< 28.0	25.0-300.0			
Diagenesis - reduced	Cemented	Carbonate	0.01-0.05	0.004-0.8	< 8.0	670.0-4400.0			



**Figure 5.93. Summary diagram of capillary pressure behavior for 40 carbonate samples sorted by pore type. Green=carbonates with depositional pores. Orange=Hybrid I (moldic) pores. Blue=intercrystalline pores. Red = vuggy pores. White=cement-reduced pores.**



**Figure 5.94. Summary diagram of pore-throat distributions for 40 carbonate samples sorted by pore type. Green=carbonates with depositional pores. Orange=Hybrid I-b (moldic) pores. Blue=intercrystalline pores. Red = diagenetic vuggy pores. White= cement-reduced pores.**



**Figure 5.95. Summary diagram of wetting-phase saturation for 40 carbonate samples by pore type. Green=carbonates with depositional pores. Orange=Hybrid I-b (moldic) pores. Blue=intercrystalline pores. Red = vuggy pores. White=cement-reduced pores.**



## ELECTRON MICROPROBE

Sandstones*Depositional Pores*

Microprobe analysis was used to determine if particular pore types (or rocks) contained paramagnetic minerals that might affect assumptions used in NMR-derived pore size calculations. Of the 3 examined sandstone samples, all contained paramagnetic, framboidal pyrite. The pyrite was identified as an admixture with interstitial clays. In other several instances the framboidal pyrite was attached to the pore walls (Fig. 5.96).

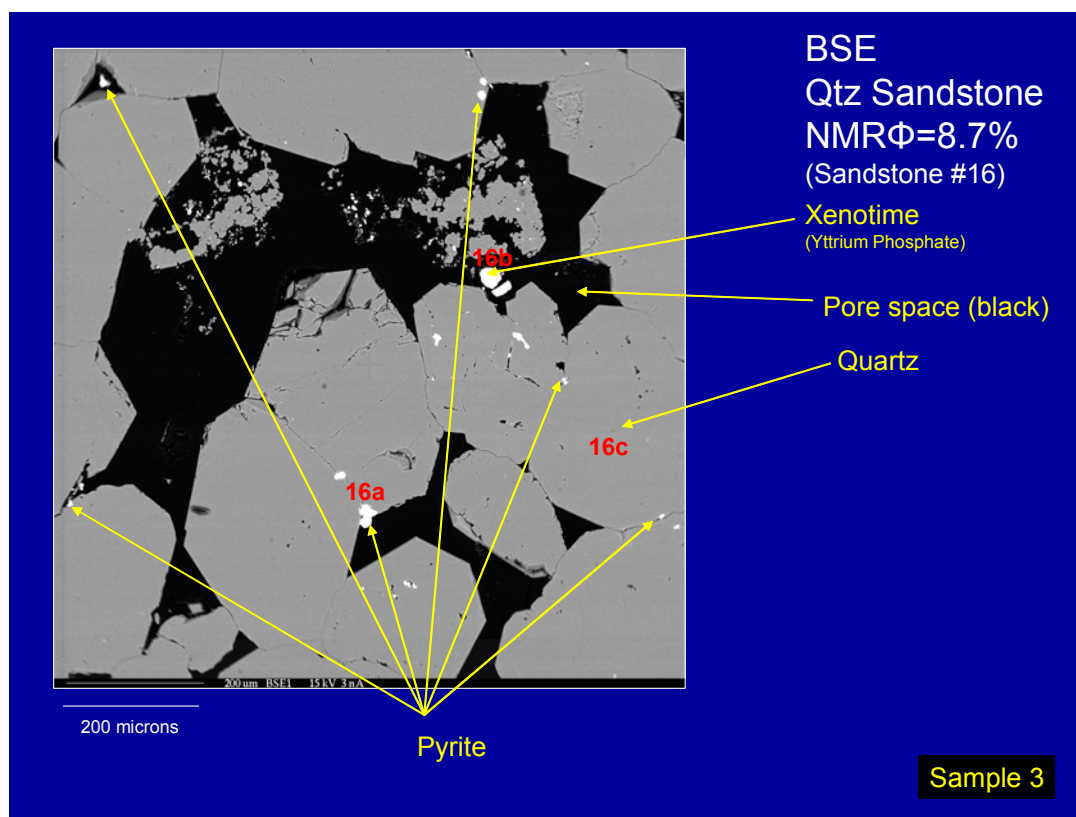
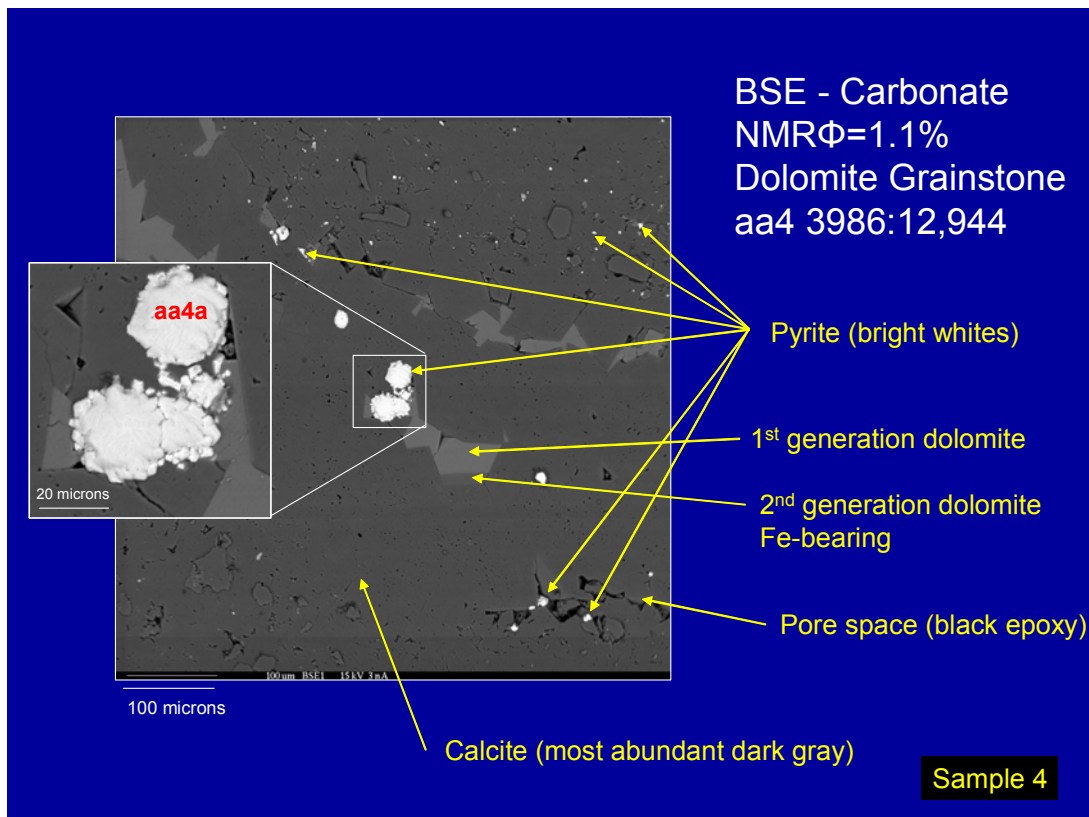


Figure 5.96. BSE image of framboidal pyrite on the interparticle pore walls of sandstone.

## Carbonates

### *Depositional and Hybrid 1-a Pores*

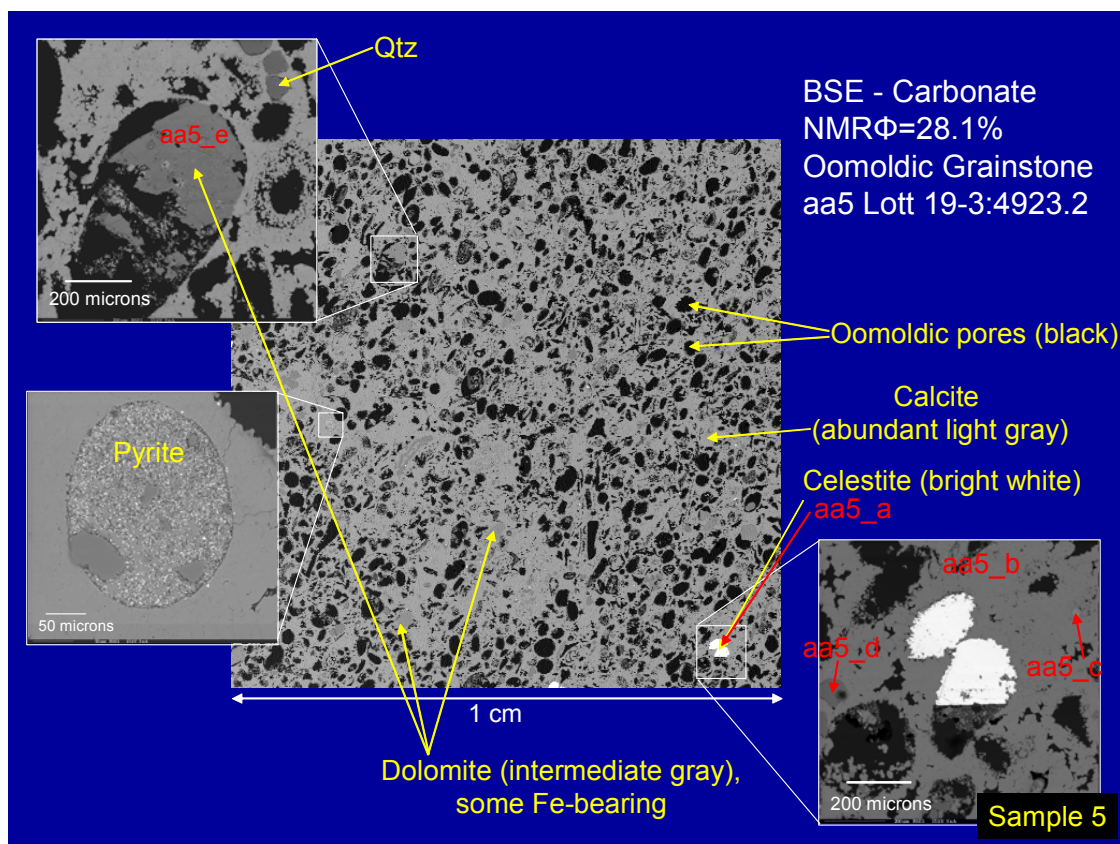
Carbonates with strong depositional attributes exhibited interparticle pore space, though altered by cementation. Of six examined carbonate samples, framboidal pyrite and ferroan dolomite were identified in pores of this type. Both of these minerals were found attached to the pore walls (Fig. 5.97).



**Figure 5.97.** BSE image of framboidal pyrite in carbonate pores exhibiting depositional attributes.

*Hybrid 1-b (moldic) Pores*

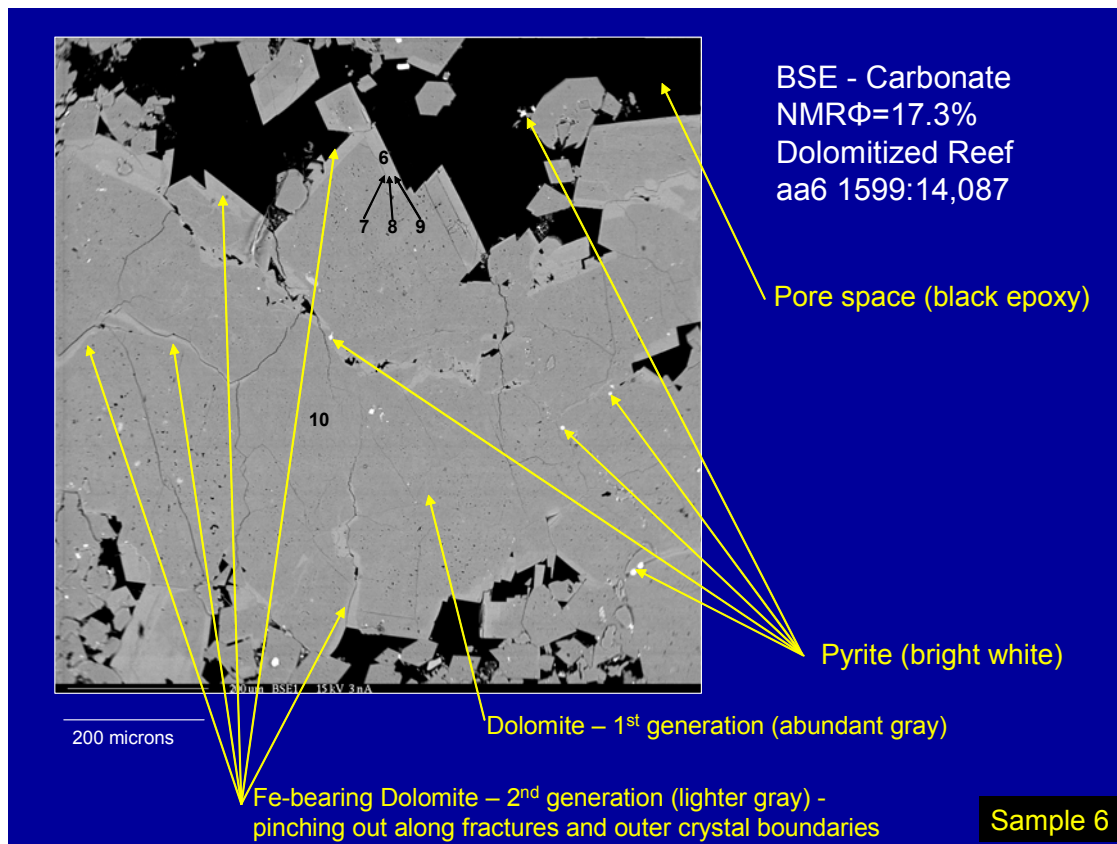
Of six carbonate samples, moldic pore space contained minor amounts of both pyrite and Fe-dolomite (Fig. 5.98).



**Figure 5.98.** BSE image of Hybrid 1-b (moldic) pores in carbonate.

*Vugs: Purely Diagenetic, Enhanced Porosity*

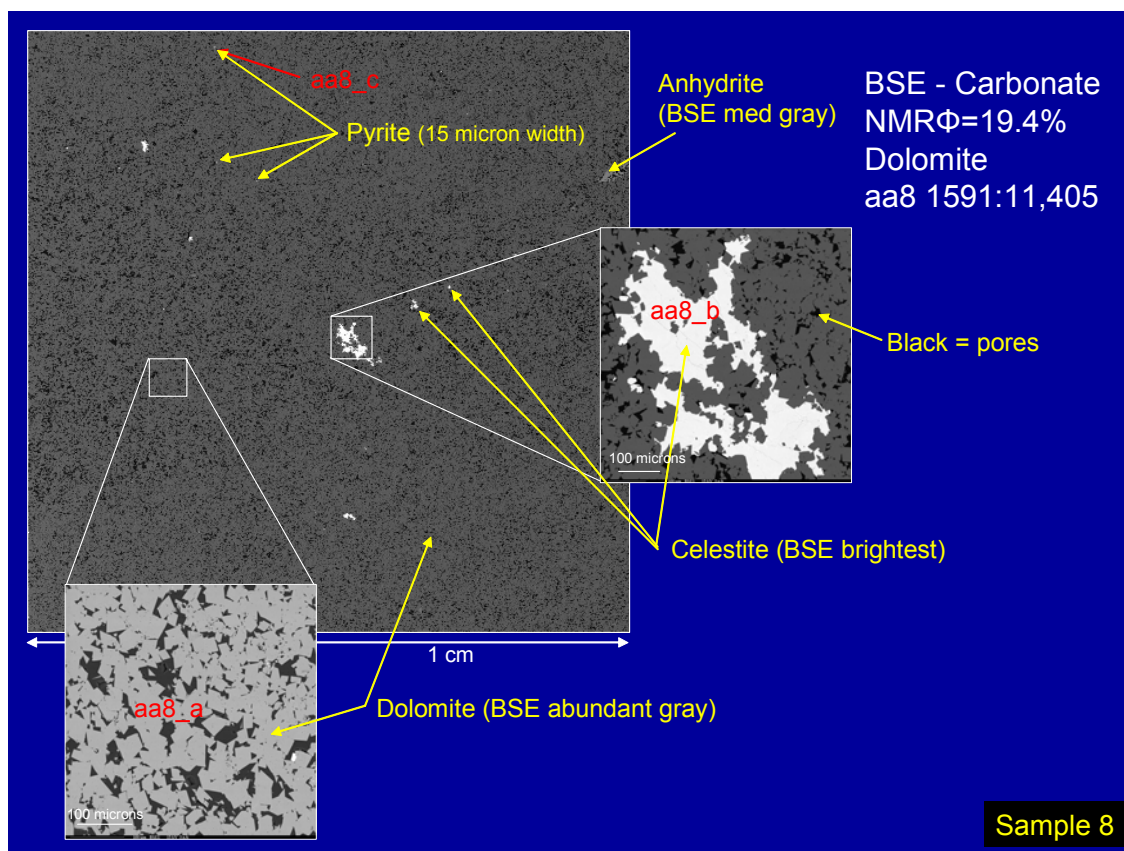
Ferroan dolomite is present in the samples that exhibited vuggy pores (Fig. 5.99). Pyrite was rare, but present along vug pore walls. Up to 60% of the pore walls in samples with vuggy porosity are lined with ferroan dolomite and the dolomite shows a higher concentration of Fe at pore walls than in crystal interiors (Appendix F).



**Figure 5.99.** BSE image of vugs in dolomite.

### *Diagenetic - Intercrystalline Pores*

Carbonate rocks with intercrystalline pores exhibited the lowest abundances of paramagnetic minerals. Pyrite was present in trace amounts only across the examined rock chip (Fig. 5.100).

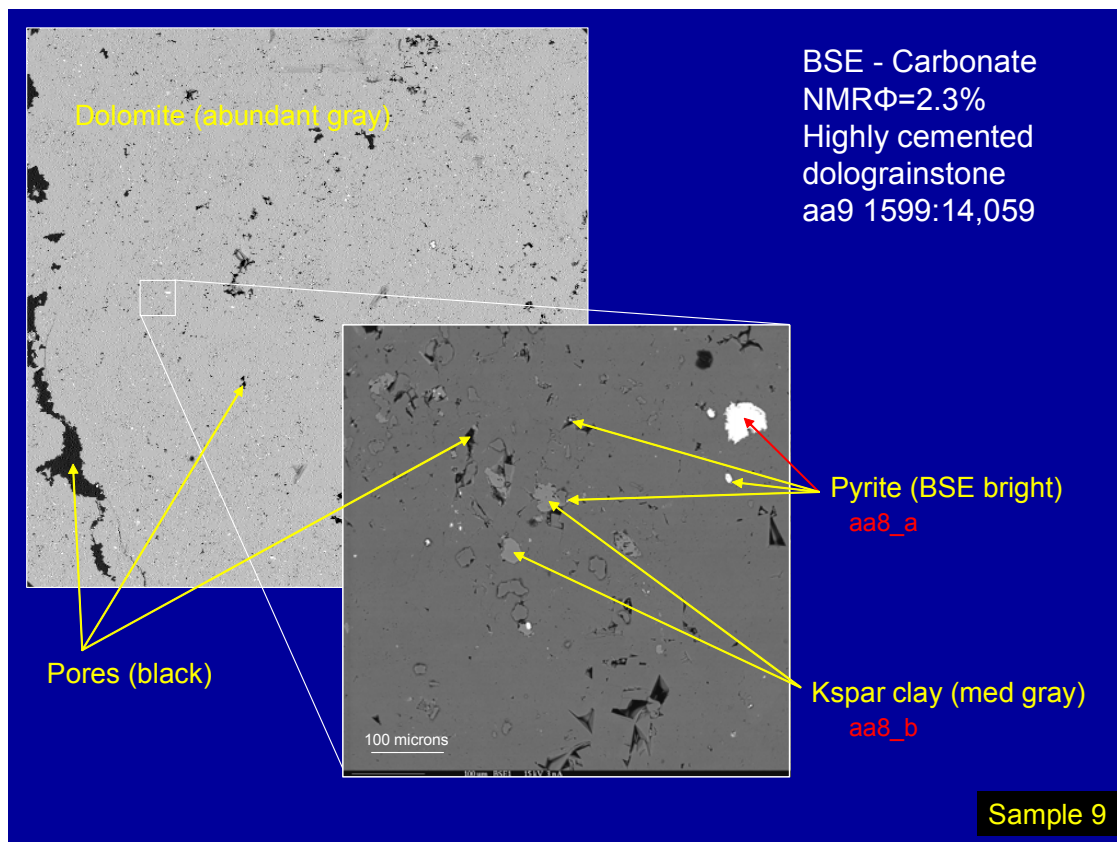


**Figure 5.100.** BSE image of fine-grained dolostone with intercrystalline pores.



### *Cement-Reduced Pores*

Carbonate rocks that contained pores reduced by cementation exhibited only trace amounts of pyrite (Fig. 5.101). Where present, the pyrite occurred in locations isolated from pore walls.



**Figure 5.101. BSE image of cement-reduced pores in dolomite.**

### Summary of Microprobe Analyses

Microprobe analysis was used to identify the composition and distribution of paramagnetic minerals (Table 5.5). X-ray maps and quantitative data on mineral composition were collected and show the location of iron-bearing minerals relative to pore walls in ferroan dolomite (Appendix F).

The search for paramagnetic minerals using the scanning electron microprobe revealed that framboidal pyrite is present in all of the sandstones either as isolated mineral clusters or admixed with clay. Both pyrite and ferroan dolomite are present in the carbonates to differing degrees. Iron-bearing minerals tend to be more abundant in samples with vuggy pore types than in all others. This is particularly true of ferroan dolomite, where iron is highly concentrated along 60% of the pore perimeter. In other pore types, these minerals do not line pore perimeters but occur at the corners of the pores. Because paramagnetic minerals interfere with NMR measurements by increasing T2 relaxation times, the pore volumes calculated from T2 relaxation times were too low in all instances. NMR-derived pore sizes were perhaps as much as 3 orders of magnitude too low in the vuggy dolostones. Exact corrections for the iron are beyond the scope of this study. Carbonates with hybrid 1-a pores exhibited rare paramagnetic minerals that are generally located away from pore walls, and do not significantly effect the NMR pore size calculation.

**Table 5.5. Summary of microprobe measurements and distribution of paramagnetic minerals by pore type.**

Summary of SEM measurements and observations								
Pore Origin	Pore Type	Lithology	Paramagnetic Minerals					
			Type(s) of Paramagnetic Minerals	Location of Paramagnetic Minerals	% coverage of 2-D area (image analysis)	% coverage of pore perimeter (if measurable)	expected effect on NMR T2 value	likely underestimate of NMR pore sizes
Depositional	Interparticle	Sandstone	framboidal pyrite	in clays and <b>often at pore wall contacts</b>	trace	N/A	minor accelerated relaxation time	<1 order mag
					trace	N/A		
		Carbonate	framboidal pyrite and Fe-dolomite	some pore wall contacts, and away from pore walls	0.5	N/A	negligible	<1 order mag
					trace	N/A		
Hybrid 1	Moldic	Carbonate	Fe-dolomite	within pores	2.5	N/A	minor accelerated relaxation time	<1 order mag
Diagenesis - enhanced	Vugs	Carbonate	Fe-dolomite	<b>pore wall contacts</b>	N/A	< 60	accelerated relaxation time	<b>&gt;1 order mag</b>
	Intercrystalline	Carbonate	framboidal pyrite	away from pore walls	trace	N/A	negligible	<1 order mag
Diagenesis - reduced	Cemented	Carbonate	framboidal pyrite	away from pore walls	0.5	N/A	minor accelerated relaxation time	<1 order mag



## HOW PORE SIZES COMPARE BETWEEN METHODS

Pore size determined from NMR response, PIA, and pore-throat sizes determined from capillary pressure measurements are compared in Figures 5.102-5.107. These six samples each exhibit distinct pore types. Note that all data are plotted on a common length scale and include: 1) a pore size curve estimated from T2 relaxation times using Timur's (1972) assumptions about pore geometry and surface relaxation effects, 2) an identically shaped alternative curve that does consider the affect of iron on T2 relaxation time, 3) the distribution of all pore-throats for the sample including the median throat size, 4) the average sizes of small, medium, and large pores as measured using PIA.

The graphs show the relative proximity of pore-throat size to pore size measured in 2-D and pore size calculated from T2 relaxation times. In 5 of 6 samples including depositional, moldic, or intercrystalline pores, Timur's (1972) assumptions were within one order of magnitude of the proposed pore size curve. However, pore size based on T2 relaxation times was underestimated by 3 orders of magnitude in ferroan dolomite exhibiting vugs. The true size of the large vugs was independently verified in thin section.

The broadest ranges of pore-throat sizes occurred in samples with vugs. Samples exhibiting depositional and moldic pores exhibited the most uniform pore-throat sizes. Pore-throats in rocks with vugs were calculated to be even larger than some pores measured in thin section. This is interpreted to be a 3-D effect because what appeared to be a pore-throat in 2-D may have actually been a view of the pore body in 3-D.

Pore shape as measured in 2-D is useful in discriminating pores originating from depositional, diagenetic, and hybrid geologic processes. Spheres are the best proxy in determining pore sizes from T2 relaxation times, and are particularly representative of samples with ooid molds, and to a lesser extent in depositional interparticle pores.

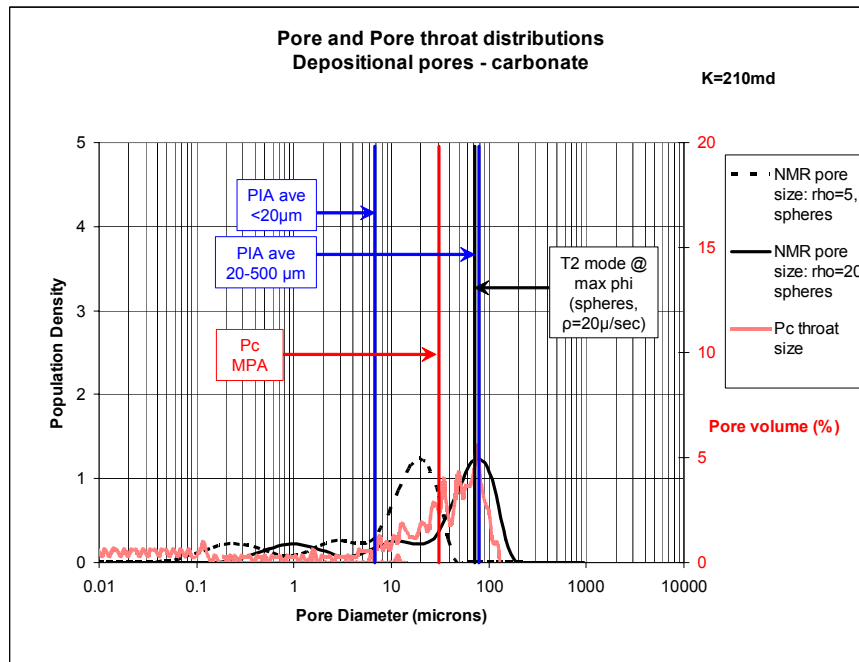


Figure 5.102. Pore size comparison for carbonate samples exhibiting pores with depositional attributes.

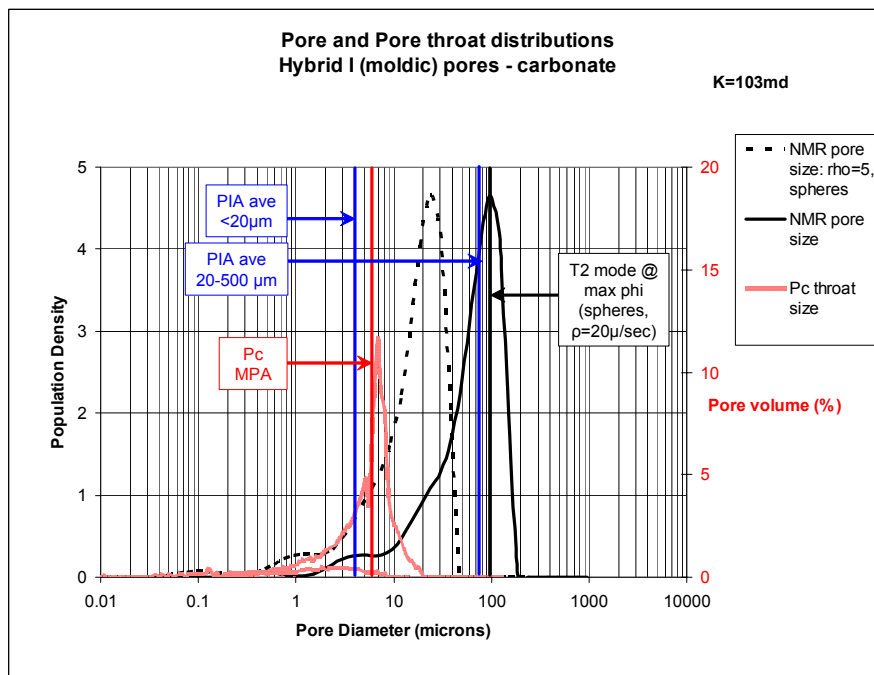


Figure 5.103. Pore size comparison for carbonate samples with moldic pores.

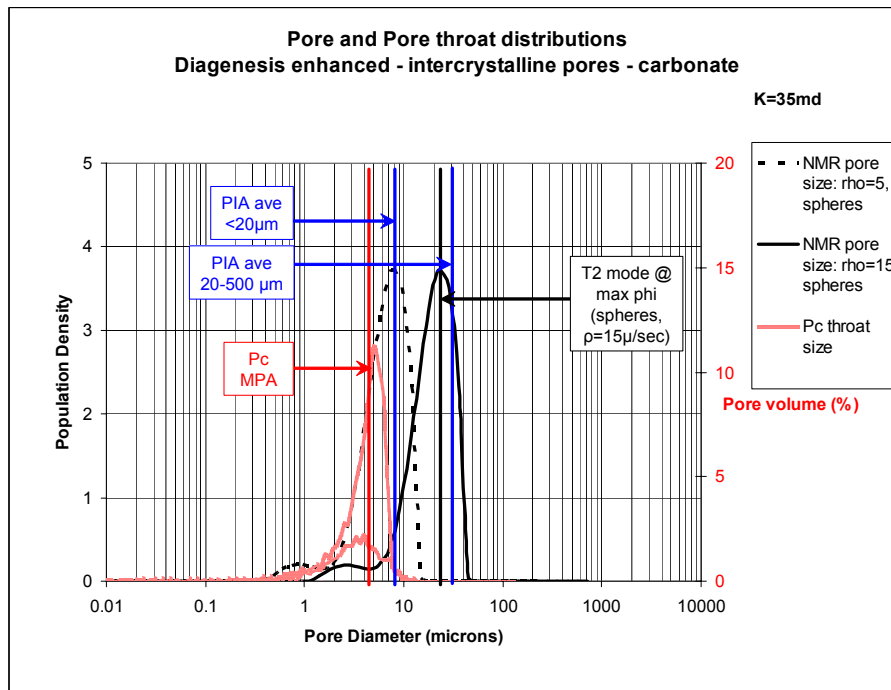


Figure 5.104. Pore size comparison for intercrystalline pores in carbonates.

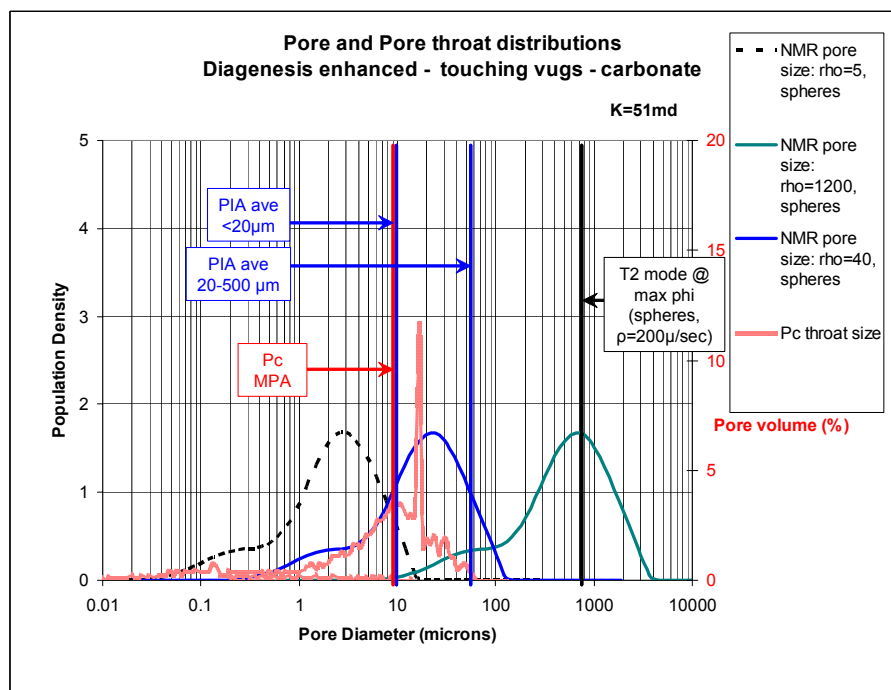


Figure 5.105. Pore size comparison for carbonates with touching vugs.

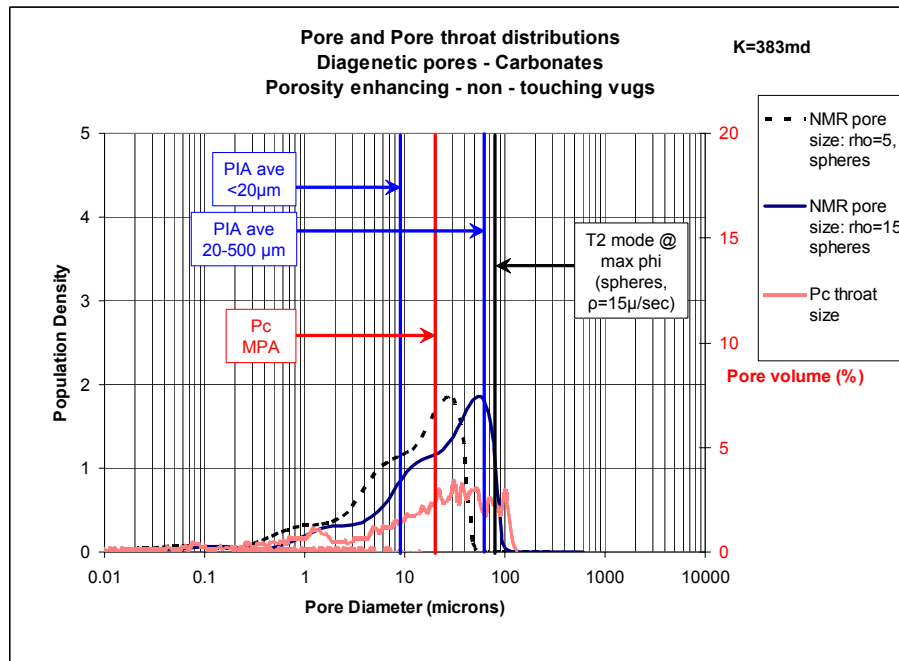


Figure 5.106. Pore size comparison for carbonates with non-touching vugs.

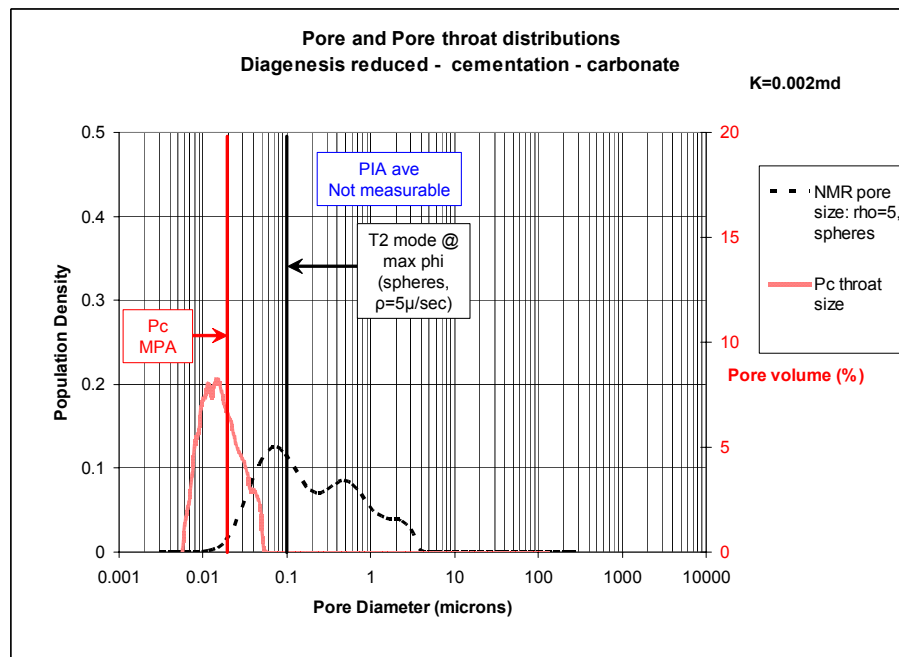


Figure 5.107. Pore size comparison for carbonates with cement-reduced pores.

## CHAPTER VI

### DISCUSSION AND INTERPRETATION

Shape templates were measured as test objects with PIA (Chapter IV) and compared to pore geometry in thin sections. PIA distinguished between depositional, diagenetic, and hybrid pores on the basis of pore sizes and shapes. Pore geometry was found to correlate strongly with pore origin. PIA measurements were useful in estimating measured core analysis values of porosity particularly on rocks with depositional pores. Diagenetic (vuggy) and hybrid 1-b (moldic) pores underestimated measured core analysis porosity by approximately 7 and 15%, respectively. Other diagenetic pore types such as intercrystalline and cemented pores were difficult to measure with PIA because of their small sizes and such measurements showed little or no direct relationship between 2-D and 3-D porosity. The value of PIA to estimate 3-D from 2-D porosity in carbonate core plugs decreased in relation to the degree and type of diagenetic alteration. Pore origin was a useful indicator in grouping and comparing the relative precision of 2-D and 3-D porosity measurements, however.

NMR T2 curves were converted into pore size distributions, and compared to distributions of pore size as measured in 2-D using PIA. Distributions of small (<0.02mm), medium (0.02-0.5mm), and large (>0.5mm) pores showed that medium pores were the most useful in discriminating pore geometry in depositional, hybrid, and intercrystalline pores; the larger pore sizes were most useful in samples with vugs. Estimates of T2 relaxation times for small, medium, and large pores were shown to

agree with sizes obtained by PIA and are of key importance in relating pore origin to the T2 relaxation curves.

Capillary pressure curves, both measured and synthetic, exhibited similar shapes when samples on which measurements had been made were grouped by pore origin. Pore-throat sizes in all samples with depositional, moldic, intercrystalline, and vuggy pores exhibited distinctive characteristics, as did cement-reduced pores. MICP-measured median pore-throat sizes were found to cluster in a narrow size range when grouped by pore origin. Samples with depositional intergranular pores had the largest median throat apertures, and the greatest volumes of pore space filled at low pressure. Cement-reduced pores had very small pore-throats and minimal pore space was filled even at high pressure. Samples with moldic, intercrystalline, and vuggy pores exhibited intermediate volumes of pore space occupied by non-wetting phase. Individual differences in curve shapes reflect diagenetic and hybrid processes that affected the pore-throat system. Elements of the pore-throat system identified by Wardlaw (1976) such as pore-to-throat ratio, accessibility, and coordination number are discussed later.

NMR measurements were found useful for identifying flow units. Paramagnetic minerals such as iron must be considered when calculating a pore size distribution from T2 relaxation data or inferring pore origin. Samples with high porosity and companion values of high permeability contained depositional intergranular pores with narrow T2 relaxation curves. Samples with cement-reduced pores had low measured porosity and companion values of low permeability. These samples had T2 relaxation curves that were asymmetrically shaped, with abundant small pores detected by NMR but too small

to resolve in thin section. Samples exhibiting diagenetic pores had high, low, and intermediate paired values of porosity and permeability depending on pore type. T2 relaxation curves and knowledge of pore types are combined into a model which ranks reservoir quality on the basis of permeability. The types of T2 curves with poor, intermediate, and best reservoir quality are then used to generate a hypothetical NMR logging signature. The concept of mapping flow units in carbonates (at field scale) using the NMR log is a potential cost-effective alternative to special core analysis.

## PIA, PORE GEOMETRY, AND THEIR RELATIONSHIP TO THE GENETIC CLASSIFICATION OF POROSITY

### Purely Depositional and Hybrid 1-a Pores

Sandstones and carbonates with depositional pores, those formed by detrital sedimentation, were found to have the comparatively simple and geometrically-similar pore geometry. Samples with these types of pores can be used as shape standards with which the other pore types can be compared. Near-equant, triangular pores typically have aspect ratios of 1.8 (unitless) illustrating that they are rarely elongate, particularly in the sandstones. Detrital sedimentation is a key factor in creating the most reproducible pore geometry in interparticle pore space, particularly in middle sized (0.02-0.5mm) pores. Pore geometry measurements in the interparticle pores of carbonates generally mimic the sandstones, but the data are not as tightly clustered together. This is because some carbonate pore space, though exhibiting strong depositional interparticle attributes (hybrid 1-a pores), are slightly altered by cementation around grains which may not be



uniform in shape. In these cases pore geometry is changed to include some elongate, square-like, or otherwise different interparticle pore geometry than is exhibited in interparticle sands. Note however that depositional interparticle pore geometry measurements are more alike between sandstones and carbonates than with any other pore type (Fig. 6.1).

#### Hybrid I-b (Moldic) Pores

Moldic pores are the result of depositional and diagenetic processes; typically, the dissolution of allochems. Where ooids were the common framework grains, original grain shape exhibited more rounded, and in turn spherical shapes than the purely detrital depositional pores. Moldic pore geometry was found to be similar to standard, depositional pore shapes because perfect circular ooid molds and near-perfect triangular pores in the sandstones have similar roundness values as calculated by the imaging software. Skeletal grain molds accounted for even higher variability in aspect and roundness relative to the standard pore shapes. They differed in having either greater or lesser roundness and greater or lesser aspect values than the depositional pores (Fig. 6.1). Pore geometry was therefore not as uniform in samples with hybrid 1-b (moldic) pores as in the samples with purely depositional intergranular pores.

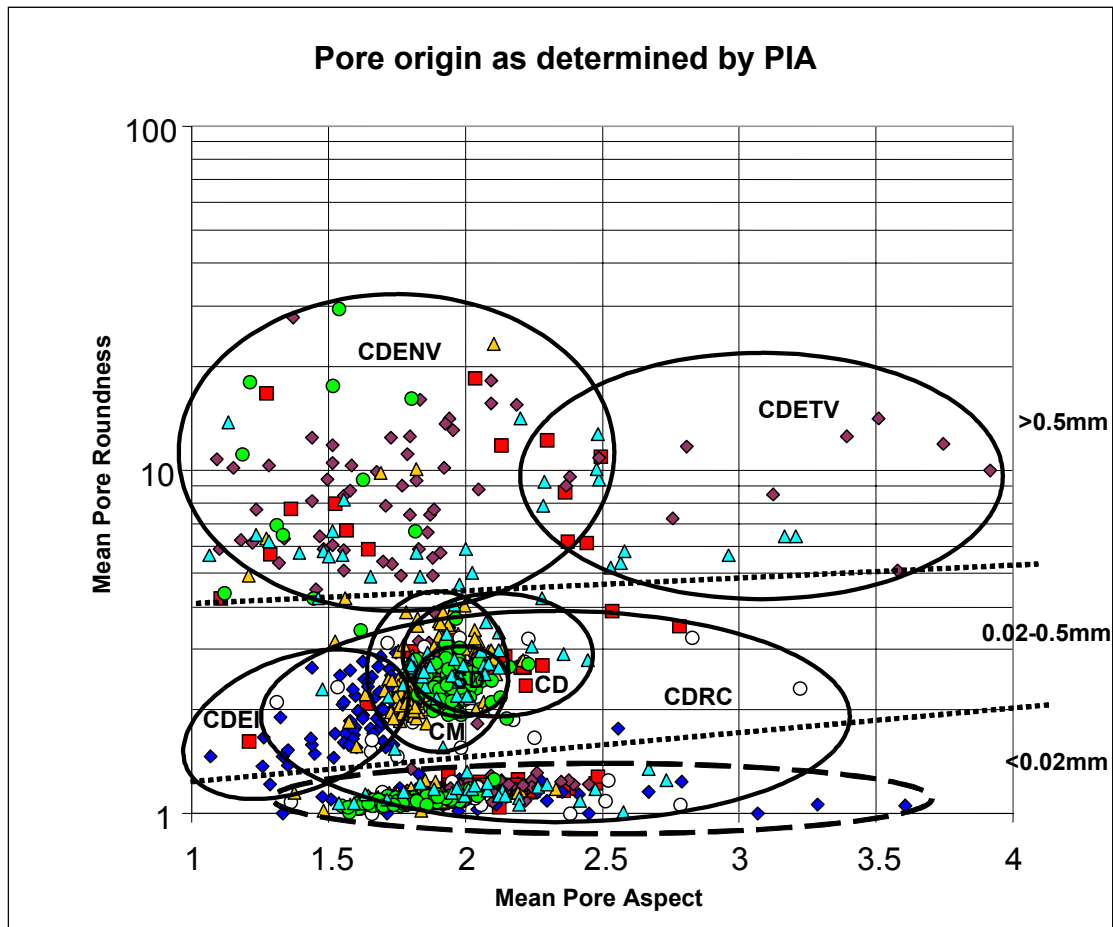
#### Intercrystalline Pores

Geometry of diagenetic pores is, in general, distinct from that of standard, depositional-intergranular pores. For example, intercrystalline pores in dolostones

exhibit the lowest aspect and roundness values of all examined pore types.

Dolomitization is interpreted to have been important in the formation of pores shapes (i.e. equant examples) in the idealized geometrical models illustrated in Chapter IV.

Wardlaw (1976) observed that dolomitization was related to progressive changes of pore geometry in resin pore casts of dolostone. Polyhedral pores (star-like geometrical models) were altered to tetrahedral shapes (triangular-like geometrical models). This shape evolution occurred as the number of crystal faces was reduced from 5 to 3 during dolomitization. Further dolomite crystal growth resulted in compromise crystal boundaries with triple junctions creating more equant, tetrahedral pore shapes. In many pore casts, Wardlaw (1976) found that the tetrahedral pores became sheet like as dolomitization progressed. This geometry in the small (<0.02mm) pores is interpreted to be similar to the sheet-like shape observed by Wardlaw (1976). The more equant shapes in dolostones with medium pores indicate that the dolomitization process was effective in creating equant pore geometry; even more so than depositional processes. As a result, pore geometry in dolomitized rocks is distinguishable in both medium and small pores (Figs. 6.1-6.2).



**Figure. 6.1.** PIA measured pore geometry for pores of different origin. Each data point is the average pore aspect and average pore roundness measured for 100's of pores of a given size class, within a single petrographic field of view. SD = sandstone depositional pore. CD = carbonate depositional pores. CM = carbonate moldic pores. CDEI = intercrystalline pores. CDENV = non-touching vugs. CDETV = touching vugs. CDRC = cement-reduced pores.

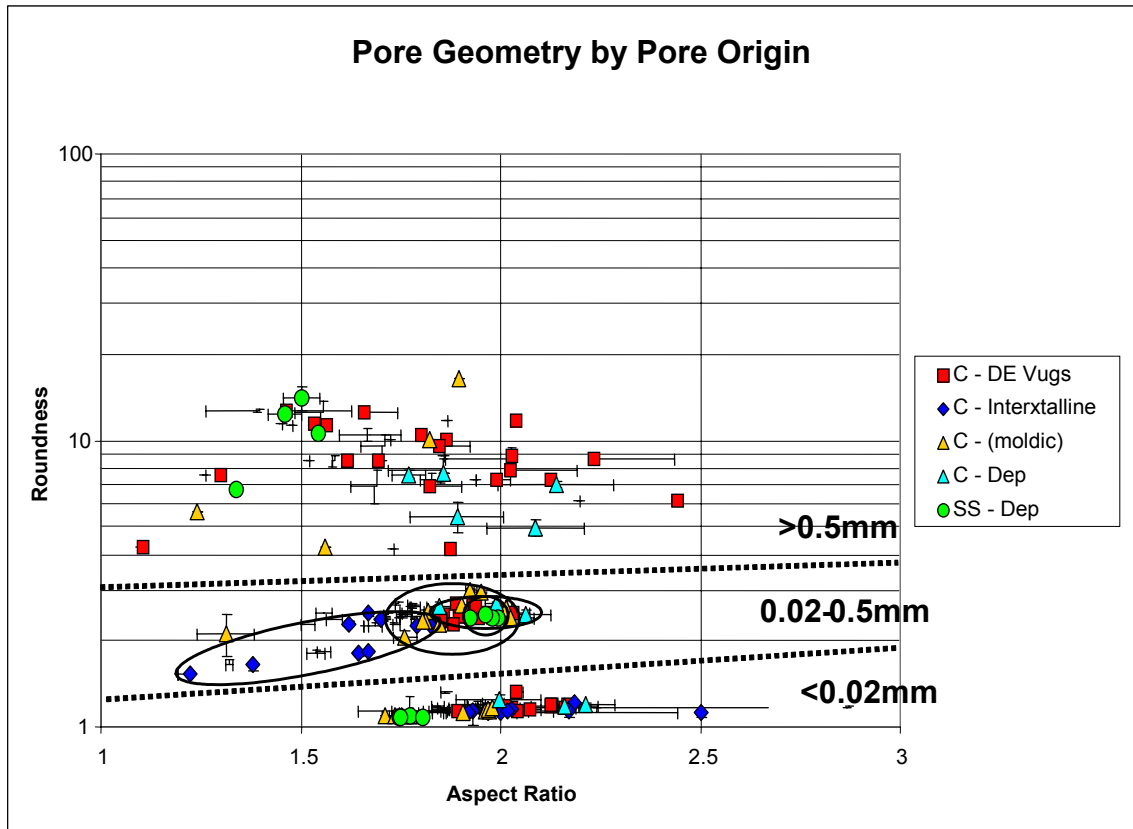


Figure. 6.2. Similarity in pore geometry for pores of different origin. Each data point represents the average roundness and aspect ratios for all examined pores within a given thin section. 95% confidence intervals shown.

### Vugs: Purely Diagenetic, Enhanced Porosity

Both separate and touching vugs were present in the studied samples. Because vugs are larger ( $>0.5\text{mm}$ ) than other pores, they are readily identifiable with PIA. Touching vugs were differentiated from non-touching vugs by their higher aspect ratios. Occasional dissolved volcanic grains in sandstones and a few moldic pores in carbonates also exhibited high roundness values in large pores. Large vuggy pores were found to be 3 times less round than the standard, medium sized depositional pores.

The roundness values in vugs suggest that dissolution diagenesis typically produces non-round shapes. This is observed in thin section as pores with many angular pore corners and akin to the stars on the shape template (Chapter 4). Dissolution processes in dolostones do not create pores with simple circular, triangular, or square-like pore geometry. The dissolution process (vug and mold creation, volcanic grain dissolution) is a key factor which complicates pore geometry, especially in large pores, regardless of rock type.

### Cement-Reduced Pores

Cement-filled pores exhibit a wide scatter of geometrical measurements. Cements occur as isopachous rims, syntaxial overgrowths, radial fibers, at grain contacts or as pendulums in the vadose zone, as isolated patchworks, etc. Cementation alters size and pore geometry in all cases. Measurements of pore geometry in samples with cement-reduced pores did not show clusters or groups of measured values, probably because pores reduced by cementation seldom retained their original shapes.

Cementation did not preserve pore shapes as pore sizes were concurrently reduced. Rather, cemented pores showed a wide variety of aspect and roundness values across all three pore size groups.

#### Relation to the Genetic Classification of Porosity

An objective of this study was to investigate the degree to which pore geometry and pore origin may be linked. Based on the results of this study, PIA pore geometry measurements are interpreted as successful discriminators of pore origin using Ahr's genetic classification of porosity within discrete pore size classes (Fig. 6.3).

In medium sized pores (0.02-0.5mm), the depositional pores exhibited greatest similarity to one another – and distinct from both Hybrid I and diagenetic types of pores. Diagenetic pores were most easily distinguished by a combination of pore size and pore shape. In pores >0.5mm it was observed that depositional, hybrid, and enlarged diagenetic pores may overlap in pore geometry. Thin sections had to be viewed to discriminate the origins and lithology containing the largest pores. Pore geometry was a useful tool to discriminate different forms of diagenetic enhanced pores (vugs) in some thin sections – differentiating touching from non-touching forms by greater aspects.

In summary, 2-D measurements of pore geometry may be used to distinguish carbonate pore types of depositional, diagenetic, and hybrid origins. Roundness values are the key measurements needed discriminate pore origin in 2-D images in medium sized pores. Aspect ratios are useful in differentiating touching from non-touching vugs in large pores.

## COMPARISON OF POROSITY MEASURED BY PIA AND CORE ANALYSIS

Another objective of this study was to evaluate the reliability of 2-D PIA measurements as indicators of 3-D porosity in different pore types. Several workers have made such comparisons but with varying degrees of success (Etris et al., 1988; Kenyon et al., 1989; Mowers and Budd, 1996; Anselmetti et al., 1998; Wiltkowski, 2000; Layman, 2002). In this study, 2-D PIA measurements were the most reliable indicators of 3-D porosity inferred from NMR measurements on sandstone samples with depositional, intergranular pores.

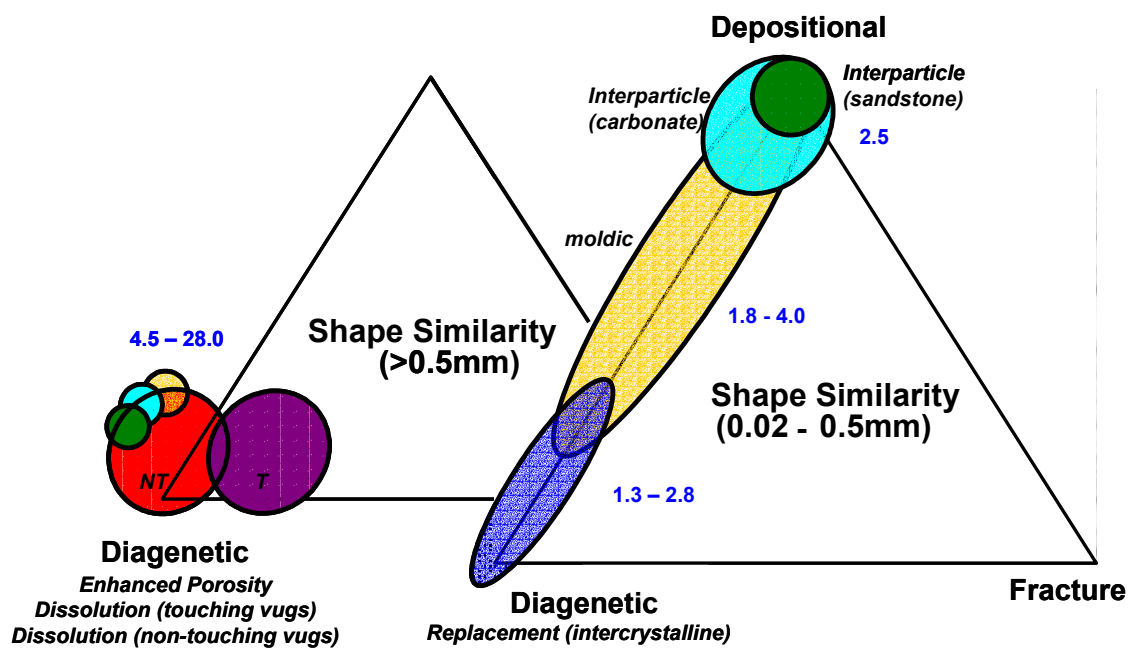


Figure 6.3. Relationship of pore geometry to genetic pore types within specific size classes. Each color indicates a pore type derived from a specific genetic origin. Overlapping colors indicate similarity in measurements of pore geometry. Two triangles are shown to illustrate patterns of pore geometry by size class. Blue numbers are roundness values.

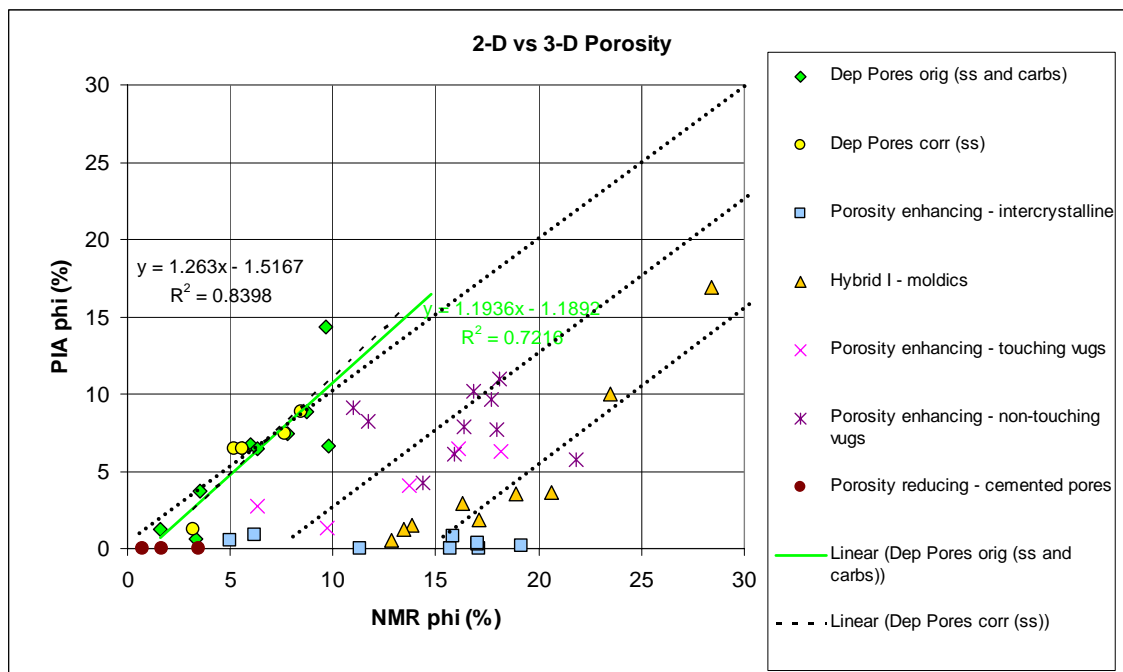
Recent work by Kong et al. (2005) explains how such a transform from 2-D to 3-D space is accomplished. They developed a mathematical model to relate spherical objects from 2-D to 3-D and vice versa. Non-spherical objects are more complicated and are more difficult to image in 2-D views.

The correspondence between 2-D and 3-D calculations of porosity was notably decreased from depositional, intergranular sandstone and carbonate pores to carbonates commonly exhibiting hybrid 1-a pores (altered pores with strong depositional attributes). Other carbonate depositional pores such as fenestral, shelter, keystone, and reef-related pores were not common in the samples used in this study. A general decrease in the correspondence of 2-D and 3-D porosity is observed in diagenetic and hybrid pores (Fig. 6.4). This decrease occurs because skelmoldic and vuggy pores have more complex pore geometry than detrital interparticle pores when measured in 2-D.

Mowers and Budd (1996) found that PIA underestimated 3-D porosity values by 3-7% in dolomites from Kansas and Wyoming (Table 6.1; Fig. 6.5). Measurements of pore shape would be a helpful addition in differentiating which pore types were most and least useful in finding correlation of porosity, sizes, and shapes of pores across 2-D and 3-D space.



The results of this study highlight the obstacles to establishing correspondence between 3-D porosity and 2-D measurements. Pore origin is linked to pore geometry; and pore origin can be best identified in the 0.02-0.5mm, or medium-sized pores. In the case of small (<0.02mm) pores, either cement reduced or otherwise diagenetic, PIA did not reliably demonstrate a relationship between 2-D and 3-D-measured porosity. The small pores were simply below the reliable resolving power of the method.

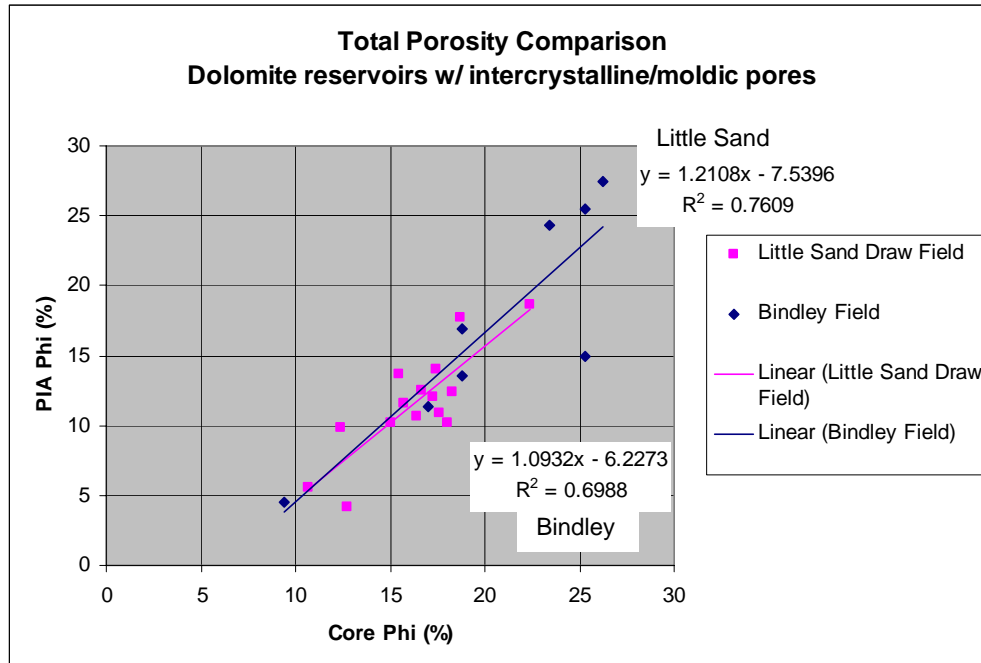


**Figure 6.4. 2-D vs 3-D porosity by pore origin. Data points are averaged values of PIA porosity for a given thin section. Data grouped by common pore origin. Note that sandstones and carbonate samples with depositional attributes are grouped together (green). Sandstone NMR porosity values calibrated from core porosity are shown by yellow circles. Dotted lines are ‘eyeball’ approximations only.**

**Table 6.1. Comparison of 2-D and 3-D porosity as measured in dolomite reservoirs from Kansas and Wyoming. Data taken from Mowers and Budd, 1996.**

Well	Depth (ft)	Core Plug ; PIA	
		Phi (%)	Phi (%)
<b>Little Sand Draw Field</b>			
Nelson 30	6108.7	18	10.2
Nelson 30	6109.9	18.7	17.7
Nelson 30	6116.8	15.7	11.6
Nelson 30	6125.6	17.3	12
Nelson 30	6133.1	22.4	18.7
Nelson 14	6188.1	16.7	12.5
Nelson 14	6191.1	17.4	14
Nelson 14	6196.2	15.5	13.7
Nelson 14	6199.0	12.4	9.8
Nelson 14	6201.8	17.6	10.9
Nelson 14	6204.9	18.3	12.4
Nelson 14	6208.0	16.4	10.7
Nelson 14	6209.4	15	10.2
Nelson 14	6227.3	12.7	4.2
Nelson 14	6235.0	10.7	5.6

Well	Depth (ft)	Core Plug ; PIA	
		Phi (%)	Phi (%)
<b>Bindley Field</b>			
Bindley 3	4605.2	18.8	13.6
Deutsch 1	4627.7	25.3	25.5
Deutsch 1	4635.4	18.8	16.9
Deutsch 5	4664.1	17	11.3
Smith 1	4659.1	9.4	4.5
Deutsch 3	4657.1	23.4	24.3
Deutsch 3	4665.9	25.3	14.9
Deutsch 6	4655.5	26.2	27.5
Deutsch 3	4683.0		1.5
Walter 1	4684.2		14



**Figure 6.5. Comparisons of core and PIA measurements of porosity in dolomite reservoirs. Chart derived from Table 6.1, after Mowers and Budd, 1996. Unit line reference shows that PIA underestimates 3-D values by 3-7%, but does not discriminate pore types.**

## RELATIONSHIPS BETWEEN PORE SIZES AS DETERMINED BY PIA AND NMR

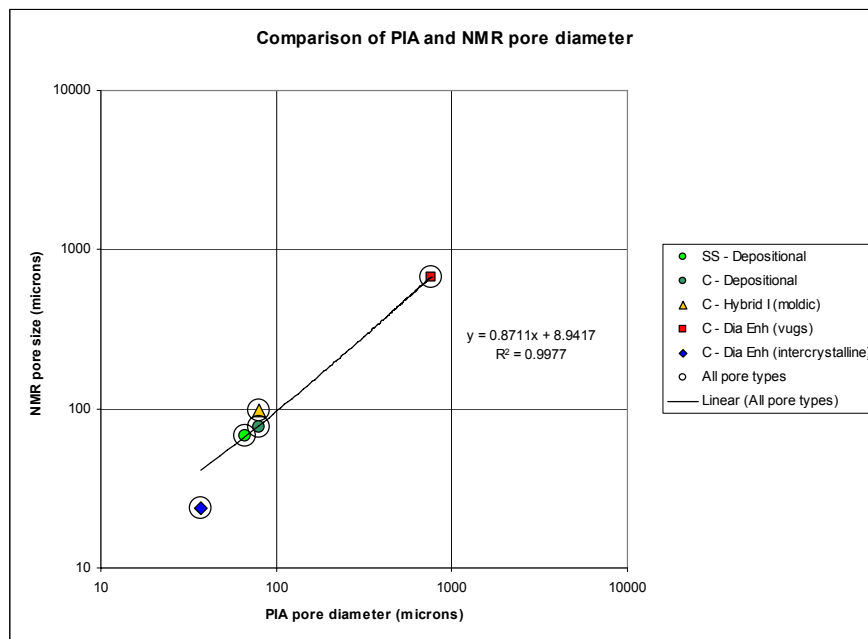
Pore size distributions measured by PIA and NMR compared best when small, medium, and large pore sizes were treated separately (Table 6.2). Cumulative distribution functions of PIA pore diameter (electronic files) showed that medium PIA pore sizes were most indicative of NMR pore diameter in depositional pores. Medium-sized pores of Hybrid I-b (moldic) origin underestimated NMR pore diameter by about 20 microns, but was a better comparison than using either the small or the large pores.

Diagenetic pores were more difficult to correlate across techniques than depositional pores. Middle-sized intercrystalline pores had narrow, symmetric T2 distributions, but average pore sizes varied from rock to rock reflecting differences in how dolomite crystal size (and associated pores) changed between samples. Diagenetic pores (vugs) rocks often showed bimodal or tri-modal pore size distributions from NMR. Likewise, pores measured by PIA showed a substantial presence of large pores in frequency histograms of pore size. Pore diameter measurements in rocks exhibiting vugs compared best by when the large pore size group was used.

Figure 6.6 shows the good correlation between PIA and NMR pore diameter measurements; considering both medium and large pore sizes according to pore origin.

**Table 6.2. Summary table of pore sizes as determined by PIA and NMR techniques.**

Summary Comparison of Pore and Pore Throat size								
Pore Origin	Pore Type	Lithology		Pore Diameter (microns)			MPA Diameter (microns)	
				PIA Pore Size (from PIA CDF)				NMR Pore Size at peak amplitude
				<0.02	0.02-0.5	>0.5		
Depositional	Interparticle	Sandstone	Ave	10.4	66.6	641.8	69.6	Not available
			SD	5.1	56.3	117.1		
	Interparticle	Carbonate	Ave	8.7	79.4	811.8	76.4	30.0
			SD	4.9	80.8	28.5		
Hybrid 1	Moldic	Carbonate	Ave	10.4	79.5	554.9	97.2	6.2
			SD	5.2	64.7	48.3		
Diagenesis - enhanced	Vugs	Carbonate	Ave	10.8	65.8	763.1	672.6	20.3
			SD	5.1	67.4	236.4		
	Intercrystalline	Carbonate	Ave	9.6	36.9	none	23.7	4.6
			SD	4.7	21.9	none		
Diagenesis - reduced	Cemented	Carbonate	Ave	none	none	none	0.1	0.02
			SD	none	none	none		



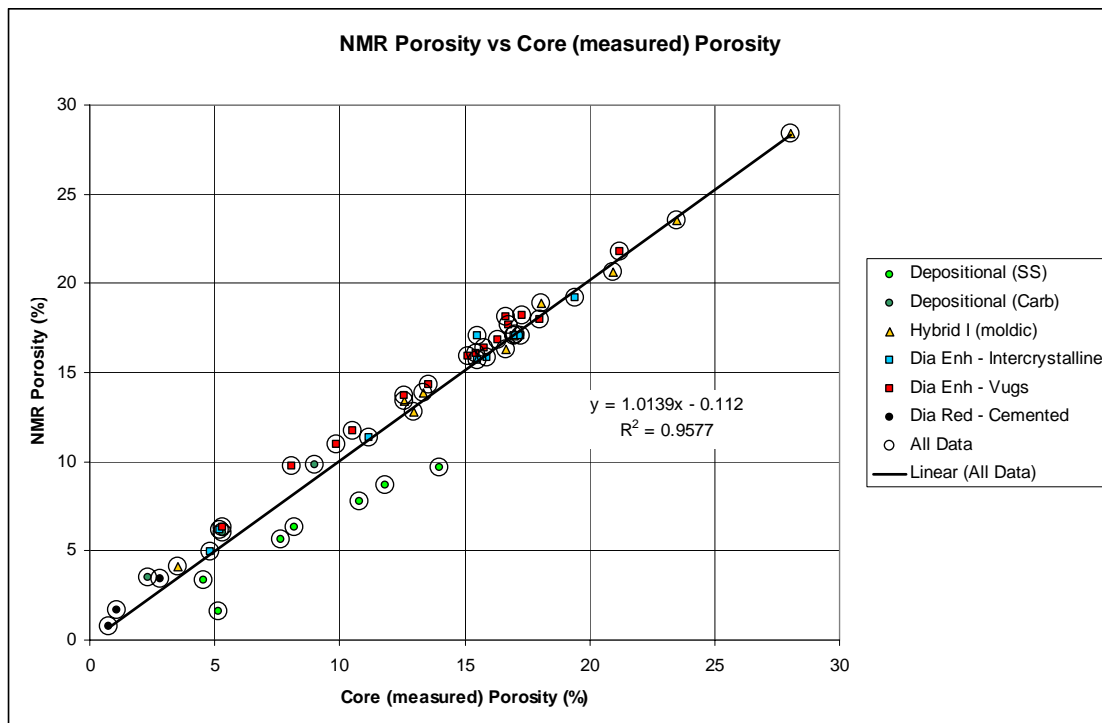
**Figure 6.6. Comparison of medium and large pore diameter as determined from PIA and T2 relaxation times.**

## RELATIONSHIPS BETWEEN POROSITY, PERMEABILITY, PORE SIZE AND PORE-THROAT SIZE

Once pore types were identified, linked to their genetic origin, and size distributions reasonably matched between techniques, petrophysical properties of the pore types were investigated to determine relationships between porosity, permeability, and pore types by incorporating MICP measurements. Given the expense of MICP testing, it is beneficial to relate MICP measurements to petrophysical responses from less expensive sources such as NMR and thin sections.

### Porosity and Pore Types

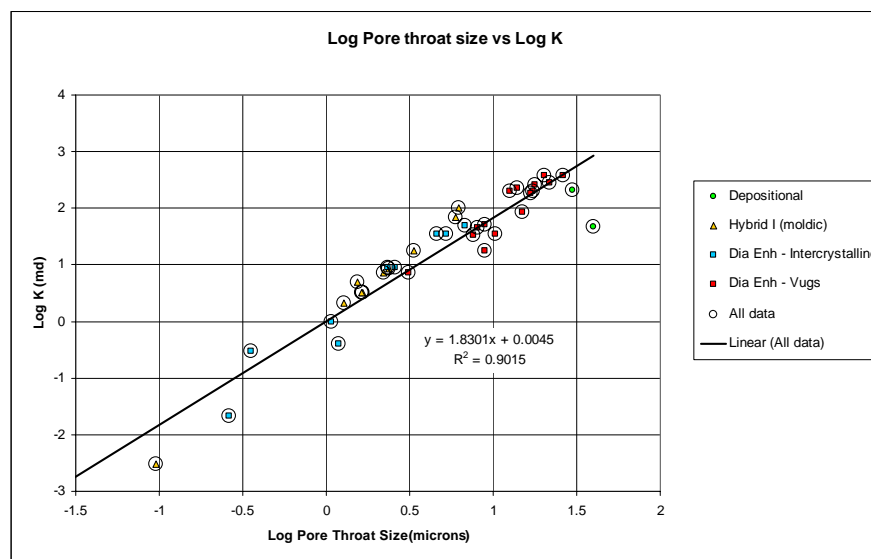
NMR measurements of porosity correlate very strongly ( $R^2=0.95$ ) with porosity measured by core analyses across all rock types (Fig. 6.7). This was not surprising because porosity is determined from T2 relaxation times and is essentially unaffected by lithology (Coates et al., 1999). Sandstones exhibited the poorest fit to the regression line. This may be due to several reasons including: 1) the friable nature of some sandstone samples which affected the pore volumes and bulk volumes used in estimating core plug porosity, 2) helium measurements were only available for the carbonate samples, 3) rapid relaxation times in samples with clay cannot be adequately resolved by the NMR spectrometer, and 4) there may be procedural or proprietary differences used in different labs when measuring T2 relaxation times.



**Figure 6.7. Comparison of NMR and core analysis porosity values by pore type. Helium was used to obtain the core porosity values in the carbonates only. Estimates of core porosity in the sandstones were determined by bulk measurements of pore volume and sample volume.**

### Permeability and Median Throat Diameter

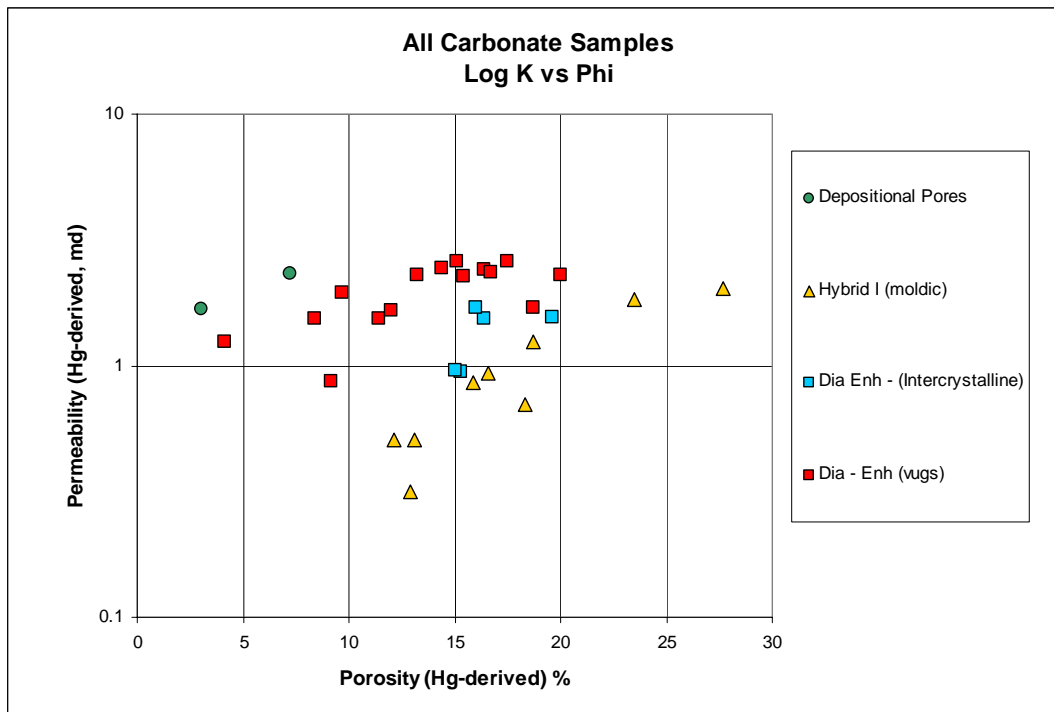
The correlation between median pore aperture (MPA) and permeability (Fig. 6.8) is strong ( $R^2=0.90$ ). This correlation suggests that pore aperture is directly linked to permeability. Krumbein and Monk (1943) have shown that permeability varies with the square of average grain diameter by weight in sand samples with non-uniform sorting. Beard and Weyl (1973) examined eight grain size and six sorting groups which, although difficult to uniformly pack, also agreed well with permeability values computed by the Krumbein and Monk formula. The carbonate samples exhibiting pores with strong depositional attributes (where original grain textures are best preserved) and samples with vugs have larger pore apertures and correspondingly higher permeability values. The relationship between pore-throat size and permeability has a slope of 1.8, approaching the theoretical value of 2 by earlier workers. Pore origin therefore has a significant influence on permeability.



**Figure 6.8.** Comparison of median pore-throat size and permeability by pore type.

### Core Analysis Porosity and Permeability

Figure 6.9 shows the relationship between core analysis porosity and permeability in 40 carbonate samples. Note the clear separation of the data when grouped by pore type. High permeability is best estimated from core porosity where samples exhibit depositional intergranular pores or touching vugs. Low permeability is better estimated from porosity where moldic (particularly skeletal molds) are common. Intermediate permeability may be estimated from porosity where either separate vugs, intercrystalline, or moldic pores are common.

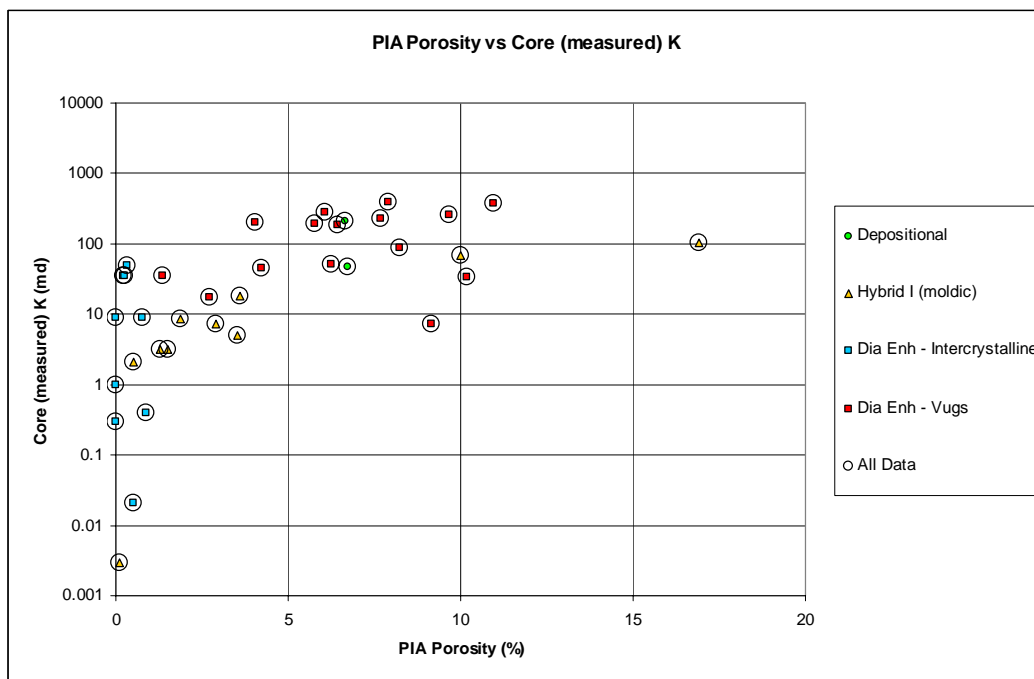


**Figure 6.9.** Comparison of core porosity and permeability in 40 carbonates.



### PIA Porosity and Permeability

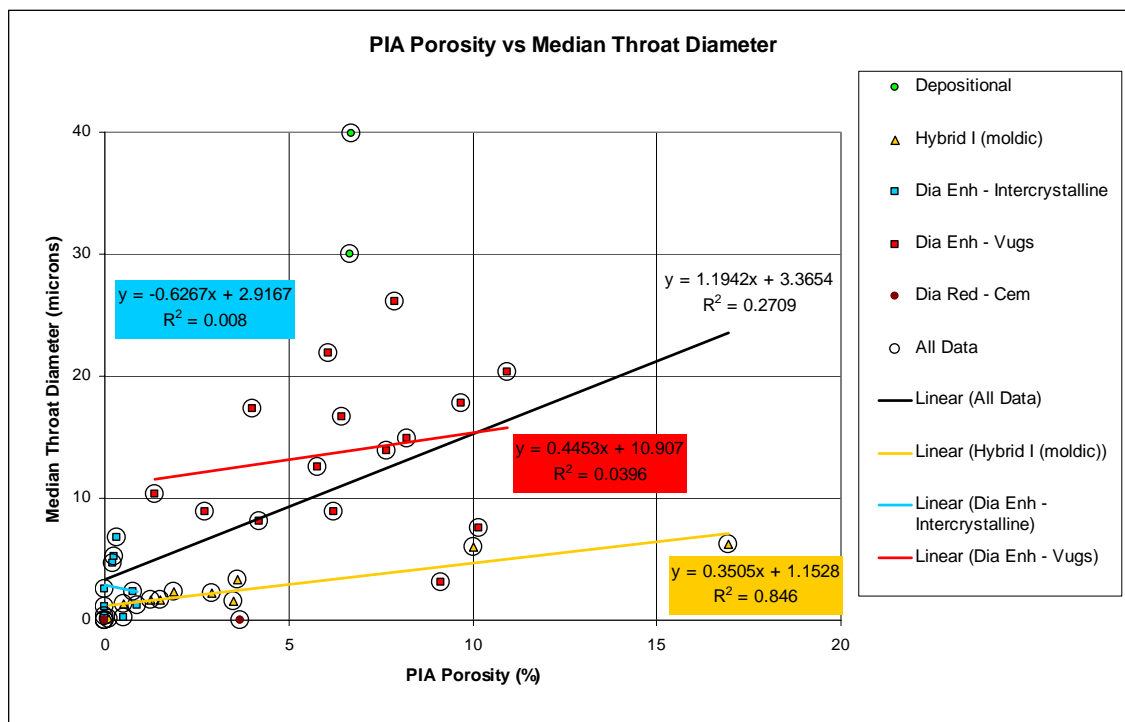
Where special core analysis is not available, geologists and engineers routinely estimate permeability from measured porosity or from calculated values from log measurements. This must be done with caution as conventional porosity logs do not make a distinction between pores of different origin, and perhaps with the exception of interparticle depositional textures, are not useful to distinguish pore types in carbonates (Chapter I; Statement of Problem). Figure 6.10 illustrates the relationship between PIA measured porosity and measured permeability. All pore types except intercrystalline pores show a positive correspondence. Due to the high percentage of small (<0.02mm) intercrystalline pores in dolostones, a wide range of permeability values were obtained in spite of very low PIA measured porosity values.



**Figure 6.10. Relationship of PIA porosity and core permeability by pore type.**

### PIA (2-D) Porosity and Median Throat Diameter

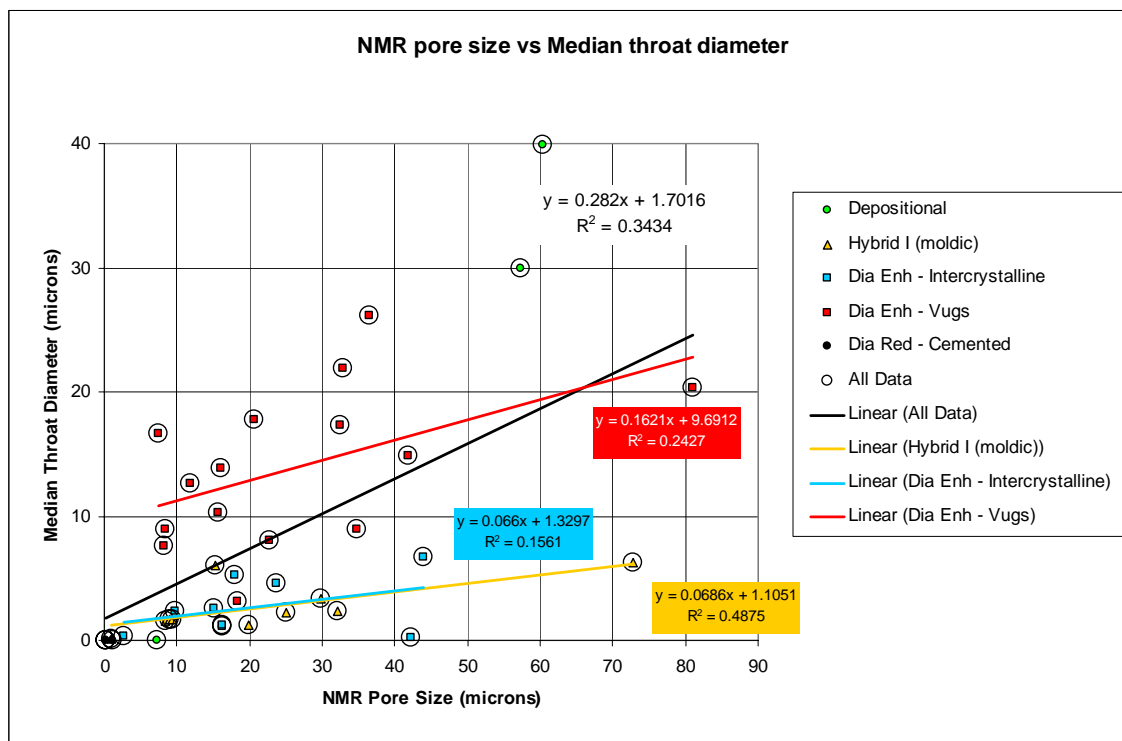
MPA diameter data was not available for the sandstones but a strong correlation would be expected between porosity and pore-throat size because porosity and permeability are closely paired in detrital depositional textures. Of the available data, PIA measured porosity was most strongly correlated with median throat diameter in hybrid 1-b (moldic) pores ( $R^2=0.85$ ). PIA measured porosity was not strongly correlated to median throat diameter in exclusively diagenetic pores of any kind (Fig. 6.11). This pattern suggests 2-D measurements which can distinguish depositional processes may be a key factor in estimating MPA, and in turn permeability.



**Figure 6.11. Comparison of PIA-measured porosity and median throat aperture.**

### Pore Size and Pore-Throat Size Relationships

Figure 6.12 shows the relationships of pore sizes calculated from NMR T2 relaxation times to MPA and pore origin. Pore-throat data was not available for the sandstones. Carbonates with depositional intergranular pores and hybrid 1-a pores (strong depositional attributes) show the best relationship between pore size and pore-throat size. Given the similarity in pore geometry and pore size to the sandstones, it stands to reason that clean sandstones would also show good agreement between pore-throat size and pore size. In carbonates, pores of depositional origin show the greatest correspondence, followed by hybrid pores ( $R^2=0.49$ ), then diagenetic pores ( $R^2=0.24$ ).



**Figure 6.12. Pore size determined from T2 times as compared with median throat aperture.**

A poor correlation exists between median pore diameters and median pore-throat diameters (Fig. 6.13). In these instances MPA shows no relationship to median PIA pore diameter ( $R^2=0.17$ ). Examining the comparison by pore size categories improves the correlation in small pores ( $R^2=0.22$ ), but is worse in both the large ( $R^2=0.16$ ) and medium ( $R^2=0.09$ ) pore size groups. In other words, median pore diameter calculated from PIA measurements is not a good indicator of MPA as calculated from capillary pressure measurements.

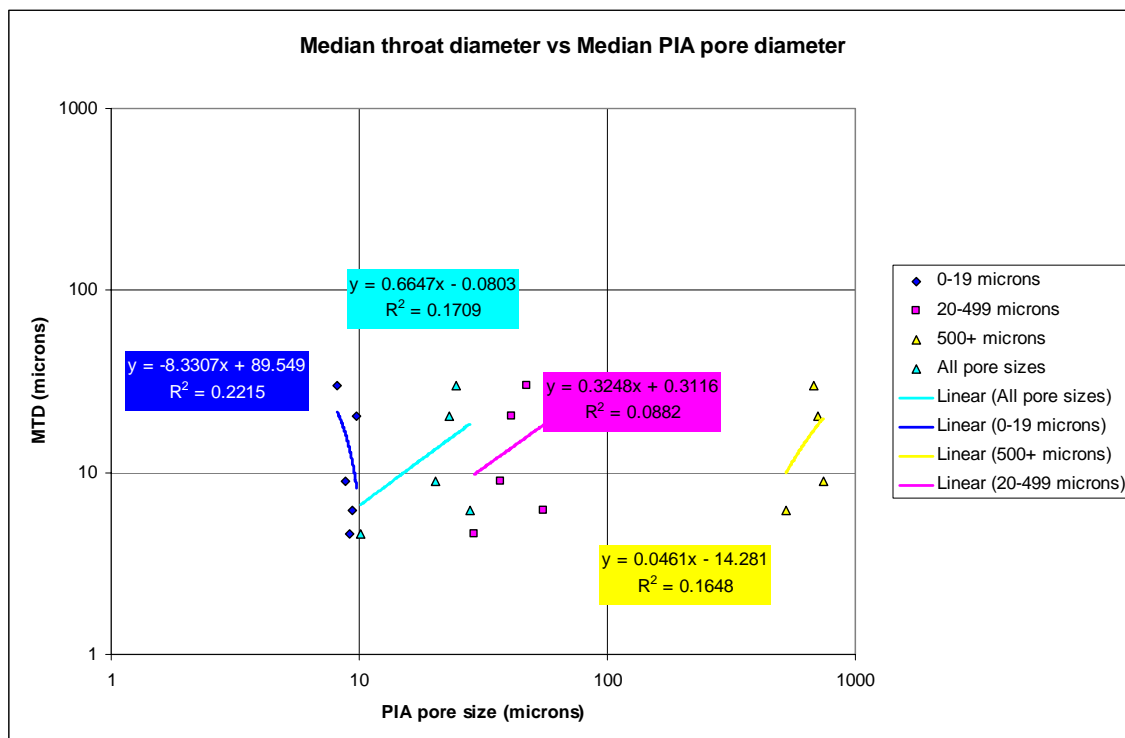


Figure 6.13. Relationship of median throat diameter and median PIA pore diameter.

## PORE GEOMETRY MEASURED BY NMR AS A PROXY FOR RESERVOIR QUALITY IN CARBONATES

Ebanks et al. (1992) defined flow units as a means of mapping reservoirs where geological and petrophysical properties that govern fluid flow were consistent, predictable, and distinct from properties of other reservoir rock volumes. Flow units share several common characteristics though no specific rules are required to identify them.

1. A flow unit is a specific volume of the reservoir – including both reservoir and non-reservoir quality rock types within that volume, and the fluids they contain.
2. A flow unit is correlative and mappable at the interwell scale.
3. A flow unit is recognizable on wireline logs.
4. A flow unit may be in communication with other flow units.

In this study, a flow unit can be generally thought of as a volume of rock containing a pore system that is effectively ranked by poroperm values as being of good, intermediate, or poor reservoir quality. Differences in pore geometry are key elements in discriminating pores of depositional, diagenetic, and hybrid origins. Pore origin, in turn, is used to identify characteristic NMR signatures.

Pore geometry was compared to companion values of porosity and permeability (Fig. 6.14) to distinguish relative flow unit quality. Geologists and engineers working with NMR need to recognize a variety of common, intermediate, and rare T2 curve shapes when mapping at interwell scales and evaluating reservoir quality. Best quality flow units may exhibit common T2 curve shapes, for example, as shown in the general reservoir model diagram (Fig. 6.15). Reservoir quality is best where samples commonly

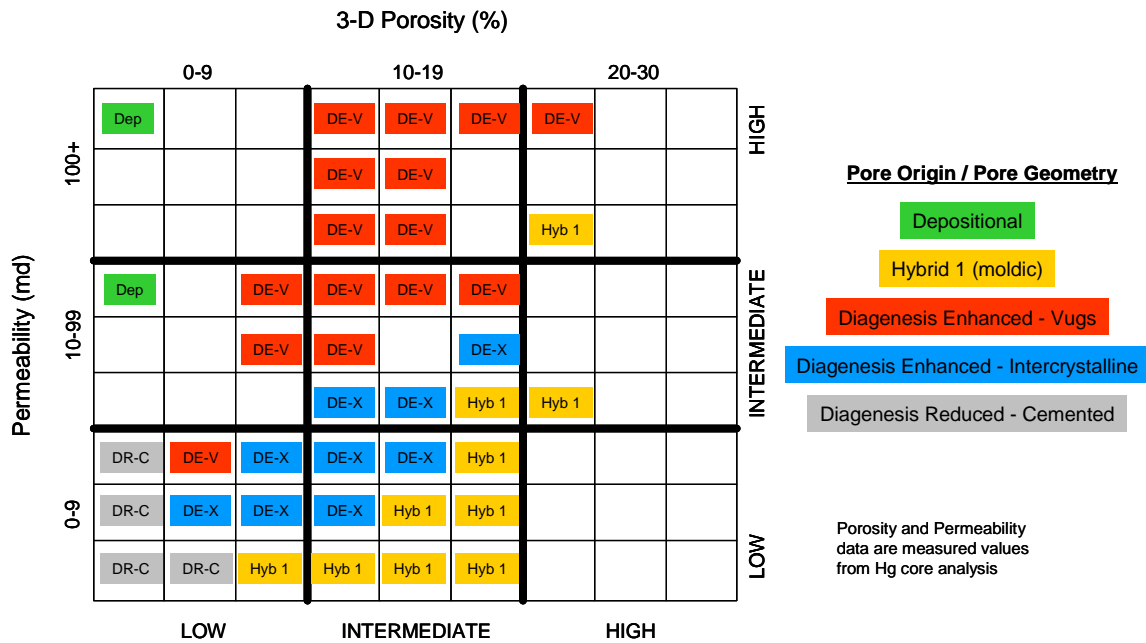


Figure 6.14. Paired values of porosity and permeability grouped by pore origin.

exhibit detrital depositional pores or vugs. Reservoir quality is poorest where T2 curves from cement-reduced and skelmoldic pores are common. T2 curves of oomoldic pores are of better quality than skelmoldic pores, and T2 curves of intercrystalline pores occur in both the intermediate and poor ranking.

The following observations regarding all of the studied carbonate rock suggest:

- 1) the best reservoir quality flow-units are found in samples containing depositional, intergranular pores,
- 2) cementation decreases reservoir quality by a factor of 10 on average,
- 3) high percentages of vugs (especially touching forms) improve reservoir quality,
- 4) moldic and intercrystalline pores are present in all flow unit ranks; therefore, the specific sizes and shapes of the molds and intercrystalline pore spaces must be determined because they have more influence on reservoir quality than genetic pore type.

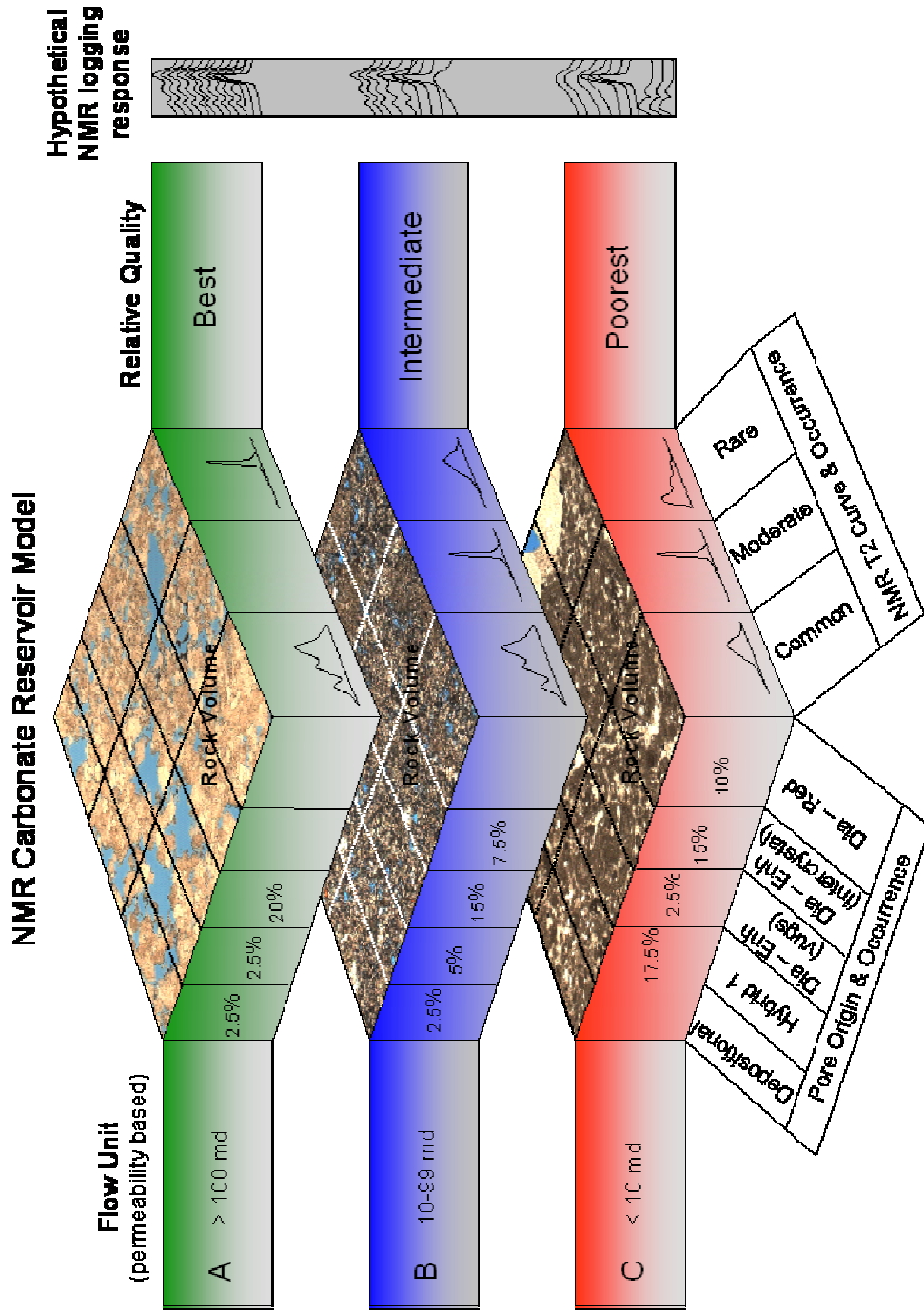


Figure 6.15. Hypothetical NMR logging response in carbonate reservoir flow units of best, intermediate, and poorest quality. Flow units relative quality rank determined by paired values of permeability and porosity. Common, moderate, and rare T2 curves from pores of differing origins show T2 response and are extrapolated onto the hypothetical NMR log.

## WHAT DOES IT ALL MEAN?

It is critical to examine real rock, particularly in carbonates, in order to make interpretations about its pore and pore-throat system. PIA is a rapid and inexpensive method which can provide good estimates of 2-D measured porosity and pore size distributions, particularly in samples dominated by depositional interparticle or hybrid pores exhibiting strong depositional attributes. Pores of depositional, diagenetic, and hybrid origins are quickly distinguished on the basis of pore geometry and size using PIA.

The difficulty in using PIA to estimate reservoir properties, such as porosity and permeability, becomes more challenging as diagenesis progresses. Layman (2002) determined that a moderate correlation of all genetic pore types ( $R^2=.61$ ) was found between PIA-measured porosity and permeability in carbonates from Happy field. This study also shows a positive correspondence between the techniques (Fig. 6.10) except in the case of intercrystalline pores. In other words MPA, and in turn permeability, may be reasonably estimated from 2-D measurements as long as intercrystalline pores are not the dominant pore type. Where diagenesis has reduced pore space by cementation, the accuracy of the method diminishes because the smallest pores are difficult to resolve. For any pore larger than 20 microns, however, PIA can readily distinguish enough information about pore geometry in 2-D to determine pore origin.

NMR technology can be used to obtain T2 measurements that can be converted into a distribution of pore sizes. Portions of the T2 curve which correspond to small, medium, and large pores as seen in thin section, can also be identified as having come



from depositional, diagenetic, or hybrid origins. To do this requires some knowledge about the real rock; 1) the geometry of the pores, and 2) minerals which influence estimates of the corresponding NMR pore size. Knowing these two factors, estimates of pores size from T2 relaxation times are improved, and pore origin is better approximated from the individual T2 curve shapes. For all carbonate samples, median throat aperture is best estimated by NMR pore sizes in depositional pores, followed by moldic pores. Diagenetic forms of pores do not show correlation between NMR pore size and median pore-throat size (Fig. 6.12).

Capillary pressure measurements and calculated pore-throat sizes correspond with permeability. Distributions of pore-throat size are best distinguished by genetic pore type. Therefore permeability and genetic pore type are directly related. Carbonate rock samples with companion values of high, intermediate, or low porosity and permeability have characteristic T2 relaxation curves. These paired properties, measured on the same rocks from which T2 relaxation times were measured, are related to depositional, diagenetic, and hybrid pore types. Using all of the integrated data, NMR under the conditions mentioned, may alone be used estimate reservoir quality where other data types may be unavailable.

## CHAPTER VII

### SUMMARY AND CONCLUSIONS

#### SUMMARY

Forty carbonate and seven sandstone rock samples were evaluated from four different locations of the world. Wet and dry core scale photos were obtained for each sample according to location. Cores were prepared into one-inch diameter core plugs, and cleaned. Thin sections were prepared from the core plugs, and T2 relaxation and MICP measurements were obtained.

Routine petrographic methods were used to identify dominant pore types and the origin of the pores after Ahr's genetic classification of porosity. Small, medium, and large pore sizes, and their associated pore shape, were determined for each thin section using commercial software. Histograms and scatter plots of the distributions of pore sizes, shapes, and porosity were used to distinguish pore origin.

NMR T2 curves were obtained on all samples. Rocks exhibiting pores of similar origin had T2 curves of similar shape. The T2 curves were converted to size distributions and compared with 2-D size distributions. Estimates of pore size as determined from T2 relaxation times were reasonable, except where a large portion of the pore perimeter included paramagnetic minerals.

MICP curves and distributions of pore-throat aperture were calculated and compared with distributions of pore sizes obtained by the other techniques. Permeability values derived from core measurements, together with T2 response, were used to develop an ideal NMR reservoir model concept which has immediate industry

application. The final model suggests how NMR logging might be used to estimate pore origins in the reservoir, and identify best quality flow units in carbonate reservoirs and aquifers.

## CONCLUSIONS

- Pores of different genetic origin are successfully discriminated from one another using a combination of pore geometry and pore size.
- Dolomitization generally changes pore geometry to more simplistic shapes, and dissolution generally complicates pore geometry in 2-D.
- Porosity measured in 2-D best estimates core analysis porosity on the same rock when depositional interparticle pores are common. Moldic and purely diagenetic pores decrease the correspondence between 2 and 3-D measurements, and depend on the type of pores present and the magnitude and direction of diagenetic change.
- Pore size determined from T2 relaxation times in carbonates may be affected by paramagnetic minerals that result in underestimates of large vug size in dolostones.
- 2-D measured pores, and pore sizes determined from T2 relaxation times compare best in middle sized (0.02-0.5mm) pores.
- Median pore-throat apertures are strongly correlated to permeability.
- Flow units, which have high companion values of porosity and permeability, also have characteristic T2 curve shapes, which in turn are related to pore origin.

## REFERENCES CITED

- Adams, J. E., H. N. Frenzel, M. L. Rhodes, and D. P. Johnson, 1951, Starved Pennsylvanian Midland Basin: AAPG Bulletin, v. 35, p. 2600-2607.
- Ahr, W. M., 1973, The carbonate ramp: An alternative to the shelf model: GCAGS Transactions, v. 23, p. 221-225.
- Ahr, W. M., and B. S. Hammel, 1999, Identification and mapping of flow units in carbonate reservoirs: An example from the Happy Spraberry (Permian) field, Garza County, Texas, USA: Energy Exploration and Exploitation, v. 17, p. 311-334.
- Ahr, W. M., 2005. Carbonate Reservoir Geology ©, Texas A&M University class notes, College Station, 213 p.
- Ahr, W. M., D. Allen, A. Boyd, H. Bachman, T. Smithson, E. Clerke, K. Gzara, J. Hassall, C. Murty, H. Zubari, and R. Ramanoorthy, 2005, Confronting the carbonate conundrum: Oilfield Review, Spring 2005, p. 18-30.
- Aivano, R., and J. Howard, 2001, NMR relaxation times and related pore geometry in the Morrow Group (Pennsylvanian), Hemphill County, Texas and Texas County, Oklahoma: AAPG Bulletin, v. 85, p. 1689-1696.
- Allen, D., S. Crary, B. Freedman, M. Andreani, W. Klopff, R. Badry, C. Flaum, B. Kenyon, R. Kleinberg, P. Gossenberg, J. Horkowitz, D. Logan, J. Singer, and J. White, 1997, How to use borehole nuclear magnetic resonance: Oilfield Review, v. 9, p. 34-57.
- Anselmetti, F. S., S. Luthi, and G.P. Eberli, 1998, Quantitative characterization of carbonate pore systems by digital image analysis: AAPG Bulletin, v. 82, p. 1815-1836.
- Archie, G. E., 1952, Classification of carbonate reservoir rocks and petrophysical considerations: AAPG Bulletin, v. 36, p. 278-298.
- Atchley, S. C., M. G. Kozar, and L. A. Yose, 1999, A predictive model for reservoir distribution in the Permian (Leonardian) Clear Fork and Glorieta Formations, Robertson Field Area, West Texas: AAPG Bulletin, v. 83, p. 1031-1056.
- Ausbrooks, R., 1999, Quantification of vuggy porosity and lithology using borehole images, core, and logs, Bohai Basin, offshore China: M.S. thesis, Colorado School of Mines, Golden, CO, 168 p.

- Ausbrooks, R., N. F. Hurley, A. May, and D. G. Neese, 1999, Pore-size distributions in vuggy carbonates from core images, NMR, and capillary pressure: Society of Petroleum Engineers (SPE paper #56506), p.1-14.
- Avila, J. C., 2002, A petrophysics and reservoir performance-based reservoir characterization of Womack Hill (Upper Smackover) field (Alabama), M.S. thesis, Texas A&M University, College Station, Texas, 214 p.
- Beard, D. C., and P. K. Weyl, 1973, Influence of texture on porosity and permeability of unconsolidated sand: AAPG Bulletin, v. 57, p. 349-369.
- Benson, D. J., 1985, Diagenetic controls on reservoir development and quality, Smackover Formation of southwest Alabama: GCAGS Transactions, v. 35, p. 317-326.
- Bradley, H. B., 1987, Petroleum engineering handbook: Richardson, Society of Petroleum Engineers Publishing, Chapter 26 (Properties of Reservoir Rocks), p. 24.
- Brown, R. J. S., and B. W. Gammon, 1960, Nuclear magnetism logging: Journal of Petroleum Technology, v. 12, p. 199-201.
- Bryant, S., C. Cade, and D. Mellor, 1993, Permeability prediction from geologic models: AAPG Bulletin, v. 77, p. 1338-1350.
- Butcher, B. P., 1989, The Northwest Shelf of Australia *in* J. D. Edwards and P. A. Santogrossi eds., Divergent/ passive margin basins: AAPG Memoir 48, p. 81-115.
- Camden, D., 1994, NMR theory made simple: DiaLOG, London Petrophysical Society, v. 2, p. 4-5.
- Chang, D., H. Vinegar, C. Morriss, and C. Straley, 1997, Effective porosity, producible fluid, and permeability in carbonates from NMR logging: The Log Analyst, March-April 1997, p. 60-72.
- Choquette, P. W., and Pray, L. C., 1970, Geologic nomenclature and classification of porosity in sedimentary carbonates: AAPG Bulletin, v. 54, p. 207-250.
- Coates, G. R., L. Xiao, and M. G. Prammer, 1999, NMR logging: Principles and applications: Halliburton Energy Services, Houston, TX, 234 p.
- Coope, D. F., 1994, Petrophysical applications of NMR: DiaLOG, London Petrophysical Society, v. 2, p. 8-10.

- Crabaugh, J. P., 1988, Depositional history of the Lower Permian Abo Formation and Lower Meseta Blanca Member of the Yeso Formation, north central New Mexico: M.S. Thesis, University of Texas (Arlington), Arlington, TX, 214 p.
- Crevello, P. D., and P. M. Harris, 1984, Depositional models for Jurassic reefal buildups, *in* W. P. S. Ventress, D. G. Bebot, B. F. Perkins, and C. H. Moore, eds., *The Jurassic of the Gulf Rim: Gulf Coast Section SEPM, Proceedings of the Third Annual Research Conference*, Baton Rouge, LA, p. 57-102.
- Davies, D. K., 1990, Image analysis of reservoir pore systems: state of the art in solving problems related to reservoir quality: Society of Petroleum Engineers (SPE paper# 19407), p. 73-82.
- Dunn, K. J., D. J. Bergman, and G. A. Latorraca, 2002, Handbook of geophysical exploration – Seismic Exploration, K. Helbig and S. Treitel, eds., Nuclear Magnetic Resonance Petrophysical and Logging Applications, 293 p.
- Ebanks, W. J. Jr., M. H. Scheihing, and C. D. Atkinson, 1992, Flow units for reservoir characterization: Part 6, Geological Methods: AAPG Special Publications, p. 282-285.
- Edwards, D.S., J.M Kennard, J.C. Preston, C.J. Boreham, R.E. Summons, and J.E. Zumberge, 2001, Geochemical evidence for numerous Mesozoic petroleum systems in the Bonaparte and Browse Basins, Northwestern Australia: AAPG Bulletin, v. 85, no. 13 (supplement).
- Ehrlich, R., S. K. Kennedy, S. J. Crabtree, and R. L. Cannon, 1984, Petrographic image analysis, I. Analysis of reservoir pore complexes: *Journal of Sedimentary Petrology*, v. 54, p. 1365-1378.
- Ehrlich, R., and D. K. Davies, 1989, Image analysis of pore geometry: Relationship to reservoir engineering and modeling. Society of Petroleum Engineers (SPE paper #19054), p. 15-30.
- Ehrlich, R., S. J. Crabtree, K. O. Horkowitz, and J. P. Horkowitz, 1991a, Petrography and reservoir physics I. Objective classification of reservoir porosity: AAPG Bulletin, v. 75, p. 1547-1562.
- Ehrlich, R., E. L. Etris, D. Brumfield, L. P. Yuan, and S. J. Crabtree, 1991b, Petrography and Reservoir Physics III. Physical models for permeability and formation factor: AAPG Bulletin, v. 75, p. 1579-1592.

- Etris, E. L., D. S. Brumfield, R. Ehrlich, and S. J. Crabtree, 1988, Relations between pores, throats and permeability: A petrographic/physical analysis of some carbonate grainstones and packstones: *Carbonates and Evaporites* v. 3, p. 17-32.
- Feazel, C.T., A. P. Byrnes, J. W. Honefenger, R. J. Leibrecht, R. G. Loucks, S. McCants, and A. H. Saller, 2004, Carbonate reservoir characterization and simulation: From facies to flow units: Report from the March 2004 Hedberg Research Symposium: *AAPG Bulletin*, v. 88, p. 1467-1470.
- Foley, I., S. A. Farooqui, and R. L. Kleinberg, 1996, Effect of paramagnetic ions on NMR relaxation of fluids at solid surfaces: *Journal of Magnetic Resonance, Series A*, v. 123, p. 95-104.
- Forrest, J. T., and E. L. Horstman, 1986, The northwest shelf of Australia – geologic review of a potential major petroleum province of the future: *AAPG Bulletin* v. 68, p. 457-486.
- Hammel, B. S., 1996, High resolution reservoir characterization of the Permian (Upper Leonardian) Spraberry Formation, Happy Spraberry Field, Garza County, Texas. M.S. Thesis, Texas A&M University, College Station, TX, 156 p.
- Handford, C. R., 1981, Sedimentology and genetic stratigraphy of Dean and Spraberry Formations (Permian), Midland Basin, Texas: *AAPG Bulletin*, v. 65, p. 1602-1616.
- Hodgkins, M. A., and Howard, J. J., 1999. Application of NMR logging to reservoir characterization of low-resistivity sands in the Gulf of Mexico: *AAPG Bulletin*, v. 83, p. 114-127.
- Hopkins, T. L., 2002, Integrated petrographic and petrophysical study of the Smackover formation, Womack Hill field, Clarke and Choctaw Counties, Alabama: M.S. Thesis, Texas A&M University, College Station, TX, 156 p.
- Hughes, D., 1968, Salt tectonics as related to several Smackover fields along the northeast rim of the Gulf of Mexico basin: *GCAGS Transactions*, v. 18, p. 320-330.
- Imlay, R. W., 1945, Jurassic fossils from the southern states, no. 2: *Journal of Paleontology*, v. 19, p. 253-276.
- Jeary, G. L., 1978, Leonardian strata in northern Midland basin of west Texas (abs): *AAPG Bulletin*, v. 62, p. 526-526.

- Johnston, J. E., P. V. Heinrich, J. K. Lovelace, R. P. McCulloh, and R. K. Zimmerman, 2000, Stratigraphic Charts of Louisiana, Folio Series No. 8, Louisiana Geological Survey. <http://www.lgs.lsu.edu/pubs/lacharts.pdf> (accessed Apr. 27, 2005)
- Kasap, E., M. Altunbay, and D. Georgi, 1999, Flow units from integrated WFT and NMR data, *in* R. Schatzinger and J. Jordan, eds., Reservoir characterization-recent advances, AAPG Memoir 71, p. 179-190.
- Kenyon, W. E., J. J. Howard, A. Swzginer, C. Straley, A. Matteson, K. Horkowitz, and R. Ehrlich, 1989, Pore-size distribution and NMR in microporous cherty sandstones: SPWLA Thirteenth Annual Logging Symposium, June 11-14, p. 1-19.
- Kenyon, W. E., 1997, Petrophysical principles of applications of NMR logging: The Log Analyst, March-April 1997, p. 21-43.
- Kong, M., R. Bhattacharya, C. James, and A. Basu, 2005, A statistical approach to estimate the 3D size distribution of spheres from 2D size distributions: Geological Society of America Bulletin, v. 117, p. 244-249.
- Kopaska-Merkel, D. C., and S. D. Mann, 1993, Upward shoaling cycles in Smackover carbonates of southwest Alabama: GCAGS Transactions, v. 43, p.173-181.
- Krumbein, W. C. and G. D. Monk, 1943, Permeability as a function of the size parameters of unconsolidated sand: Transactions of the American Institute of Mining and Metallurgical Engineers, v. 151, p. 153-163.
- Layman, J. M., 2002, Porosity characterization utilizing petrographic image analysis: Implications for identifying and ranking reservoir flow units, Happy Spraberry field, Garza County, Texas, M.S. Thesis, Texas A&M University, College Station, Texas, 103 p.
- Lodola, D., 2004, Identification of pore type and origin in a Lower Cretaceous carbonate reservoir using NMR T2 relaxation times: M.S. Thesis, Texas A&M University, College Station, TX, 67p.
- Longley, I. M, M. T. Bradshaw, and J. Heberger, 2002, Australian petroleum provinces of the twenty-first century, *in* M. W. Downey, J. C. Threet, and W. A. Morgan, eds., Petroleum provinces of the twenty-first century: AAPG Memoir 74, p. 287-317.
- Lucia, F.J., 1983, Petrophysical parameters estimated from visual descriptions of carbonate rocks: A field classification of carbonate pore space. Journal of Petroleum Technology (JPT), v. 35, p. 629-637.



- Lucia, F.J., and R.P. Major, 1994, Porosity evolution through hypersaline reflux dolomitization: Special Publications of the International Association of Sedimentologists, v. 21, p. 325-341.
- Lucia, F.J., 1995, Rock-fabric/petrophysical classification of carbonate pore space for reservoir characterization: AAPG Bulletin, v. 79, p. 1275-1300.
- Mallett, M., M. B. Clennell, J. H. Strange, and Q. J. Fisher, 2000, Imaging pore connectivity through sealing fault rocks with NMR: AAPG Bulletin, v. 84, No. 13 (supplement).
- Mancini, E. A., and D. J. Benson, 1980, Regional stratigraphy of upper Jurassic Smackover carbonates of southwest Alabama: GCAGS Transactions, v. 30, p. 151-165.
- Mancini, E. A., B. H. Tew, and R. M. Mink, 1990, Jurassic sequence stratigraphy in the Mississippi Interior Salt Basin of Alabama: GCAGS Transactions, v. 40, p. 521-529.
- Mancini, E. A., D. J. Benson, B. S. Hart, R. S. Balch, W. C. Parcell, and B. J. Panetta, 2002, Appleton field case study (eastern Gulf coastal plain): Field development model for Upper Jurassic microbial reef reservoirs associated with paleotopographic basement structures: AAPG Bulletin, v. 84, p. 1699-1717.
- Mancini, E. A., T. A. Blasingame, R. Archer, B. J. Panetta, J. C. Llinas, C. D. Haynes, and D. J. Benson, 2004, Improving recovery from mature oil fields producing from carbonate reservoirs: Upper Jurassic Smackover Formation, Womack Hill field (eastern Gulf Coast, U.S.A.): AAPG Bulletin, v. 88, p. 1629-1651.
- Mann, S. D., 1990, Depositional facies of saltern evaporates of the Buckner anhydrite member of the Haynesville formation of southwestern Alabama (abs.): Southeastern Section GSA, Abstracts with Programs, v. 22, p. 24.
- McCreech, C. A., R. Ehrlich, and S. J. Crabtree, 1991, Petrography and reservoir physics II. Relating thin section porosity to capillary pressure, the association between pore types and throat size: AAPG Bulletin, v. 75, p. 1563-1578.
- Meyers, J. D., 1975, Petroleum geology of Choctaw County, Alabama: GCAGS Transactions, v. 25, p. 208-216.
- Mollan, R. G., R. W. Craig, and J. W. Lofting, 1970, Geologic framework of continental shelf off northwest Australia: AAPG Bulletin, v. 54, no. 4, p. 583-600.

- Morgan, D., 2003, Mapping and ranking flow units in reef and shoal reservoirs associated with paleohighs: Upper Jurassic (Oxfordian) Smackover formation, Appleton and Vocation fields, Escambia and Monroe Counties, Alabama: M.S. Thesis, Texas A&M University, College Station, TX, 157 p.
- Mowers, T. T., and D. A. Budd, 1996, Quantification of porosity and permeability reduction due to calcite cementation using computer-assisted petrographic image analysis techniques: AAPG Bulletin, v. 80, p. 309-322.
- Nurmi, R., S. Denoo, and R. Dennis, 1998, NMR logging applications in carbonate exploration plays and pilot development and horizontal wells: AAPG Annual Convention Abstract, Salt Lake City, Utah (May 17-28, 1998), p. 1-2.
- Parcell, W. C., 1999, Stratigraphic architecture of Upper Jurassic (Oxfordian) reefs in the northeastern Gulf Coast, U.S., and the Eastern Paris Basin, France: GCAGS Transactions, v. 49, p. 412-417.
- Parcell, W. C., 2002, Sequence stratigraphic controls on the development of microbial fabrics and growth forms – implications for reservoir quality distribution in the Upper Jurassic (Oxfordian) Smackover formation, Eastern Gulf Coast, USA: Carbonates and Evaporites, v. 17, p. 166-181.
- Parra, J. O., C. L. Hackert, H. A. Collier, and M. Bennet, 2001, NMR and acoustic signatures in vuggy carbonate aquifers: 42<sup>nd</sup> Annual SPWLA Meeting, Houston, TX, June 2001, p. 1-12.
- Prensky, S. E., 2001, Recent developments in logging technology: AAPG Bulletin, v. 85, No. 13 (supplement).
- Purcell, W. R., 1949, Capillary pressures - their measurement and the calculation of permeability therefrom: Journal of Petroleum Technology (JPT), v. 1, p. 39-48.
- Quintero, L., A. Boyd, A. Gyllensten, and R. El-Wazeer, 1999, Comparison of permeability from NMR and production analysis in carbonate reservoirs: Society of Petroleum Engineers (SPE paper #56798), p. 1-8.
- Robertson, G. A., D. E. Powell, and G. M. Edmond, 1976, Australian northwest continental shelf-results of ten years of exploration: Hydrocarbons, in M.T. Halbouty, J.C. Maher and H.M. Lian (eds.) Circum-Pacific Energy and Mineral Resources, v. 25, p. 231-238.
- Romero, P. A., Y. Golindano, I. Dedillo, I. Azpirtxaga, and A. Perarnau, 2000, NMR as a tool for reservoir characterization and lithofacies recognition: AAPG Bulletin, v. 84, No. 13 (supplement).

- Ross, C. A., 1986, Paleozoic evolution of southern margin of Permian basin: Geological Society of America Bulletin, v. 97, p. 536-554.
- Roy, E. C., 1998, High resolution mapping of flow units for enhanced recovery program planning, Happy Spraberry Lime Field, Garza County, TX: M.S. Thesis, Texas A&M University, College Station, Texas, 91 p.
- Salvador, A., 1987, Late Triassic-Jurassic paleogeography and the origin of the Gulf of Mexico Basin: AAPG Bulletin, v. 71, p.419-451.
- Selley, R. C., 1998, Elements of petroleum geology: San Diego, Academic Press, 470 p.
- Swanson, B. F., 1981, A simple correlation between permeabilities and mercury capillary pressures: Journal of Petroleum Technology, v. Dec, p. 2498-2504.
- Tedesco, W. A., 2002, Dolomitization and reservoir development of the upper Jurassic Smackover formation, Womack Hill Field, Eastern Gulf Coastal Plain: Ph.D. Dissertation, University of Mississippi (Ole Miss), Oxford, 251 p.
- Tew, B. H., R. M. Mink, E. A. Mancini, S. D. Mann, and D. C. Kopaska-Merkel, 1993, Geologic framework of the Jurassic (Oxfordian) Smackover formation, Alabama and panhandle Florida coastal waters area and adjacent federal waters area: GCAGS Transactions, v. 43, p. 399-411.
- Tiab, D. and E.C. Donaldson, 2004, Petrophysics: Theory and practice of measuring reservoir rock and fluid transport properties: Boston, Gulf Professional Publishing, 889 p.
- Timur, A., 1972, Nuclear magnetic resonance study of carbonate rocks: SPWLA 13<sup>th</sup> Annual Logging Symposium, May 7-10, p.1-15.
- Townsend, R. N., 1986, The depositional environment and diagenesis of the upper Smackover member in Womack Hill field, Clarke and Choctaw Counties, Alabama: M.S. Thesis, Northeast Louisiana University, Monroe, LA, 98 p.
- Walper, J. L., and C. L. Rowett, 1972, Plate tectonics and the origin of the Caribbean Sea and the Gulf of Mexico: GCAGS Transactions, v. 22, p. 105-116.
- Ward, R. F., C. G. Kendall and P. M. Harris, 1986, Upper Permian (Guadalupian) facies and their association with hydrocarbons-Permian basin, West Texas and New Mexico: AAPG Bulletin, v. 70, p. 239-262.

- Wardlaw, N. C., and R. P. Taylor, 1976, Mercury capillary pressure curves and the interpretation of pore structure and capillary behavior in reservoir rocks: *Bulletin of Canadian Petroleum Geology*, v. 24, p. 225-262.
- Wardlaw, N. C., 1976, Pore geometry of carbonate rocks as revealed by pore casts and capillary pressure: *AAPG Bulletin*, v. 60, p. 245-257.
- Wardlaw, N. C., and J. P. Cassan, 1978, Estimation of recovery efficiency by visual observation of pore systems in reservoir rocks: *Bulletin of Canadian Petroleum Geology*, v. 26, p. 572-585.
- Wardlaw, N. C., 1979, Pore systems in carbonate rocks and their influence on hydrocarbon recovery efficiency: *Short Course on Carbonate Porosity*, April 1979, p. 1-24.
- Wardlaw, N. C., M. McKellar, and L. Yu, 1988, Pore and throat size distributions determined by mercury porosimetry and by direct observation: *Carbonates and Evaporites*, v. 3, p. 1-15.
- Watson, A. T., and C. T. P. Chang, 1997, Characterizing porous media with NMR methods: *Progress in Nuclear Magnetic Resonance Spectroscopy*, v. 31, p. 343-386.
- Wilkerson, R. P., 1981, Environments of deposition of the Norphlet Formation (Jurassic) in south Alabama: M.S. thesis, University of Alabama, Tuscaloosa, 141 p.
- Witkowski, F. W., D. J. Blundell, P. Gutteridge, A. D. Horbury, N. H. Oxtoby, and H. Qing, 2000, Video cathodoluminescence microscopy of diagenetic cements and its applications: *Marine and Petroleum Geology*, v. 17, p. 1085-1093.
- Yang, K. M., and S. L. Dorobek, 1994, The Permian Basin of west Texas and New Mexico: Tectonic history of a 'composite' foreland basin and its effect on stratigraphic development, *in* S. L. Dorobek and G. M. Ross, eds., *Stratigraphic evolution of foreland basins*, SEPM Special Publication no. 52, p. 147-172.

## SUPPLEMENTAL SOURCES CONSULTED

- Bowers, M. C., M. B. Carr, and C. J. Murray, 1998, Correlation of porosity types derived from NMR data and petrographic image analysis (abs.): AAPG Annual Convention, Salt Lake City, UT, May 17-28, 1998. p. 1-4.
- Gingras, M. K., C. A. Mendoza, and S. G. Pemberton, 2004, Fossilized worm burrows influence the resource quality of porous media: AAPG Bulletin, v. 88, p. 875-883.
- Hidajat, I., K. K. Mohanty, M. Flaum, and G. Hirasaki, 2004, Study of vuggy carbonates using NMR and X-Ray CT scanning: Society of Petroleum Engineers (SPE paper #88995), p. 365-377.
- Image-Pro® Plus for Windows, 1994. Reference Guide. Media Cybernetics L.P., 566p.
- Longman, M. W., 1981, Carbonate diagenesis as a control on stratigraphic traps (with Examples from the Williston Basin), AAPG Education Course Note Series 21, p. 56-91.
- Lyne, A., G. Varini, and G. Ghilardotti, 1996, Determination of petrophysical properties of carbonate rocks by NMR relaxometry: Society of Petroleum Engineers (SPE paper #36852), p. 331-339.
- Nurmi, R., A. J. Lomando, and B. Katz, 2001, Status and future of carbonate formation evaluation using well logs: AAPG Bulletin, v. 85, No. 13 (supplement).
- Rink, M., and J. R. Schopper, 1978, On the application of image analysis to formation evaluation: Log Analyst, Jan-Feb 1978, p. 12-22.
- Vavra, C. L., J. G. Kaldi, and R. M. Sneider, 1993, Capillary pressure, *in* D. Morton-Thompson and A. M. Woods, eds., Development geology reference manual: AAPG Methods in Exploration Series, No. 10, Tulsa, Oklahoma, AAPG, p. 221-225.
- Willard, G. J., A. P. Byrnes, J. H. Doveton, and E. K. Franseen, 1998, Influence of lithology and pore geometry on NMR prediction of permeability and effective porosity in Mississippian carbonates, Kansas: 1998 AAPG Annual Convention Abstract, Salt Lake City, Utah (May 17-28, 1998), p. 1-6.

**APPENDIX A**

**THIN SECTION DESCRIPTIONS**

**Sample # Lott 19-7 (5009 ft)**

Carbonate - Skeletal grainstone, abundant quartz with traces of feldspar. Abundant echinoderm fragments, echinoderm spines common, brachiopods common (up to 3 mm length), mollusk fragments common, forams sparse. Porosity is mostly moldic due to dissolved allochems, with some minor solution enhanced interparticle porosity. Calcite is the binding cement. Quartz grains range from angular to sub-rounded, are moderately well sorted. Neomorphosed ooids are present but sparse. No dolomite present.

**Sample # Lott 19-7 (4956 ft)**

Carbonate – Skeletal packstone with abundant echinoderm plates, sparse echinoderm spines, sparse brachiopods, common mollusks, sparse benthic forams, common bryozoans. Porosity is moldic, due to the dissolution of skeletal allochems. There are minor amounts of intraskeletal (intraparticle) porosity. Sample composed of heavily neomorphosed micrite, and minor calcite epitaxial overgrowths on echinoderm skeletal clasts. No dolomite present. Small erosional lines occur through grains with some residual hydrocarbons in the erosional lines.

**Sample # Lott 19-3 (4972.5 ft)**

Carbonate – Skeletal packstone, sparse ooids, sparse brachiopods, sparse bryozoans, sparse mollusks, common echinoderm plates. Abundant quartz occurs in two size modes. The larger quartz grains are rounded, and the smaller mode are angular, about one-third the size of the larger mode. Porosity is dominated by intramatrix style. Some echinoderm fragments have minor fractures (due to compaction?). Calcite cements grains of all types together, but is moderately micritized. Also, a few parallel dissolution seams are present, filled with quartz/calcite matrix including minor amounts of residual hydrocarbons.

**Sample # Lott 19-3 (4956.5 ft)**

Carbonate – Skeletal packstone, common brachiopods, common echinoderms, sparse mollusk (bivalves), sparse bryozoans. Sand-sized well-rounded monocrystalline quartz fragments common, feldspar grains sparse. Calcite cement present. Porosity is dominated by moldic (dissolved skeletal allochems), with minor porosity contributions from pelloid molds. Intramatrix porosity also abundant.

**Sample # Lott 19-3 (4925.0 ft)**

Carbonate – Ooid-peloid grainstone. Ooids are nearly completely dissolved away. Benthic forams common, bryozoans sparse, and a few large lithoclasts are present. Porosity is ooid moldic, and the sample is only cemented by calcite, no dolomite present.

**Sample # Lott 19-3 (4923.2 ft)**

Carbonate – Ooid-peloid-skeletal grainstone. Ooids, forams, echinoderm spines, and brachiopods all present but sparse. Quartz grains are sparse, well-rounded, and well-sorted. Primary porosity dominated by dissolution of ooids, peloids, and skeletal allochems, and some dissolved intramatrix porosity. Grains/allochems dissolved, then phreatic calcite cements coat most edges of existing porosity with abundant mostly blocky calcite. Distinct dissolved outlines of forams present.



## Northwest Australian Shelf

### Sample # 16

Sandstone – Quartz arenite. Abundant monocrystalline quartz, common undulose quartz grains. Grains have tiny bubble trails in them, and many have fractures within the grain. Overgrowths and quartz cements rare to absent. Grains are moderately sorted, moderate to well rounded, and grains commonly display interpenetrating contacts likely due to compaction effects. Porosity is >90% intergranular (depositional), with some microporosity contributed from volcanic? fragments.

### Sample # 20

Sandstone – Quartz arenite. Abundant monocrystalline quartz, common undulose quartz grains. Grains have tiny bubble trails in them, and many have fractures within the grain. Overgrowths and quartz cements rare to absent. Grains are very well sorted, moderate to well rounded, and grains commonly display interpenetrating contacts likely due to compaction effects. Similar to Sample #16, but overall smaller grains with chert common. Polycrystalline quartz sparse, and mica sparse. Porosity is >90% intergranular (depositional), with minor contributions from volcanic fragments.

### Sample # 23

Sandstone – Quartz arenite. Abundant monocrystalline quartz, common undulose quartz grains, and common polycrystalline/chert grains. Sparse mica present. Quartz grains have tiny bubble trails in them, and many have fractures within the grain. Overgrowths and quartz cements rare to absent. Grains are subrounded to subangular, with flat and often interpenetrating contacts between adjacent grains. Compromise boundaries poorly developed but sparsely present. Porosity is visually estimated >90% intergranular (depositional). Of particular mention in this sample are large pores, typically 2-3 times the adjacent pores. These may be the result of 1) pounding surf (shallow marine environment, Howard, personal comm.) which created keystone pores which survived compaction, or 2) 'vug's formed from plucked grains during thin section preparation, 3) dissolved glauconite?, or 4) most likely, preferential dissolution of interspersed volcanic rock fragments from the Australian mainland, as evidenced by volcanic terrains on a geologic map. See <http://www.geoscience.gov.au/geoportal/maps.html>. in NW Australia.

### Sample # 21

Sandstone – Quartz arenite. Abundant monocrystalline quartz, common undulose quartz grains. Grains have tiny bubble trails in them, and many

have fractures within the grain. Overgrowths and quartz cements rare to absent. Grains are very well sorted, moderate to well rounded, and grains commonly display interpenetrating contacts likely due to compaction effects. Chert grains common and show abundant microporosity. Moderate development of  $120^\circ$  compromise boundaries (compaction effect), and sutured contacts present but rare. Trace amounts of cherty cement present? Quartz overgrowths present on some grains, but likely developed prior to deposition of this rock, inasmuch as many overgrowths are non-planar contacts. Porosity is visually estimated  $>90\%$  intergranular (depositional), with minor contributions from volcanic/or chert grains.

#### **Sample # 27**

Sandstone – Quartz arenite. Monocrystalline and undulose quartz grains abundant, sparse polycrystalline quartz, and chert common. Estimate of 50% of host ‘ghost’ grains are typically round and discernable from silica overgrowths.  $120^\circ$  contacts between grains are common but not omnipresent. Grain contacts often irregular or wavy in appearance. Non-host (ghost) grains are angular to very angular due to cementation and compaction effects. Porosity is visually estimated  $>90\%$  interparticle, the depositional porosity reduced due to cementation. A minor amount of porosity is in isolated chert grains and small fractures within quartz grains as well as a few isolated volcanic grains with microporosity.

#### **Sample #24**

Sandstone – Quartz arenite. This thin section is dominated by abundant undulose quartz, commonly occurring monocrystalline quartz, and sparse chert grains. About 20% of grains show silicious cement overgrowths. Grain contacts are often irregular and interpenetrating, but no distinct sutural pattern evident. Grains are moderately well sorted, with two modes of grain size. The larger mode is exclusively quartz, and the smaller mode includes all grain types listed above, mostly angular in shape. Porosity is reduced by cementation by dominated by interparticle origin, accounting for  $>90\%$  of visible porosity. Minor amounts of porosity occur within individual, isolated chert grains, and patches of clayey matrix. Multiple hydrocarbon stringers reside in semi-parallel bands, visible on the macro scale.

#### **Sample # 19**

Sandstone – Quartz arenite. Both monocrystalline and undulose quartz grains are abundant, and chert is common. Ghost silica grains and overgrowths are sparse. Patches of cherty? Cements occur with microporosity in both grains themselves and the surrounding cherty cement. The cherty cement patches are sparse feature. Angular grains

and irregular grain contacts are common, a few with  $120^\circ$  compromise boundaries. Sparse stringers of residual hydrocarbon occur in sub-parallel pattern. Minor patches of clay matrix? Porosity is interparticle, and visually estimated at  $>90\%$  of the total porosity, but reduced from depositional conditions by cementation around quartz grains.

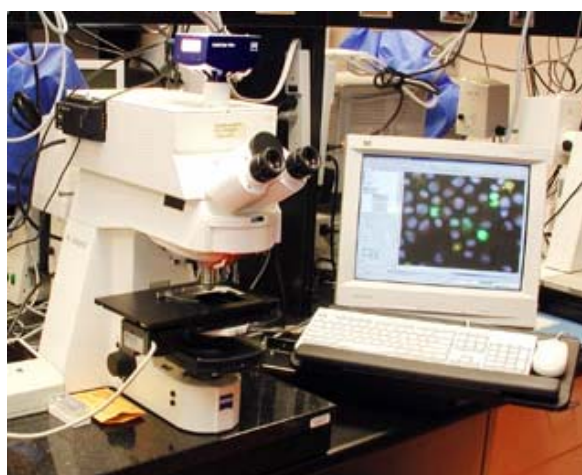
**APPENDIX B**

**PIA WORKFLOW USING IMAGEPRO PLUS©**

## I. OBTAINING THIN SECTION PHOTOS.

### Step 1. Obtain digitized photos of thin sections.

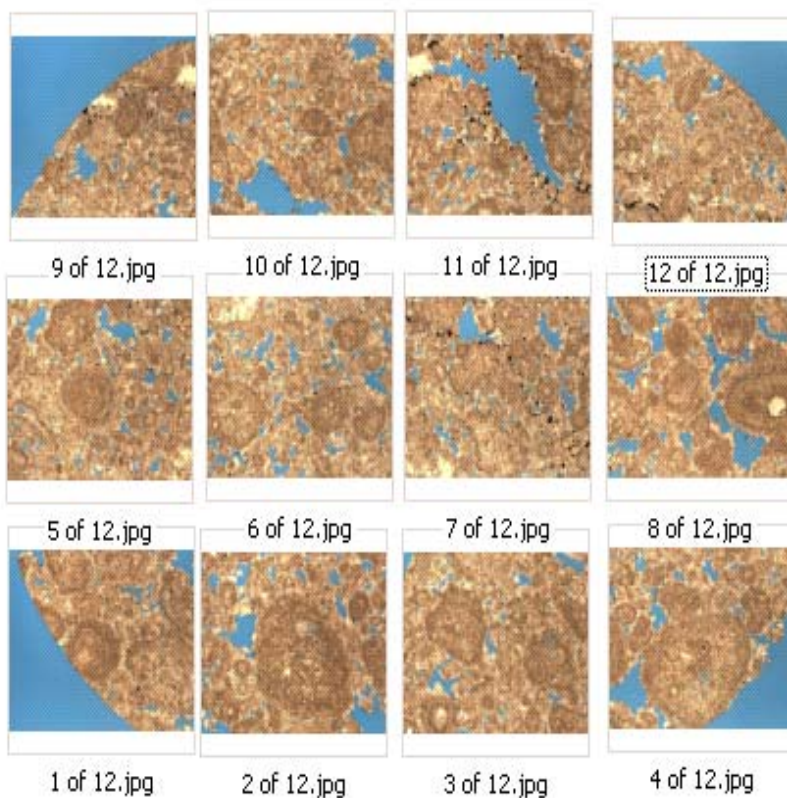
Obtain the best quality digital images possible, maintaining consistency in light, color, and detail. For this study a Zeiss Axioplan II imaging petrographic microscope was used in combination with the Zeiss Axiocam and Axiovision 3.1© imaging software Fig.B-1. Other imaging software such as Spot© and SpotBasic© were experimentally used, but generally gave slower results than the Axiovision program and were less user-friendly. Image light intensity was typically set at 27-45 milliseconds of exposure, adjusted when necessary to obtain maximum color contrast in both the live camera and snapshot formats. This is particularly important when the thin section possessed some slight differences in thickness across the surface of the thin section. All thin section photos used in the actual image analysis measurements were taken using a 2.5x objective and 10x ocular lens, resulting in image magnifications of 25x. Experiments at 12.5x, 100x, and 250x were done, but often resulted in individual pores larger than the viewfield, or a multitude of pores so small (ie. <20 microns diameter) that they were difficult to discern without continually 'zooming' in and out of the digital photo. Furthermore, 20 microns is about the thickness of a thin section, and thus the limit of resolution of the optical microscope. Anselmetti et al. (1998) recognized this limitation when evaluating microporosity. Such work with SEM was not the nature of this study, but could be a focus of future work.



**Figure B-1. Example setup of Petrographic Setup/Camera/and computer station. Image courtesy of [www.umanitoba.ca/.../GCCRD\\_Equipment\\_No3.htm](http://www.umanitoba.ca/.../GCCRD_Equipment_No3.htm)**

## Step 2. Sampling of the thin section.

The idea here is to sample the entire thin section. The ease and rapidity of measurements with the imaging software begs attention to the entire thin section. Workers such as Mowers and Budd (1996) have successfully used 25 viewfields at 100x magnification, but such was decided to maximize observation of the pores. This crude guide is superseded by better observation of the pores at different magnification. When the entire thin section is photographed, the best possible variation in individual pore characteristics can be observed and measured. Care should be taken to move the mechanical stage such that adjacent viewfields are captured. This is particularly important when summing all pores to obtain a total optical porosity for the given sample. The sampling routine in this study yields a tiled set of digital photos similar to the Figure B-2.

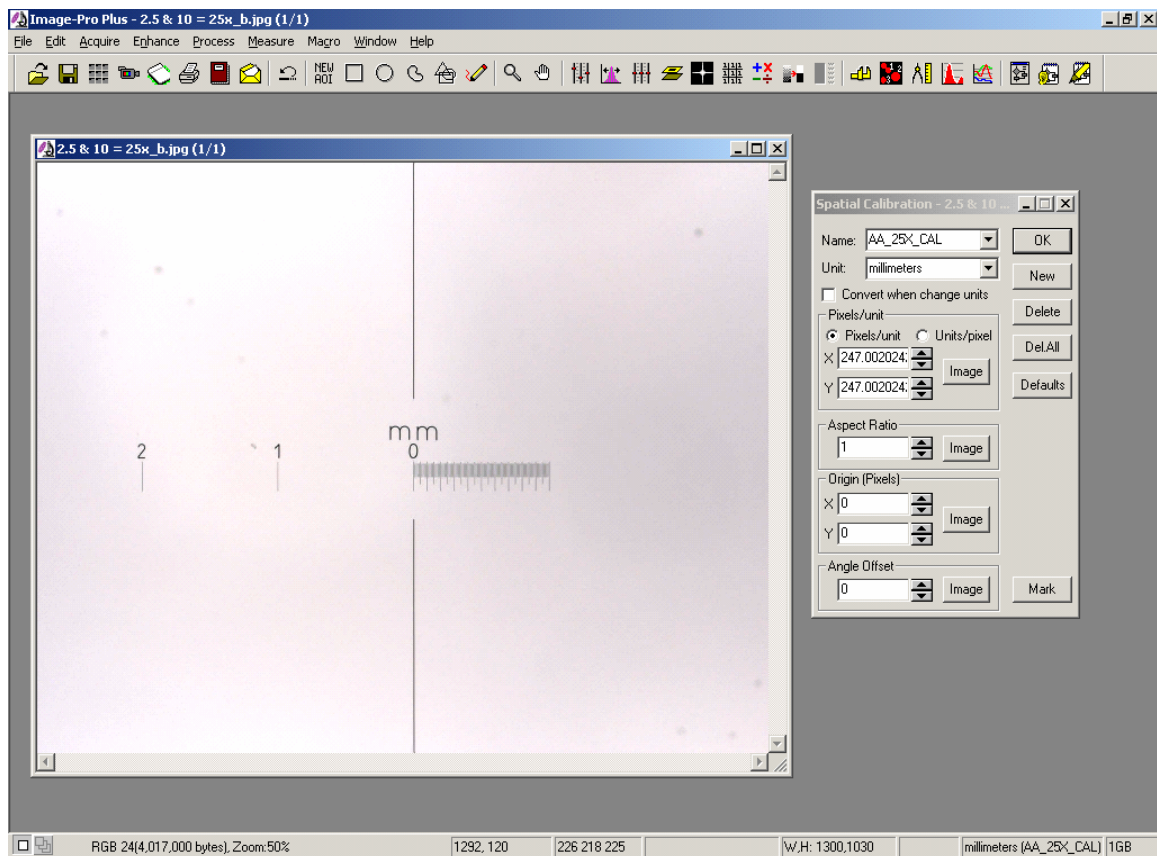


**Figure B-2. Mosaic image showing basic sampling procedure of an entire thin section viewfield.**

## II. USING IMAGEPRO PLUS©

### Step 1. Calibration

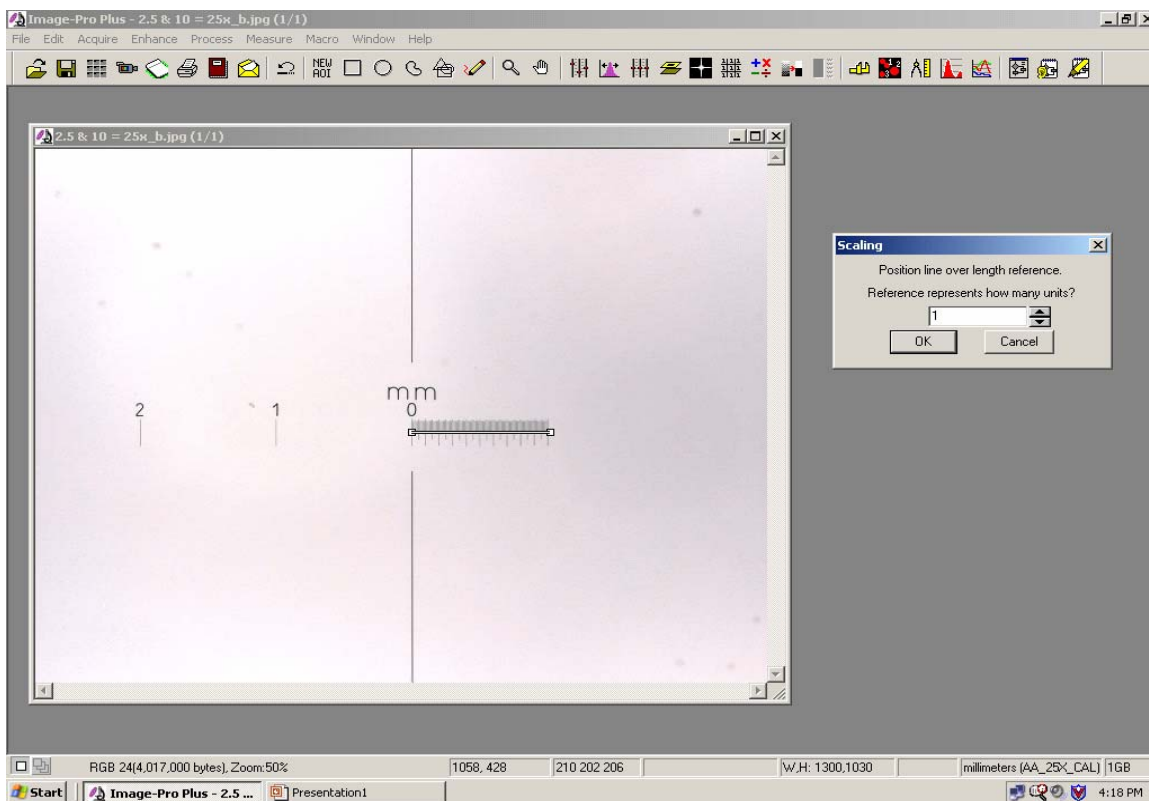
Serious errors in measurement will occur if proper calibration is not made prior to using the software. A calibration slide is provided with the software (Fig. B-3). One simply takes a digital photo of the slide (as outlined previously) and then opens the file in ImagePro Plus to determine spatial correspondence. Desired output units must be selected from the Spatial Calibration dialog box. Then the Image button in the Pixels/Units box must be selected.



**Figure B-3. Screen capture of Spatial Calibration dialog box used in calibration.**

## Step 2. Scaling

Scaling is simply the process of identifying a standard length used to calibrate the image. Using the digitized photo from the calibration slide (photo taken at the correct magnification), enter the correct units from the calibration slide. The Scaling dialog box will require the user to manually adjust the length of the reference bar to the known length on the photo (Figure B-4). This is done by dragging the small boxes at the ends of the reference bar to the desired locations.



**Figure B-4. Scaling dialog box and reference bar superimposed on digital image of calibration slide.**



### Step 3. Verify calibration using measurement tool.

To determine that the calibration is correct, select Measurements from the Measure menu. This dialog box (Fig. B-5) will appear. Select the line button and then drag the arrows across the calibration slide. A corresponding measurement label of L1 will appear with the line, and its length appears in the Measurements dialog box under the Measurements tab. The value should be 1mm (or very close to it) since millimeters was selected in the calibration and scaling steps previously. This same option can be used whenever length or area measurements are desired on individual objects, or to cross-check supposed lengths on grains or pores.

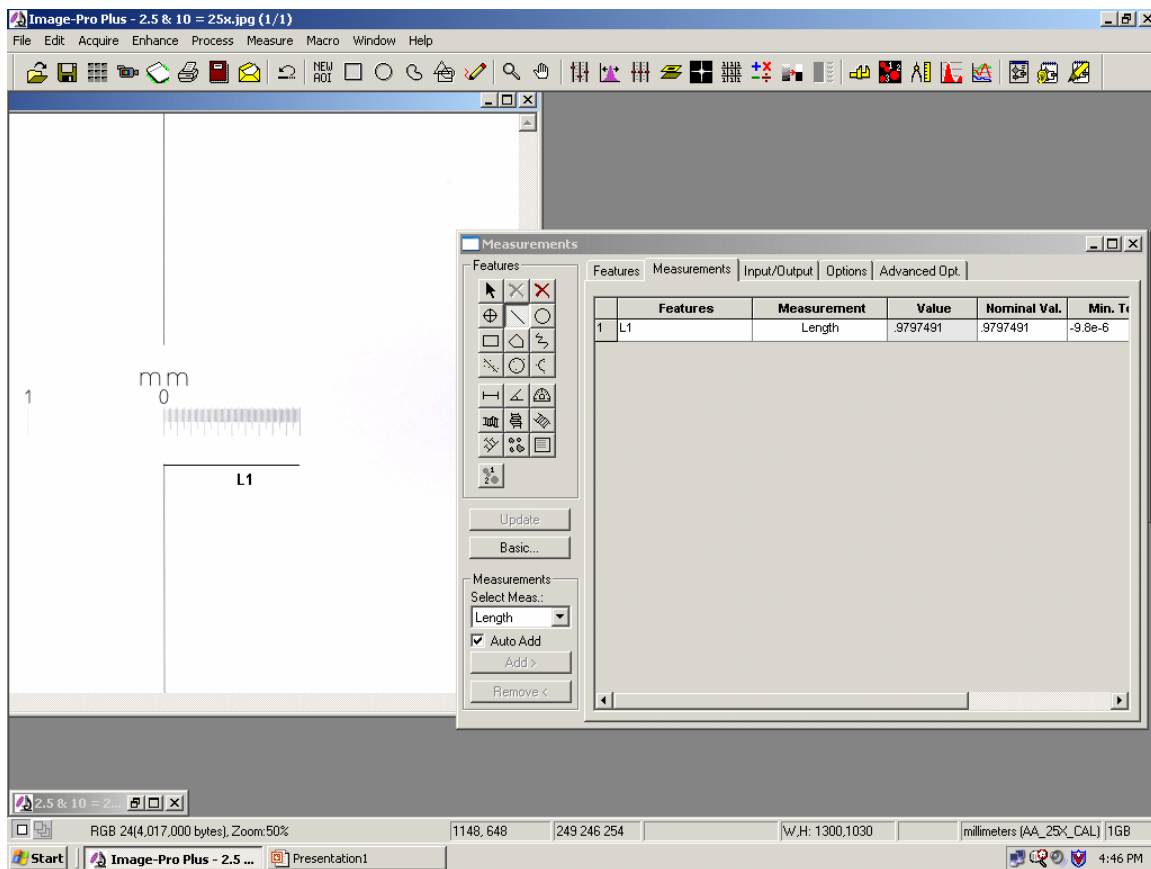
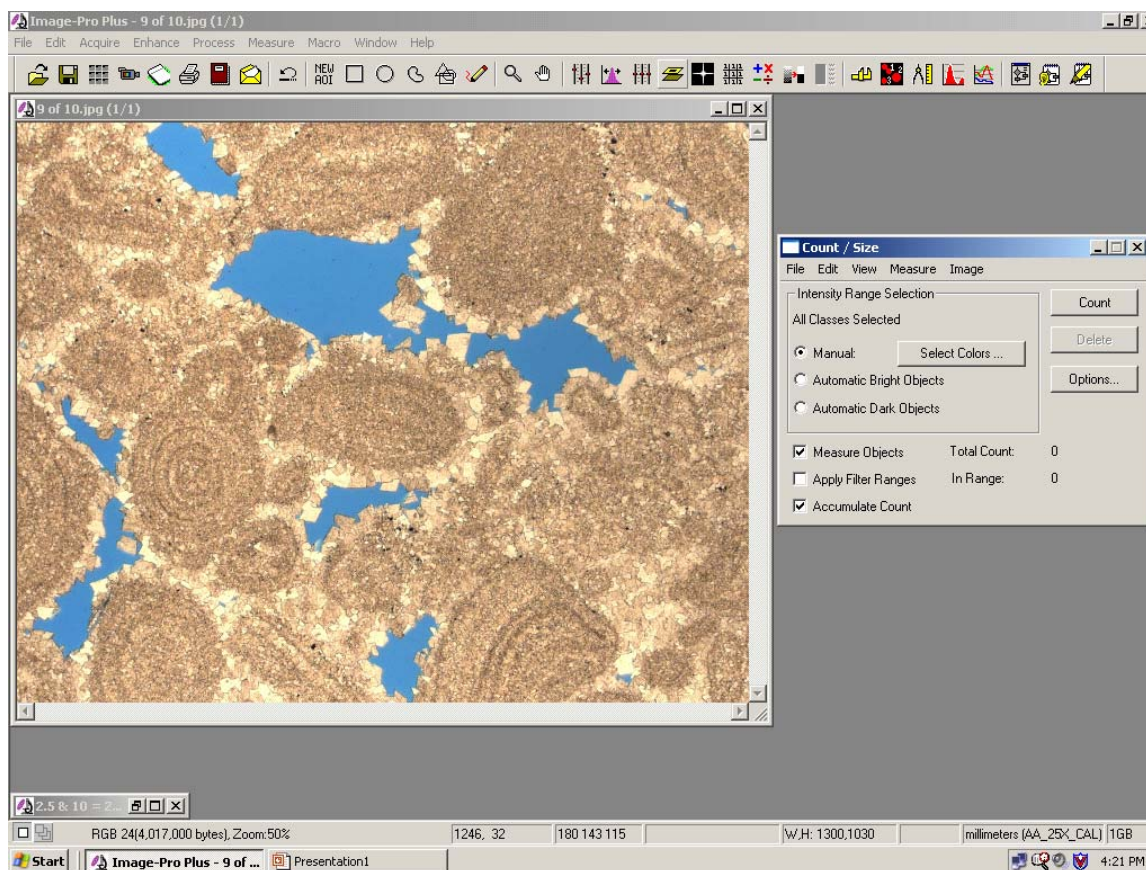


Figure B-5. Measurements dialog box showing verification of calibration process.

#### Step 4. Selection of Pore space in thin section.

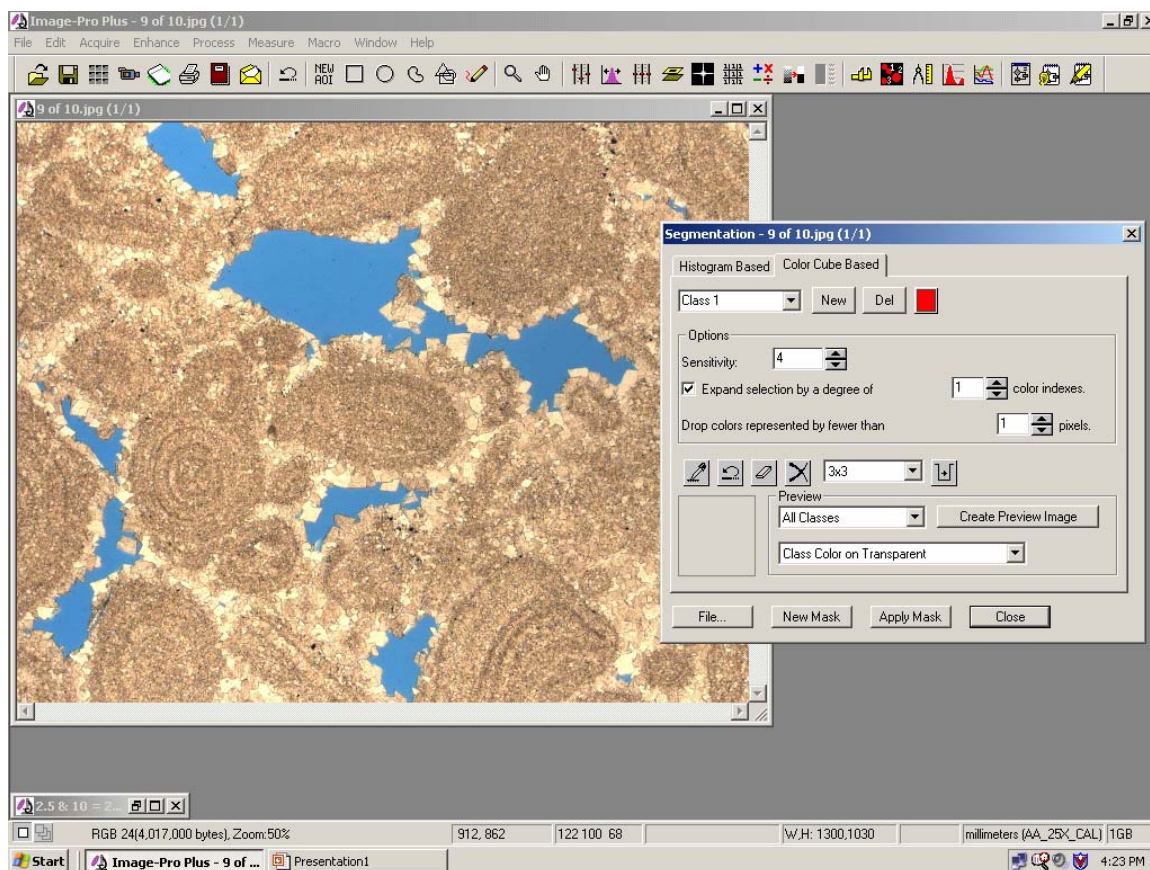
Use the Open File command to find the desired thin section digital photographs. They will automatically open to the dimensions shown below, the result of following the pattern outlined in digital image capturing described above. Since the thin sections were impregnated with blue epoxy during their preparation, the blue shown in plane light on the scope is the porosity. Since micropores may be inaccessible to the penetrating epoxy, the blue better represents effective porosity. Select the Count/Size option from the Measurements dialog box (Fig. B-6). With the “measure objects” and “accumulate count”, and “manual” button positively checked, push the Select Colors button.



**Figure B-6. Count/Size dialog box shown with example photomicrograph.**

## Step 5. Segmentation

Color segmentation should be set on the color cube tab. Sensitivities are left on default settings as shown in Figure B-7. A 3x3 pixel color cube is used to select the pores of interest. Larger pixel grid are available if consistently small pores are present, however using a consistent pixel cube is important to minimize error in selecting marginal areas. Press the eyedropper button and move the cursor over the desired area to select the color of interest (in this case blue).

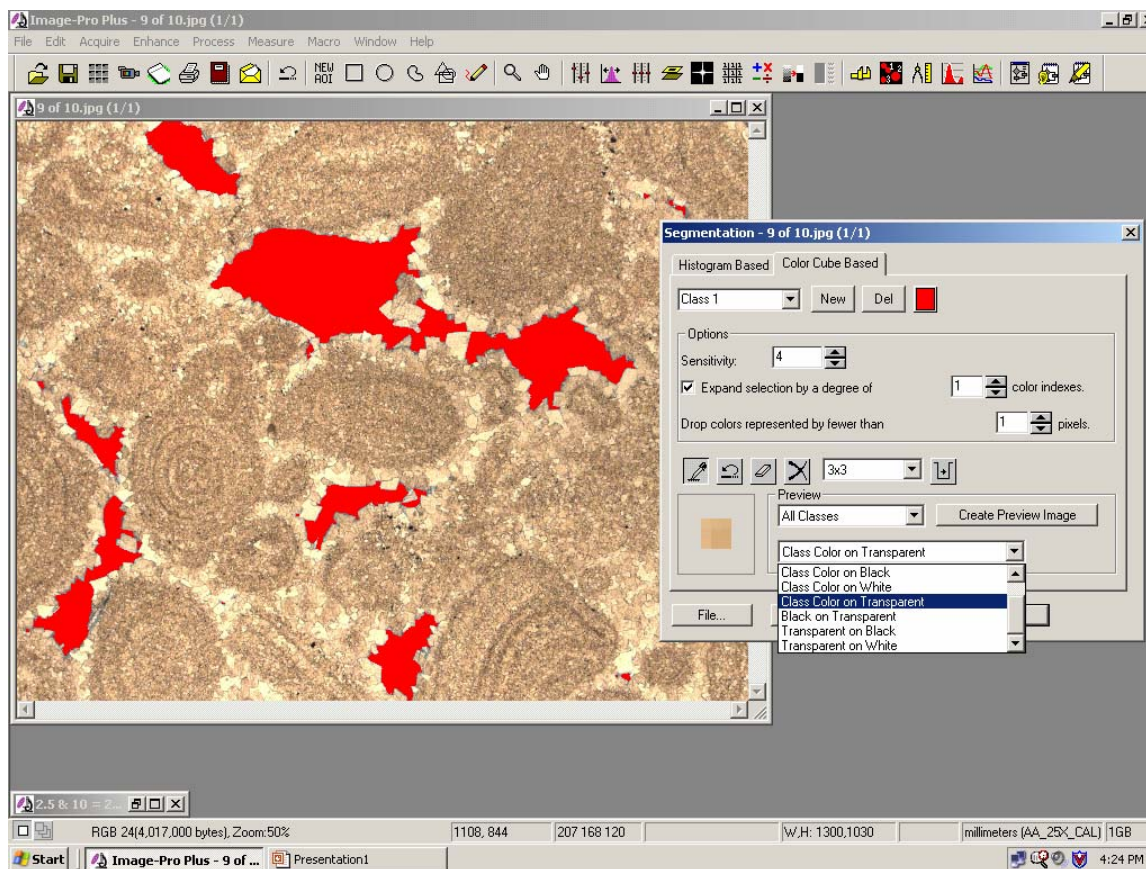


**Figure B-7. Dialog box showing color cube-based segmentation options.**



## Step 6. Assign False Color to desired objects.

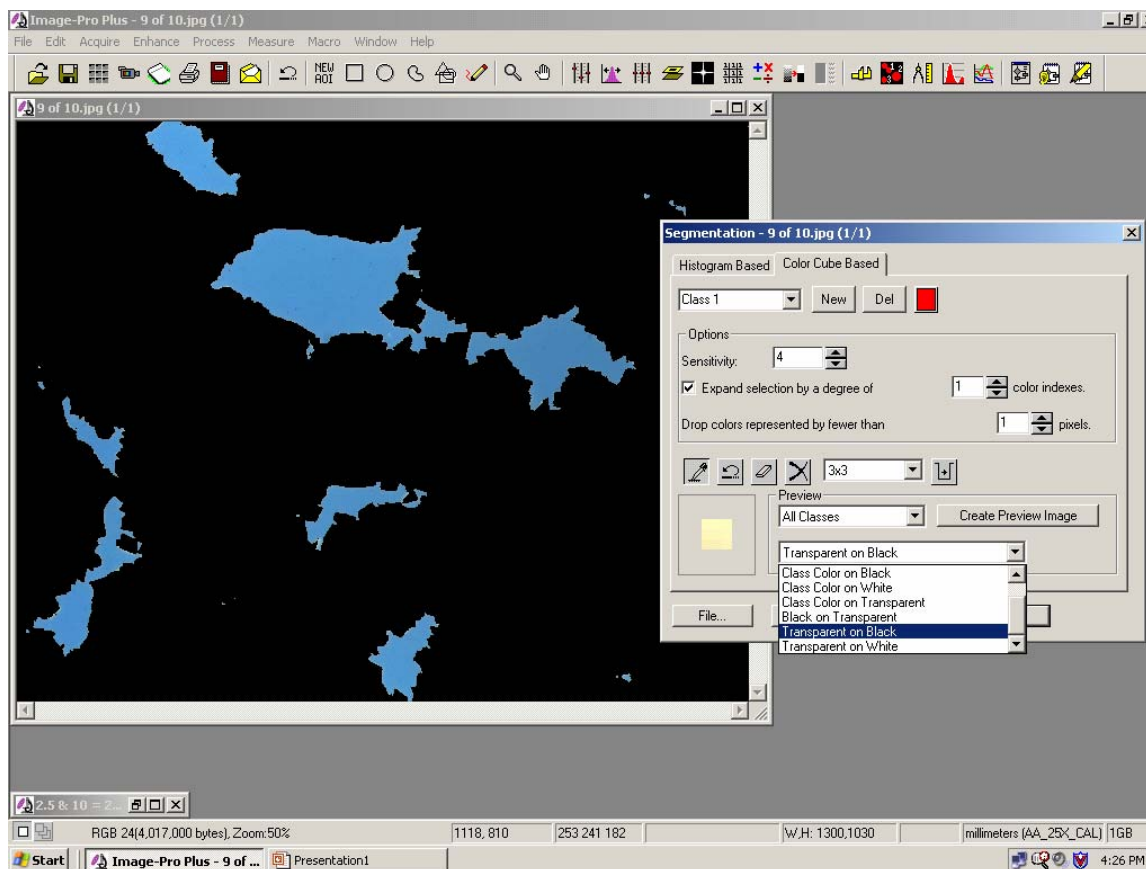
As the cursor is moved over desired pixel and selected, the pixels with 3x3 dimensions containing blue colors will be selected. This is an iterative process to select the blue pixels thereby assigning the false color. The color can be changed using the color button on the segmentation dialog box. Care should be taken to initially select the class color (red) on a transparent background (Fig. B-8). It is then advised to check for “overpicking” of pixels. This is done by toggling back and forth between the color class on transparent, transparent on black, and transparent on white backgrounds. Additional background options are also available from the drop down menu. All of this back-and-forth toggling is done to ascertain that only the desired blue pixels have been selected. This minimizes the error in picking marginal areas beyond the boundaries of the pore, or “underpicking” pore pixels.



**Figure B-8. False color assignment of picked objects (pores), and menu for background color toggles.**

Step 7. Double check selection of pores using background toggle.

The menu allows the user to choose various backgrounds (Fig. B-9). Toggling back and forth from “class color on transparent” to “transparent on black” allows for the most accurate choosing of desired objects, particularly at object margins or where variations in thin section thickness have occurred.



**Figure B-9. Background toggle example showing iterative process in selecting desired objects (pores).**

Step 8. Select the Count/Size option.

Under the measurements menu select the Count/Size option (Fig. B-10). The corresponding dialog box will appear. After the objects (pores) have been identified and assigned a false color, push the count button. Note the total count in the lower right portion of the dialog box. Count of dozens to hundreds of objects are typical for this project given the magnifications used.

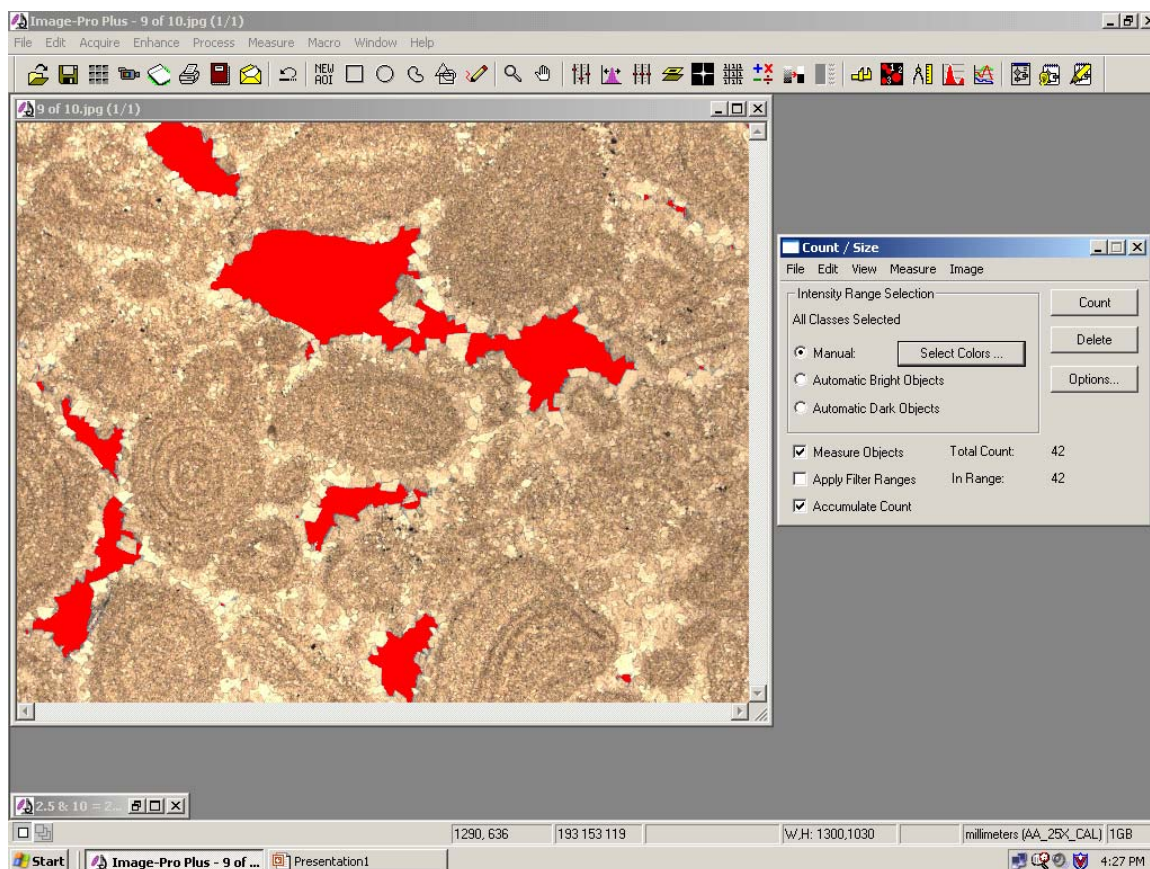


Figure B-10. Count/size dialog box showing total counted objects.



Step 9. Select “No Borders” from the count/size options dialog box.

The options button on the count/size dialog box shows several options regarding the areas of interest. Select the ‘No Borders’ option (Fig. B-11). This will allow the program to include all pixels up to the borders of the view field. Otherwise, any object (pore) which has selected pixels in contact with the photo border will not be included. In order to obtain a total porosity for the thin section, all border should be included. If adjacent view field were captured as adjacent digital photos, then this procedure should be most accurate in obtaining the total pore space across the entire thin section.

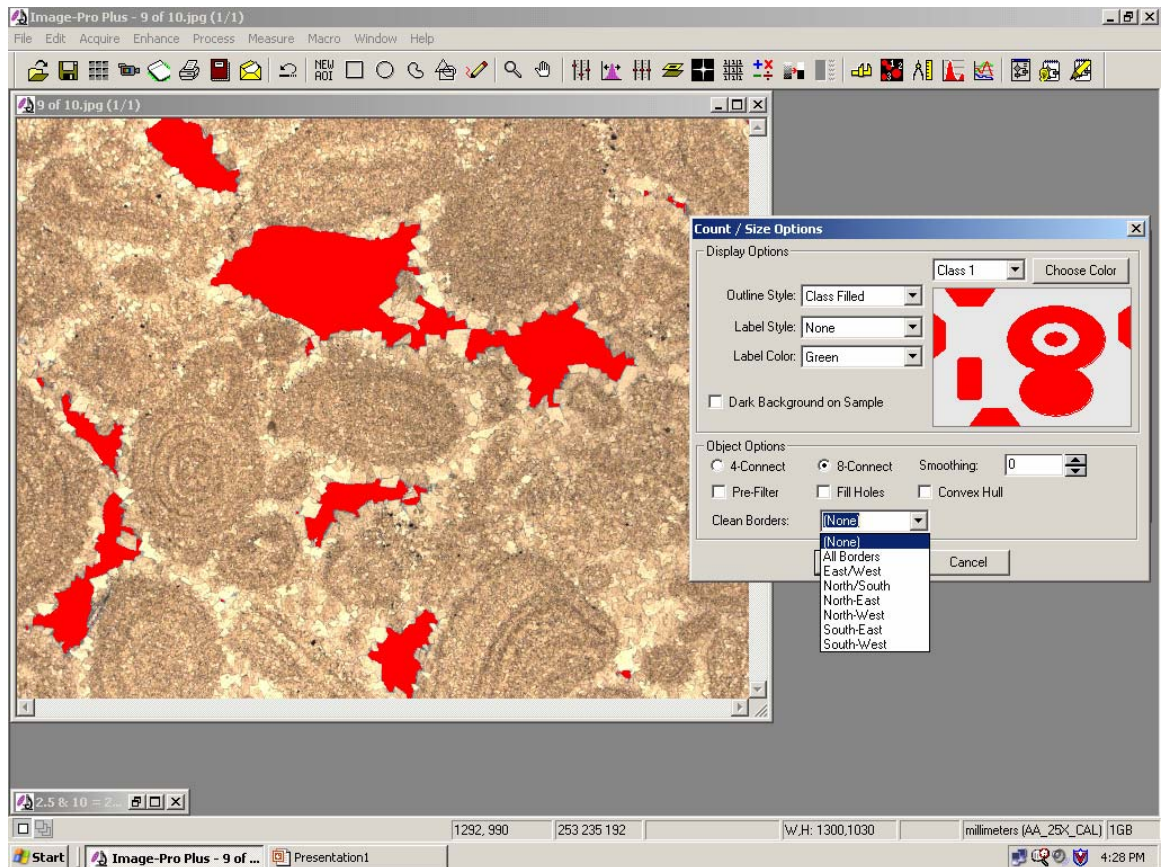
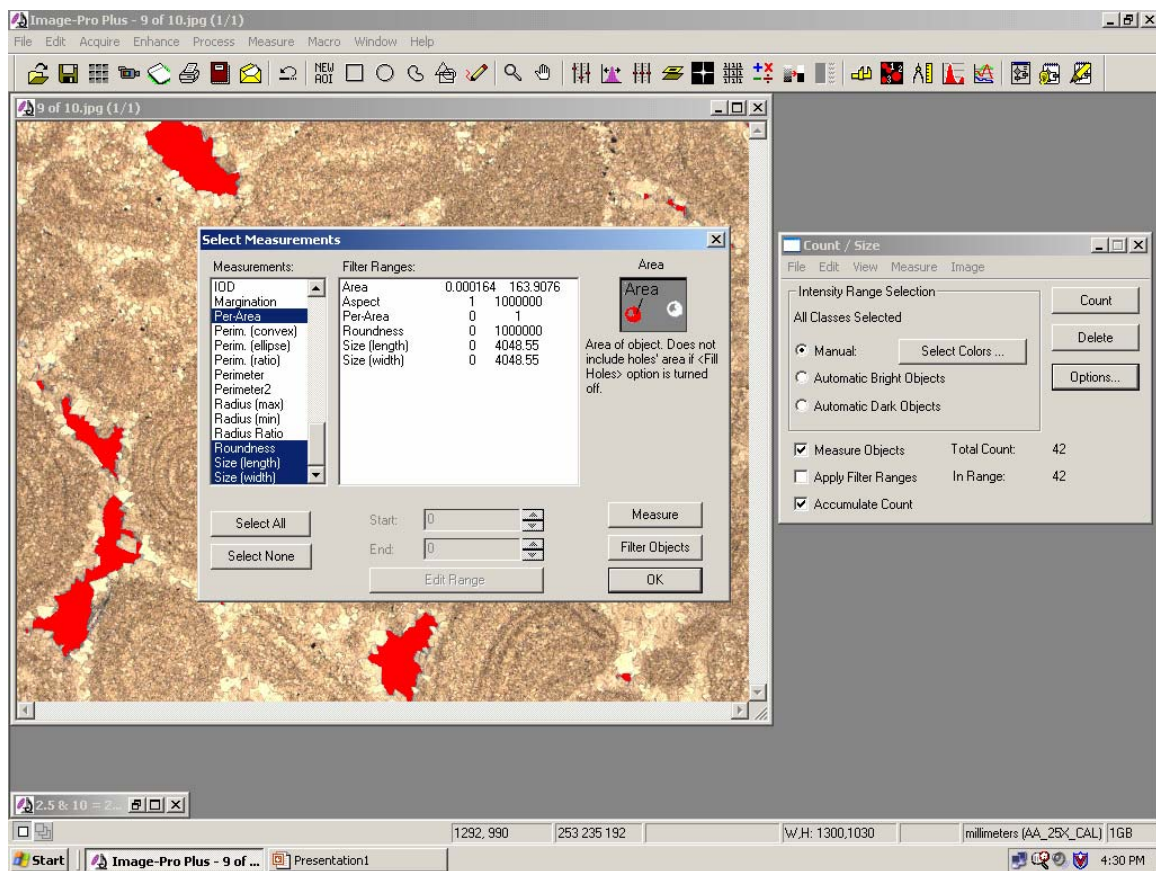


Figure B-11. Count/Size - Options dialog box showing selection of No Borders.

### Step 10. Selection of Measurements.

Under the measure menu, select the “Select Measurements” option. A corresponding dialog box will appear (Fig. B-12). All measurements can be selected, but would include things not used in this project. My experience has shown that the volume of data associated with all measurements becomes too much to manage, and occasionally overwhelms the program, causing it to unpredictably shut down. Therefore, the following six measurements should be manually selected: Area, Aspect, Per-Area, Roundness, Size (length), and Size (width). The program will measure these dimension on each selected object (pore), including maximum and minimum values of each where appropriate.

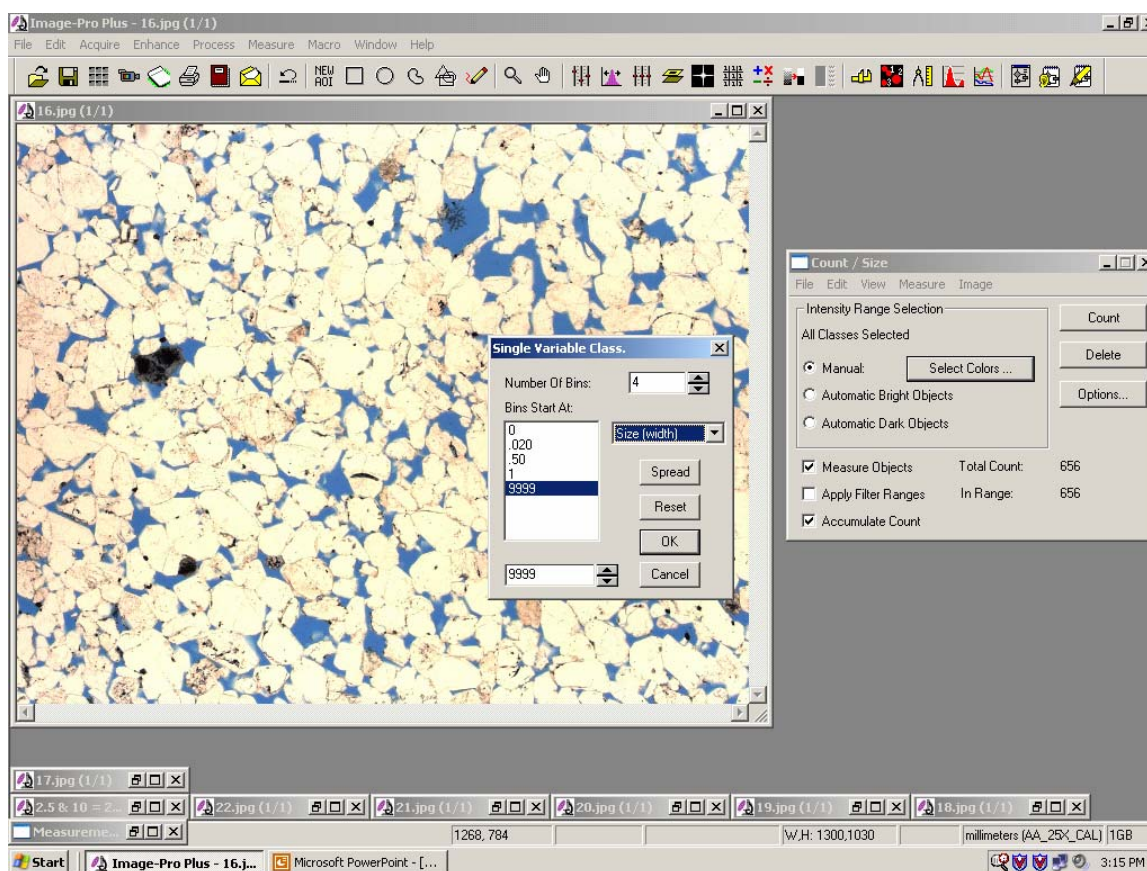


**Figure B-12.** Select Measurements dialog box showing six relevant measurement types for this study.



### Step 11. Single Variable Class.

This step will essentially sort the measured objects into a particular bin class. To do so, choose the Single Variable Class option from the Measure menu of the Count/Size dialog box (Fig. B-13). First set the bin type (i.e. size width), then set the number of bins to 4. The software will automatically place bin parameters in the window. These must be manually reset to desired cutoff values. For this study 0, 0.02, 0.5, 1.0, and 9999 were chosen. All objects will fall into one of these classified bin sizes, according to the millimeter units specified in the initial calibration setup.



**Figure B-13. Single Variable class dialog box showing five bin size cutoff values.**

## Step 12. Classification

This data table will appear after the single variable class has been specified (Fig. B-14). To obtain the maximum information about individual measurements, select View All from the View menu of the Classification dialog box. Some basic statistics (i.e. mean, standard deviation, and minimum/maximum values will also be displayed with each bin class. This data is now prepared for export into Excel using the DDE (Dynamic Data Exchange) option.

The screenshot shows the Image-Pro Plus software interface. The main window displays a micrograph of a material with two classes: red and cyan. The Classification dialog box is open, showing a table of measurement data. The table has the following columns: % Objects, Total Area, % Area, Mean Area, Std.dev. Area, Min Area, Max Area, and Total Aspect. The data is as follows:

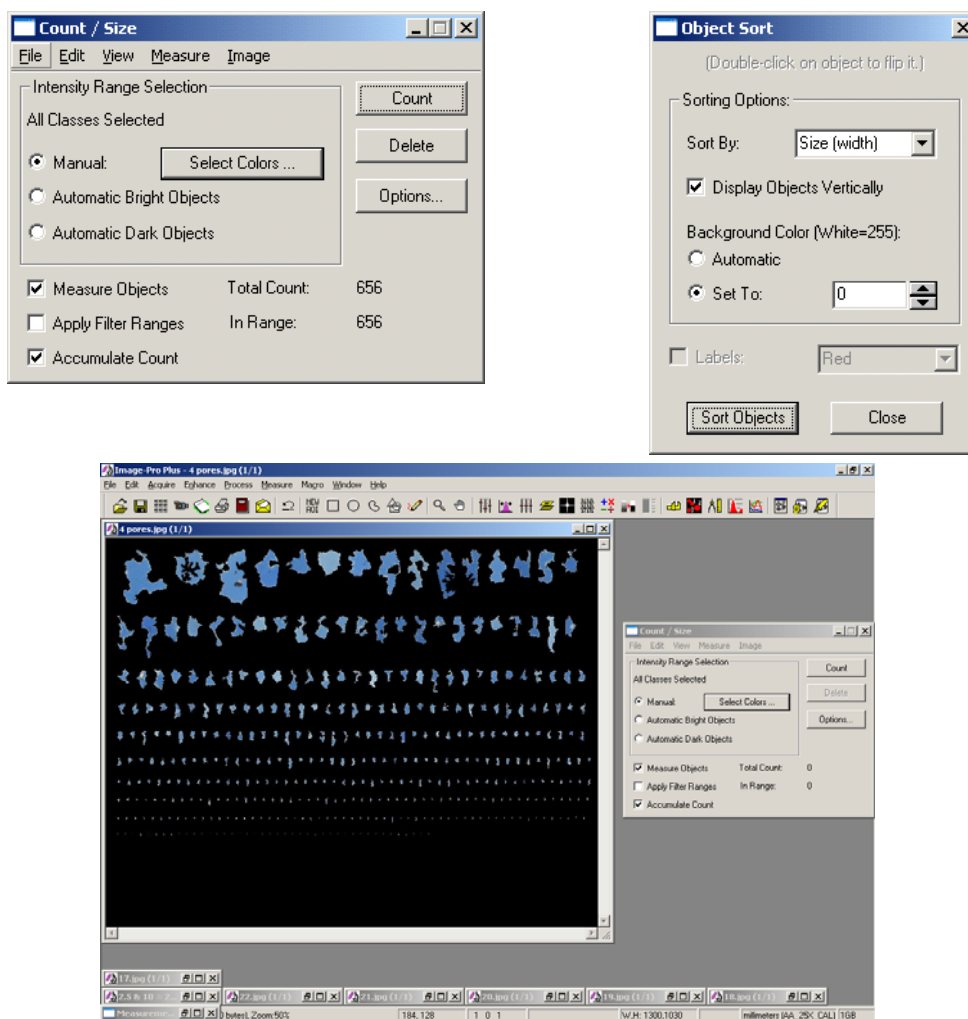
Class	% Objects	Total Area	% Area	Mean Area	Std.dev. Area	Min Area	Max Area	Total Aspect
Class 1 (Red)	51.676830	.03356878	1.4171777	.00009902	.00015202	.00001665	.00101622	575.13190
Class 2 (Cyan)	48.323170	2.3351381	98.582825	.00736636	.01368713	.00033318	.12046447	667.9870
Mean <measure>	0	0	0	0	0	0	0	0
Std.Dev. <measure>	0	0	0	0	0	0	0	0
Min. <measure>								
Max. <measure>								
Class Range								

The Classification dialog box also shows the 'View ALL' option selected in the View menu. The 'Count / Size' dialog box is also visible, showing 'All Classes Selected' and 'Manual' selection mode.

**Figure B-14.** Classification dialog box showing measurement data preparatory to export into spreadsheet.

### Step 13. Creating a sorted objects file.

The first purpose in creating a sorted objects image and file is to minimize error on subsequent analyses of the objects. By completing this step, the user need not rapid the objects (pores) for any given view field of the thin section. To create a sorted object image, select Object Sort from the Image menu of the Count/Size dialog box. The window will request a sorting parameter. For this study, the size (width) or area option was the most useful choice. Background color must be set to 0, which the computer recognized as any non-black pixel. Figure B-15 shows the sorted object image which can then be saved as a separate file. It is recommended that the file name for the sorted objects be linked with the original digital photo from whence it was derived.



**Figure B-15. Dialog boxes and sorted object image preparatory to saving as a linked file with the host thin section digital photo from whence it was derived.**

**APPENDIX C****PIA SUMMARY OF MEASUREMENTS ON THIN SECTIONS**

NW Australian Shelf		Average of entire thin section for pore...								
Sample #	Pore size (mm)	Objects (%)	Porosity Area (%)	Porosity Norm (%)	Mean Area (mm <sup>2</sup> )	Mean Aspect	Mean Roundness	Mean Size (length,mm)	Mean Size (width,mm)	
16	< 0.02	45.940	1.170	1.170	0.0001	1.823	1.104	0.010	0.005	
16	0.02 - 0.5	53.283	96.347	96.401	0.0087	1.980	2.417	0.133	0.078	
16	0.5 - 1.0	0.598	2.428	2.429	0.1883	1.466	14.577	0.829	0.613	
16	> 1.0	0.000	0.000	0.000	0.0000	0.000	0.000	0.000	0.000	
TOTAL			99.944	100.000						
19	< 0.02	62.856	3.506	3.510	0.0001	1.817	1.075	0.007	0.003	
19	0.02 - 0.5	37.722	96.374	96.490	0.0055	1.863	2.441	0.101	0.062	
19	0.5 - 1.0	0.000	0.000	0.000	0.0000	0.000	0.000	0.000	0.000	
19	> 1.0	0.000	0.000	0.000	0.0000	0.000	0.000	0.000	0.000	
TOTAL			99.880	100.000						
20	< 0.02	59.674	3.047	3.073	0.0001	1.753	1.083	0.009	0.004	
20	0.02 - 0.5	40.306	95.301	96.094	0.0052	1.980	2.382	0.100	0.059	
20	0.5 - 1.0	0.228	0.826	0.833	0.1940	1.557	12.632	0.824	0.597	
20	> 1.0	0.000	0.000	0.000	0.0000	0.000	0.000	0.000	0.000	
TOTAL			99.174	100.000						
21	< 0.02	66.202	3.173	3.169	0.0001	1.759	1.079	0.008	0.004	
21	0.02 - 0.5	34.633	93.529	93.402	0.0060	1.967	2.478	0.107	0.063	
21	0.5 - 1.0	0.406	3.434	3.429	0.2439	1.315	7.408	0.767	0.591	
21	> 1.0	0.000	0.000	0.000	0.0000	0.000	0.000	0.000	0.000	
TOTAL			100.136	100.000						
23	< 0.02	57.431	1.177	1.177	0.0001	1.731	1.078	0.008	0.003	
23	0.02 - 0.5	42.313	88.333	88.333	0.0098	2.060	2.839	0.146	0.084	
23	0.5 - 1.0	0.352	10.490	10.490	0.2385	1.852	11.972	0.950	0.634	
23	> 1.0	0.000	0.000	0.000	0.0000	0.000	0.000	0.000	0.000	
TOTAL			100.000	100.000						
24	< 0.02	71.429	7.008	7.008	0.0001	1.889	1.084	0.006	0.003	
24	0.02 - 0.5	29.932	92.992	92.992	0.0076	1.845	2.665	0.118	0.073	
24	0.5 - 1.0	0.000	0.000	0.000	0.0000	0.000	0.000	0.000	0.000	
24	> 1.0	0.000	0.000	0.000	0.0000	0.000	0.000	0.000	0.000	
TOTAL			100.000	100.000						
27	< 0.02	65.127	2.927	2.927	0.0001	1.813	1.086	0.009	0.004	
27	0.02 - 0.5	34.839	93.689	93.689	0.0062	1.915	2.399	0.104	0.063	
27	0.5 - 1.0	0.147	3.384	3.384	0.1873	1.543	10.647	0.742	0.525	
27	> 1.0	0.000	0.000	0.000	0.0000	0.000	0.000	0.000	0.000	
TOTAL			100.000	100.000						

Happy Field		Average of entire thin section for pore...							
Sample #	Pore size (mm)	Objects (%)	Porosity Area (%)	Porosity Norm (%)	Mean Area (mm <sup>2</sup> )	Mean Aspect	Mean Roundness	Mean Size (length,mm)	Mean Size (width,mm)
19-3:4923.2	< 0.02	64.358	1.896	1.896	0.0001	1.728	1.095	0.008	0.004
19-3:4923.2	0.02 - 0.5	35.631	97.626	97.626	0.0085	1.953	2.947	0.125	0.074
19-3:4923.2	0.5 - 1.0	0.117	0.477	0.477	0.1676	1.896	16.479	0.875	0.556
19-3:4923.2	> 1.0	0.000	0.000	0.000	0.0000	0.000	0.000	0.000	0.000
TOTAL			100.000	100.000					
19-3:4925.0	< 0.02	62.641	3.667	3.667	0.0001	1.827	1.100	0.010	0.005
19-3:4925.0	0.02 - 0.5	37.348	95.635	95.635	0.0064	1.994	2.556	0.109	0.063
19-3:4925.0	0.5 - 1.0	0.228	0.698	0.698	0.3031	1.821	10.076	1.056	0.611
19-3:4925.0	> 1.0	0.000	0.000	0.000	0.0000	0.000	0.000	0.000	0.000
TOTAL			100.000	100.000					
19-3:4956.5	< 0.02	78.122	11.367	11.367	0.0001	1.791	1.086	0.008	0.004
19-3:4956.5	0.02 - 0.5	22.915	87.051	87.051	0.0031	1.789	2.407	0.075	0.046
19-3:4956.5	0.5 - 1.0	0.104	1.581	1.581	0.3412	1.563	4.240	0.927	0.616
19-3:4956.5	> 1.0	0.000	0.000	0.000	0.0000	0.000	0.000	0.000	0.000
TOTAL			100.000	100.000					
19-3:4972.5	< 0.02	75.054	14.999	14.999	0.0001	1.788	1.088	0.010	0.005
19-3:4972.5	0.02 - 0.5	24.946	85.001	85.001	0.0020	1.857	2.224	0.065	0.039
19-3:4972.5	0.5 - 1.0	0.000	0.000	0.000	0.0000	0.000	0.000	0.000	0.000
19-3:4972.5	> 1.0	0.000	0.000	0.000	0.0000	0.000	0.000	0.000	0.000
TOTAL			100.000	100.000					
19-7:4956.0	< 0.02	77.113	10.973	10.973	0.0001	1.746	1.098	0.009	0.004
19-7:4956.0	0.02 - 0.5	22.887	89.027	89.027	0.0031	1.925	3.011	0.079	0.046
19-7:4956.0	0.5 - 1.0	0.000	0.000	0.000	0.0000	0.000	0.000	0.000	0.000
19-7:4956.0	> 1.0	0.000	0.000	0.000	0.0000	0.000	0.000	0.000	0.000
TOTAL			100.000	100.000					
19-7:5009	< 0.02	76.125	16.554	16.925	0.0001	10.799	1.427	0.015	0.005
19-7:5009	0.02 - 0.5	25.013	77.483	79.219	0.0025	2.029	2.306	0.073	0.042
19-7:5009	0.5 - 1.0	0.000	3.772	3.856	0.0000	0.000	0.000	0.000	0.000
19-7:5009	> 1.0	0.000	0.000	0.000	0.0000	0.000	0.000	0.000	0.000
TOTAL			97.809	100.000					

Womack Hill Field		Average of entire thin section for pore...							
Sample #	Pore size (mm)	Objects (%)	Porosity Area (%)	Porosity Norm (%)	Mean Area (mm <sup>2</sup> )	Mean Aspect	Mean Roundness	Mean Size (length,mm)	Mean Size (width,mm)
P4575:11,120	< 0.02	78.086	23.075	23.075	0.0001	2.027	1.119	0.014	0.007
P4575:11,120	0.02 - 0.5	21.914	76.925	76.925	0.0023	1.668	2.416	0.063	0.042
P4575:11,120	0.5 - 1.0	0.000	0.000	0.000	0.0000	0.000	0.000	0.000	0.000
P4575:11,120	> 1.0	0.000	0.000	0.000	0.0000	0.000	0.000	0.000	0.000
TOTAL			100.000	100.000					
P4575:11,129	< 0.02	70.322	11.412	11.412	0.0002	1.969	1.142	0.016	0.008
P4575:11,129	0.02 - 0.5	29.678	88.588	88.588	0.0038	1.817	2.561	0.080	0.050
P4575:11,129	0.5 - 1.0	0.000	0.000	0.000	0.0000	0.000	0.000	0.000	0.000
P4575:11,129	> 1.0	0.000	0.000	0.000	0.0000	0.000	0.000	0.000	0.000
TOTAL			100.000	100.000					
P4575: 11,146	< 0.02	73.016	20.285	20.285	0.0002	1.980	1.134	0.016	0.008
P4575: 11,146	0.02 - 0.5	26.984	79.715	79.715	0.0018	1.806	2.374	0.062	0.038
P4575: 11,146	0.5 - 1.0	0.000	0.000	0.000	0.0000	0.000	0.000	0.000	0.000
P4575: 11,146	> 1.0	0.000	0.000	0.000	0.0000	0.000	0.000	0.000	0.000
TOTAL			100.000	100.000					
P4575: 11,156	< 0.02	71.859	13.490	13.564	0.0002	1.964	1.146	0.016	0.008
P4575: 11,156	0.02 - 0.5	28.058	81.408	81.854	0.0026	1.901	2.597	0.073	0.043
P4575: 11,156	0.5 - 1.0	0.141	4.558	4.582	0.2356	1.241	5.615	0.677	0.600
P4575: 11,156	> 1.0	0.000	0.000	0.000	0.0000	0.000	0.000	0.000	0.000
TOTAL			99.456	100.000					
P4575: 11,174	< 0.02	60.417	11.542	11.542	0.0002	1.960	1.172	0.017	0.009
P4575: 11,174	0.02 - 0.5	39.583	88.458	88.458	0.0023	1.758	2.061	0.065	0.041
P4575: 11,174	0.5 - 1.0	0.000	0.000	0.000	0.0000	0.000	0.000	0.000	0.000
P4575: 11,174	> 1.0	0.000	0.000	0.000	0.0000	0.000	0.000	0.000	0.000
TOTAL			100.000	100.000					
P4575: 11,192	< 0.02	79.966	45.231	44.665	0.0002	1.908	1.117	0.016	0.009
P4575: 11,193	0.02 - 0.5	20.647	56.035	55.335	0.0010	1.654	1.815	0.045	0.030
P4575: 11,194	0.5 - 1.0	0.000	0.000	0.000	0.0000	0.000	0.000	0.000	0.000
P4575: 11,195	> 1.0	0.000	0.000	0.000	0.0000	0.000	0.000	0.000	0.000
TOTAL			101.266	100.000					
P1591: 11,405	< 0.02	72.989	32.563	32.563	0.0002	1.960	1.112	0.015	0.008
P1591: 11,405	0.02 - 0.5	27.011	67.437	67.437	0.0013	1.627	1.755	0.048	0.032
P1591: 11,405	0.5 - 1.0	0.000	0.000	0.000	0.0000	0.000	0.000	0.000	0.000
P1591: 11,405	> 1.0	0.000	0.000	0.000	0.0000	0.000	0.000	0.000	0.000
TOTAL			100.000	100.000					
P1591: 11,411	< 0.02	87.500	34.810	34.810	0.0001	1.931	1.141	0.014	0.007
P1591: 11,411	0.02 - 0.5	12.500	65.190	65.190	0.0017	1.791	2.248	0.062	0.038
P1591: 11,411	0.5 - 1.0	0.000	0.000	0.000	0.0000	0.000	0.000	0.000	0.000
P1591: 11,411	> 1.0	0.000	0.000	0.000	0.0000	0.000	0.000	0.000	0.000
TOTAL			100.000	100.000					
P1591: 11,413	< 0.02	92.603	75.851	75.851	0.0002	2.144	1.102	0.014	0.008
P1591: 11,413	0.02 - 0.5	9.862	24.149	24.149	0.0008	1.223	1.535	0.041	0.031
P1591: 11,413	0.5 - 1.0	0.000	0.000	0.000	0.0000	0.000	0.000	0.000	0.000
P1591: 11,413	> 1.0	0.000	0.000	0.000	0.0000	0.000	0.000	0.000	0.000
TOTAL			100.000	100.000					

P1591: 11,515	< 0.02	80.831	44.374	44.374	0.0002	1.999	1.145	0.015	0.008
P1591: 11,515	0.02 - 0.5	19.169	55.626	55.626	0.0009	1.572	2.103	0.043	0.029
P1591: 11,515	0.5 - 1.0	0.000	0.000	0.000	0.0000	0.000	0.000	0.000	0.000
P1591: 11,515	> 1.0	0.000	0.000	0.000	0.0000	0.000	0.000	0.000	0.000
TOTAL			100.000	100.000					

P1591: 11,528	< 0.02	53.078	5.504	5.504	0.0002	1.945	1.130	0.015	0.008
P1591: 11,528	0.02 - 0.5	46.922	94.496	94.496	0.0040	1.709	2.318	0.080	0.051
P1591: 11,528	0.5 - 1.0	0.000	0.000	0.000	0.0000	0.000	0.000	0.000	0.000
P1591: 11,528	> 1.0	0.000	0.000	0.000	0.0000	0.000	0.000	0.000	0.000
TOTAL			100.000	100.000					



Vocation Field	Average of entire thin section for pore...								
	Pore size (mm)	Objects (%)	Porosity Area (%)	Porosity Norm (%)	Mean Area (mm <sup>2</sup> )	Mean Aspect	Mean Roundness	Mean Size (length,mm)	Mean Size (width,mm)
2935:14,078	< 0.02	60.927	12.195	12.195	0.0002	2.189	1.206	0.017	0.008
2935:14,078	0.02 - 0.5	39.073	87.805	87.805	0.0020	1.818	2.224	0.067	0.040
2935:14,078	0.5 - 1.0	0.000	0.000	0.000	0.0000	0.000	0.000	0.000	0.000
2935:14,078	> 1.0	0.000	0.000	0.000	0.0000	0.000	0.000	0.000	0.000
TOTAL			100.000	100.000					
2935:14,144	< 0.02	54.430	15.096	15.096	0.0002	24.822	1.159	0.017	0.009
2935:14,144	0.02 - 0.5	45.570	84.904	84.904	0.0030	1.878	2.320	0.078	0.046
2935:14,144	0.5 - 1.0	0.000	0.000	0.000	0.0000	0.000	0.000	0.000	0.000
2935:14,144	> 1.0	0.000	0.000	0.000	0.0000	0.000	0.000	0.000	0.000
TOTAL			100.000	100.000					
2935:14,150	< 0.02	50.046	3.754	3.754	0.0002	7.123	1.157	0.017	0.009
2935:14,150	0.02 - 0.5	49.861	90.011	90.011	0.0046	1.855	2.465	0.092	0.056
2935:14,150	0.5 - 1.0	0.233	6.235	6.235	0.1869	1.703	9.176	0.796	0.558
2935:14,150	> 1.0	0.000	0.000	0.000	0.0000	0.000	0.000	0.000	0.000
TOTAL			100.000	100.000					
1599:13,987	< 0.02	43.185	0.614	0.614	0.0001	2.172	1.191	0.015	0.007
1599:13,987	0.02 - 0.5	55.372	52.280	52.280	0.0108	2.013	2.722	0.139	0.080
1599:13,987	0.5 - 1.0	1.299	30.050	30.050	0.2979	1.704	7.597	1.049	0.705
1599:13,987	> 1.0	0.756	17.055	17.055	1.4278	1.857	7.686	2.464	1.350
TOTAL			100.000	100.000					
1599:14,017	< 0.02	43.076	0.465	0.487	0.0005	1.928	1.211	0.024	0.013
1599:14,017	0.02 - 0.5	51.586	31.070	32.545	0.0467	2.135	2.835	0.300	0.149
1599:14,017	0.5 - 1.0	5.518	47.284	49.530	0.5954	2.105	4.883	1.391	0.776
1599:14,017	> 1.0	3.207	16.647	17.438	0.8540	2.021	5.347	1.622	0.856
TOTAL			95.465	100.000					
1599:14,059	< 0.02	44.832	1.140	1.140	0.0002	2.057	1.163	0.017	0.009
1599:14,059	0.02 - 0.5	53.664	69.213	69.213	0.0137	1.875	2.659	0.149	0.087
1599:14,059	0.5 - 1.0	2.645	16.623	16.623	0.4120	2.213	7.563	1.266	0.674
1599:14,059	> 1.0	2.235	13.023	13.023	1.6721	2.514	6.060	2.657	1.197
TOTAL			100.000	100.000					
1599:14,087	< 0.02	48.053	3.452	3.452	0.0002	3.337	1.169	0.017	0.009
1599:14,087	0.02 - 0.5	51.873	87.003	87.003	0.0050	1.924	2.461	0.098	0.057
1599:14,087	0.5 - 1.0	0.227	4.314	4.314	0.4431	2.029	8.797	1.541	0.745
1599:14,087	> 1.0	0.281	5.231	5.231	1.1636	1.106	4.217	1.633	1.441
TOTAL			100.000	100.000					
1599:14,131	< 0.02	46.920	2.231	2.231	0.0002	23.011	1.153	0.017	0.009
1599:14,131	0.02 - 0.5	52.858	85.808	85.808	0.0068	1.930	2.494	0.114	0.067
1599:14,131	0.5 - 1.0	0.444	11.961	11.961	0.2349	2.037	11.774	1.050	0.592
1599:14,131	> 1.0	0.000	0.000	0.000	0.0000	0.000	0.000	0.000	0.000
TOTAL			100.000	100.000					
5779:13,946	< 0.02	38.496	1.383	1.383	0.0002	2.058	1.160	0.016	0.008
5779:13,946	0.02 - 0.5	61.368	93.699	93.699	0.0076	1.942	2.641	0.124	0.072
5779:13,946	0.5 - 1.0	0.273	4.918	4.918	0.2110	1.535	11.468	0.896	0.668
5779:13,946	> 1.0	0.000	0.000	0.000	0.0000	0.000	0.000	0.000	0.000
TOTAL			100.000	100.000					

Appleton Field		Average of entire thin section for pore...							
Sample #	Pore size (mm)	Objects (%)	Porosity Area (%)	Porosity Norm (%)	Mean Area (mm <sup>2</sup> )	Mean Aspect	Mean Roundness	Mean Size (length,mm)	Mean Size (width,mm)
3986:12,944	< 0.02	0.000	0.000	0.000	0.0000	0.000	0.000	0.000	0.000
3986:12,944	0.02 - 0.5	0.000	0.000	0.000	0.0000	0.000	0.000	0.000	0.000
3986:12,944	0.5 - 1.0	0.000	0.000	0.000	0.0000	0.000	0.000	0.000	0.000
3986:12,944	> 1.0	0.000	0.000	0.000	0.0000	0.000	0.000	0.000	0.000
TOTAL									
3986:12,964	< 0.02	51.280	3.132	3.132	0.0002	2.016	1.167	0.017	0.009
3986:12,964	0.02 - 0.5	48.537	75.091	75.091	0.0049	1.864	2.331	0.092	0.055
3986:12,964	0.5 - 1.0	0.240	6.197	6.197	0.2980	2.118	7.476	1.015	0.593
3986:12,964	> 1.0	0.315	15.580	15.580	4.7004	1.299	7.622	3.137	2.600
TOTAL			100.000	100.000					
3986:12,970	< 0.02	44.119	2.622	2.622	0.0002	2.116	1.187	0.018	0.009
3986:12,970	0.02 - 0.5	55.697	88.617	88.617	0.0059	1.957	2.409	0.106	0.062
3986:12,970	0.5 - 1.0	0.550	8.761	8.761	0.3155	2.271	9.390	1.181	0.684
3986:12,970	> 1.0	0.000	0.000	0.000	0.0000	0.000	0.000	0.000	0.000
TOTAL			100.000	100.000					
3986:12,999	< 0.02	46.194	1.540	1.540	0.0001	2.166	1.158	0.014	0.007
3986:12,999	0.02 - 0.5	53.453	81.631	81.631	0.0070	1.933	2.764	0.117	0.069
3986:12,999	0.5 - 1.0	0.561	14.449	14.449	0.2297	1.699	13.352	0.910	0.619
3986:12,999	> 1.0	0.308	2.380	2.380	0.5072	1.565	11.337	1.469	1.037
TOTAL			100.000	100.000					
3986:13,024	< 0.02	48.790	4.298	4.298	0.0002	2.152	1.204	0.017	0.008
3986:13,024	0.02 - 0.5	51.000	76.753	76.753	0.0039	1.984	2.527	0.092	0.052
3986:13,024	0.5 - 1.0	0.625	12.526	12.526	0.4943	1.875	4.184	1.221	0.769
3986:13,024	> 1.0	0.645	6.422	6.422	1.4936	2.443	6.156	2.608	1.106
TOTAL			100.000	100.000					
4633-B:12,868	< 0.02	0.000	0.000	0.000	0.0000	0.000	0.000	0.000	0.000
4633-B:12,868	0.02 - 0.5	0.000	0.000	0.000	0.0000	0.000	0.000	0.000	0.000
4633-B:12,868	0.5 - 1.0	0.000	0.000	0.000	0.0000	0.000	0.000	0.000	0.000
4633-B:12,868	> 1.0	0.000	0.000	0.000	0.0000	0.000	0.000	0.000	0.000
TOTAL									
4633-B:12,948	< 0.02	49.856	4.463	4.463	0.0002	2.116	1.199	0.017	0.009
4633-B:12,948	0.02 - 0.5	50.110	91.231	91.231	0.0041	1.891	2.413	0.089	0.053
4633-B:12,948	0.5 - 1.0	0.207	4.306	4.306	0.4205	2.125	7.276	1.343	0.765
4633-B:12,948	> 1.0	0.000	0.000	0.000	0.0000	0.000	0.000	0.000	0.000
TOTAL			100.000	100.000					
4633-B:12,969	< 0.02	42.721	3.741	3.741	0.0002	2.010	1.175	0.018	0.009
4633-B:12,969	0.02 - 0.5	57.279	96.259	96.259	0.0039	1.880	2.307	0.089	0.053
4633-B:12,969	0.5 - 1.0	0.000	0.000	0.000	0.0000	0.000	0.000	0.000	0.000
4633-B:12,969	> 1.0	0.000	0.000	0.000	0.0000	0.000	0.000	0.000	0.000
TOTAL			100.000	100.000					
4633-B:12,984	< 0.02	45.411	1.760	1.760	0.0002	2.123	1.199	0.017	0.008
4633-B:12,984	0.02 - 0.5	54.216	81.330	81.330	0.0072	1.940	2.635	0.117	0.068
4633-B:12,984	0.5 - 1.0	0.525	14.179	14.179	0.2331	1.950	11.009	0.941	0.598
4633-B:12,984	> 1.0	0.290	2.731	2.731	0.7175	1.922	10.123	1.716	1.119
TOTAL			100.000	100.000					

4633-B:13,014	< 0.02	44.419	1.517	1.517	0.0002	2.049	1.138	0.016	0.008
4633-B:13,014	0.02 - 0.5	55.209	67.848	67.848	0.0065	1.906	2.518	0.110	0.064
4633-B:13,014	0.5 - 1.0	0.326	14.276	14.276	0.3130	2.156	8.728	1.111	0.615
4633-B:13,014	> 1.0	0.223	16.359	16.359	0.9803	1.863	10.038	1.807	1.151
TOTAL			100.000	100.000					

4633-B:13,016	< 0.02	50.693	8.204	8.204	0.0003	2.029	1.238	0.020	0.011
4633-B:13,016	0.02 - 0.5	48.931	68.430	68.430	0.0122	1.889	3.187	0.142	0.084
4633-B:13,016	0.5 - 1.0	0.514	12.210	12.210	0.3529	1.958	9.618	1.100	0.653
4633-B:13,016	> 1.0	0.223	11.156	11.156	1.9207	1.424	13.986	2.282	1.767
TOTAL			100.000	100.000					

3854:12,885	< 0.02	0.000	0.000	0.000	0.0000	0.000	0.000	0.000	0.000
3854:12,885	0.02 - 0.5	0.000	0.000	0.000	0.0000	0.000	0.000	0.000	0.000
3854:12,885	0.5 - 1.0	0.000	0.000	0.000	0.0000	0.000	0.000	0.000	0.000
3854:12,885	> 1.0	0.000	0.000	0.000	0.0000	0.000	0.000	0.000	0.000
TOTAL									

3854:12,890	< 0.02	83.962	64.731	64.731	0.0001	2.444	1.145	0.016	0.008
3854:12,890	0.02 - 0.5	26.731	35.269	35.269	0.0007	1.389	1.526	0.037	0.026
3854:12,890	0.5 - 1.0	0.000	0.000	0.000	0.0000	0.000	0.000	0.000	0.000
3854:12,890	> 1.0	0.000	0.000	0.000	0.0000	0.000	0.000	0.000	0.000
TOTAL			100.000	100.000					

3854:12,891.5	< 0.02	46.317	1.551	1.551	0.0002	1.882	1.140	0.016	0.009
3854:12,891.5	0.02 - 0.5	53.114	63.679	63.679	0.0068	1.850	2.356	0.102	0.062
3854:12,891.5	0.5 - 1.0	0.557	26.801	26.801	0.3833	1.918	7.021	1.142	0.680
3854:12,891.5	> 1.0	0.227	7.969	7.969	0.9967	1.618	8.533	1.821	1.154
TOTAL			100.000	100.000					

**APPENDIX D****NMR DATA FOR SANDSTONES**

Sample # 16					
Distribution	TC/1000	Porosity 0.2 TE			
TC (microsecs, $\mu$ s)	T2 (milliseconds, ms)	CCALC	Incremental phi (%)	normalized phi (%)	cumulative phi (%)
100	0.1	0	0	0	0
125.91082	0.12591082	0	0	0	0
158.53535	0.15853535	0	0	0	0
199.61316	0.19961316	0	0	0	0
251.33458	0.25133458	0	0	0	0
316.45743	0.31645743	0	0	0	0
398.45416	0.39845416	0	0	0	0
501.6969	0.5016969	0	0	0	0
631.69073	0.63169073	0	0	0	0
795.36694	0.79536694	0	0	0	0
1001.4531	1.0014531	0	0	0	0
1260.9379	1.2609379	0	0	0	0
1587.6572	1.5876572	0	0	0	0
1999.0322	1.9990322	0	0	0	0
2516.9978	2.5169978	0	0	0	0
3169.1729	3.1691729	0	0	0	0
3990.3315	3.9903315	0	0	0	0
5024.2593	5.0242593	0	0	0	0
6326.0859	6.3260859	0	0	0	0
7965.2271	7.9652271	0	0	0	0
10029.083	10.029083	0	0	0	0
12627.701	12.627701	0	0	0	0
15899.642	15.899642	298.05298	0.009555889	0.009555889	0.083055967
20019.369	20.019369	588.76862	0.018876536	0.028432425	0.247123265
25206.553	25.206553	330.17838	0.010585863	0.039018288	0.339131352
31737.779	31.737779	0	0	0.039018288	0.339131352
39961.297	39.961297	0	0	0.039018288	0.339131352
50315.598	50.315598	0	0	0.039018288	0.339131352
63352.785	63.352785	0	0	0.039018288	0.339131352
79768.016	79.768016	0	0	0.039018288	0.339131352
100436.56	100.43656	0	0	0.039018288	0.339131352
126460.5	126.4605	0	0	0.039018288	0.339131352
159227.45	159.22745	0	0	0.039018288	0.339131352
200484.59	200.48459	1719.1127	0.055116545	0.094134833	0.818182316
252431.81	252.43181	5284.7695	0.169435219	0.263570052	2.290845466
317838.97	317.83897	7282.0898	0.23347139	0.497041442	4.320085399
400193.66	400.19366	7282.6592	0.233489645	0.730531087	6.349484002
503887.13	503.88713	5556.6377	0.178151597	0.908682684	7.897906423
634448.44	634.44844	2848.2329	0.091317316	1	8.691600005
798839.19	798.83919	0	0	1	8.691600005
1005825	1005.825	0	0	1	8.691600005
1266442.6	1266.4426	0	0	1	8.691600005
1594588.3	1594.5883	0	0	1	8.691600005
2007759.1	2007.7591	0	0	1	8.691600005
2527986	2527.986	0	0	1	8.691600005
3183008	3183.008	0	0	1	8.691600005
4007751.8	4007.7518	0	0	1	8.691600005
5046193	5046.193	0	0	1	8.691600005
6353703	6353.703	772.25836	0	1	8.691600005
8000000	8000	1810.3912	0	1	8.691600005
	all	33773.151	326.5150566	Geo Mean	
	all-end	31190.502			
<b>NMR Phi mathematic Phi</b>		<b>8.6916</b>			

<b>Sample #19</b>					
Distribution TC (microsecs, μs)	TC/1000 T2 (millisecs, ms)	Porosity 0.2 TE			
		CCALC	Incremental phi (%)	normalized phi (%)	cumulative phi (%)
100	0.1	32.266602	0.001942868	0.001942868	0.006508867
125.91082	0.12591082	73.535713	0.004427805	0.006370673	0.021342601
158.53535	0.15853535	138.05594	0.00831276	0.014683433	0.049191452
199.61316	0.19961316	220.71228	0.013289745	0.027973178	0.093713863
251.33458	0.25133458	309.03943	0.018608186	0.046581364	0.15605376
316.45743	0.31645743	388.19717	0.02337451	0.069955874	0.234361474
398.45416	0.39845416	446.99319	0.026914793	0.096870667	0.324529609
501.6969	0.5016969	483.16965	0.029093086	0.125963753	0.421995314
631.69073	0.63169073	507.54355	0.030560711	0.156524464	0.524377758
795.36694	0.79536694	544.62646	0.032793584	0.189318048	0.634240622
1001.4531	1.0014531	624.69006	0.037614452	0.2269325	0.760254036
1260.9379	1.2609379	765.38281	0.046085982	0.273018483	0.914648202
1587.6572	1.5876572	952.54492	0.057355571	0.330374054	1.106796988
1999.0322	1.9990322	1138.3666	0.068544449	0.398918503	1.336430002
2516.9978	2.5169978	1264.9805	0.07616825	0.475086752	1.591603761
3169.1729	3.1691729	1299.5757	0.07825133	0.553338082	1.853756116
3990.3315	3.9903315	1255.8645	0.075619348	0.62895743	2.107090982
5024.2593	5.0242593	1185.0759	0.071356955	0.700314386	2.346146266
6326.0859	6.3260859	1140.0626	0.06864657	0.768960956	2.5761214
7965.2271	7.9652271	1135.25	0.068356789	0.837317745	2.805125728
10029.083	10.029083	1124.6465	0.067718321	0.905036066	3.031991103
12627.701	12.627701	997.84723	0.060083359	0.965119424	3.233278339
15899.642	15.899642	579.28662	0.034880576	1	3.350132903
20019.369	20.019369	0	0	1	3.350132903
25206.553	25.206553	0	0	1	3.350132903
31737.779	31.737779	0	0	1	3.350132903
39961.297	39.961297	0	0	1	3.350132903
50315.598	50.315598	0	0	1	3.350132903
63352.785	63.352785	0	0	1	3.350132903
79768.016	79.768016	0	0	1	3.350132903
100436.56	100.43656	0	0	1	3.350132903
126460.5	126.4605	0	0	1	3.350132903
159227.45	159.22745	0	0	1	3.350132903
200484.59	200.48459	0	0	1	3.350132903
252431.81	252.43181	0	0	1	3.350132903
317838.97	317.83897	0	0	1	3.350132903
400193.66	400.19366	0	0	1	3.350132903
503887.13	503.88713	0	0	1	3.350132903
634448.44	634.44844	0	0	1	3.350132903
798839.19	798.83919	0	0	1	3.350132903
1005825	1005.825	0	0	1	3.350132903
1266442.6	1266.4426	0	0	1	3.350132903
1594588.3	1594.5883	0	0	1	3.350132903
2007759.1	2007.7591	0	0	1	3.350132903
2527986	2527.986	0	0	1	3.350132903
3183008	3183.008	0	0	1	3.350132903
4007751.8	4007.7518	0	0	1	3.350132903
5046193	5046.193	0	0	1	3.350132903
6353703	6353.703	0	0	1	3.350132903
8000000	8000	3330.2644	0	1	3.350132903
	all	19937.9783	2.635964916	Geo Mean	
	all-end	16607.7139			
<b>NMR Phi mathematic Phi</b>		<b>3.3501329</b>			

Sample #20					
Distribution	TC/1000	Porosity 0.2 TE			
TC	T2	CCALC	Incremental phi (%)	cumulative phi (%)	cumulative phi (%)
(microsecs, $\mu$ s)	(milliseecs, ms)				
100	0.1	0	0	0	0
125.91082	0.12591082	0	0	0	0
158.53535	0.15853535	0	0	0	0
199.61316	0.19961316	0	0	0	0
251.33458	0.25133458	0	0	0	0
316.45743	0.31645743	0	0	0	0
398.45416	0.39845416	0	0	0	0
501.6969	0.5016969	0	0	0	0
631.69073	0.63169073	4.6355634	0.000160651	0.000160651	0.001249798
795.36694	0.79536694	50.080162	0.001735587	0.001896237	0.014751954
1001.4531	1.0014531	106.79967	0.003701268	0.005597505	0.043546306
1260.9379	1.2609379	175.41043	0.006079054	0.011676559	0.090838864
1587.6572	1.5876572	252.36722	0.008746081	0.02042264	0.15887981
1999.0322	1.9990322	326.40677	0.011312009	0.031734649	0.246882622
2516.9978	2.5169978	379.27454	0.013144203	0.044878852	0.34913916
3169.1729	3.1691729	390.93488	0.013548306	0.058427158	0.454539453
3990.3315	3.9903315	345.67603	0.011979807	0.070406965	0.547737467
5024.2593	5.0242593	237.54387	0.008232361	0.078639326	0.611781876
6326.0859	6.3260859	76.659897	0.002656738	0.081296064	0.632450217
7965.2271	7.9652271	0	0	0.081296064	0.632450217
10029.083	10.029083	0	0	0.081296064	0.632450217
12627.701	12.627701	0	0	0.081296064	0.632450217
15899.642	15.899642	0	0	0.081296064	0.632450217
20019.369	20.019369	0	0	0.081296064	0.632450217
25206.553	25.206553	106.21825	0.003681118	0.084977182	0.661087812
31737.779	31.737779	538.71417	0.01866977	0.103646952	0.806331007
39961.297	39.961297	1144.8341	0.039675565	0.143322517	1.114990723
50315.598	50.315598	1978.9194	0.068581768	0.211904285	1.6485289
63352.785	63.352785	3048.8904	0.105662865	0.31756715	2.470542888
79768.016	79.768016	4198.0947	0.145489885	0.463057035	3.602394844
100436.56	100.43656	5051.8472	0.175077677	0.638134711	4.964427753
126460.5	126.4605	5114.855	0.177261286	0.815395997	6.34344825
159227.45	159.22745	3960.6243	0.13726007	0.952656067	7.411275606
200484.59	200.48459	1366.104	0.047343933	1	7.779592092
252431.81	252.43181	0	0	1	7.779592092
317838.97	317.83897	0	0	1	7.779592092
400193.66	400.19366	0	0	1	7.779592092
503887.13	503.88713	0	0	1	7.779592092
634448.44	634.44844	0	0	1	7.779592092
798839.19	798.83919	0	0	1	7.779592092
1005825	1005.825	0	0	1	7.779592092
1266442.6	1266.4426	0	0	1	7.779592092
1594588.3	1594.5883	0	0	1	7.779592092
2007759.1	2007.7591	0	0	1	7.779592092
2527986	2527.986	0	0	1	7.779592092
3183008	3183.008	0	0	1	7.779592092
4007751.8	4007.7518	0	0	1	7.779592092
5046193	5046.193	0	0	1	7.779592092
6353703	6353.703	315.03149	0	1	7.779592092
8000000	8000	3113.8889	0	1	7.779592092
	all	32283.81094	70.39903258	Geo Mean	
	all-end	28854.89055			
NMR Phi mathematic Phi		7.779592092			

Sample #21					
Distribution	TC/1000	Porosity 0.2 TE			
TC	T2	CCALC	Incremental phi (%)	normalized phi (%)	cumulative phi (%)
(microsecs, μs)	(millisecs, ms)				
100	0.1	0	0	0	0
125.91082	0.12591082	0	0	0	0
158.53535	0.15853535	0	0	0	0
199.61316	0.19961316	0	0	0	0
251.33458	0.25133458	0	0	0	0
316.45743	0.31645743	0	0	0	0
398.45416	0.39845416	0	0	0	0
501.6969	0.5016969	0	0	0	0
631.69073	0.63169073	0	0	0	0
795.36694	0.79536694	0	0	0	0
1001.4531	1.0014531	0	0	0	0
1260.9379	1.2609379	0	0	0	0
1587.6572	1.5876572	0	0	0	0
1999.0322	1.9990322	0	0	0	0
2516.9978	2.5169978	0	0	0	0
3169.1729	3.1691729	0	0	0	0
3990.3315	3.9903315	0	0	0	0
5024.2593	5.0242593	0	0	0	0
6326.0859	6.3260859	0	0	0	0
7965.2271	7.9652271	0	0	0	0
10029.083	10.029083	329.49255	0.016906454	0.016906454	0.095027263
12627.701	12.627701	701.57745	0.035998346	0.0529048	0.29736563
15899.642	15.899642	880.77112	0.045192878	0.098097678	0.551384329
20019.369	20.019369	795.58801	0.040822083	0.138919761	0.780835802
25206.553	25.206553	413.46423	0.02121509	0.16013485	0.900080908
31737.779	31.737779	0	0	0.16013485	0.900080908
39961.297	39.961297	0	0	0.16013485	0.900080908
50315.598	50.315598	0	0	0.16013485	0.900080908
63352.785	63.352785	0	0	0.16013485	0.900080908
79768.016	79.768016	0	0	0.16013485	0.900080908
100436.56	100.43656	0	0	0.16013485	0.900080908
126460.5	126.4605	871.03241	0.044693179	0.204828029	1.151290914
159227.45	159.22745	3106.395	0.159390931	0.36421896	2.047190424
200484.59	200.48459	4835.7935	0.248127372	0.612346332	3.441856918
252431.81	252.43181	4936.2637	0.253282556	0.865628888	4.86549951
317838.97	317.83897	2618.7798	0.134371112	1	5.620768411
400193.66	400.19366	0	0	1	5.620768411
503887.13	503.88713	0	0	1	5.620768411
634448.44	634.44844	0	0	1	5.620768411
798839.19	798.83919	0	0	1	5.620768411
1005825	1005.825	0	0	1	5.620768411
1266442.6	1266.4426	0	0	1	5.620768411
1594588.3	1594.5883	0	0	1	5.620768411
2007759.1	2007.7591	0	0	1	5.620768411
2527986	2527.986	0	0	1	5.620768411
3183008	3183.008	0	0	1	5.620768411
4007751.8	4007.7518	0	0	1	5.620768411
5046193	5046.193	0	0	1	5.620768411
6353703	6353.703	233.40939	0	1	5.620768411
8000000	8000	3241.9683	0	1	5.620768411
	all	22964.53546	142.727784	Geo Mean	
	all-end	19489.15777			
<b>NMR Phi mathematic Phi</b>		<b>5.620768411</b>			

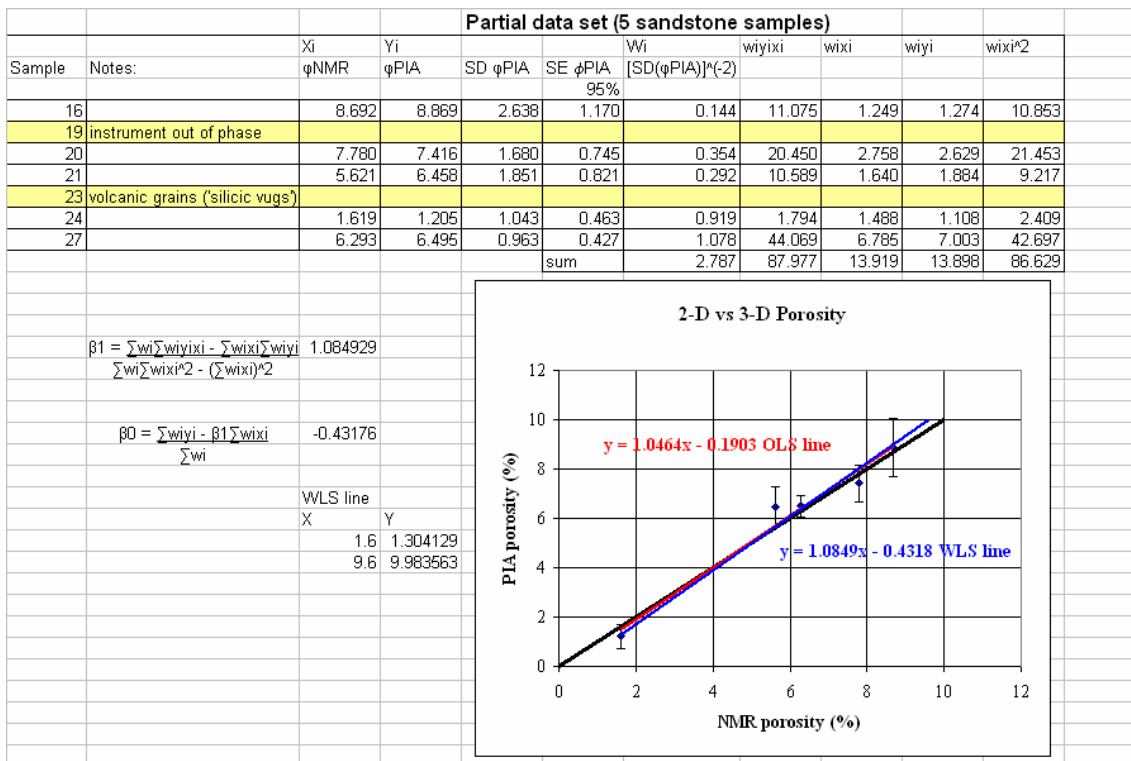
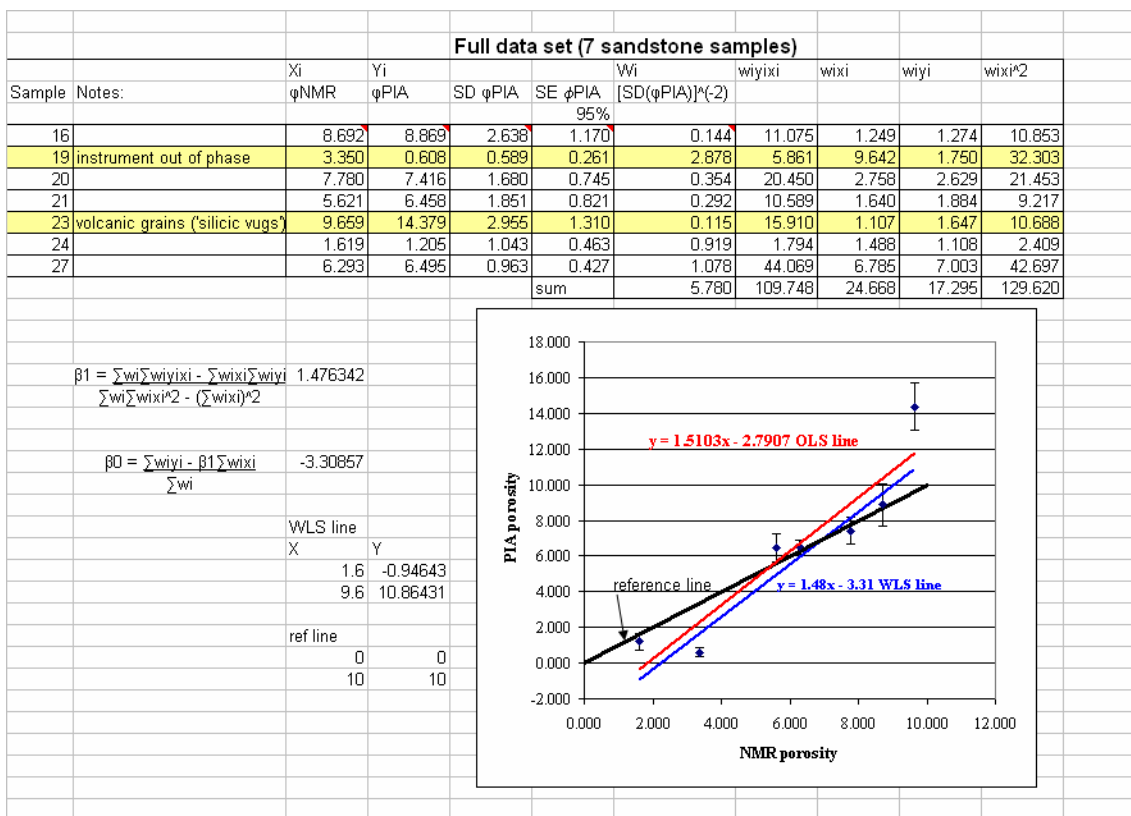


Sample #23					
Distribution	TC/1000	Porosity 0.2 TE			
TC	T2	CCALC	Incremental phi (%)	normalized phi (%)	cumulative phi (%)
(microsecs, $\mu$ s)	(millisecs, ms)				
100	0.1	18.181969	0.000479321	0.000479321	0.004629975
125.91082	0.12591082	42.390293	0.001117511	0.001596832	0.015424515
158.53535	0.15853535	82.193703	0.002166826	0.003763658	0.036354855
199.61316	0.19961316	136.19629	0.003590465	0.007354123	0.071036765
251.33458	0.25133458	196.55716	0.005181724	0.012535847	0.121089359
316.45743	0.31645743	250.8369	0.00661267	0.019148517	0.184964101
398.45416	0.39845416	286.84186	0.007561848	0.026710366	0.258007379
501.6969	0.5016969	296.50555	0.007816607	0.034526972	0.333511483
631.69073	0.63169073	274.71738	0.007242218	0.04176919	0.403467305
795.36694	0.79536694	213.40936	0.005625989	0.047395179	0.457811253
1001.4531	1.0014531	97.405487	0.002567845	0.049963025	0.482615221
1260.9379	1.2609379	0	0	0.049963025	0.482615221
1587.6572	1.5876572	0	0	0.049963025	0.482615221
1999.0322	1.9990322	0	0	0.049963025	0.482615221
2516.9978	2.5169978	0	0	0.049963025	0.482615221
3169.1729	3.1691729	0	0	0.049963025	0.482615221
3990.3315	3.9903315	0	0	0.049963025	0.482615221
5024.2593	5.0242593	0	0	0.049963025	0.482615221
6326.0859	6.3260859	0	0	0.049963025	0.482615221
7965.2271	7.9652271	0	0	0.049963025	0.482615221
10029.083	10.029083	0	0	0.049963025	0.482615221
12627.701	12.627701	108.0033	0.002847229	0.052810254	0.510117884
15899.642	15.899642	591.29675	0.015588019	0.068398273	0.660689538
20019.369	20.019369	957.2196	0.025234634	0.093632907	0.904442168
25206.553	25.206553	1146.9435	0.030236217	0.123869125	1.196507328
31737.779	31.737779	1109.5568	0.029250613	0.153119738	1.479052095
39961.297	39.961297	792.8869	0.020902425	0.174022163	1.680957977
50315.598	50.315598	173.62471	0.004577169	0.178599332	1.725170903
63352.785	63.352785	0	0	0.178599332	1.725170903
79768.016	79.768016	0	0	0.178599332	1.725170903
100436.56	100.43656	0	0	0.178599332	1.725170903
126460.5	126.4605	0	0	0.178599332	1.725170903
159227.45	159.22745	374.37967	0.009869558	0.18846889	1.820505379
200484.59	200.48459	2692.3008	0.070975591	0.25944448	2.506090382
252431.81	252.43181	4984.3057	0.131398409	0.390842889	3.775326433
317838.97	317.83897	6432.2847	0.169570653	0.560413542	5.413285283
400193.66	400.19366	6554.2319	0.172785478	0.73319902	7.082297562
503887.13	503.88713	5400.3765	0.142367046	0.875566066	8.457484591
634448.44	634.44844	3439.8135	0.090681842	0.966247907	9.333421094
798839.19	798.83919	1280.3104	0.033752093	1	9.659447669
1005825	1005.825	0	0	1	9.659447669
1266442.6	1266.4426	0	0	1	9.659447669
1594588.3	1594.5883	0	0	1	9.659447669
2007759.1	2007.7591	0	0	1	9.659447669
2527986	2527.986	0	0	1	9.659447669
3183008	3183.008	0	0	1	9.659447669
4007751.8	4007.7518	0	0	1	9.659447669
5046193	5046.193	4.9281168	0.000129917	1.000129917	9.660702596
6353703	6353.703	794.33246	0	1.000129917	9.660702596
8000000	8000	1521.4852	0	1.000129917	9.660702596
	all	40253.51646	188.2582649	Geo Mean	
	all-end	37932.77068			
NMR Phi mathematic Phi		9.659447669			

Sample #24					
Distribution	TC/1000	Porosity 0.2 TE			
TC	T2	CCALC	Incremental phi (%)	normalized phi (%)	cumulative phi (%)
(microsecs, $\mu$ s)	(millisecs, ms)				
100	0.1	38.099876	0.006161289	0.006161289	0.009973444
125.91082	0.12591082	86.429726	0.013976909	0.020138198	0.032598242
158.53535	0.15853535	160.72279	0.025991148	0.046129345	0.074670813
199.61316	0.19961316	252.33134	0.040805546	0.086934891	0.140723847
251.33458	0.25133458	342.28815	0.055352834	0.142287725	0.230324969
316.45743	0.31645743	408.68002	0.066089338	0.208377064	0.337305559
398.45416	0.39845416	436.43018	0.070576932	0.278953995	0.451550337
501.6969	0.5016969	424.16739	0.068593865	0.34754786	0.562585071
631.69073	0.63169073	385.26047	0.062302066	0.409849926	0.663435101
795.36694	0.79536694	343.49713	0.055548343	0.465398269	0.753352699
1001.4531	1.0014531	325.12939	0.05257802	0.517976289	0.838462154
1260.9379	1.2609379	349.14377	0.056461485	0.574437774	0.929857879
1587.6572	1.5876572	418.8638	0.067736199	0.642173973	1.039504287
1999.0322	1.9990322	516.74445	0.083564885	0.725738858	1.174773014
2516.9978	2.5169978	601.18073	0.097219425	0.822958283	1.332144713
3169.1729	3.1691729	606.36639	0.09805802	0.921016303	1.490873868
3990.3315	3.9903315	448.96558	0.072604083	0.993620386	1.60840005
5024.2593	5.0242593	39.449947	0.006379614	1	1.618726903
6326.0859	6.3260859	0	0	1	1.618726903
7965.2271	7.9652271	0	0	1	1.618726903
10029.083	10.029083	0	0	1	1.618726903
12627.701	12.627701	0	0	1	1.618726903
15899.642	15.899642	0	0	1	1.618726903
20019.369	20.019369	0	0	1	1.618726903
25206.553	25.206553	0	0	1	1.618726903
31737.779	31.737779	0	0	1	1.618726903
39961.297	39.961297	0	0	1	1.618726903
50315.598	50.315598	0	0	1	1.618726903
63352.785	63.352785	0	0	1	1.618726903
79768.016	79.768016	0	0	1	1.618726903
100436.56	100.43656	0	0	1	1.618726903
126460.5	126.4605	0	0	1	1.618726903
159227.45	159.22745	0	0	1	1.618726903
200484.59	200.48459	0	0	1	1.618726903
252431.81	252.43181	0	0	1	1.618726903
317838.97	317.83897	0	0	1	1.618726903
400193.66	400.19366	0	0	1	1.618726903
503887.13	503.88713	0	0	1	1.618726903
634448.44	634.44844	0	0	1	1.618726903
798839.19	798.83919	0	0	1	1.618726903
1005825	1005.825	0	0	1	1.618726903
1266442.6	1266.4426	0	0	1	1.618726903
1594588.3	1594.5883	0	0	1	1.618726903
2007759.1	2007.7591	0	0	1	1.618726903
2527986	2527.986	0	0	1	1.618726903
3183008	3183.008	0	0	1	1.618726903
4007751.8	4007.7518	0	0	1	1.618726903
5046193	5046.193	0	0	1	1.618726903
6353703	6353.703	0	0	1	1.618726903
8000000	8000	3362.9194	0	1	1.618726903
	all	9546.670529	0.954217426	Geo Mean	
	all-end	6183.751129			
<b>NMR Phi mathematic Phi</b>		<b>1.618726903</b>			

Sample #27					
Distribution	TC/1000	Porosity 0.2 TE			
TC (microsecs, $\mu$ s)	T2 (milliseconds, ms)	CCALC	Incremental phi (%)	normalized phi (%)	cumulative phi (%)
100	0.1	0	0	0	0
125.91082	0.12591082	0	0	0	0
158.53535	0.15853535	0	0	0	0
199.61316	0.19961316	0	0	0	0
251.33458	0.25133458	0	0	0	0
316.45743	0.31645743	0	0	0	0
398.45416	0.39845416	0	0	0	0
501.6969	0.5016969	0	0	0	0
631.69073	0.63169073	0	0	0	0
795.36694	0.79536694	0	0	0	0
1001.4531	1.0014531	0	0	0	0
1260.9379	1.2609379	0	0	0	0
1587.6572	1.5876572	95.438416	0.004312877	0.004312877	0.027139953
1999.0322	1.9990322	264.48148	0.011951961	0.016264838	0.102350913
2516.9978	2.5169978	421.92422	0.019066823	0.035331662	0.222334081
3169.1729	3.1691729	543.27905	0.024550868	0.059882529	0.376827088
3990.3315	3.9903315	602.43579	0.02722417	0.0871067	0.548142579
5024.2593	5.0242593	584.85321	0.026429611	0.11353631	0.714458086
6326.0859	6.3260859	498.04196	0.022506596	0.136042907	0.85608696
7965.2271	7.9652271	367.37054	0.016601534	0.152644441	0.960556624
10029.083	10.029083	221.62456	0.01001525	0.16265969	1.023580303
12627.701	12.627701	87.936691	0.003973873	0.166633564	1.04858698
15899.642	15.899642	1.1294183	5.10386E-05	0.166684602	1.048908154
20019.369	20.019369	10.020534	0.00045283	0.167137432	1.051757707
25206.553	25.206553	169.92734	0.007679044	0.174816476	1.100080178
31737.779	31.737779	529.10193	0.023910201	0.198726677	1.250541618
39961.297	39.961297	1116.7317	0.050465285	0.249191962	1.56810814
50315.598	50.315598	1927.6405	0.087110385	0.336302347	2.116273907
63352.785	63.352785	2885.3931	0.130391379	0.466693726	2.936797092
79768.016	79.768016	3770.7668	0.170401559	0.637095285	4.009095208
100436.56	100.43656	4144.4839	0.187289895	0.82438518	5.187667768
126460.5	126.4605	3334.7004	0.150695648	0.975080828	6.135961085
159227.45	159.22745	551.42914	0.024919172	1	6.292771744
200484.59	200.48459	0	0	1	6.292771744
252431.81	252.43181	0	0	1	6.292771744
317838.97	317.83897	0	0	1	6.292771744
400193.66	400.19366	0	0	1	6.292771744
503887.13	503.88713	0	0	1	6.292771744
634448.44	634.44844	0	0	1	6.292771744
798839.19	798.83919	0	0	1	6.292771744
1005825	1005.825	0	0	1	6.292771744
1266442.6	1266.4426	0	0	1	6.292771744
1594588.3	1594.5883	0	0	1	6.292771744
2007759.1	2007.7591	0	0	1	6.292771744
2527986	2527.986	0	0	1	6.292771744
3183008	3183.008	0	0	1	6.292771744
4007751.8	4007.7518	0	0	1	6.292771744
5046193	5046.193	0	0	1	6.292771744
6353703	6353.703	0	0	1	6.292771744
8000000	8000	3367.5938	0	1	6.292771744
	all	25496.3045	48.82490597	Geo Mean	
	all-end	22128.7107			
	<b>NMR Phi mathematic Phi</b>	<b>6.29277174</b>			

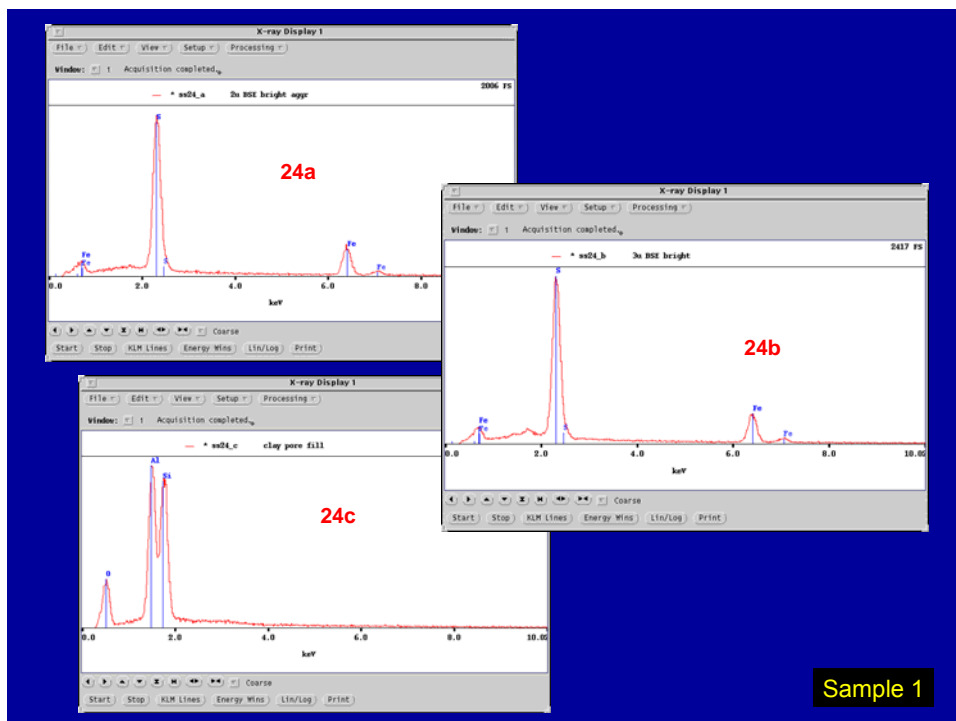
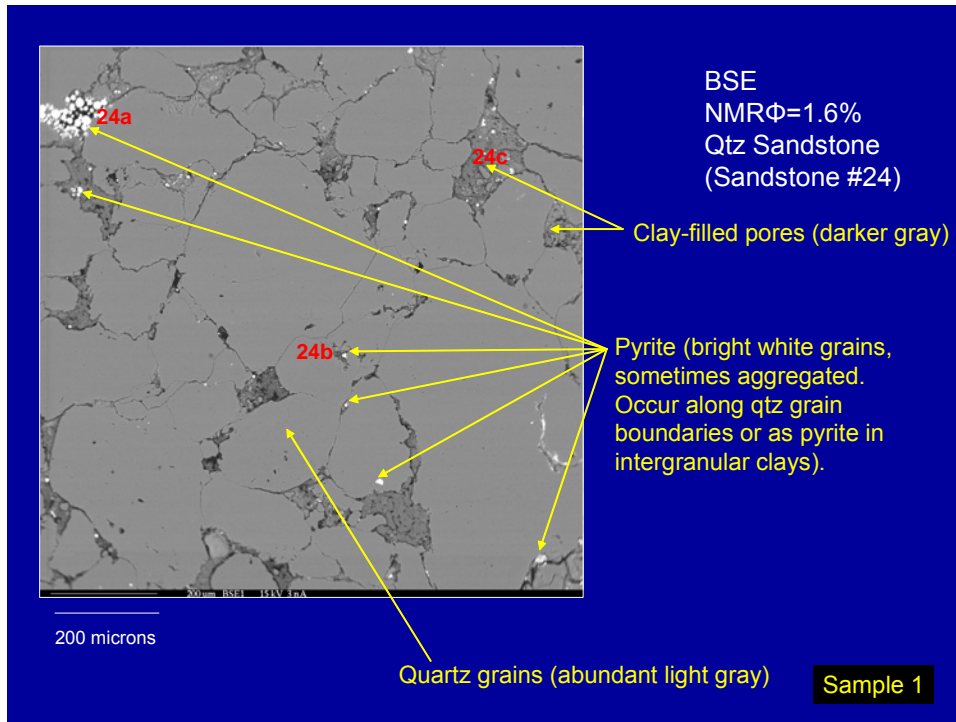
**APPENDIX E****OLS AND WLS REGRESSION DATA**

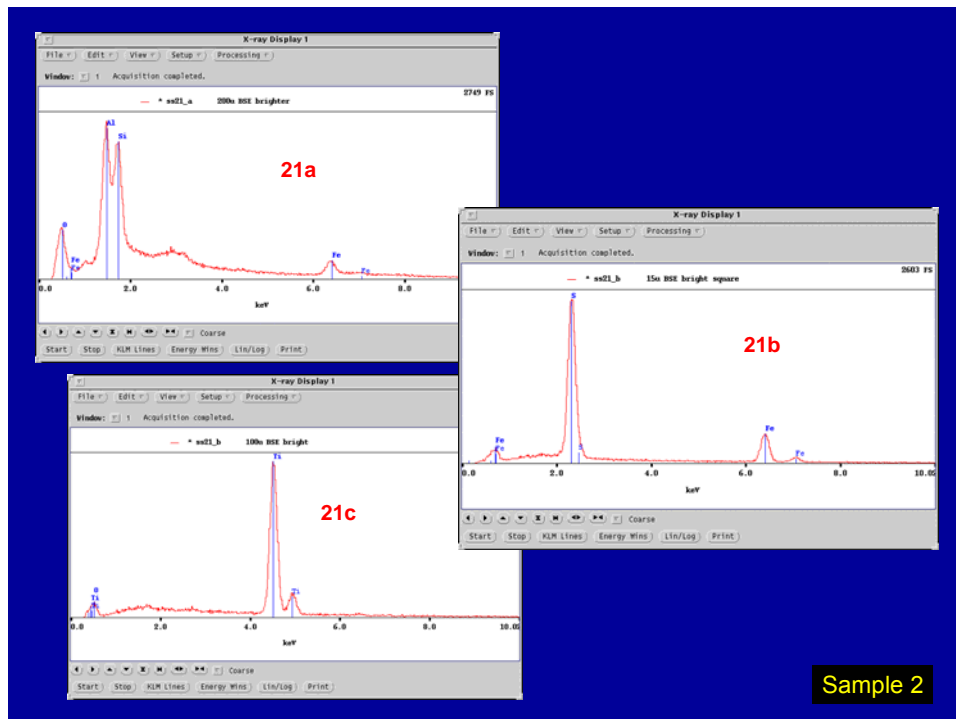
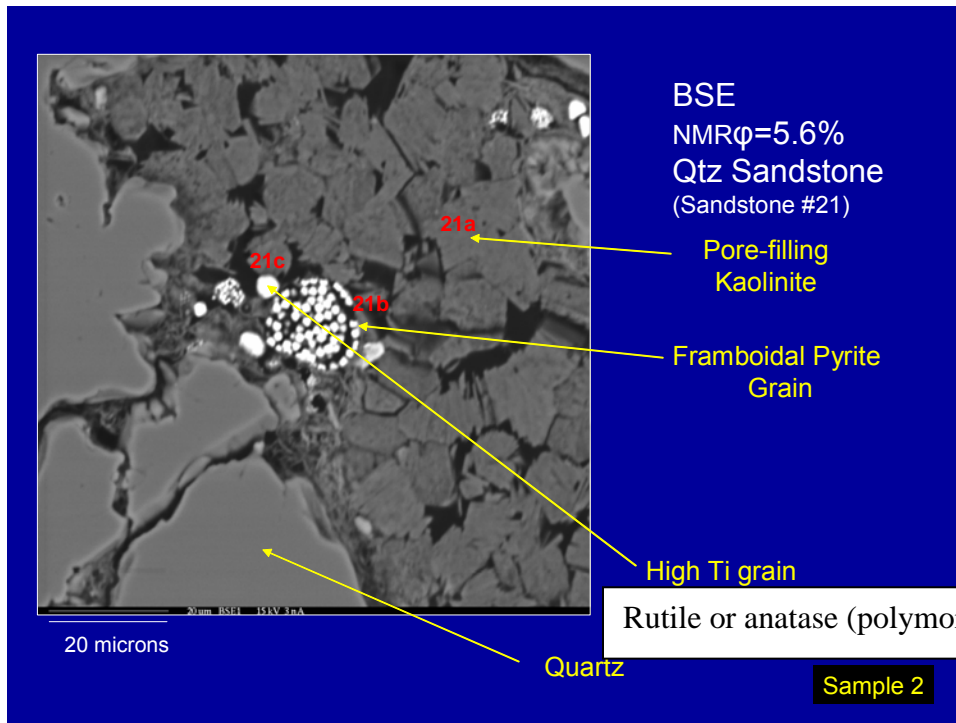


**APPENDIX F**

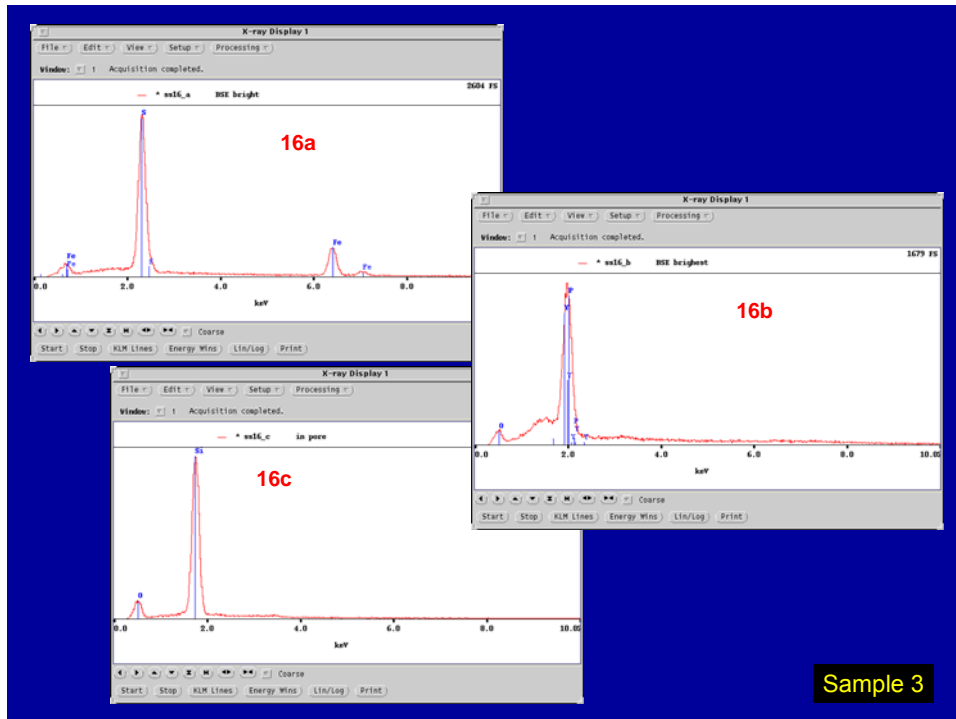
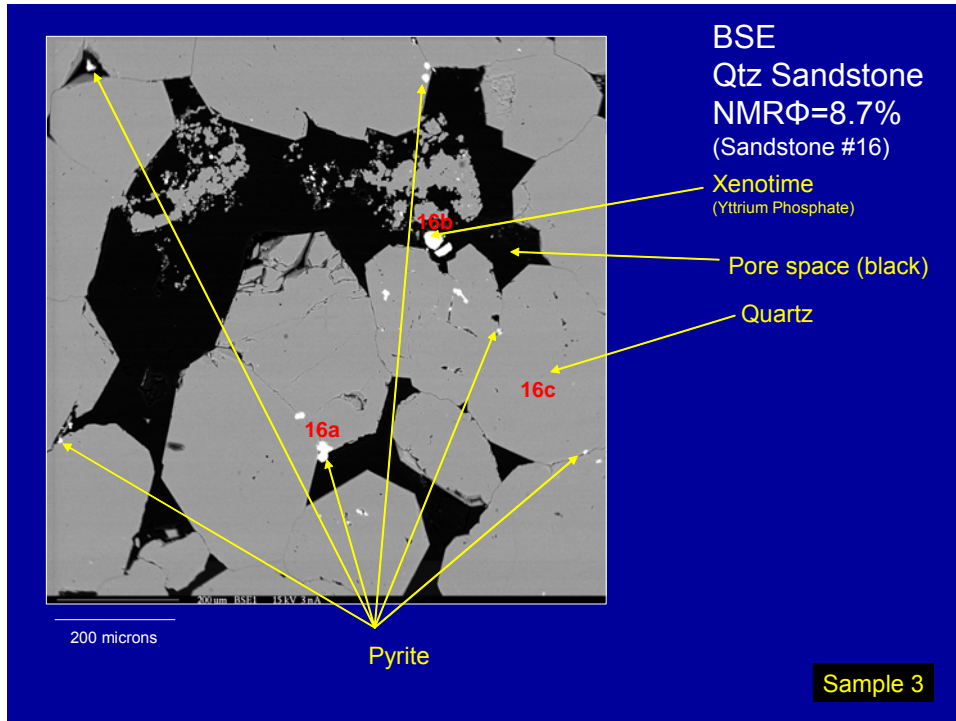
**SEM PHOTOS AND MICROPROBE DATA**

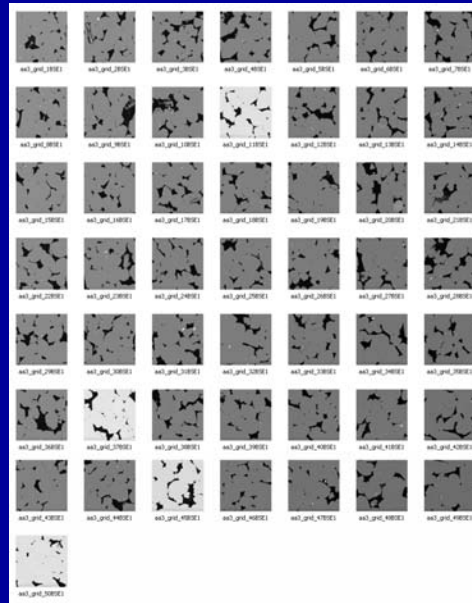
SANDSTONES











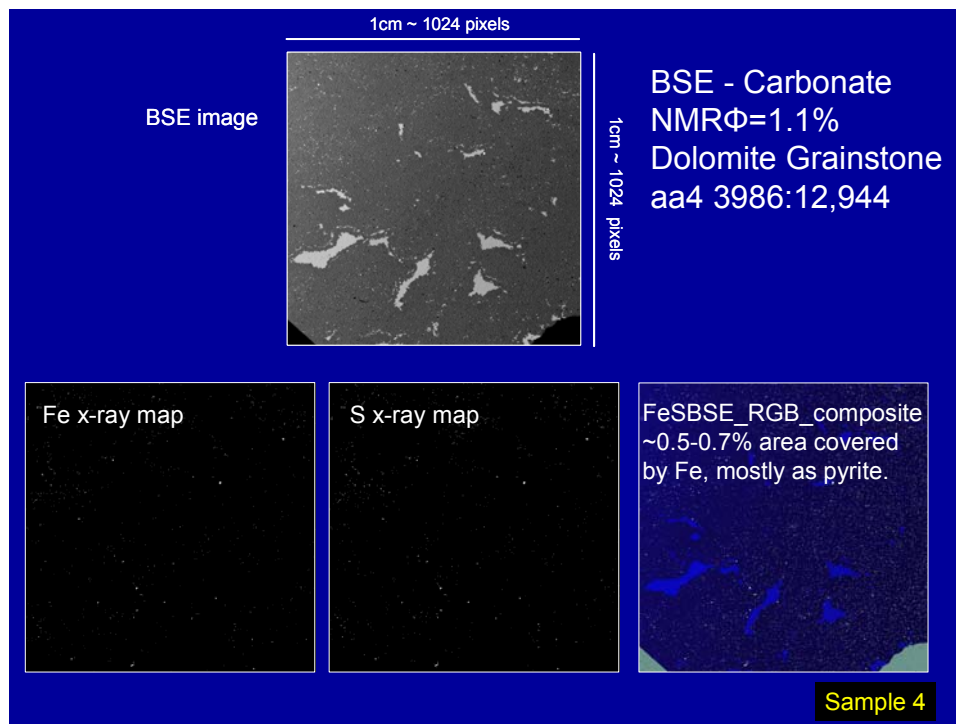
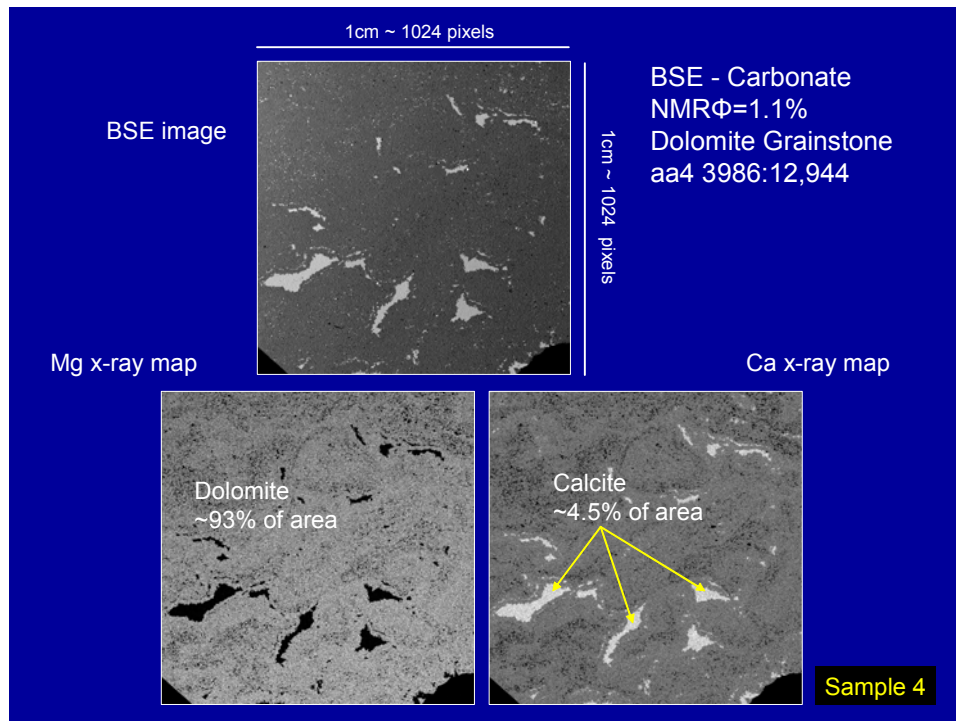
Sample #16  
Sandstone

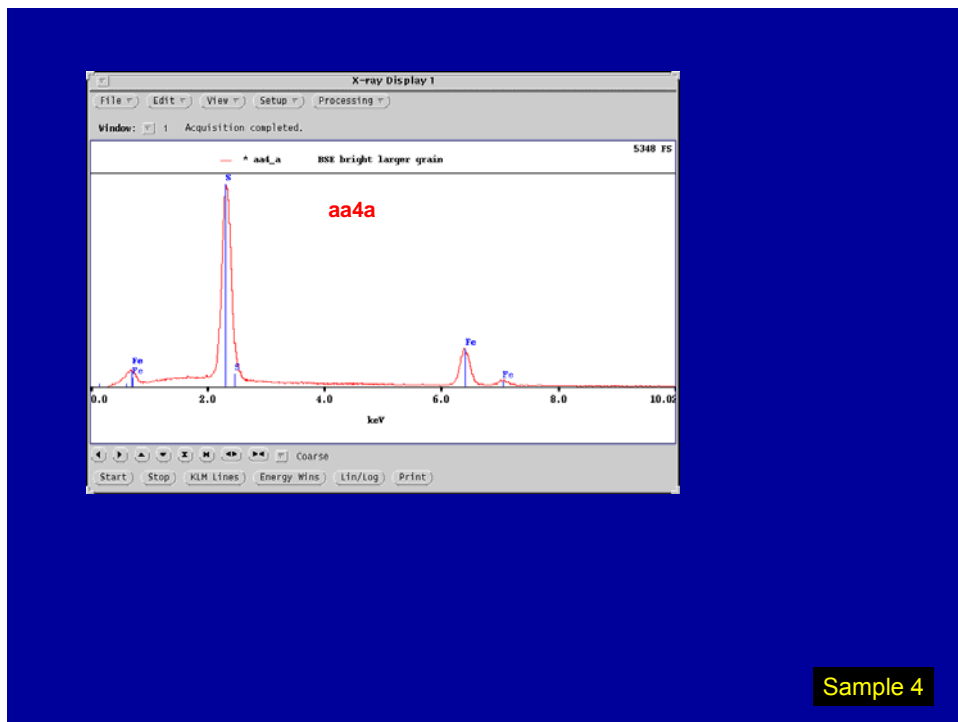
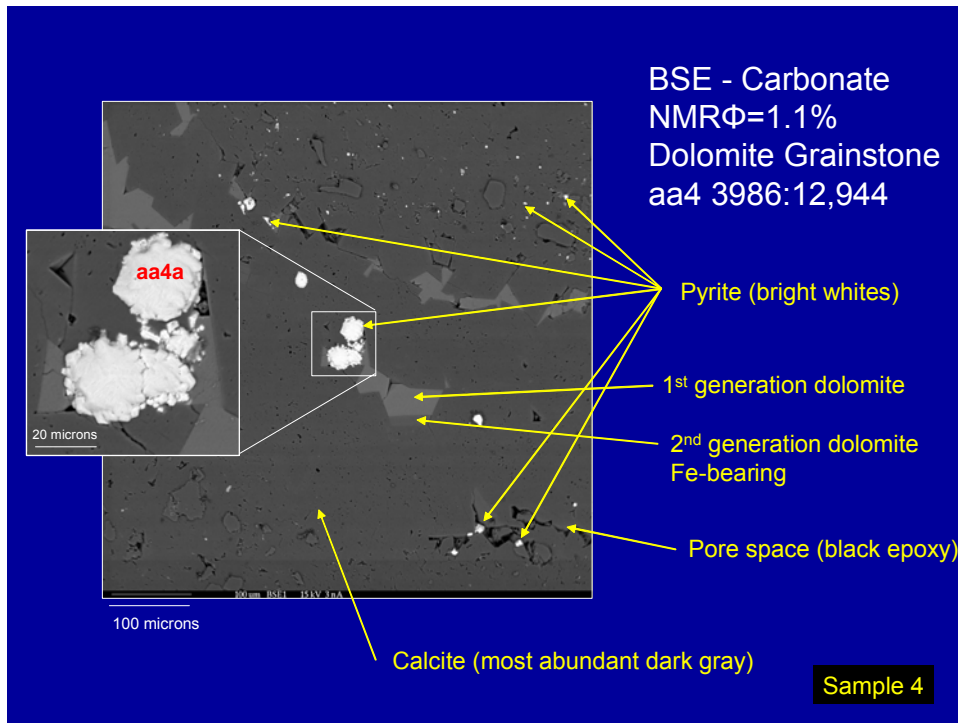
Mosaic of 50  
BSE images.

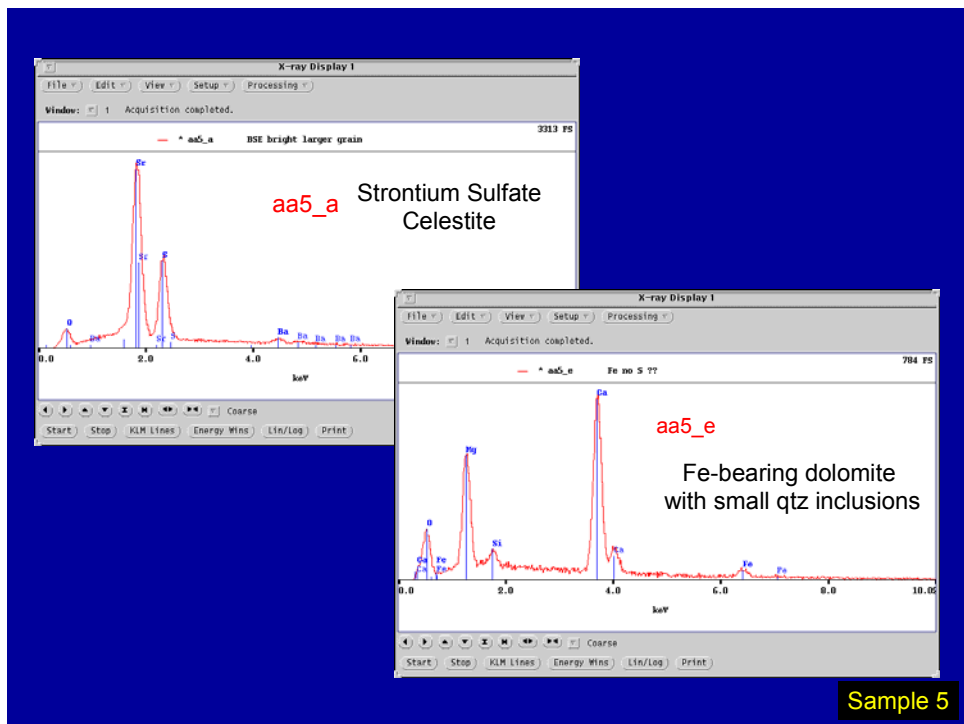
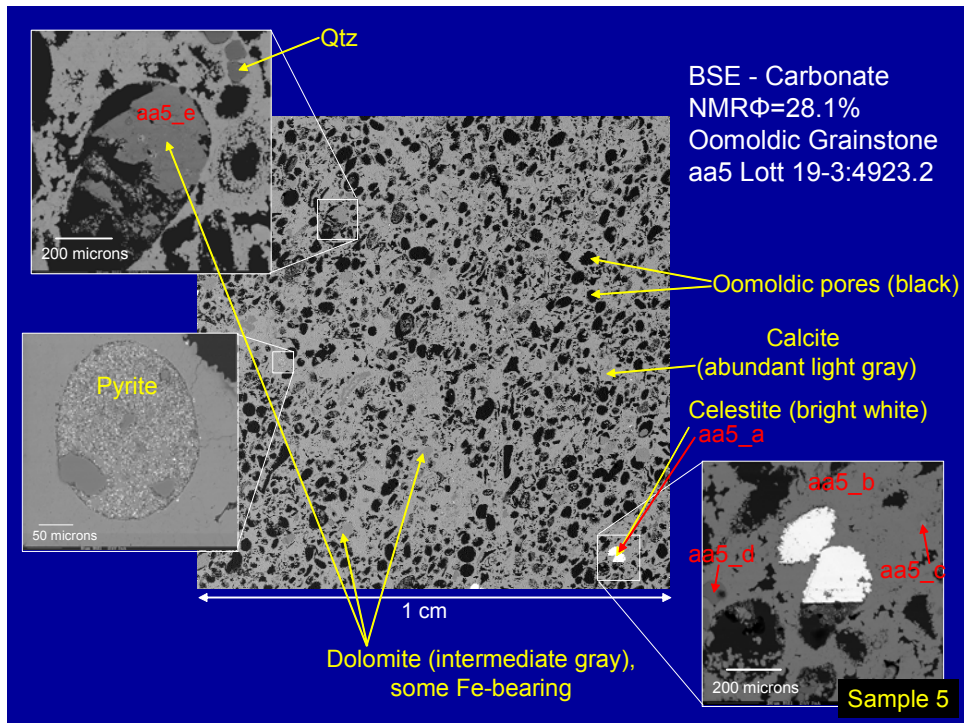
Individual views  
are 1 mm<sup>2</sup>.

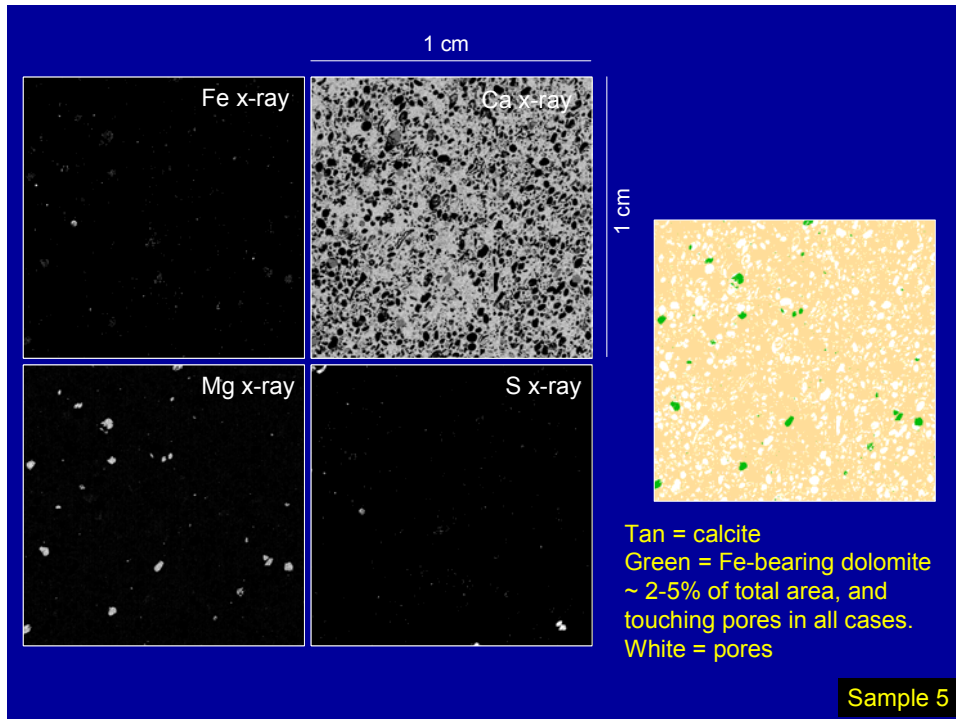
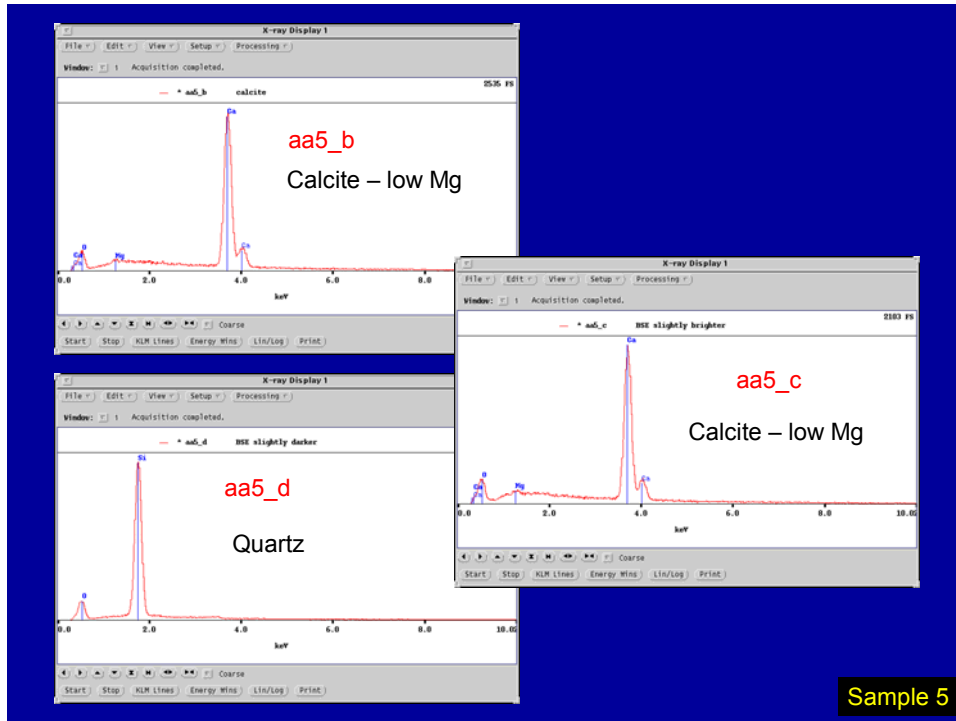
Sample 3

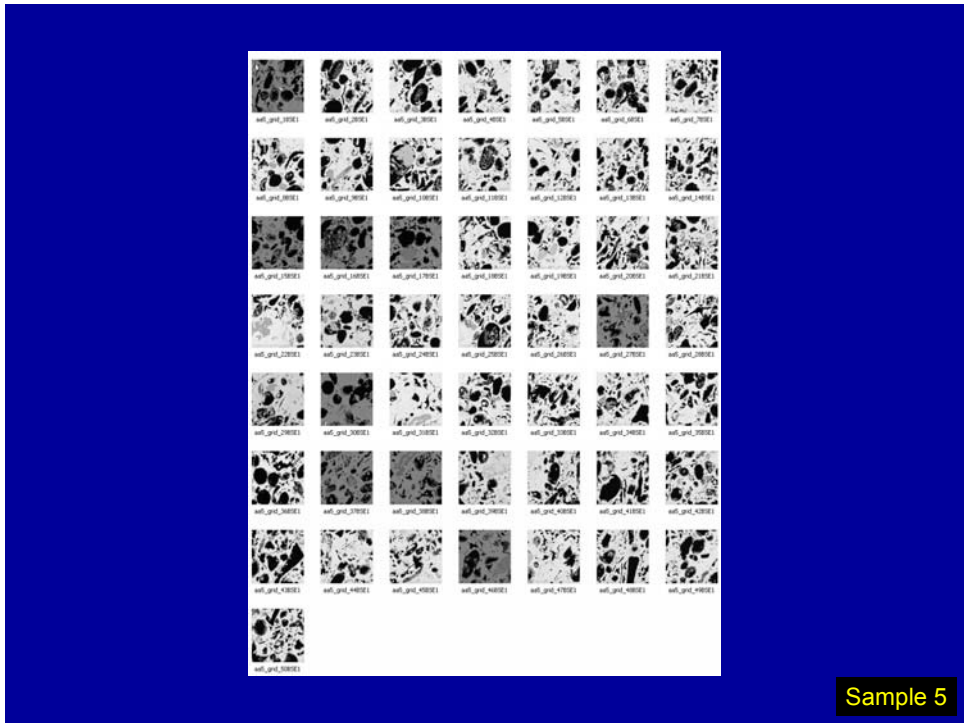
## CARBONATES





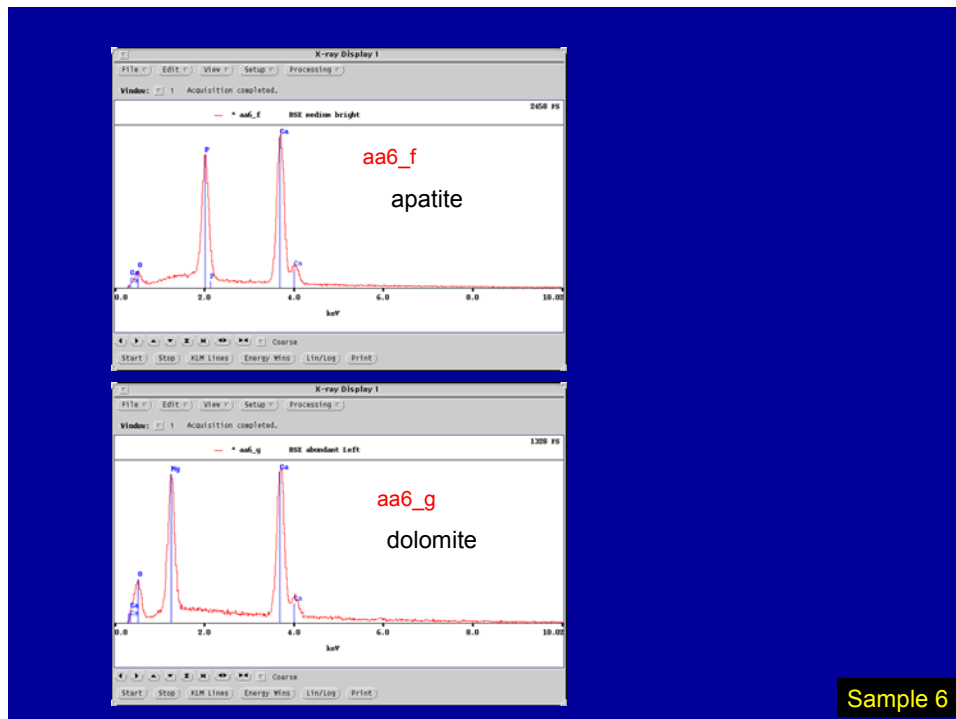
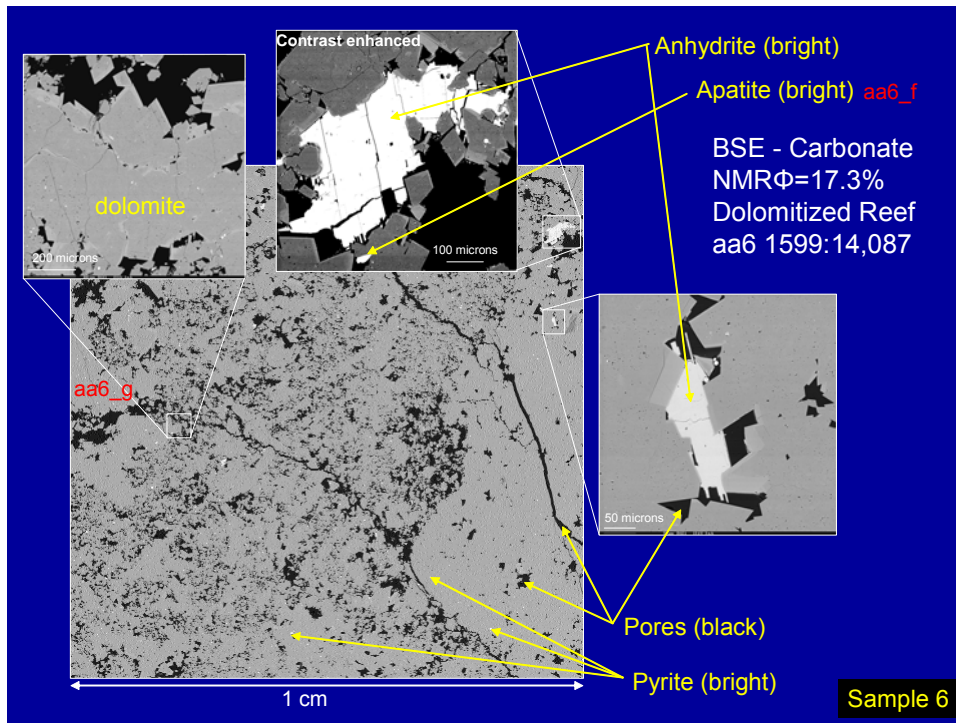






Sample 5

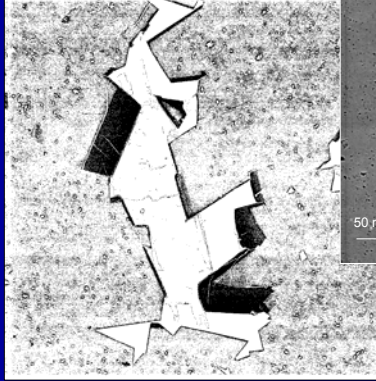


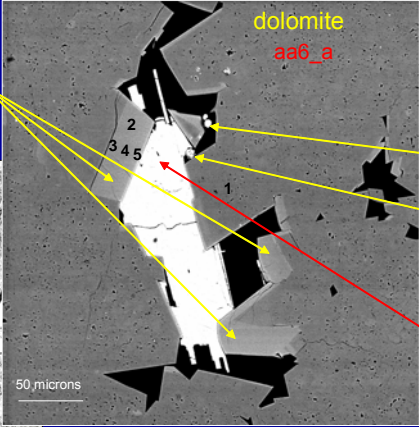






**Dolomite - High Fe & Mn**  
aa6\_e





Pyrite  
aa6\_c

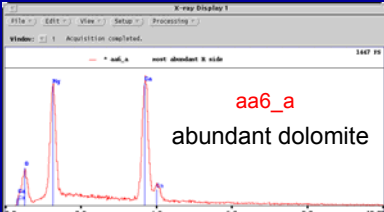
Pyrite  
aa6\_d

Anhydrite  
aa6\_b

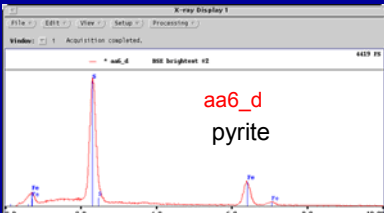
High Fe & Mn dolomite shown in black, which line all pore walls. Images contrast enhanced.

Analysis	MgCO3 (wt%)	CaCO3 (wt%)	MnCO3 (wt%)	FeCO3 (wt%)	Total (wt%)	Mg (cat)	Ca (cat)	Mn (cat)	Fe (cat)
aa6_a_pt1	43.43	54.75	0.85	0.17	99.20	0.96	1.02	0.01	0.00
aa6_a_pt2	37.74	53.47	2.62	5.47	99.30	0.85	1.02	0.04	0.09
aa6_a_pt3	42.24	57.49	2.71	5.67	108.11	0.87	1.00	0.04	0.09
aa6_a_pt4	37.57	53.91	2.41	6.86	100.75	0.84	1.01	0.04	0.11
aa6_a_pt5	36.31	53.03	2.18	8.16	99.68	0.82	1.01	0.04	0.13

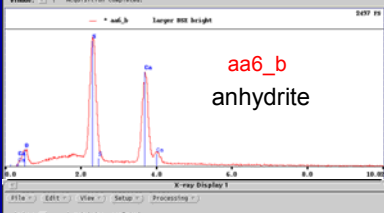
**Sample 6**



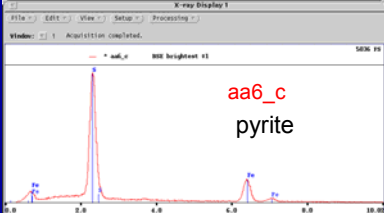
aa6\_a  
abundant dolomite



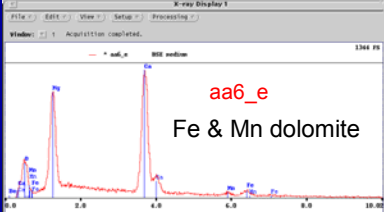
aa6\_d  
pyrite



aa6\_b  
anhydrite

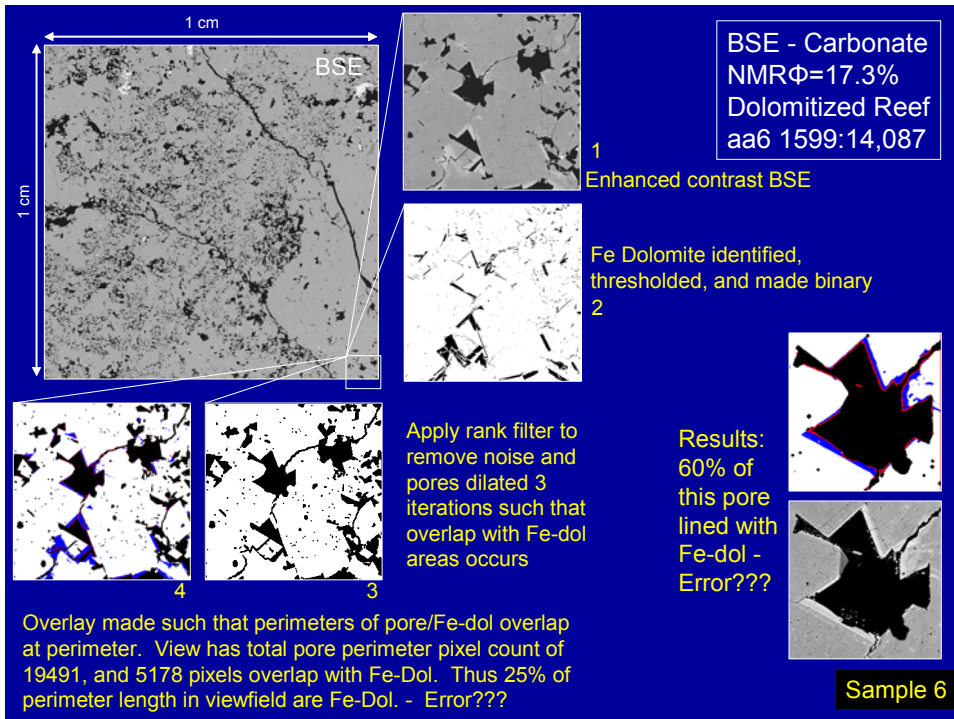
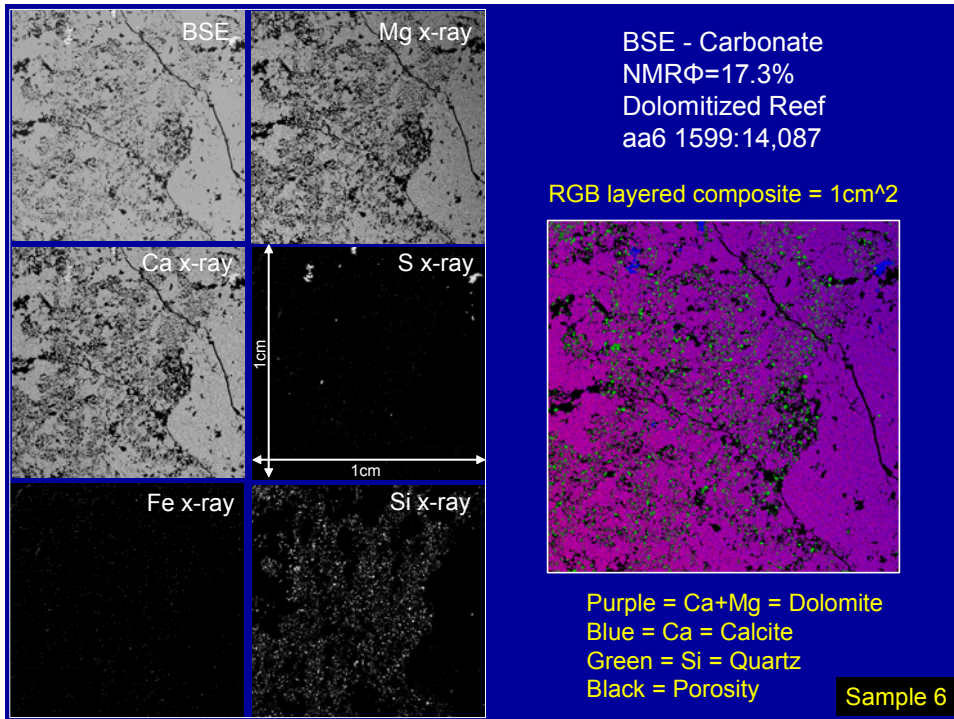


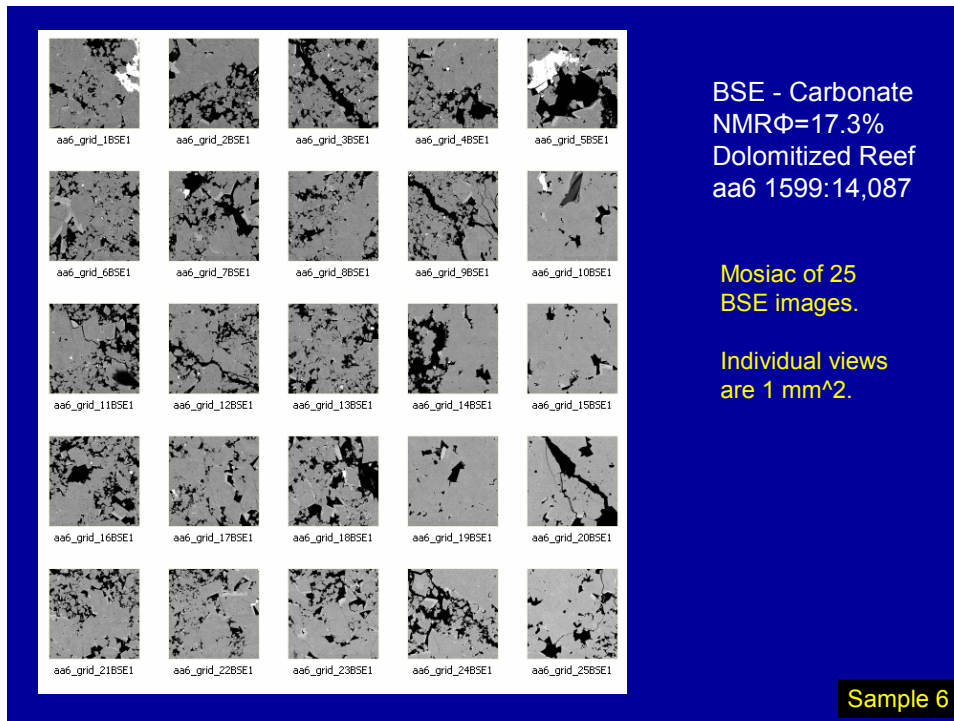
aa6\_c  
pyrite

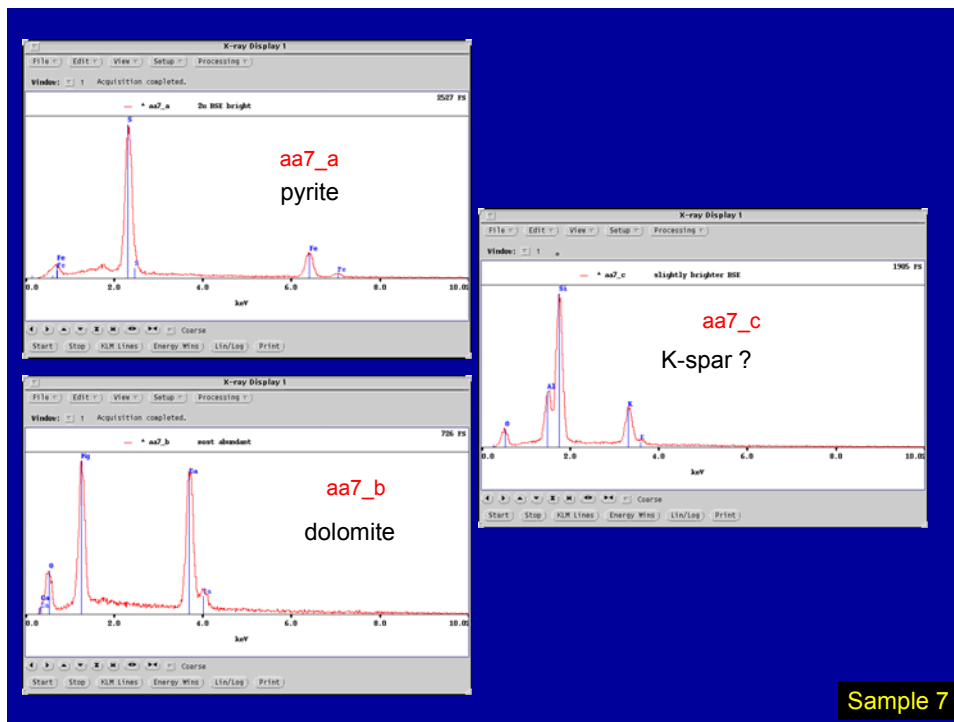
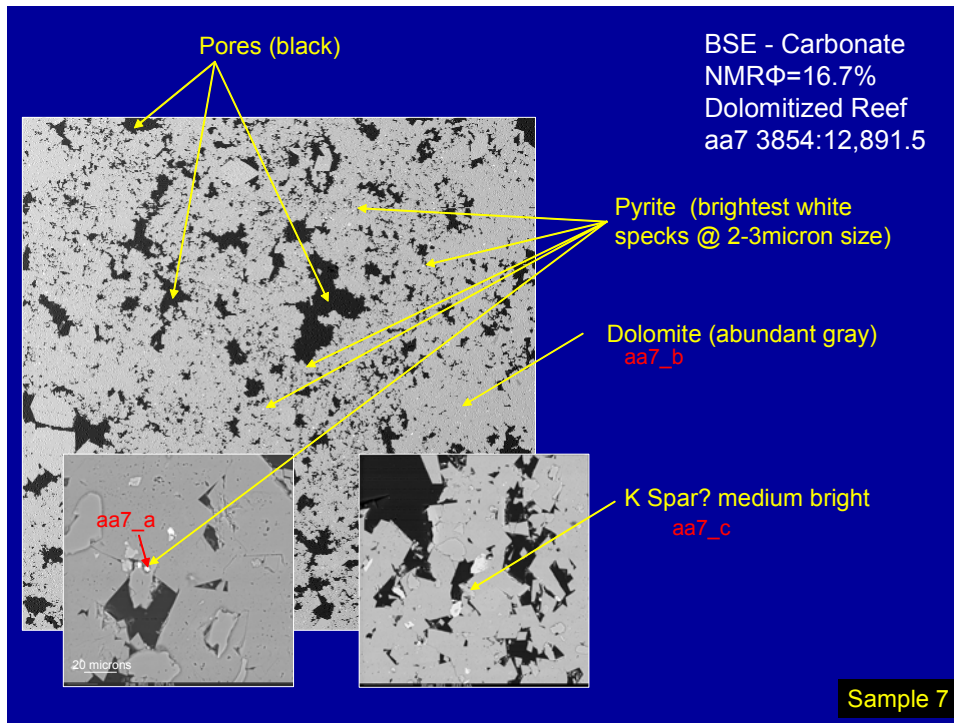


aa6\_e  
Fe & Mn dolomite

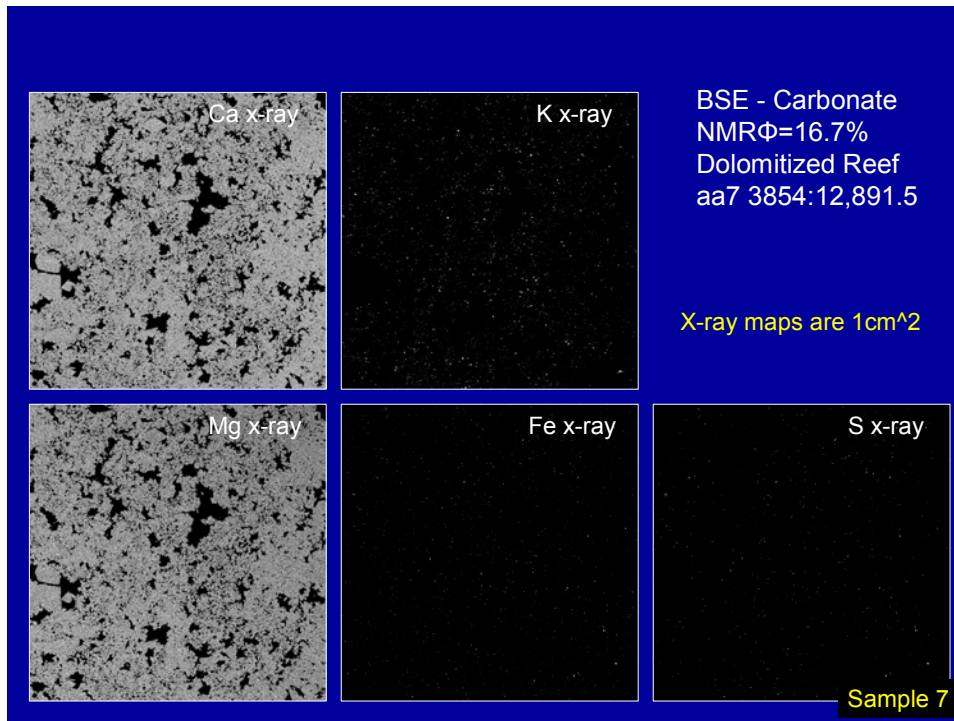
**Sample 6**

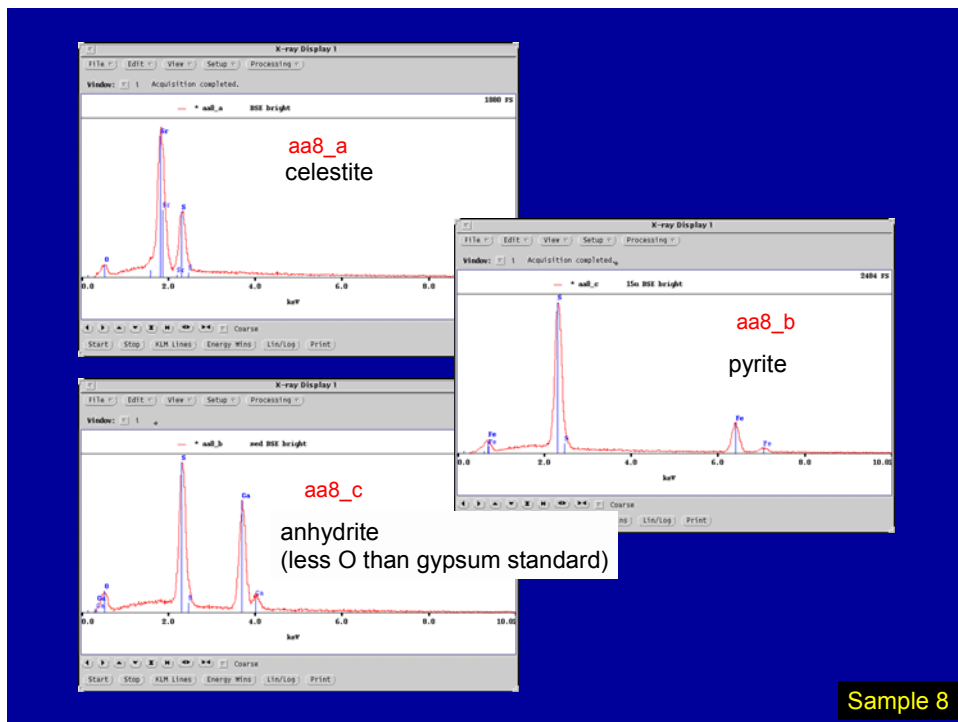
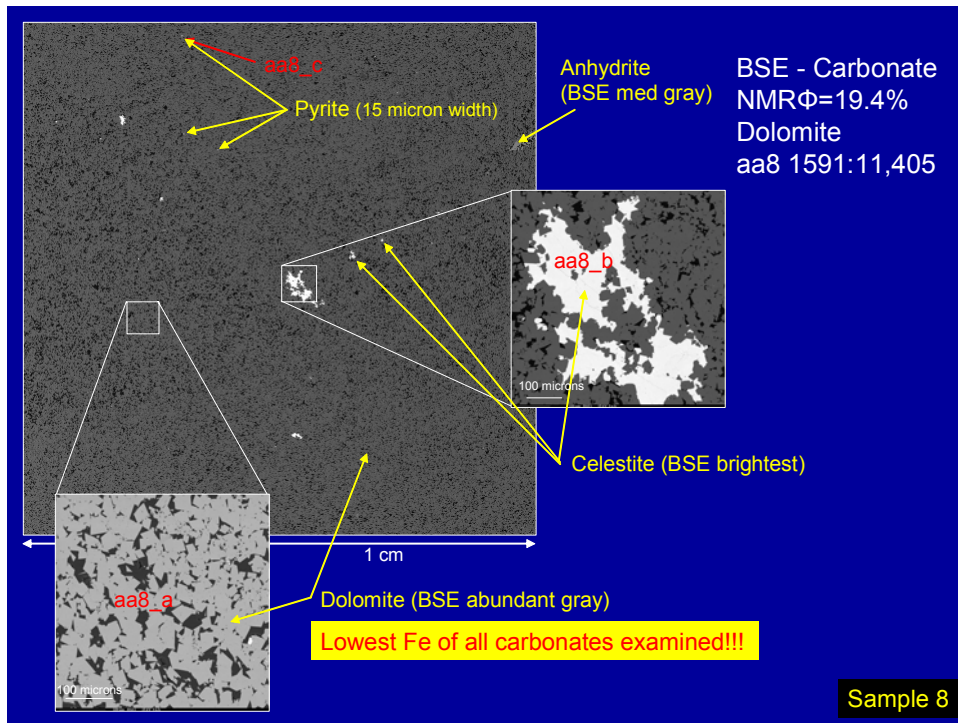


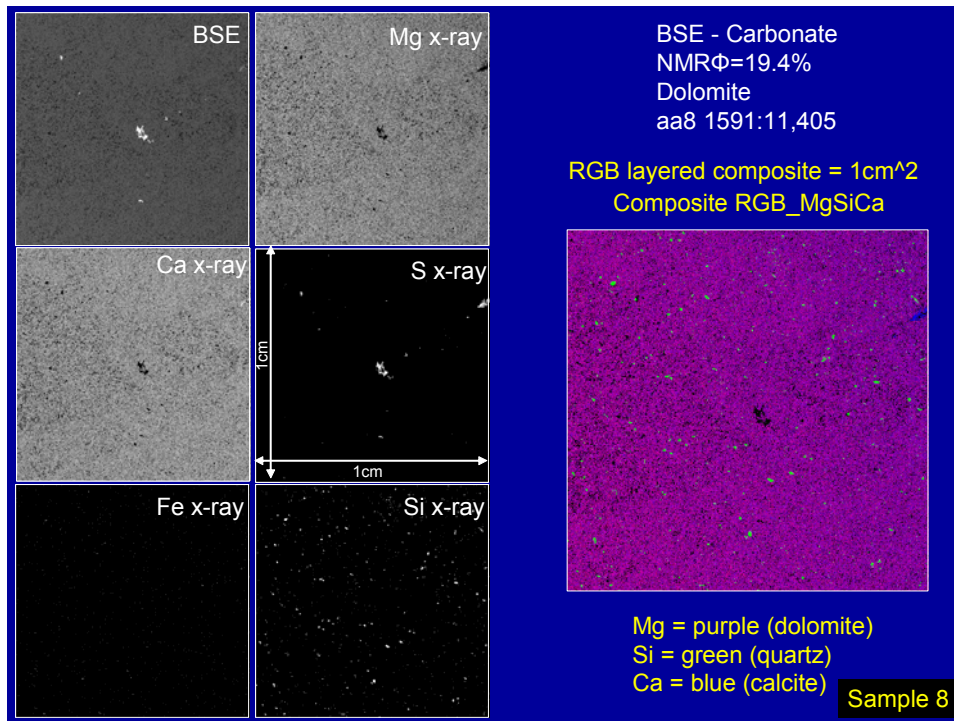




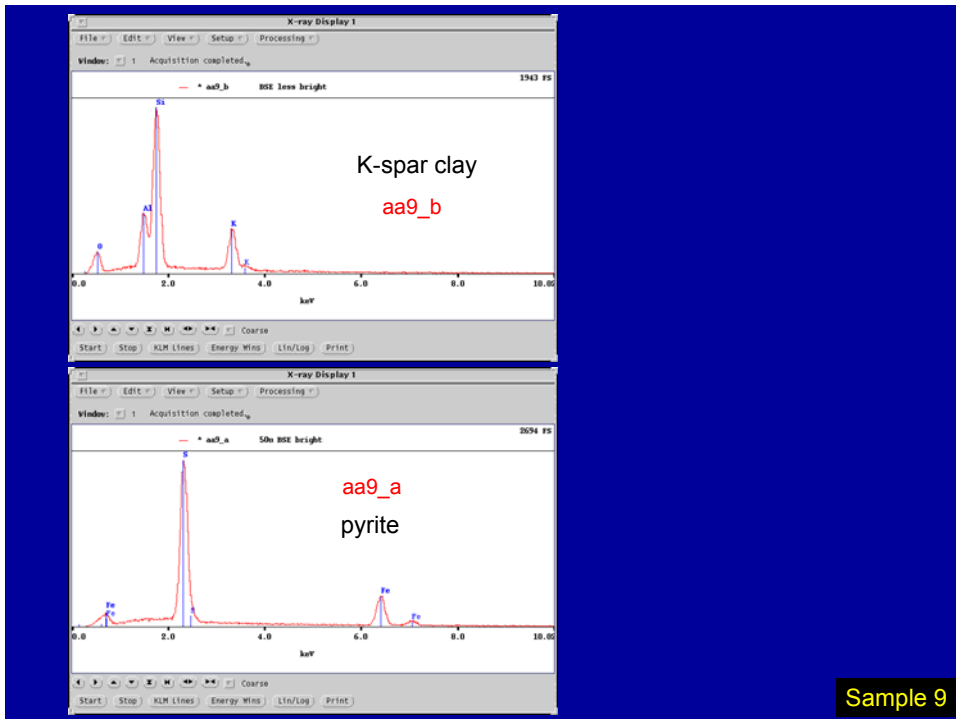
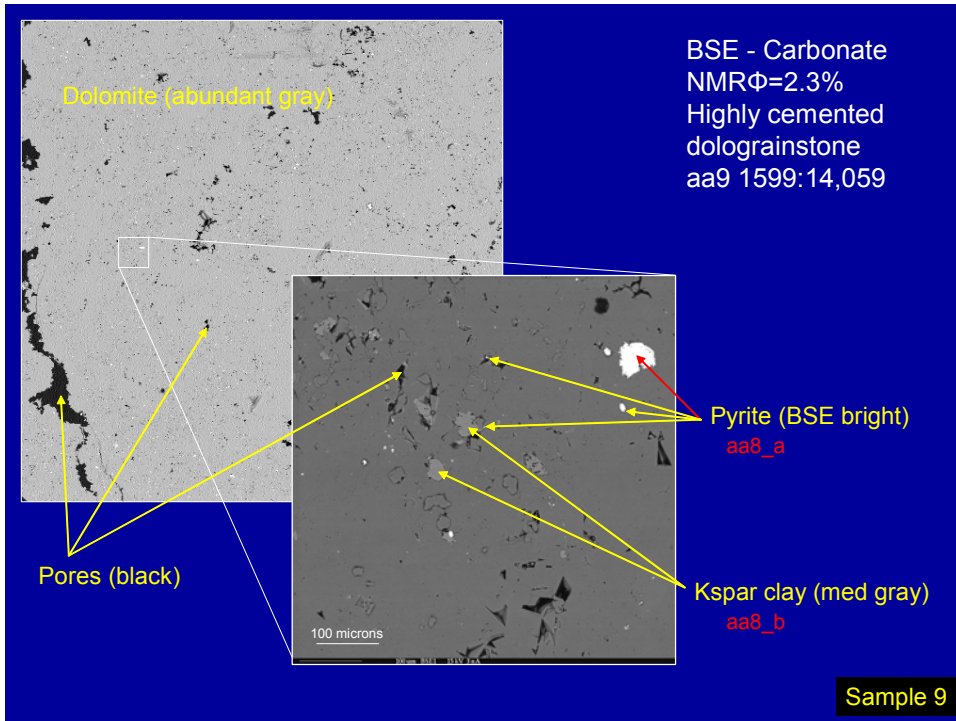


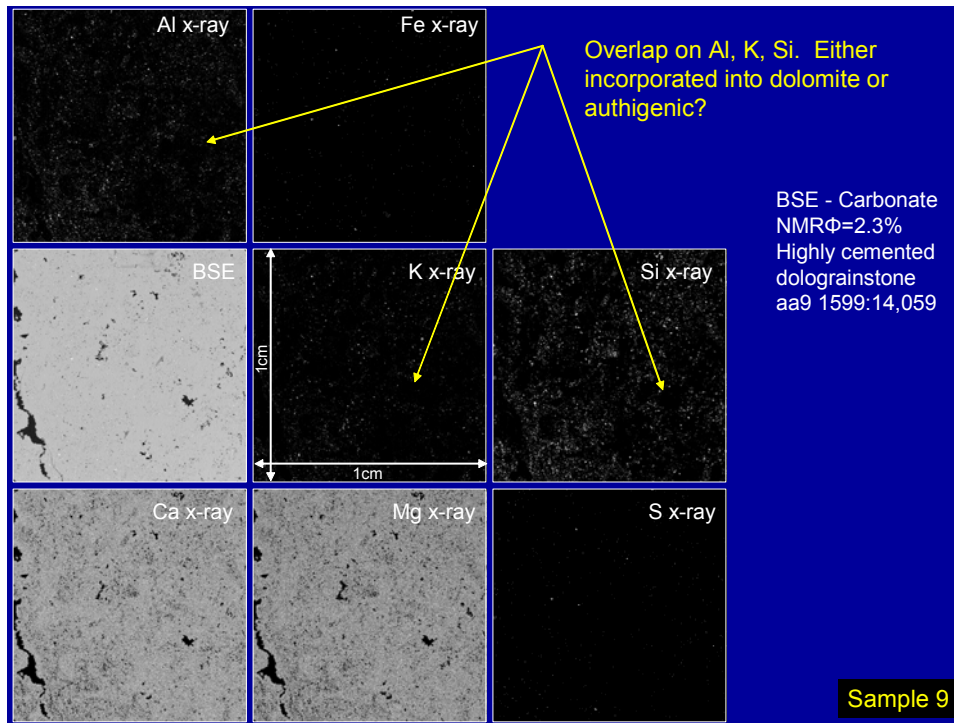












**APPENDIX G**

**VARIATIONS OF  $\rho$  (SURFACE RELAXIVITY) AND SHAPE (S/V)  
TO DETERMINE DESIRED T2 BOUNDARY VALUE**

boundary	microns	microns/sec	shape	desired T2 (seconds)	desired T2 (milliseconds)
			6=spheres		
			4=cylinders		
			2= sheets		
			S/V		
diameter	rho	shape	desired T2 (seconds)	desired T2 (milliseconds)	
20	200	6	0.02	16.67	
20	150	6	0.02	22.22	
20	120	6	0.03	27.78	
20	100	6	0.03	33.33	
20	75	6	0.04	44.44	
20	50	6	0.07	66.67	
20	40	6	0.08	83.33	
20	25	6	0.13	133.33	
20	15	6	0.22	222.22	
20	10	6	0.33	333.33	
20	5	6	0.67	666.67	
20	200	5	0.02	20.00	
20	150	5	0.03	26.67	
20	120	5	0.03	33.33	
20	100	5	0.04	40.00	
20	75	5	0.05	53.33	
20	50	5	0.08	80.00	
20	40	5	0.10	100.00	
20	25	5	0.16	160.00	
20	15	5	0.27	266.67	
20	10	5	0.40	400.00	
20	5	5	0.80	800.00	
20	200	4	0.03	25.00	
20	150	4	0.03	33.33	
20	120	4	0.04	41.67	
20	100	4	0.05	50.00	
20	75	4	0.07	66.67	
20	50	4	0.10	100.00	
20	40	4	0.13	125.00	
20	25	4	0.20	200.00	
20	15	4	0.33	333.33	
20	10	4	0.50	500.00	
20	5	4	1.00	1000.00	
20	200	3	0.03	33.33	
20	150	3	0.04	44.44	
20	120	3	0.06	55.56	
20	100	3	0.07	66.67	
20	75	3	0.09	88.89	
20	50	3	0.13	133.33	
20	40	3	0.17	166.67	
20	25	3	0.27	266.67	
20	15	3	0.44	444.44	
20	10	3	0.67	666.67	
20	5	3	1.33	1333.33	
20	200	2	0.05	50.00	
20	150	2	0.07	66.67	
20	120	2	0.08	83.33	
20	100	2	0.10	100.00	
20	75	2	0.13	133.33	
20	50	2	0.20	200.00	
20	40	2	0.25	250.00	
20	25	2	0.40	400.00	
20	15	2	0.67	666.67	
20	10	2	1.00	1000.00	
20	5	2	2.00	2000.00	

boundary	microns	microns/se S/V	shape	desired T2 (seconds)	desired T2 (milliseconds)
	diameter	rho			
	500	200	6=spheres	0.42	416.67
	500	150	6=cylinders	0.56	555.56
	500	120	6=cylinders	0.69	694.44
	500	100	6=cylinders	0.83	833.33
	500	75	6=cylinders	1.11	1111.11
	500	50	6=cylinders	1.67	1666.67
	500	40	6=cylinders	2.08	2083.33
	500	25	6=cylinders	3.33	3333.33
	500	15	6=cylinders	5.56	5555.56
	500	10	6=cylinders	8.33	8333.33
	500	5	6=cylinders	16.67	16666.67
	500	200	5=sheets	0.50	500.00
	500	150	5=sheets	0.67	666.67
	500	120	5=sheets	0.83	833.33
	500	100	5=sheets	1.00	1000.00
	500	75	5=sheets	1.33	1333.33
	500	50	5=sheets	2.00	2000.00
	500	40	5=sheets	2.50	2500.00
	500	25	5=sheets	4.00	4000.00
	500	15	5=sheets	6.67	6666.67
	500	10	5=sheets	10.00	10000.00
	500	5	5=sheets	20.00	20000.00
	500	200	4=cylinders	0.63	625.00
	500	150	4=cylinders	0.83	833.33
	500	120	4=cylinders	1.04	1041.67
	500	100	4=cylinders	1.25	1250.00
	500	75	4=cylinders	1.67	1666.67
	500	50	4=cylinders	2.50	2500.00
	500	40	4=cylinders	3.13	3125.00
	500	25	4=cylinders	5.00	5000.00
	500	15	4=cylinders	8.33	8333.33
	500	10	4=cylinders	12.50	12500.00
	500	5	4=cylinders	25.00	25000.00
	500	200	3=spheres	0.83	833.33
	500	150	3=spheres	1.11	1111.11
	500	120	3=spheres	1.39	1388.89
	500	100	3=spheres	1.67	1666.67
	500	75	3=spheres	2.22	2222.22
	500	50	3=spheres	3.33	3333.33
	500	40	3=spheres	4.17	4166.67
	500	25	3=spheres	6.67	6666.67
	500	15	3=spheres	11.11	11111.11
	500	10	3=spheres	16.67	16666.67
	500	5	3=spheres	33.33	33333.33
	500	200	2=sheets	1.25	1250.00
	500	150	2=sheets	1.67	1666.67
	500	120	2=sheets	2.08	2083.33
	500	100	2=sheets	2.50	2500.00
	500	75	2=sheets	3.33	3333.33
	500	50	2=sheets	5.00	5000.00
	500	40	2=sheets	6.25	6250.00
	500	25	2=sheets	10.00	10000.00
	500	15	2=sheets	16.67	16666.67
	500	10	2=sheets	25.00	25000.00
	500	5	2=sheets	50.00	50000.00

boundary	microns	microns/se	S/V	shape	desired T2 (seconds)	desired T2 (milliseconds)
	diameter	rho				
	1000	200	6	6=spheres	0.83	833.33
	1000	150	6	4=cylinders	1.11	1111.11
	1000	120	6	2=sheets	1.39	1388.89
	1000	100	6		1.67	1666.67
	1000	75	6		2.22	2222.22
	1000	50	6		3.33	3333.33
	1000	40	6		4.17	4166.67
	1000	25	6		6.67	6666.67
	1000	15	6		11.11	11111.11
	1000	10	6		16.67	16666.67
	1000	5	6		33.33	33333.33
	1000	200	5		1.00	1000.00
	1000	150	5		1.33	1333.33
	1000	120	5		1.67	1666.67
	1000	100	5		2.00	2000.00
	1000	75	5		2.67	2666.67
	1000	50	5		4.00	4000.00
	1000	40	5		5.00	5000.00
	1000	25	5		8.00	8000.00
	1000	15	5		13.33	13333.33
	1000	10	5		20.00	20000.00
	1000	5	5		40.00	40000.00
	1000	200	4		1.25	1250.00
	1000	150	4		1.67	1666.67
	1000	120	4		2.08	2083.33
	1000	100	4		2.50	2500.00
	1000	75	4		3.33	3333.33
	1000	50	4		5.00	5000.00
	1000	40	4		6.25	6250.00
	1000	25	4		10.00	10000.00
	1000	15	4		16.67	16666.67
	1000	10	4		25.00	25000.00
	1000	5	4		50.00	50000.00
	1000	200	3		1.67	1666.67
	1000	150	3		2.22	2222.22
	1000	120	3		2.78	2777.78
	1000	100	3		3.33	3333.33
	1000	75	3		4.44	4444.44
	1000	50	3		6.67	6666.67
	1000	40	3		8.33	8333.33
	1000	25	3		13.33	13333.33
	1000	15	3		22.22	22222.22
	1000	10	3		33.33	33333.33
	1000	5	3		66.67	66666.67
	1000	200	2		2.50	2500.00
	1000	150	2		3.33	3333.33
	1000	120	2		4.17	4166.67
	1000	100	2		5.00	5000.00
	1000	75	2		6.67	6666.67
	1000	50	2		10.00	10000.00
	1000	40	2		12.50	12500.00
	1000	25	2		20.00	20000.00
	1000	15	2		33.33	33333.33
	1000	10	2		50.00	50000.00
	1000	5	2		100.00	100000.00

**VITA**

**Name** Aaron J. Adams

**Address** MS 3115 TAMU, Department of Geology and Geophysics, Texas  
A&M University, College Station, TX, 77843

**Email Address** geoaaron@hotmail.com

**Education** B.A., Geology, Utah State University, 1999  
M.S., Geology, Brigham Young University, 2001  
Ph.D., Geology, Texas A&M University, 2005

**Professional  
Affiliations** American Association of Petroleum Geologists (AAPG)  
Geological Society of America (GSA)

**Professional  
Experience** Occidental Oil and Gas Corporation, Houston, TX – Intern  
ChevronTexaco, Bakersfield, CA – Intern  
Anadarko Petroleum Corporation, Houston, TX - Geologist